Pressure Infiltration Behaviour and Properties of Aluminium Alloy - Oxide Ceramic Preform Composites

by

Bernd Arthur Huchler

A thesis submitted to the

School of Metallurgy and Materials
College of Engineering and Physical Sciences

of

The University of Birmingham

for the degree of

Doctor of Philosophy

University of Birmingham
Birmingham B15 2TT
United Kingdom

July 2009

ABSTRACT

In the pressure infiltration processing of Metal Matrix Composites (MMCs), molten metal is injected into a porous preform. This research investigated ways to optimize the processing and properties of MMCs with Al alloy matrices. A ceramic volume fraction of 0.30 to 0.40 was used to keep a preponderant metallic behaviour and the reactivity of MgO, TiO_2, Al_2O_3-SiO_2 and Al_2O_3-TiO_2 preforms was compared to pure Al_2O_3.

Two stages were found during infiltration: first, flow initiation characterised by the dynamic wetting angle θ_{dyn} and, second, the advancing flow in the preform capillaries. Reactions were detected in the MMC but did not significantly influence the θ_{dyn}. Unsaturated fluid flow was evaluated for the subsequent infiltration stage and good agreement was found between a numerical model and experimental data.

The MMCs had improved properties compared to the pure alloy. Elastic moduli up to 148 GPa, bending strengths up to 456 MPa as well as reduced wear rate were found. The wear performance of extended ceramic ligaments, found in MMCs with spherical metal ligaments, exceeded all other materials. The improved understanding of the infiltration of preforms and the resulting MMC properties obtained in this research should lead to the development of tailorable composite materials.

ACKNOWLEDGEMENTS

I express my deepest gratitude to my supervisors at the University of Birmingham, Prof. Stuart Blackburn and Dr. Richard Harding for their excellent supervision, advice and guidance. This work would not have been possible without their help and support. I am grateful to Dr. Alwin Nagel and Prof. Gerhard Schneider of the University of Aalen for constant support and for enabling this work.

I owe my sincere thanks to the research teams at the University of Birmingham and the University of Aalen. Especially I thank Dirk Staudenecker for his constant help. I would not have been able to carry out the experimental work without his help. For their `open ears` I would like to thank Timo Bernthaler, Markus Schwenger, Mr. Salzwedel and the other team members at Aalen University and especially Marek Kremzer of Gliwice University, Poland for his support during his sabbaticals. Further I am also grateful to Paul Davies, Mick Wickins and John Wedderburn for their support in Birmingham.

I would like to thank Prof. Klein and his co-workers and especially Eugenius Pokora who enabled modelling of the infiltration process. I also want to express my appreciation to the project partners of the University of Karlsruhe, Dr. Andreas Mattern and Dr. Achim Neubrand of the Fraunhofer Institute in Freiburg. Financial support from the Landesstiftung Baden-Württemberg, Germany is acknowledged.

Most of all I would like to thank my wonderful and best friend Eva for her encouragement and patience almost throughout the course of this research work.

CONTENTS

NOMENCLATURE

Symbol	Meaning
α	shape parameter of infiltration curve
a	gradient in the infiltration curve
A_5	fracture elongation in tension
A_{gate}	gate cross-sectional area
A_{pl}	surface area of the plunger
c_{iso}	relative isostatic compression of preform
$c_{iso,max}$	maximum isostatic compression
$c_{iso,per}$	permanent isostatic compression after pressure release
$c_{iso,100}$	compression at 100 MPa isostatic pressure
c_p	heat capacity
CP, CF	constant pressure and constant flux infiltration mode
c_{pf}	specific heat capacity of fibre preform
c_{pr}	compression of the preform due to infiltration process
CT	compact tension method
CTE	coefficient of thermal expansion
c_v	volumetric compression of preform
d_{50}	median particle size
ΔG_0	free energy of formation
$\Delta\gamma_r$	contribution of reduced interfacial tension due to reaction
ΔG_r	heat of reaction due to formation of an interfacial phase
D_{Hg}	median pore size in mercury porosimetry
DSQC	direct squeeze casting infiltration
E	Young´s modulus
E_c, E_1, E_2	Young´s modulus of the composite, reinforcement phase 1 and 2
$E_{c,lower}$, $E_{c,upper}$	lower and upper bound of composite Young´s modulus
$E_{c,ROM}$	Young´s modulus calculated using rule of mixture (ROM)
E_{dyn}	Young´s modulus measured in resonance mode
E_{iso}	volumetric modulus in isostatic compression
F_N	normal force in tribological testing
f_{PFA}	fraction pore forming agent in green part
F_R	friction force
G	Gibbs energy
γ_{Hg}	surface tension of mercury
γ_{lv}	surface tension of a liquid
GP	gas pressure infiltration mode
γ_{Rl}	surface energy of the liquid-solid reaction product interface

Symbol	Meaning
γ_{Rv}	surface energy of the interface reaction product- atmosphere
γ_{sv}, γ_{sl}	surface energies of solid-vapour, solid-liquid interfaces
η	viscosity of water in permeabilty measurements
H_M	heat of fusion of metal phase
HPDC	high pressure die casting
ISQC	indirect squeeze casting
K	preform permeability
k	ratio of window to cell size in foamed preforms
K_{IC}	fracture toughness in mode I
K_{MIP}	permeability in mercury porosimetry
K_r	relative preform permeability
K_s	specific preform permeability
K_{si}	specific permeability in pressing direction
$K_{s\parallel}$	specific permeability for flow parallel to the fibre axis
K_{sp}	specific permeability parallel to pressing direction
$K_{s\perp}$	specific permeability for flow perpendicular to the fibre axis
λ	geometrical factor of powder bed
l_c	length of steel cylinder
μ	fluid viscosity
m	Weibull modulus
m_0	preform mass weighed in air
m_1	preform mass saturated with fluid
m_2	preform mass weighed immersed in the fluid
μ_i	chemical potential
N_1, N_2	solvent mole fractions of liquid 1 and 2
ν_i	stoichiometric coefficient
P_{appl}	applied pressure
PC	cellulose particle pore former
P_f	probability of failure
PF	carbon fibre pore former
PFA	pore forming agent
P_H	initial Hertzian pressure
P_{iso}	isostatic compression pressure
P_{loc}	local pressure
P_{met}	melt pressure in the direct squeeze casting tool
P_{MMC}, P_{IS}	performance coefficient of MMC and infiltration alloy IS
$p_{O2,calc}$	calculated oxygen partial pressure
θ	contact or wetting angle

Symbol	Meaning
θ_0	initial contact angle in reactive wetting
θ_c	volume fraction of the ceramic phase
θ_{dyn}	dynamic contact angle
θ_{eq}	contact angle in equilibrium in reactive wetting
θ_{Hg}	wetting angle of mercury on ceramics
θ_{intr}	intrinsic wetting angle
θ_l	volume fraction of the intruded liquid
θ_{min}	intermediate minimum contact angle due to reactions
θ_{st}	static contact angle
R_a	arithmetic mean surface roughness
r_c	radius of steel cylinder
ρ_f	fibre density
ρ_{fl}	density of fluid
ρ_M	metal melt density
ρ_p	bulk density of ceramic particle
ρ_r	raw density
r_{sf}	mean radius of fibre
S	saturation of preform
σ_0	characteristic stress at fracture
s_c	Compression strength
σ_c, $\sigma_{f,}$ σ_m	frailure strength of composite, fibre, matrix
SDTA	simultaneous thermal differential method
SEVNB	single edge V-notched bars
S_i	surface area per unit volume of porosity
S_{iHg}	specific surface area per unit of volume porosity
S_{int}	integral saturation
S_{loc}	local saturation
S_{ml}	specific area per unit preform volume of newly formed aluminium
S_{pHg}	surface area per unit volume preform from mercury porosimetry
$s_{plunger}$	displacement of the upper punch
S_{sBET}	surface area per unit mass from gas absorption measurements
S_{sHg}	specific surface area per unit of mass - Hg intrusion method
s_x, s_y, s_z	dimensional change in the x, y and z-direction of the preform
T_m	melting temperature of a solid
$T_{melt,die}$	melt temperature in the die
$T_{preform}$, T_{edge}, T_{centre}	Local temperatures in the direct squeeze casting tool
T_{ref}	reference temperature in differential thermal analysis
T_{sample}	sample temperature in differential thermal analysis

Symbol	Meaning
TYS	tensile yield strength
UTS	ultimate tensile strength in tension
v_0	superficial fluid velocity
V_f	volume fraction of fibres in a preform
V_p	volume fraction of particles
v_{pl}	velocity of the plunger
V_{po}	pore volume fraction in foamed preforms
V_{tot}	total intrusion volume in mercury porosimetry
W_{ad}	work of adhesion
We	Weber number
W_i	work of immersion
w_w	width of wear path after tribology test
κ	geometrical factor of fibre
Φ_C	closed cell porosity
Φ_{ext}	residual filled porosity after mercury intrusion porosimetry
Φ_{Hg}	total porosity intruded by mercury
Φ_{op}	open cell porosity
Φ_P	open porosity
Φ_{PFA}	porosity formed by pore forming agent
Φ_{Tot}	total porosity

1. INTRODUCTION

To make a lightweight material possessing high strength even at higher temperatures, it would be desirable to take advantage of the high strength of low density ceramic materials. Ceramics exhibit brittle behaviour, lacking the required fracture toughness for most heavy duty applications. In contrast, low density metallic materials such as aluminium and magnesium and their alloys, which possess the desired fracture toughness, show low strength at temperatures above 250°C. Thus, for such applications, a composite material combining the desirable properties of two different phases might be vastly superior. The main problem is to effect the combination in such a manner as to exploit the desirable features of both components and thereby maximize the material properties.

Aluminium alloys are quite attractive due to their low density, their capability to be strengthened by precipitation, their good corrosion resistance, high thermal and electrical conductivity, and their high damping capacity. The combination of an aluminium alloy and a ceramic material gives a group of materials known as aluminium matrix composites and these have been widely studied since the 1920s [(1)] and now are used in sporting goods, electronic packaging and automotive industries. They offer a large variety of mechanical properties depending on the chemical composition of the matrix alloy and the reinforcing phase which is predominantly alumina or silicon carbide but MgO, TiO_2, SiO_2 and CaO may also be considered. The aluminium matrices are in general Al-Si, Al-Cu or Al-Mg alloys. In the 1980s, the transportation industries began to develop discontinuously-reinforced aluminium matrix composites. These aluminium alloy matrices with dispersed ceramic particles are very attractive due to their isotropic room temperature mechanical properties. They are low cost due to cheap processing routes and low cost discontinuous reinforcements. Due to the solely three dimensional connectivity of the metal phase, the main drawbacks of

these materials are the detrimental properties regarding creep and mechanical properties at temperatures above 250°C.

In recent years, there has been interest in metal matrix composites with interpenetrating networks [2]. Using the Newnham taxonomy [3], which is based on phase connectivity, such materials are designated 3-3 composites since both phases have connectivity in three dimensions. The combination of materials means not only choosing component phases with the right properties, but also coupling them in the best manner. Connectivity is a key feature in property development in multiphase solids, since physical properties can change by many orders of magnitude depending on the manner in which connections are made.

The infiltration of a porous ceramic body, called the preform, with a liquid metal represents an attractive route to fabricate interpenetrated composite materials. The preform route offers a wide variety of types, morphologies and metal volume contents. Thus tailored microstructures with interpenetrated networks can be realised. The properties of the porous ceramics, the metal melt and their interactions are most important regarding the resulting material properties. Furthermore, the local reinforcement of cast metal components is possible. However, industrial applications are often limited mainly by lack of precise knowledge of the influencing factors.

Concerning the metal volume fraction, there two forms which have been well studied. One with less than 0.50 and one with more than 0.70. For the higher content chopped fibre and foam-based ceramic materials are used and for metal-reinforced ceramics not more than 0.50 of the metallic phase is used in order to maintain a predominant ceramic behaviour of the resulting materials. The range between 0.50 and 0.70 has not been widely investigated up to date. This is mainly due to the lack of commercially available preforms.

The present work concentrates on preforms of particulate oxide ceramics in the porosity range of 60 to 70%. To investigate the infiltration behaviour, the preform pore structure and chemistry were varied across this porosity range. The influence of pore structure and reactivity on dynamic wetting angle and high velocity infiltration behaviour was investigated and modelling this infiltration behaviour with a unsaturated flow model was validated.

An investigation of the MMC microstructures by detailed image analysis was carried out to determine the important microstructural parameters. The mechanical properties of strength and toughness as well as tribological characteristics were investigated and compared to the unreinforced alloy and MMCs based on commercially available preforms.

2. LITERATURE REVIEW

2.1. Materials selection

The objective in research on new composite materials is to optimise a number of parameters. Common parameters are strength to weight ratio and to cost. Conflicts arise, because the choice that optimises one parameter will not in general do the same for the others. Then the best choice is a compromise, optimising none but pushing all as close to their optima as their interdependence allows. When there are two or more objectives, solutions rarely exist that optimise all properties at once.

Metal matrix composites consist in general of a metallic matrix and a ceramic reinforcing phase. Along with the ceramic volume content there are other parameters which determine the properties, either of material performance or technological interest. The general properties and the factors that influence them are presented in this Literature Review. To achieve the maximum potential from a new material, all interacting parameters have to be taken into account when selecting the reinforcement and the metal matrix.

2.1.1. Metal Matrix

Apart from pure aluminium, alloys of the groups of Al-Si and Al-Mg are predominantly used in technical applications including the matrix in aluminium MMCs. Aluminium-silicon alloys are light alloys widely used for casting components for commercial and safety critical applications. The Al-Si alloys comprise 85% to 90% of the total weight of cast aluminium components produced [(4)]. Silicon is found to improve the fluidity in the molten state, providing excellent castability to the alloy [(5)].

For infiltration of a porous body, the properties of the liquid metal are of interest. The rate of oxidation of liquid Al and its alloys is orders of magnitude faster than that of the solidified

material [6]. The oxide film is formed all along the liquid-gas interfaces when oxygen is present. Nearly all oxygen on the surface reacts with the melt to form alumina, since the solubility of oxygen in aluminium is extremely low, given to be 0.006 at. % [7]. In Al melts exposed to atmospheres, the oxygen consumption is the dominant reaction. As reported by Zheng and Reddy [8], aluminium melts enclosed in a sealed container with residues of atmosphere showed complete consumption of oxygen before the atmospheric nitrogen was consumed to form aluminium nitride (AlN).

For pure aluminium and AlSi alloys, the oxide film is initially an amorphous film which transforms instantaneously to crystalline γ-alumina, which is a metastable allotropic phase of Al_2O_3. After an incubation period, the crystal lattice changes to the most stable α-Al_2O_3 modification, usually referred to as corundum. The change in crystalline structure results in considerable tensile stress which eventually leads to rupture of the oxide film. This rupture enables oxidation at a faster rate. The formation of Al_2O_3 on liquid aluminium is prevented from forming at an oxygen partial pressure below 10^{-49} bar which is lower than the oxygen partial pressure in outer space [9].

Measurements of the rate of thickening of the film show its growth to be impressively fast and it depends strongly on the surrounding atmosphere. For example, when water vapour is present, the oxidation rate is increased by a factor of 4, as described by Gourmi and Joud [10]. In dry atmospheres,the oxide formation rate reaches approximately $7x10^{-7}$ kg per square meter of melt surface per second which means formation of more than two monolayers of aluminium oxide per second.

The oxidation behaviour of liquid Al-Mg alloys is different to that of pure Al and AlSi alloys. Campbell [6] proposed that the addition of more than 0.05 wt.% Mg to aluminium results in

changes in the oxide film chemistry. A mixed oxide $MgO \cdot Al_2O_3$ spinel is formed. According to Ransley and Neufeld [11], above 2 wt.% Mg, the oxide film is pure MgO.

This is in accordance with the thermodynamic calculations of McLeod *et al.* [12] who showed that the spinel phase on Al-Mg melts did not occur until a Mg content of 0.5 wt.% is reached (Figure 2.1). At fixed Mg content and higher melt temperatures, α-Al_2O_3 is the thermodynamically preferred phase. At temperatures slightly above the melting point, solely MgO is formed at Mg contents higher than 0.8 wt.%. The stability decreases towards higher temperatures to form the spinel phase.

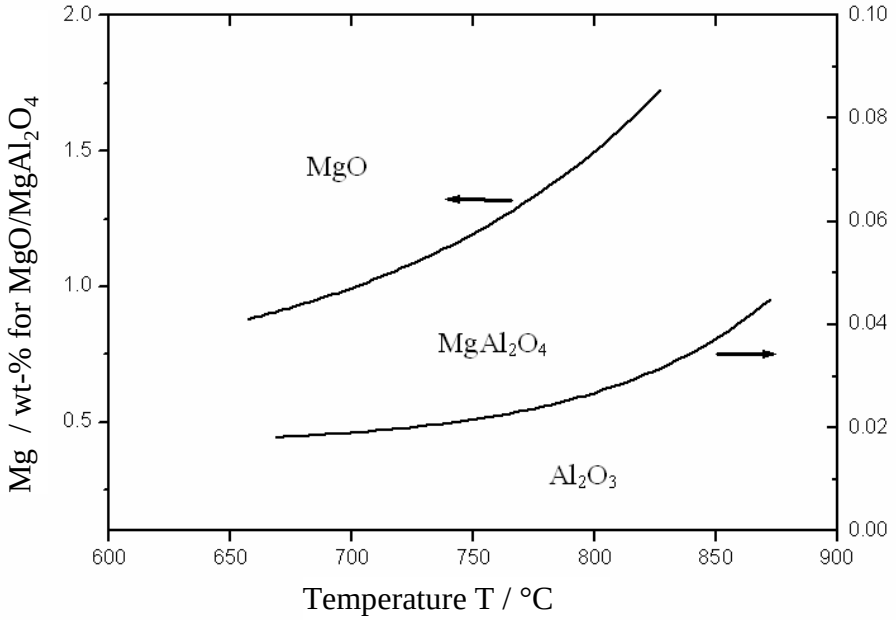

Figure 2.1 Thermodynamic stabilities of Al-Mg oxide in Al-Mg alloys [12].

The vapour pressure of Mg at a given temperature is significantly higher than that of Al [13]. In high vacuum experiments, the evaporation of Mg from liquid Al-Mg-Si alloys resulted in protection of the melt pool from oxidation of Al. Samples containing Mg generally had a visually perfect, mirror like finish upon melting. The Mg vapour as well as Mg deposited on the furnace walls, acted as an oxygen getter, thus protecting the sample surface from heavy oxidation. This conclusion is supported by Silva and Talbot [14] who showed that in liquid Al-

Mg alloys, Mg oxidizes preferentially to form MgO and that this is the only oxide found during the initial stages of oxidation.

Magnesium is a powerful surfactant as well as a reactive element. The basic principles involved in improving the wetting of ceramics by a metal melt are categorized into three different groups as suggested by Pai *et al.* [15]:

1. Increasing the surface energy of the solid
2. Decreasing surface tension of the liquid
3. Decreasing the solid/liquid interfacial energy at the reinforcement/matrix interface

Mg is a highly reactive element and can form a thermodynamically stable oxide by reducing oxide-based ceramics at the synthesizing temperature of most metal-ceramic contacts.

The pressureless infiltration of preforms with aluminium alloys has been realized using the Lanxide process [16]. Here Mg addition allows wetting of the preform. Using a N_2 atmosphere and temperatures above 1000°C, magnesium nitride is formed in front of the advancing melt, enabling wetting and capillary rise in the pores. A route for the pressureless infiltration of Al_2O_3 is enabled using the oxygen-gettering properties of Mg [17].

Commercially used Al-Mg cast alloys contain up to 10 wt.% of Mg. As shown in the binary phase diagram of the Al-Mg system in Figure 2.2, the main phases at room temperature are the α- and the β-phases. The equilibrium solubility of Mg is about 2 wt.% and the β-phase consists of the stoichiometric intermetallic Al_3Mg_2.

Surface tension is an intrinsic property of all liquids and is due to an incomplete coordination of the atoms at the liquid-gas interface. Atoms in the bulk of the liquid are completely surrounded by other atoms, while those at the surface are in contact with others on the surface

or inside the bulk fluid only. Interatomic attractions cause an uneven pull on the surface atoms, drawing them into the body of the liquid and resulting in a curvature of the surface as the liquid tries to assume a shape that has the minimum surface area. Thermodynamically γ_{lv} is defined as the surface free energy per unit area (J/m²). From a dynamic point of view, γ_{lv} represents the work required to create one unit of additional surface area at constant temperature. The units J/m² are equivalent to N/m.

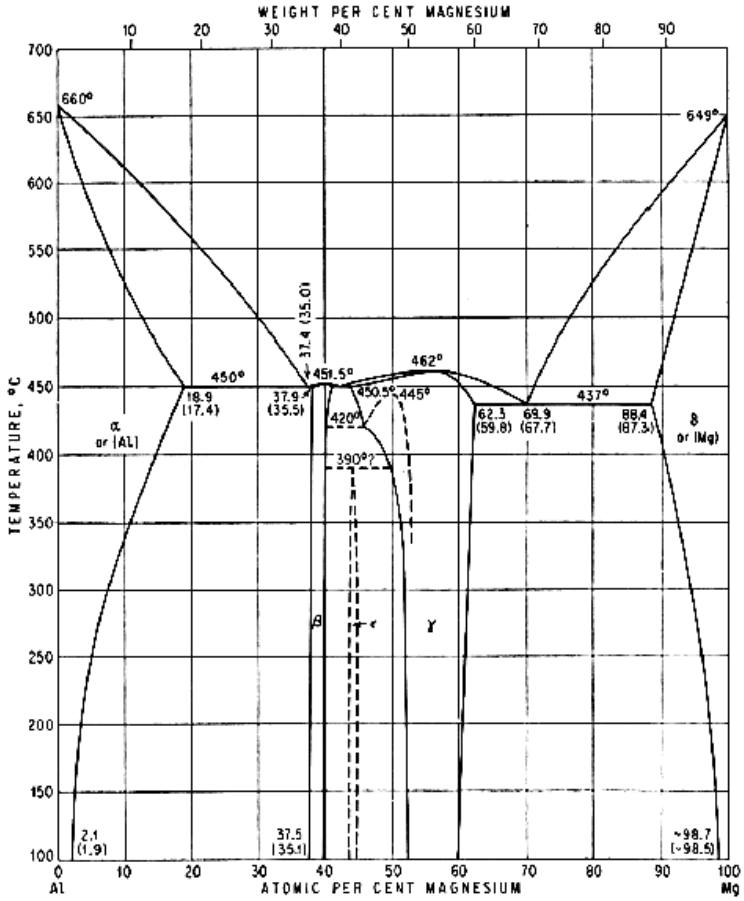

Figure 2.2 Binary phase diagram of the system Al-Mg [27].

The γ_{lv} of liquids usually decrease with increasing temperature. Allen [18] reviewed the γ_{lv} of liquid metals and proposed that the value for pure Al could be calculated as a function of temperature as:

$$\gamma_{lv(Al)} = (0.914 - 0.0036(T - T_m)) \qquad \text{Equation 1}$$

with T, the actual temperature and T_m the melting point and γ_{lv} in N/m. The effect of oxygen on the γ_{lv} of liquid aluminium was evaluated by Gourmi and Joud [10] who found that the reduction of the surface tension was proportional to the oxide coverage on the surface. A mean value of 1.050 N/m was found for the surface tension of atomically clean aluminium at 700°C. In contrast, a mean value of 0.871 N/m corresponded to saturation coverage by a homogenous layer [19,20]. The higher values resulted from chemically pure aluminium and the lower values are determined using contaminated conditions which led to oxygen coverage as shown in Figure 2.3. It could be shown that the surface coverage of one monolayer led to a reduction in surface tension of more than 11%.

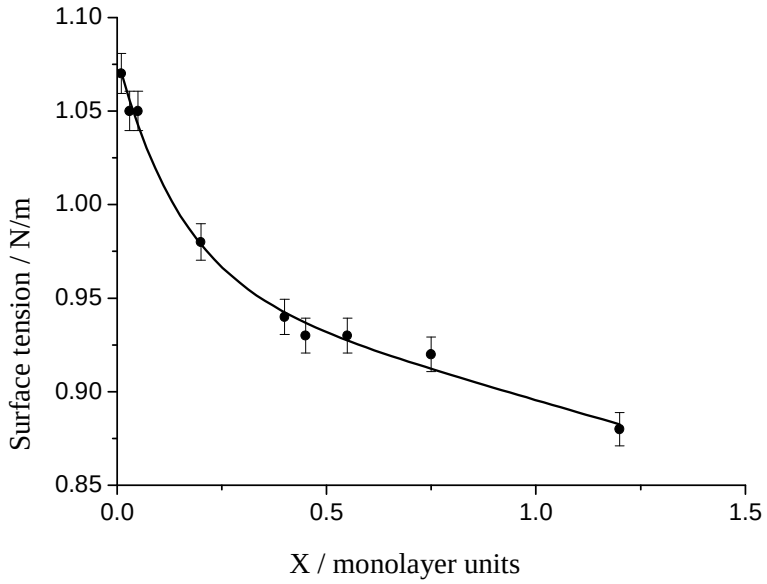

Figure 2.3 Variation of surface tension of molten Al with level of oxide coverage [20].

Rocher *et al.* [21] achieved metallic surfaces on Al melts even at relatively high oxygen partial pressures. The thin Al_2O_3 layer on the liquid melt was removed by additions of K_2ZrF_6, a well known fluxing agent used in Al melts. The predominant effect to improve cleanliness of the melt is the dissolution of the thin alumina layer coating the liquid metal by the fluorides.

The surface tension of a pure liquid melt is significantly affected by binary additions [18]. In general the γ_{lv} of Al is observed to decrease with increasing levels of Si, Mg and Sr. Solutes

that are most effective in decreasing the surface tension of the solvent typically exhibit surface tensions lower than the solvent [22]. Si, Mg and Sr exhibit lower surface energies as compared to Al and hence also decrease the surface tension [23].

The linear rule of mixture provides a first approximation for the surface tension of the resulting solution in terms of the surface tensions γ_{lv1} and γ_{lv2} of the pure components 1 and 2 respectively [18]. Thus

$$\gamma_{lv12} = N_1\gamma_{lv1} + N_2\gamma_{lv2} \qquad \text{Equation 2}$$

where N_1 and N_2 are the solvent mole fractions of the components 1 and 2 respectively. Experimentally, the surface tension almost always deviates negatively from that predicted by Equation 2. Moreover, the latter is inconsistent with thermodynamics since the liquid surface is found to be enriched with the component with the lower γ_{lv} [24].

The addition of Si to the Al melt results in minor reductions in γ_{lv} as shown by Koerber and Loehberg [25]. The addition of 12 wt.% Si to pure Al reduces it from 0.84 N/m to 0.83 N/m which is in the range of γ_{lv} scatter of contaminated pure Al melts. In presumably more accurate measurements, the latter value was confirmed with an A356 alloy where γ_{lv} ranged between 0.801 and 0.889 N/m [19]. Koerber and Loehberg evaluated the effect of other alloying elements on the surface tension of Al melts. It is interesting to note that very low additions of Na in the range of 0.1 wt.% reduce γ_{lv} by more than 35%.

The Si in Al alloys plays an important role in the production of Al/SiC MMCs. As an alloying element it retards the formation of the unwanted intermetallics Al_4C_3 and Al_4SiC_4 [26] which account for the brittle character of the composite materials. Compared to pure Al in oxide ceramic systems, no significant influence of Si additions on composite ductility could be observed. There is a eutectic in the Al-Si system at a Si mass fraction of 11.7 % (Figure 2.4).

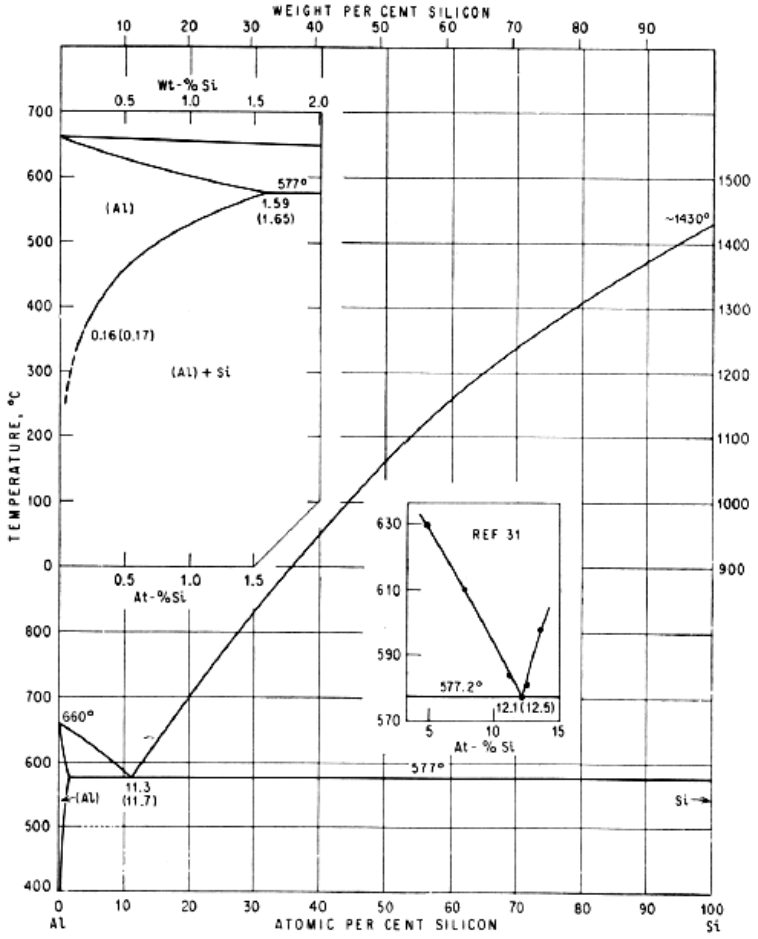

Figure 2.4 Binary phase diagram of the Al-Si system [27].

Apart from modified AlSi alloys with additions of Sr and Na [28], solidification at typical casting cooling rates results in needle-like shaped eutectic Si precipitates. As shown by experimental studies on Al-Si alloys, for a fixed volume content of the brittle Si precipitates, the number of particles has a strong influence on the resulting mechanical properties. The phenomenon was verified by Saigal and Berry [5] who showed that smaller and more numerous particles led to improved mechanical properties. It was found empirically that, for a given volume fraction of silicon, the tensile strength and ductility are strongly related to the dendrite arm spacing. However, finite element analysis showed that the particle size and not the dendrite arm spacing controls the bulk mechanical properties. A reduction in particle size by a factor of two at a constant volume fraction resulted in a significant reduction in the crack

initiation stress of 25 %. Further, it was shown, that the aspect ratio of the particles has an influence on crack initiation where larger aspect ratios of 4 showed lower crack initiation stresses than those of perfect round particles. This important conclusion almost certainly applies to other systems containing hard, brittle particles in a ductile matrix, such as particulate-reinforced metal matrix composites [6].

2.1.2. Size and morphology of the reinforcement

Fibrous reinforcements are of interest due to their promising properties . However, the strength of fibre-reinforced materials strongly depends on the size of the fibre itself.

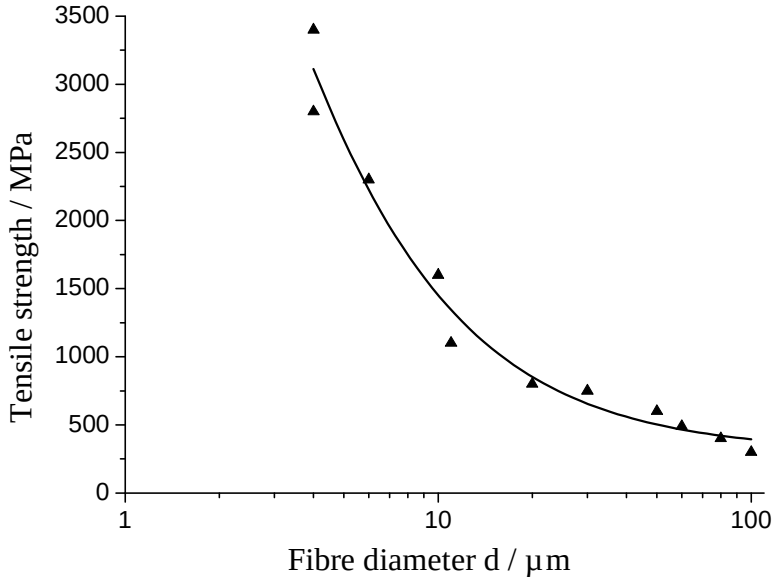

Figure 2.5 Tensile strength of glass fibres in correlation to the fibre diameter [29].

According to the Griffith law [29], at fixed length, the smaller the fibre diameter the higher the tensile strength. This effect is attributed to the increase in defect-free distance with decreasing diameter. As shown in Figure 2.5, the strength of glass fibres in correlation to the fibre diameter exhibits a steep increase below 20 µm. Nevertheless, the large increase in performance could not be achieved in Al MMCs reinforced with short fibres as shown by Kaufmann *et al.* [30] . In some cases the room temperature strength was decreased below the level of that of the unreinforced alloy.

The size and morphology of the metal and the ceramic phase play an important role on the properties of the final composite material. As reported by Clyne and Withers [31], if the reinforcement is large, which means in the range of 1-100 µm, the particles make a negligible contribution to strengthening by Orowan inhibition of dislocation motion and therefore the strengthening effect is lower than for particles with a size below 1 µm, shown in Figure 2.6.

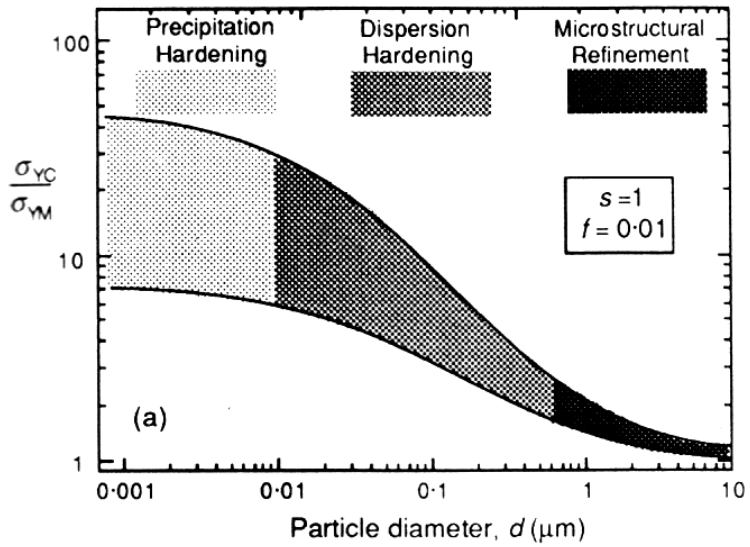

Figure 2.6 Schematic illustration of the ratio of σ_{YC} (yield strength composite) to σ_{YM} (yield strength pure metal) as a function of particle size [31] of a particle reinforced metal. The ratio was s=1 and the volume fraction f was 0.01.

For MMC materials, fabrication and final component costs are higher than those of conventional materials. Current price ratios compared to particulate ceramics are 50 for short fibres and 500 for continuous fibres [32]. Concerning the processing of MMCs, molten metal mixing or infiltration are at the low cost end of the spectrum and diffusion bonding is at the high cost end [33]. Thus particulate preform infiltration is the predestined route for economic MMC fabrication and should be the focus of further investigations.

The main types of ceramic particle reinforcements reported in the literature are α-Al_2O_3 and SiC [34]. Most of the particulate materials are taken from the abrasive industries. A highly wear resistant material embedded in a soft Al matrix possesses superior properties for frictional applications [35]. On the other hand, the machining of such materials is difficult.

Beffort [36] suggested that even though most of the components are fabricated using a near-net shape route, machining cost can become the principal cost factor which makes these materials less attractive. The higher costs are attributed to the tooling material [36].

The machinability of a MMC material depends on several factors. First of all the volume content, V_f , of the reinforcing phase plays a major role. It has been shown that an increase in Al_2O_3 V_f from 0.10 to 0.20 reduced tool life to less than 40% [37], as well as increasing the cutting forces and decreasing the surface finish quality [38]. The ceramic type has an influence in that, the higher the hardness of the reinforcement, the lower the tool life [37]. Futhermore, the structure of the MMC has an influence on machinability. At fixed volume content, finer particles are much easier to machine than coarser ones [36]. Brown and Klier [39] patented a MMC with small particles, which is much more suitable to low wear machining than materials reinforced with large particles. This was shown when comparing the machinability of Duralcan, a cast-MMC material with 20 volume % SiC-particles of 10-15 µm average particle size, with that of a MMC reinforced with fine Al_2O_3-particles of 0.2 µm mean diameter. As shown by Ejiofor [40], the machining of hypereutectic Al-Si alloys was improved as the silicon particles became finer and more evenly distributed. Even though the machining properties are improved by small particles, Clyne and Withers [31] stated that, when regarding frictional applications, the tribological properties may be diminished when using finer particles.

As well as the tribological behaviour, the mechanical properties of MMCs are determined by the reinforcement shape and volume fraction. Regarding the thermomechanical properties, it was shown in the review of Legzdins *et al.* [41] that the reinforcement volume fractions of 0 to 0.30 and of 0.45 to 0.7 have been widely investigated whereas there is little information about MMCs with a ceramic volume fraction in the range of 0.30 to 0.40.

The strengthening in MMCs is divided into two categories: direct and indirect strengthening [42]. In the direct mode, the applied load is transferred from the weaker matrix, across the matrix-reinforcement interface, to the typically stiffer reinforcement. Due to the lower aspect ratio of particulate materials, load transfer is not as efficient as in the case of continuous fibre reinforcement, but is still significant in providing strengthening [43].

Upon cooling from casting temperatures, dislocations form at the reinforcement/matrix interface due to the thermal mismatch and thermally-induced dislocation punching results in indirect strengthening of the matrix [44]. The effect of indirect strengthening is difficult to quantify. With an increase in the reinforcement volume fraction, higher elastic moduli, macroscopic yield and tensile strengths were observed, coupled with lower ductility.

Ductility falls off rapidly such that, at relatively low reinforcement volume fractions of about 0.20, the elongation of most MMCs is below 5%. The lower ductility at higher volume fractions can be attributed to the earlier onset of void nucleation with increasing amount of reinforcement. It has been found [42] that tensile ductility increases as the particle size decreases which may be attributed to an increase in the ceramic particle strength with a decrease in particle size. Therefore the probability of strength-limiting flaws existing in the volume of the reinforcement decreases.

Microplasticity in the composites has been attributed to stress concentration points in the matrix at the poles of round reinforcing particles and/or at sharp corners of irregular shaped reinforcing particles [45]. The initial micro-yielding stress decreases with increasing volume fraction, as the number of stress concentration points increases.

The primary factors which determine the yield strength of the MMC are that of the matrix and the reinforcement volume fraction. Significant secondary factors include the matrix/

reinforcement interface and reinforcement shape. Yield strength data for randomly oriented fibre reinforced MMCs is rarely found in the published literature.

Model predictions for strength are still under development since strength is a complex function of the composite microstructure [46]. Numerous models have been developed with the majority being the law of mixture, shear lag, Eshelby or dislocation type models [47]. The dislocation models can be further classified based on their selected contribution of Orowan strengthening, grain and substructure strengthening, quench hardening and work hardening [47]. There is still a lack of reliable predictive capability. Since the strength depends strongly on the matrix properties and nature of the reinforcement/matrix interface, methods which incorporate both load sharing and matrix strengthening approaches will be needed, as reported by Wu and Lavernia [48].

Long *et al.* [49] published experimental results for pure Al and Al alloy composites reinforced with continuous and chopped alumina fibres (Saffil™ - Saffil is a trademark of ICI Americas, Inc., Wilmington, DE). An extract of their results is listed in the mechanical properties summary in Table 2.1. It has been shown that, when using identical processing conditions, in general the maximum strength of continuously reinforced composites was higher than that of chopped fibre composites, even when the strength of the matrix alloy, which was pure aluminium for the continuous fibres and AlCu4MgAg for the chopped fibres, was lower in the higher strength material. This higher strength was a result of the higher volume fraction of the reinforcement in combination with the improved strengthening effect of continuous fibres. For reasons of direct comparison, an equal reinforcement volume fraction should be aimed for. However, in general for continuous fibres the lower limit in volume fraction was around 0.50 and the upper limit of chopped fibres was 0.30, excluding direct comparison of these two MMC material groups.

Long *et al.* [49] proposed a model to predict the strength of fibre reinforced MMCs based on a modified Rule of Mixture (RoM) as follows (Equation 3):

$$\sigma_c = \kappa\sigma_f V_f + (1 - V_f)\sigma_m \qquad \text{Equation 3}$$

where σ_c, σ_f and σ_m refer to the failure strengths of composite, fibre and matrix, respectively; V_f refers to fibre volume fraction, κ is the geometrical factor with consideration of the interfacial bonding behaviour. For chopped fibre composites a κ of 0.27 or 0.375 has been used to account for the random orientation. Using these values, the measured composite strength was underestimated by a factor of 1.3 to 1.5 in the chopped fibre volume fraction range V_f of 0.20 to 0.30, indicating the need for better understanding of the strengthening mechanisms of discontinuously-reinforced composites. The same research group published strength data for MMCs reinforced with SiC (F500) preforms with a mean particle size of 4.6 µm [50] and a ceramic volume fraction V_f of 0.53. The matrix and the infiltration processing conditions were similar to that of a Saffil™ fibre MMC with a V_f of 0.15. The SiC reinforced MMC showed a significantly lower strength of 346 MPa compared to 514 MPa of the fibre-reinforced MMC as shown in Table 2.1.

Kniewallner [51] investigated the infiltration behaviour and the mechanical properties of Saffil™ preforms infiltrated with different Al alloys on a high pressure die casting machine. Starting from the pure alloy processed in the same conditions, the fibre volume fraction was altered from 0.135 to 0.20. The latter was reported to be the maximum in commercially available preforms. The addition of 13.5 volume % Saffil™ fibres increased the UTS of an AlSi9Cu3 alloy from 227 to 235 MPa, whereas the same addition increased the UTS of an AlMg9 alloy from 220 to 290 MPa. The same addition had no effect on the UTS of an AlSi12 alloy. At 20 volume % of reinforcement a low reinforcing effect was observed in AlSi12: the UTS was still lower than that of the pure alloys AlSi9Cu3 and AlMg9.

It is interesting to note that, for AlMg9 and AlSi9Cu3 matrices, the tensile yield strength (TYS), which is the important parameter for reversible loading capacity of a material, showed the opposite behaviour to the UTS. Comparing the pure alloy and the maximum reinforcement volume fraction, the TYS reduced from 132 MPa to 98 MPa and from 168 to 130 MPa for AlSi9Cu3 and AlMg9 respectively.

Prielipp [52] investigated Al-Al_2O_3 MMCs infiltrated using a gas pressure infiltration (GPI) method. The ceramic volume fraction was 0.75. The aim was to increase the fracture toughness of the ceramic material using a metal phase. The variation in metal ligament size, representing the size of the metal between the ceramics, influenced the strength of the metal toughened ceramics. The smallest ligaments showed an intermediate strength of 630 MPa whereas the largest size resulted in the lowest bending strength of 510 MPa. The highest strength of 710 MPa was observed for a mean ligament size of 0.25 µm.

In the work of Beyer [53], Al_2O_3-TiO_2 hybrid preforms were infiltrated with Al. The target was to synthesise $TiAl_3$ - Al_2O_3 in a reactive heat treatment step in accordance to the reaction:

$$3\ TiO_2 + 13\ Al \rightarrow 3\ TiAl_3 + 2\ Al_2O_3 \qquad \text{Equation 4}$$

The bending strength of the initial, non-reacted material was reported to be 642 MPa and after reaction it reduced to 398 MPa.

In comparison to the rather extensive experimental results published on mechanical properties of chopped fibre reinforced MMCs, information on MMCs based on particulate preforms was found to be rather scarce. For the 0.30 and 0.40 ceramic volume fraction, which was target for the MMCs of the present work, no data could be found. For MMCs based on foamed preform only elastic properties such as Young´s modulus or compressive properties like hardness and compression strength have been published [54]. This may be attributed to the lack of

appropriate specimen preparation methods or the poor mechanical properties in tensile loading.

The experimental strength testing methods of the different research groups were derived from their main research materials. In general, groups concentrating on ceramics rely on ceramic material testing methods. Therefore for strength testing, bending tests were conducted as shown in Table 2.1 by Long *et al.* [49,50] Prielipp *et al.* [52] and Beyer [53]. In contrast groups concentrating on reinforcement of light metal alloys (e.g. aluminium castings) tested the material in pure tension, as presented by Kniewallner [51].

Table 2.1 Compilation of the mechanical properties of preform MMCs from different research groups. (Refs - see table)

	Matrix alloy	Reinforcement ceramics / shape	Volume Fraction	Infiltration route	E	YTS	UTS	A_5	Test method	K_{IC}	Ref.
					GPa	MPa	MPa	%		MPa $m^{-1/2}$	
Long, S. et al. 1999	Al 99.5	Al_2O_3 (lf) Altex™	0.50	ISQC	120	-	899	-	3PB	n.a.	(49, 50)
				DSQC	120	-	891	-			
	AlCu4MgAg T6	Al_2O_3 (cf) Saffil™	0.15	ISQC	96	-	523	-			
			0.15	DSQC	95	-	514	-			
	AlCu4MgAg T6	SiC F500 (p)	0.53	DSQC	160	-	346	-		5,4	
Kniewallner, L. 1992	AlSi9Cu3	Al_2O_3 (cf) Saffil™	0	ISQC	75	132	227	1,8	Tensile test	n.a.	(51)
			0.135		80	114	235	1,6			
			0.20		90	98	280	1,4			
	AlSi12		0		75	85	190	7,5			
			0.135		80	75	190	2,5			
			0.20		85	85	220	1,6			
	AlMg9		0		68	168	225	1,5			
			0.125		82	141	290	1,6			
			0.20		95	130	295	1			
Prielipp, H. et al. 1995	Al Lig. 0.08 µm	Al_2O_3(p)	0.75	GPI	-	-	630	n.a.	4PB	2,9	(52)
	Al Lig. 0.25 µm				-	-	710			5,4	
	Al Lig. 0.8 µm				-	-	510			7,4	
Beyer, P. 2002	Al	50 % TiO_2 (p) + 50 % Al_2O_3 (p)	0.54	GPI	-	-	642	n.a.	4PB	8,7	(53)

Abbrevations:

Alloy	T6: precipitation hardened (peak hardened)
Reinforcement ceramics	(p): particles; (lf): continious fibres; (cf): chopped fibres
Infiltration route	GPI: Gas pressure infiltration; ISQC: Indirect Squeeze Casting; DSQC: Direct Squeeze Casting
YTS	Yield tensile strength
UTS	Ultimate tensile strength
A_5	Elongation to fracture
Test method	3PB (4PB): 3-(4-) point bending test
$Al_{Lig.}$	Aluminium ligament size

20

The main factors controlling the elastic modulus of MMCs are the reinforcement aspect ratio and volume fraction fo the reinforcement. The presence of interfacial reaction layers can lower the transverse moduli of many composites. Young's modulus is one of the properties least sensitive to microstructural features. It has been shown that the simple rule of mixture approach is not valid for estimating the effective modulus of particle reinforced MMC. Hashin and Shtrikman [55] proposed upper and lower bounds for prediction of a composite Young's modulus E_c with a reinforcement volume fraction V_f:

$$E_1 + \frac{V_f}{\frac{1}{E_2 - E_1} + \frac{1-V_f}{3E_1}} \leq \langle E_c \rangle \leq E_2 + \frac{1-V_f}{\frac{1}{E_1 - E_2} + \frac{V_f}{3E_2}} \qquad \text{Equation 5}$$

where E_1 and E_2 are the moduli of the matrix alloy and the reinforcement, respectively.

As an alternative to analytical modelling, numerical techniques such as FEM have become increasingly popular. One common approach is to use a unit cell model, where one or more reinforcement particles are embedded within the Al matrix, to simulate a composite material with a periodic array of reinforcement. A unit cylindrical particle has a greater stiffening effect than a spherical particle.

As reported by Feest *et al.* [56], the elastic modulus and thermal conductivity values remain relatively constant at particulate diameters greater than 10-15 µm. However, below this threshold, the modulus increases and thermal conductivity decreases as the diameter decreases. Two possible explanations are matrix microstructural refinement and increased surface area for interfacial reactions. As a result, poor correlations between predicted and measured property values may occur for small diameter reinforcements and require the use of specific bounds.

General models to predict fracture toughness have been shown to be inappropriate in many MMCs [57]. It is becoming recognized that, for composites, toughness is an engineering concept and not a material property [58]. Clustering of reinforcements is a typical manufacturing problem. Studies suggest that global thermomechanical effective properties are generally unaffected but properties such as fracture toughness, where crack initiation is a function of the local stress, are influenced by inhomogeneous distributions [59].

Much of the driving force behind the development of MMCs has been that monolithic lightweight alloys have inadequate fatigue resistance for many demanding applications. MMC fatigue failure, which is governed by the growth of very small microcracks, is also not well described by linear elastic fracture mechanics (LEFM). The single most important factor is the reinforcement volume fraction. For particulate-reinforced composites, the matrix properties dominate at low volume fraction, and the reinforcement properties dominate at high [41]. The shape or aspect ratio and alignment of the reinforcements are also important factors. For random reinforcement orientations, a minor difference in the predicted property value is seen between different reinforcement shapes, particularly at low volume fractions. The use of high stiffness ceramic reinforcement in particulate form, such as Al_2O_3, can result in a substantial increase in fatigue resistance. Several studies have shown that both, increasing volume fraction and decreasing particle size, result in enhanced fatigue resistance. In a composite, most of the load is carried by the high modulus, high strength reinforcement so, for a given stress, the composite undergoes a lower average strain than the unreinforced alloy. Thus the fatigue lives of particle-reinforced metal matrix composites are generally longer than those of unreinforced metals [42]. For a given reinforcement volume fraction, the reinforcement interparticle spacing decreases with decreasing particle size, resulting in more barriers for the reversible slip motion that takes place during fatigue, and a decrease in strain localization by cyclic slip refinement. Above a critical particle size, reinforcement fracture is predominant

and contributes to premature fatigue life, because of the increased propensity of particle cracking as the particle size decreases. Narrowing of the particle size range distribution also results in a higher fatigue failure, particularly when eliminating larger particles that are more prone to cracking [60].

Enhanced creep resistance was obtained with the higher aspect ratio whiskers than with particles, presumably due to more effective load transfer from the matrix to the high stiffness reinforcement [42].

The coefficient of thermal expansion (CTE) mismatch of metal and ceramic phases in the composites leads to thermal residual stresses and induces plastic deformation in the matrix, resulting in indirect strengthening [61]. The stresses and the strengthening in these composites were generated during the cooling after processing at a high temperature. Agrawal *et al.* [62] measured residual stresses in Al-Al_2O_3 composites with cellular ceramic structures built up of particles in the sub-micron size with a ceramic volume fraction of 0.29. A residual compressive stress of up to 100 MPa in the ceramic phase and the same order of tensile stress in the metal matrix were obtained. When regarding the ceramic phase, the compression stress is beneficial for preventing particle cracking when a tensile stress is applied to the composite. In contrast, the residual tension in the metal phase is detrimental to composite properties. Yielding of the aluminium alloy matrices is already reached at tensile stress levels of about 200 MPa at room temperature [63].

Hoffmann *et al.* [64] synthesized alumina which was toughened by interpenetration with aluminium. The metal ligament size was in the range of 0.12 to 1 µm. Due to their small ligament size, dislocation movement in the ligaments is expected to be limited. The high level of mechanical constraint induced by small ligaments tightly bonded to the ceramic is expected to raise the flow stress in the metal well above that of the bulk material which is consistent

with values observed by others for highly constrained ductile particles and thin films [65,66]. This high level of residual stresses has been confirmed experimentally. At the lower ligament size of 0.12 µm, a high residual stress of 1430 MPa were obtained whereas at a ligament size of 1 µm a lower stress level of 760 MPa was reported. On the other hand interfacial debonding occurred with a larger ligament size, as shown by Kohle *et al.* [67]. In their experiments, Al_2O_3 was toughened with Ni at a volume fraction of 0.20. The critical diameter of the Ni phase in the toughened Al_2O_3 was in the range of 1.3 to 8.5 µm.

Knechtel *et al.* [68] used metal toughened ceramics to show that the interface of Al_2O_3-Al is significantly stronger than the Al_2O_3-Cu interface. The influence of metal ligament size on both fracture toughness and fracture strength was assessed. Different average ligament sizes were proposed to be represented by using the median pore diameter of a mercury intrusion porosimetry analysis which was in the range of 0.08 µm to 0.13 µm. Fracture toughness increased with increasing metal ligament size. SEM studies of the Al_2O_3-Al composite microstructure with an average ligament size below 0.10 µm clearly showed, that the small cavities could not be infiltrated even though a gas pressure of 15 MPa and relatively high processing temperature of 1110°C were used.

From the standpoint of infiltration behaviour, large particulates are more favourable than smaller ones. Mitzumoto *et al.* [69] synthesized MMCs by a low pressure infiltration process. The pressure required to infiltrate preforms having the same volume fraction of particles increased from 0.05 MPa to 0.5 MPa with a decrease in the particle size from 100 µm to 20 µm. This indicates that, the infiltration is achieved with lower pressure at higher particle diameters.

2.2. Static wetting in metal-ceramic systems

Wetting of ceramic substrates by a molten metal plays an essential role in the fabrication and properties of metal matrix composites. The relation between the wetting angle θ and the surface energies was first proposed by Young [70] and describes the balance of horizontal forces due to surface tension acting upon a liquid drop in contact with a solid as shown schematically in Figure 2.7. It is expressed by:

$$\cos\theta = \frac{\gamma_{sv} - \gamma_{sl}}{\gamma_{lv}} \qquad \text{Equation 6}$$

Thus the characteristic contact angle θ depends on the surface energies of the liquid-vapour (γ_{lv}), solid-vapour (γ_{sv}) and solid-liquid (γ_{sl}) interfaces. Good wetting is achieved when the contact angle between metal and substrate is below 90° as shown in Figure 2.7b.

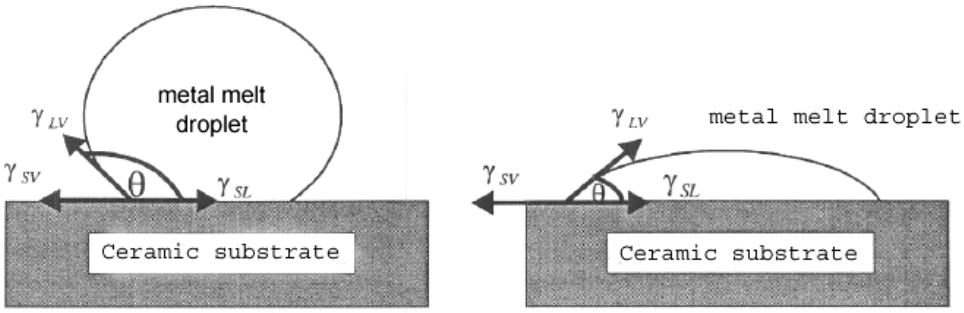

(a) (b)

Figure 2.7 Metal melt droplet on a ceramic substrate. (a) Non-wetting characterised by wetting angles of θ> 90°. (b) wetting systems with θ< 90°.

The work of adhesion W_{ad} is in direct relation to the surface energies and defined as:

$$W_{ad} = \gamma_{sv} + \gamma_{lv} - \gamma_{sl} \qquad \text{Equation 7}$$

The work of adhesion characterises the work which is necessary to separate the solid-liquid interface. Combining Equation 6 and Equation 7 results in the following expression:

$$W_{ad} = \gamma_{lv}(1+\cos\theta) \qquad \text{Equation 8}$$

Thus the work of adhesion depends only on the surface tension of the metal melt and the contact angle θ. It is usually measured by the sessile drop technique, which yields both the contact angle and the surface tension of metal through analysis of the drop´s profile [13].

The work of adhesion in metal melt-ceramic systems is subdivided into two different categories. The first one is a result of the van der Waals forces and the second is based on chemical bonding between surface atoms of the two different phases [71]. Non-reactive systems are characterised by positive reaction enthalpies, whereas reactive systems show negative reaction enthalpies. The pure metal-metal oxide systems (Me/Me_xO_y), such as Al-Al_2O_3, are in general categorized as non-reactive systems.

2.2.1. Non-reactive wetting

The interfacial energies of Me/Me_xO_y are characterized by weak van der Waals and electronic interactions. As reported by Gallois [72], the intrinsic contact angles in these systems are generally larger than 90°. It may be different when there are interactions between the oxide and the metal melt or in an reactive atmosphere. Oxygen dissolved in the metal adsorbs at the liquid metal/vapour and the liquid metal/ceramic interfaces, leading to improved wetting with contact angles as low as 70°, as shown by Diemer *et al.* [73] in the Cu-Cu_2O system. Among the metal-ceramic systems, Al-Al_2O_3 is the most important one. As the solubility of Al_2O_3 in the Al melt close to its solidus is rather low [74], less than 0.006 at-% is dissolved, there is no influence leading to the aforementioned wetting improvement in this system.

The wetting behaviour of Al_2O_3 by liquid Al has been widely studied, as reviewed by Rocha-Rangel *et al.* [75]. The principal problem that appears in this system is that wetting of Al_2O_3 by Al is a non-equilibrium phenomenon characterized by the continuous oxidation of Al. In fact the contact corresponds to the Al-Al_2O_3/Al_2O_3 system, rather than to the Al/Al_2O_3 couple. It appears that the alumina layer that coats liquid aluminium is the barrier impeding the wetting phenomenon.

The critical factors affecting the wettability of α-alumina by molten aluminium were reviewed by Shen *et al.* [76]. The reported contact angles are so scattered, ranging from 160° to 40°, that it is difficult to get a clear picture of the intrinsic wettability in this system. The large scatter is primarily because of the presence of a protective surface oxide layer on the molten aluminium, which acts as a barrier inhibiting the formation of a true Al-Al_2O_3 interface, particularly below 1000°C. The ubiquitous oxide layer results in the much larger observed contact angles. At high temperatures (>1000°C) the scatter is relatively small, which is attributed to disappearance of the aluminium oxide film. A possible mechanism for elimination of the oxide film could be the reaction between it and liquid aluminium involving the formation of a gaseous suboxide according to the reaction [7,77]:

$$4Al\,(l) + Al_2O_3(s) \rightarrow 3Al_2O\,(g) \qquad \text{Equation 9}$$

The vapour pressure of Al_2O over liquid Al and solid Al_2O_3 at 1350°C is reported to be about $3 \cdot 10^{-4}$ bar [78] and that of liquid aluminium is reported to be $1 \cdot 10^{-4}$ bar at the same temperature. Thus evaporation of both Al and Al_2O has to be assumed. The authors concluded that good wetting of aluminium on alumina is possible at elevated temperatures above 1000°C.

The intrinsic wettability of α-Al_2O_3 by molten Al, corresponding to situations where the Al surface is free of oxidation and the Al_2O_3 substrate is not attacked by the aluminium liquid

and vapour, is difficult to evaluate. This is because of the viewpoint of thermodynamic equilibrium, surface oxidation of Al can only be prevented at extremely low oxygen partial pressures, lower than 10^{-44} Pa at 700°C [6,75,76].

Apart from oxidation, the surface roughness influences the wetting behaviour [79]. Even though polished samples are used in most sessile drop tests, the surface is not totally smooth. It has been shown that when the roughness R_a is below 1 µm the influence on wettability is rather moderate. Shen *et al.* [76] proposed that, in the case of a clean Al melt surface, the effect of the substrate surface roughness is only noticeable when it exceeds 2 µm.

The effect of temperature on wettability and shear strength of Al/Al_2O_3 couples was assessed by Sobczak *et al.* [80]. They proposed the "true" contact angle at 800°C in Al/Al_2O_3 to be 80°. They concluded that low contact angles correspond to high interfacial strengths. This was indicated by comparison of the shear stresses of two different $Al\text{-}Al_2O_3$ couples where the wetting tests were done at different test temperatures. The shear strengths were 50 MPa and 28 MPa at wetting angles of 90° and 120° respectively.

The effect of an oxide layer on the contact angle has been revealed by Ksiazek *et al.* [81] through simultaneous measurement of the wetting angle θ and oxide thickness. The partial oxide breakdown on the surface in combination with open porosity allowed the metal to penetrate small pores even though the macroscopic wetting angle of the sessile drop was measured to be significantly larger than the threshold angle of spreading, which is 90°.

Wetting behaviour is extremely sensitive to test conditions which are mainly atmosphere, material purity, temperature and surface finish. In oxidation of an Al melt the submerged oxide film is in perfect atomic contact with the Al supplying liquid [6]. After solidification, the metal-oxide bond is still strong and so the surfaces of all aluminium products are covered with

an intimate aluminium oxide film. In contrast to this intimate contact, the dry side of the oxide film is not wetted by the liquid. The poor wetting behaviour is observed in similar way when examining the results of wetting angle of Al on Al_2O_3 in the sessile drop test. The large scatter of reported contact angle data in this system is reviewed by Li [82] and presented in Figure 2.8. Based on the reviewed literature, the largest deviations have been reported between the melting point and 1000°C and lie between $\theta = 50°$ and 170°. In preform infiltration, the temperature of the liquid aluminium ranged between the melting point and 900°C. In this range, the reported contact angles vary between 60° and 170°.

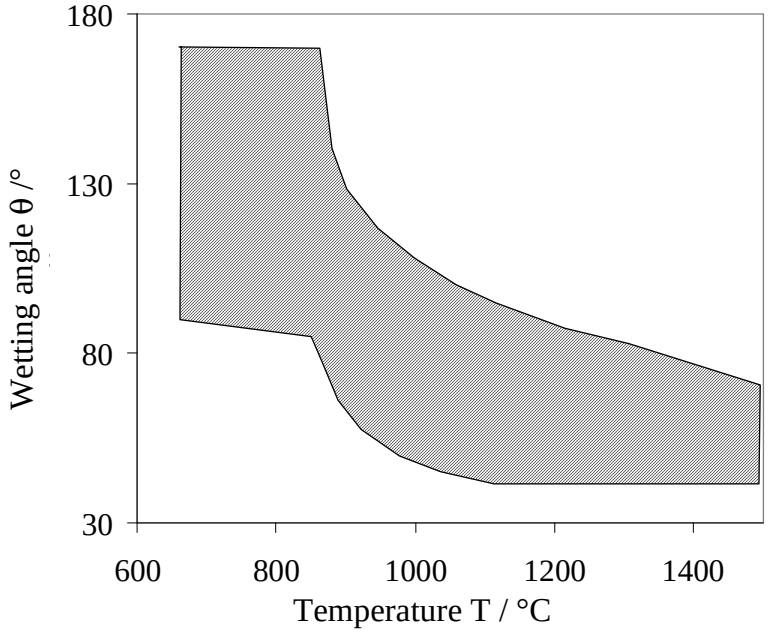

Figure 2.8 The reported temperature-dependent wetting angle scatter as a function of temperature [82].

As suggested by John and Hausner [83], the scatter is attributed to different atmospheric conditions, in particular the oxygen content and the resulting thickness of the oxide layer on the melt. The different experimental conditions are expected to be the reason for this behaviour. The authors achieved low oxygen partial pressures using oxygen-gettering materials. The melt droplet resting on the plane substrate was covered with a zirconium crucible. Therefore the droplet was optically not visible while testing and the θ could only be measured after the test. The authors stated that the equilibrium oxygen partial pressure in the

system Al-Al_2O_3 is 10^{-49} Pa at 700°C and at the same temperature that of Zr-ZrO_2 is marginally lower. Therefore the surface of the aluminium melt droplet was assumed to be oxygen-free. Under these conditions the wetting angle was measured to be 90° and therefore exactly either wetting nor non-wetting.

Since the solubility of oxygen in liquid Al is extremely low [7], different oxygen partial pressures in a sessile drop experiment will influence primarily the oxide layer thickness on the surface of the Al. At high oxygen pressures the oxide layer will prevent the formation of the equilibrium shape of the metal droplet, because of the mechanical strength of the oxide skin.

The results demonstrated that an oxygen partial pressure of ca. 10^{-13} bar is the limit for the formation of a droplet by the liquid Al. Under the experimental conditions an oxide layer on the surface of the Al completely prevented the formation of a spherical droplet. Very low values for the wetting angle were obtained if a strong oxygen getter such as Zr was present in the system. At very low oxygen partial pressures in the region of 10^{-44} Pa, the wetting angle at 700°C was as low as 90°.

Typically θ is obtuse at small contact times but decreases rapidly to a constant value θ_{eq} at long times. Asthana *et al.* [84] analysed this time-dependent spreading behaviour of liquid metals on solids. The θ(t) experimental data for selected systems were fitted to an empirical relationship of the form:

$$\theta = \theta_{eq} + \theta_{eq} e^{(B - At)} \qquad \text{Equation 10}$$

where the empirical constants A and B were determined from the graph of $\ln((\theta/\theta_{eq})-1)$ vs t as shown in Figure 2.9. It is therefore inappropriate to use equilibrium values of contact angles in modelling dynamic processes that proceed quickly. The instantaneous contact angle θ decreases progressively with contact time. The relationship appears to describe adequately the

time dependence of dynamic angles. At t=0 the droplet makes point contact with the solid which results in a wetting angle of 180°. Thereafter the droplet begins to spread onto the solid and the instantaneous value of θ progressively decreases with time. The progression of the wetting perimeter is often spearheaded by a thin precursor film [85] of liquid, so that the measured θ is an apparent rather than a true value.

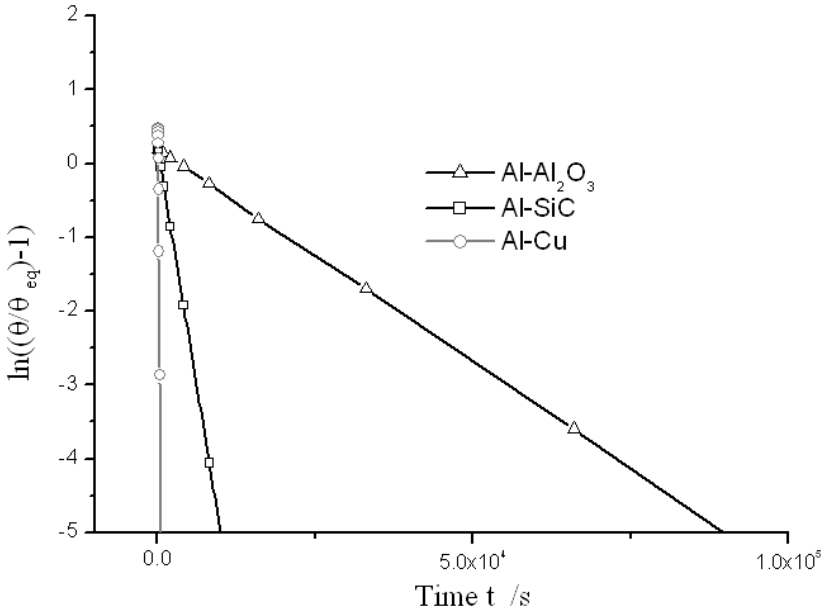

Figure 2.9 Plots of $\ln((\theta/\theta_{eq})-1)$ versus time of the metal – ceramic systems Al-Al_2O_3 and Al-SiC and the metal-metal system Al-Cu. The slope of the curve represents the parameter A and B the intercept on the t-axis [86].

According to the aforementioned work of Asthana *et al.* [84], liquid metal-ceramic or metal-metal combinations exhibit different spreading behaviours. The non-reactive Al-Al_2O_3 system shows an initial θ of 100° which decreases within 3000s to reach θ=50°. As shown in a later work of Asthana [86], the equilibrium wetting angle in the Al-Al_2O_3 system reaches 45°. It is interesting to note that even though the reactive systems Al-SiC and Al-Cu exhibit a much steeper decrease in wetting angle, the initial and the equilibrium wetting angles θ_{eq} are higher than that of the Al-Al_2O_3.

In the Al-Cu system, although the presence of oxide film could be a problem in the development of wettability, good wetting was achieved under carefully controlled conditions. A partly reducible oxide film forms at the wetting front under high vacuum. The activation energy for spreading is comparable to the activation energy for dissolution. However interference from the oxide on Al may lead to wetting being controlled by the oxide film. The dominant mechanism of wetting in a given system may change with test conditions but generally the wetting behaviour in the Al-Al_2O_3 and Al-SiC systems is controlled by oxide effects whereas that in Cu-Al systems is controlled by chemical reactions [86].

2.2.2. Reactive metal-ceramic systems

Although physical and mechanical properties may often limit constituent selection, it is the chemical reactivity of the reinforcement with the matrix alloy either during service or fabrication which will in most cases decide upon the final reinforcement/matrix combination [41]. The influence of the free energy of formation was first proposed by Aksay *et al.* [87] and Naidich [71]. They proposed that the enthalpy in the vicinity of the triple line controls the spreading of the liquid on the solid material.

Naidich [71] subdivided the work of adhesion in a reactive system into two terms as:

$$W_{ad} = W_{ad}(\text{equil.}) + W_{ad}(\text{non} - \text{equil.}) \qquad \text{Equation 11}$$

and thus calculated for the interfacial region:

$$\gamma_{sl} = \gamma_{lv} + \gamma_{sv} - W_{ad}(\text{equil.}) - W_{ad}(\text{non} - \text{equil.}) \qquad \text{Equation 12}$$

It was reported that the values obtained by calculation of W_{ad} using Equation 11 are in accordance with experimental ones within a factor of 2. The term W_{ad}(non-equil.) was calculated by integration of the free enthalpy of formation between the starting conditions and final equilibrium conditions along the interface. A rapid reaction and the formation of a

monolayer of the most stable reaction product on the substrate and the liquid melt was assumed. Naidich [71] proposed that extensive chemical reactions between the constituents to be the predominant mechanism to improve wettability.

According to Aksay *et al.* [87] the major contribution of the enthalpy of formation on wetting improvement starts at the beginning of spreading. From the initial wetting angle θ_0 it decreases towards an intermediate minimum θ_{min}, and then increases again to reach the equilibrium wetting angle θ_{eq}, as shown schematically in Figure 2.10. Thus a time-dependent driving force of spreading is subdivided into different regimes as shown in Figure 2.10. As proposed by Laurent *et al.* [88] the difference between θ_0, θ_{min} and θ_{eq} is calculated using Equation 13:

$$\cos\theta_{\min} = \cos\theta_0 - \frac{\Delta\gamma_r}{\gamma_{lv}} - \frac{\Delta G_r}{\gamma_{lv}} \qquad \text{Equation 13}$$

where $\Delta\gamma_r$ is the contribution of reduced interfacial tension due to reaction, ΔG_r the heat of reaction due to formation of an interfacial phase and γ_{lv} the surface tension of the metal melt.

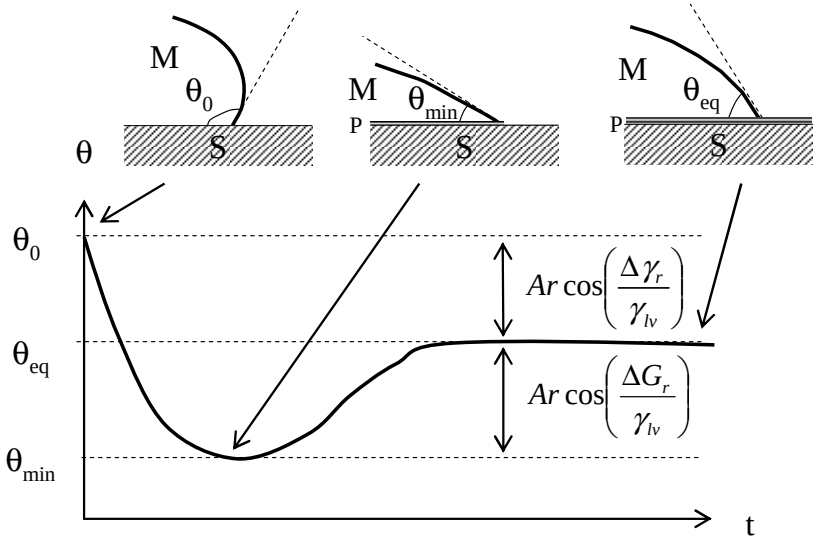

Figure 2.10 Schematic of the conditions in reactive wetting of a substrate (S) by a liquid metal melt (M). A reaction product (P) is formed along the interface [87].

The heat of reaction ΔG_r may be estimated using the Ellingham-Richardson-Jeffes diagram [89] as presented in Figure 2.11, where the free energy of formation ΔG_0 is given as a function of temperature. Metals with a high heat of formation are found at the lower end and those with low heat of formation are at the upper end of the diagram. As shown in Figure 2.11, when Ca and Mg oxidizes in the temperature range from 0 to 1000°C, the free heat of formation is larger (i.e. more negative) than that of Al_2O_3. In contrast, the oxidation of titanium and silicon emits a lower amount of heat. The heat to form ZrO_2 is close to that required to form Al_2O_3.

Landry *et al.* [90] investigated reactive metal alloy-ceramic systems such as a Cu-Si alloy in contact with vitreous carbon . The wetting angle initially decreased with increasing time. In contrast to the predictions of Aksay *et al.* [87], no minimum wetting angle and no inflection point were observed. This behaviour was attributed to the increase in surface roughness as a result of the formation of reaction products on the substrate. Thus it was proposed that the triple line was hindered from moving through pinning on the rough surface.

In contrast to Aksay *et al.* [87] and Naidich *et al.* [71], some other investigators [91,92] proposed that the influence of the enthalpy of formation in systems of low or moderate reactivity is negligible. They suggested that the decisive factors in reactive wetting were the changes in interfacial structure due to adsorption processes and the formation of new phases at the interface.

Espié *et al.* [93] investigated the wetting behaviour of CuPdTi alloys on mullite, quartz and alumina surfaces. The spreading on all three substrates was nearly identical which was attributed to the formation of Ti_2O_3. The differences in the heat of formation of the three systems, characterised by deviations in the thickness of the reaction layer, exhibited no contribution to the spreading behaviour.

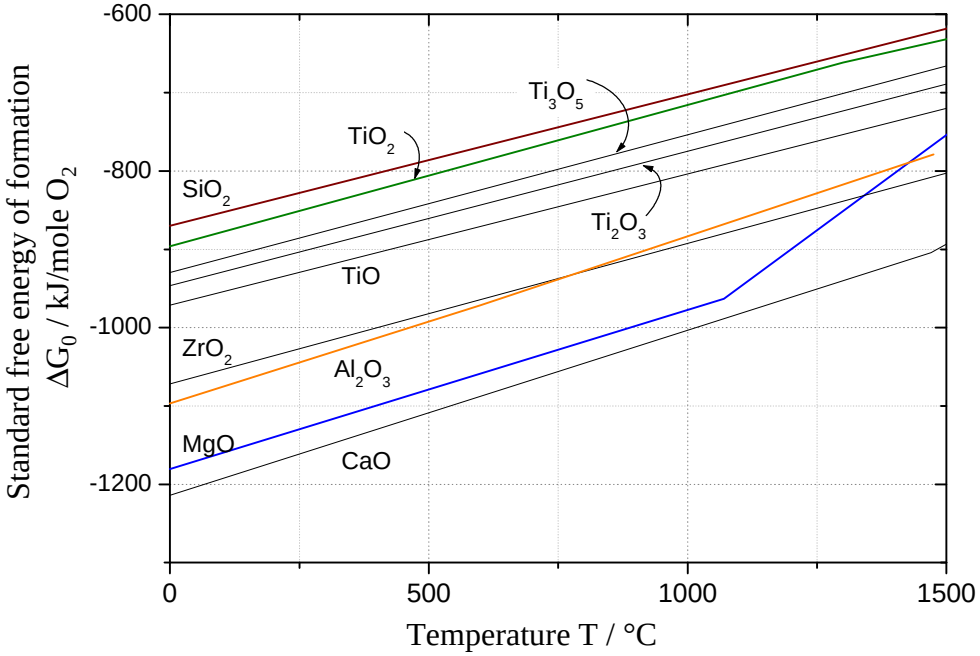

Figure 2.11 Ellingham-Richardson-Jeffes diagram of selected metal oxides [89]

Even though heavy reactions were predicted in thermodynamic calculations in the Al-TiO_2 system [94], no improved wetting in the sessile-drop test was found [95]. The formation of Al_2O_3 along the interface led to a layered system of molten Al on reaction-formed Al_2O_3. The wetting angle was of the same order or even higher than that of the Al-Al_2O_3 system. Arpon *et al.* [96] showed similar behaviour in the Al-TiC system where TiO_2 was formed on the surface of TiC as a result of preheating the carbide in an oxidizing atmosphere.

It has been suggested [97,98] that the formation of the spinel phase $MgO \cdot Al_2O_3$ affects wetting of Al_2O_3 by pure Al and AlMg-alloys. The system was investigated by Nakae *et al.* [99] with attention to the proposed three stage wetting regime. At relatively low temperatures of 900°C, no significant change from an initial θ of 130° could be observed. At higher temperatures of 1000°C and 1100°C, a steep decrease after 10^3 s resulted in wetting angles of 100° and 85° respectively. A transient minimum contact angle was not observed throughout the experiments even though reaction zones of $MgO \cdot Al_2O_3$ were found. This agrees with Shen *et*

al. [100] who found non-wetting behaviour of aluminium melts on MgO indicated by θ of 104 to 121° in sessile drop tests.

In reactive wetting of liquid metals on ceramic substrates, Zhou and Hosson [101] proposed the ceramic volume change as the key factor to improve wetting. They suggested that if the volume of a ceramic substrate decreased after the reaction, wettability was not improved by the chemical reaction. In contrast, if the volume of the ceramic substrate increased, the wettability was improved by the chemical reaction. As an example, they pointed out the Al-SiO_2 system where a volume decrease due to formation of Al_2O_3 and solution of silicon in the melt pool could be observed. In contrast, the Ti-Al_2O_3 system represents an example of volume increase by the formation of TiO_2 and titanium suboxides like TiO and Ti_2O_3.

The simple criterion of volume change proposed by the aforementioned authors was challenged by Shen *et al.* [23] who investigated the Al-SiO_2 system intensively. They observed an improved wetting resulting from the chemical reaction. The authors stated that wetting is at first a surface phenomenon.

If the change in surface energy due to reaction ($\Delta\gamma_r$) is the dominating factor in reactive wetting, there are two possible configurations at the metal-ceramic interface as shown in Figure 2.12.

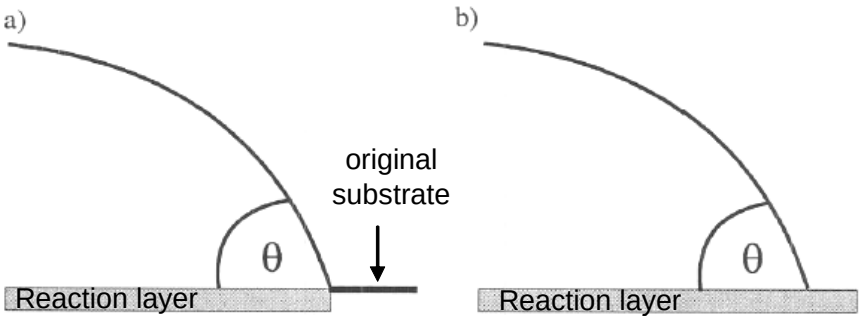

Figure 2.12 Different configurations in front of the triple line in reactive wetting after equilibration.

In the case of a), the diffusion rates of the reacting components and thus the growth rate of the reaction products are low relative to the flow rate of the liquid drop. The liquid at the periphery of the drop will remain in contact with unreacted solid. In the this case, the equilibrium wetting angle ($\cos\theta_{eq}$) is defined as:

$$\cos\theta_{eq} = \frac{\gamma_{sv} - \gamma_{Rl}}{\gamma_{lv}} \qquad \text{Equation 14}$$

where γ_{Rl} is the surface energy of the liquid-solid reaction product interface.

In the second configuration b), the diffusion rates of the reacting components in the solid are high relative to the flow rate of the liquid drop. After equilibrium is reached, the reaction layer extends beyond the triple line. In this case the equilibrium contact angle is given by:

$$\cos\theta_{eq} = \frac{\gamma_{Rv} - \gamma_{Rl}}{\gamma_{lv}} \qquad \text{Equation 15}$$

where γ_{Rv} is the surface energy of the interface reaction product- atmosphere.

There is up to now no definite model describing the influence of reactivity on wetting behaviour in metal melt-ceramic systems. The enthalpy of formation and the changes in the interface are the two factors leading to changes in the surface tension. Which of these dominates is controversial and depends on the particular system. In dynamic infiltration systems, where liquid metals are forced under pressure into a porous medium, the non-reactive and the reactive wetting are even more difficult to assess.

2.3. Infiltration of porous media

The infiltration of porous preforms consists of forcing the liquid metal to infiltrate the preform by applying pressure. The infiltration consists of an initiation step, where a certain

capillary or threshold pressure has to be applied to overcome the capillary backpressure. Once the threshold pressure has been overcome, the molten metal flows into the capillaries of the preform. Both infiltration steps will be discussed in detail below.

2.3.1. Dynamic wetting

The critical parameter that governs the wettability of a solid by liquid is the work of immersion W_i which is given by:

$$W_i = \gamma_{sl} - \gamma_{sv} \qquad \text{Equation 16}$$

where γ_{sl} and γ_{sv} are the solid/liquid and solid/vapour surface energies respectively. If $\gamma_{sv}>\gamma_{sl}$ the metal wets the solid. If $\gamma_{sv}<\gamma_{sl}$ work is required to generate the solid-liquid interface. In the non-wetting case the infiltration of a liquid into a porous body will require a minimum external pressure. This threshold or capillary pressure P_0 can be written in terms of the work of immersion:

$$P_0 = S_i\ W_i \qquad \text{Equation 17}$$

where S_i is the surface area per unit volume of porosity which has to be covered with the liquid. P_0 can be related to the contact angle θ at the liquid/solid interface by using the Young-Dupré [70] equation:

$$\gamma_{sv} = \gamma_{sl} + \gamma_{lv} \cos\theta \qquad \text{Equation 18}$$

where γ_{lv} is the liquid metal surface tension. Equation 18 can then be rewritten as:

$$P_0 = S_i \gamma_{lv} \cos\theta \qquad \text{Equation 19}$$

Thus the wettability of a liquid with known surface tension γ_{lv} may be evaluated by an accurate determination of the threshold pressure to force the liquid into the porous body with a known S_i, the particle surface area per unit volume.

The commonly used sessile drop experiment only replicates poorly the wetting conditions encountered in metal matrix composites fabrication [102]. In infiltration with constant gas pressure, the three phase contact line generally moves at a velocity of 10 cm s^{-1} inside the porous medium. The oxide layer and the influence of chemical interaction at the interface both were found to be different from what is observed in sessile drop experiments [102]. Thus, experimental procedures utilizing particles of ceramic materials to measure wettability have been established [1,103]. The molten metal is forced under pressure into a packed bed of powder held at the same temperature as the metal and the threshold pressure P_0 to initiate movement of the metal is recorded as a measure of wettability. The relation between the P_0 and the dynamic wetting angle θ_{dyn} is given by:

$$P_0 = S_i \rho_p \gamma_{lv} \cos\theta_{dyn} \frac{V_P}{1 - V_P} \qquad \text{Equation 20}$$

where ρ_P is the bulk density of the particles, γ_{lv} is the surface tension of the liquid phase and V_p is the volume fraction of particles in the packed particle bed. In the experiments by Asthana and Rohatgi [104] V_P ranged between 0.50 and 0.60. To determine the threshold pressure for infiltration, the square of the infiltrated height is plotted against the applied pressure P_{appl}. The data can be fitted to a straight line in agreement with Darcy´s law [103] and the pressure axis intercept gives the threshold pressure P_0.

Apart from packed ceramic powder beds, investigations using porous sintered preforms are rather scarce. Mortensen and Michaud [105] reported infiltration of Saffil™ fibre preforms

using constant gas pressure. Infiltration with pure aluminium resulted in apparent contact angles θ in the range of 102° to 111°. The results were much closer to sessile drop wetting angles measured in ultra high vacuum than to those measured in air or in a lower vacuum.

Jonas *et al.* [106] infiltrated preforms consisting of Al_2O_3 particles with pure Al and Al-2% Mg (wt.%) alloy. Even though Mg in Al was considered to improve wetting behaviour [15], the θ_{dyn} were 106° for pure Al and 105° for the Al-Mg alloy, indicating no significant improvement in dynamic wetting. The small effect of Mg on the wetting was attributed to the absence of reactive wetting at the infiltration speeds used and to partial disruption of the oxide layer on the surface of the liquid metal during infiltration.

As reported by Garcia-Cordovilla [103], two methods for determination of the surface area are used for packed ceramic particulates. The most common is the Braunauer, Emett and Teller (BET) nitrogen adsorption method [105]. The laser scattering method applied to the particulates before compaction shows inaccurate results for applications where wettability is evaluated [103]. Mercury intrusion porosimetry (MIP) is an alternative method which may be used to determine the surface areas of porous media. Most of the MIP measurements in MMC-fabrication [53,107] have been performed solely to determine the pore size distribution of particulate preforms with ceramic volume fraction of more than 0.50. In some cases, the ceramic contents were much lower: Cardinal *et al.* [108] investigated ceramic volume fraction of 0.35 using hybrid preforms of Al_2O_3 platelets and Al_2O_3 short fibres. The volume of intruded mercury at a specific pressure is a result of penetration into cavities larger than a particular size. In MIP measurements, Washburn's equation is applied:

$$D_{Hg} = -\frac{4\gamma_{Hg}\cos\theta_{Hg}}{P} \qquad \text{Equation 21}$$

where γ_{Hg} is the surface tension of mercury, θ_{Hg} is the wetting angle of mercury on ceramics and P is the applied pressure. It describes the dynamic equilibrium between external forces tending to force a liquid into a capillary of diameter D_{Hg} and the internal forces repelling entry into the capillary. According to Rootare and Prenzlow [109] the surface area from mercury porosimetry S_{sHg} can be calculated from:

$$S_{sHg} = \frac{1}{\gamma_{Hg}\left|\cos\theta_{Hg}\right|}\int_{0}^{V_{tot}} PdV \qquad \text{Equation 22}$$

where V_{tot} is the total intrusion volume, P is the pressure and V is the volume of the incremental intrusions.

Based on porosimetry data, Leon [110] proposed a simple relation between the product of mean volume pore diameter D_{Hg} and the permeability K_{MIP} of a porous body represented by Equation 23 with ϕ the powder bed porosity.

$$K_{MIP} = \frac{\phi\, D_{Hg}^{2}}{32} \qquad \text{Equation 23}$$

In contrast to the static intrusion when using mercury intrusion porosimetry, the preform infiltration is done in a dynamic way. Thus different approaches for modelling of the fluid flow in infiltration were considered.

2.3.2. Fluid flow in preform infiltration

Fluid flow in a porous medium depends on the properties of the medium to be penetrated and the fluid properties. A simple model for infiltration of porous media is given by the Darcy equation. Henri Darcy established empirically that the flux of water through a permeable formation is proportional to the distance between the top and bottom of the porous column.

The superficial velocity v_0 in the flow direction z is calculated in respect to the pressure gradient dP/dz at the infiltration front and the fluid viscosity μ:

$$v_0 = -\frac{K_s}{\mu} \cdot \frac{dP}{dz} \qquad \text{Equation 24}$$

The constant of proportionality is called the specific intrinsic permeability K_s [111]. Darcy's equation represents a simplification of the general equation of viscous fluid flow governed by the Navier-Stokes equation. The simplification is made by assuming incompressible fluids, laminar flow, and unidirectional, saturated flow.

The superficial Darcy velocity v_0 is a macroscopic concept, and is easily measured. It should be noted that Darcy's velocity is different from the microscopic velocities associated with the actual paths of individual volume elements of molten metal as they wind their way through the pores in the preform [103].

Darcy´s equation is limited to saturated flow. Thus complete saturation before further through-penetration is assumed. Particulate preforms used to produce MMCs generally have highly complex internal void geometries. This complexity and capillarity during infiltration render prediction of the metal flow path during infiltration too complicated to be realistically modelled at the microscopic level of the individual particles that make up the preform.

During preform infiltration, a number of physical, mechanical and chemical phenomena interact, including multiphase flow of liquid metal and air in a porous medium, heat and mass transfer related to solidification, equilibrium of mechanical forces, and chemical interfacial reactions between reinforcement and matrix. Analytical and numerical solutions have been given and compared to experimental data for (i) unidirectional infiltration under constant applied pressure, including non-isothermal infiltration by a pure metal or a binary alloy [112],

(ii) for non-isothermal infiltration by a pure metal, taking into account the influence of preform deformability, and (iii) for isothermal infiltration, taking into account the influence of capillary phenomena [113]. Most models consider only the case of saturated flow, either by ignoring any capillary pressure drop or using the 'slug-flow' assumption, which implies that the infiltration front is abrupt. It has been shown that when the applied pressure is low or when the preform pore structure exhibits a broad size distribution, this assumption breaks down, as metal penetrates the preform in a gradual manner, filling the largest pores first.

This case is relevant for industrial practice, because it is desirable to maintain the applied pressure as low as possible, to minimize preform damage and to reduce costs. In practical cases, the applied pressure is not established instantly but follows a more or less rapidly increasing function before the final infiltration pressure is established.

For most relevant metal/reinforcement systems, isothermal metal infiltration is similar to drainage in soil mechanics [113]. During drainage, wetting water is displaced by non-wetting air out of a porous soil. In MMC infiltration, air generally constitutes the wetting phase and metal the non-wetting one. Non-saturated flow through porous media and drainage phenomena have been treated in the soil mechanics literature [111]. Based on soil mechanics, Dopler *et al.* [113] developed a model for isothermal infiltration of ceramic fibres based on capillary phenomena. The relationship between local pressure and non-wetting fluid velocity is classically described by Darcy's law (Equation 25). When neglecting gravity it is valid for laminar flow in a porous medium in the following form:

$$v_0 = -K \cdot \nabla P \qquad \text{Equation 25}$$

where v_0 is the superficial velocity of the non-wetting phase, defined as the volumetric flow rate, P is the pressure and K is the permeability tensor.

The permeability K can be expressed as a function of three independent terms:

$$K = \frac{K_s \cdot K_r}{\mu}$$ Equation 26

where K_s is the specific preform permeability tensor, K_r is the relative permeability, varying with saturation between 0 and 1, and μ is the dynamic fluid viscosity. The tensor of specific permeability describes the geometrical arrangement of the porous medium. The different components of the tensor depend on the type of preform, its volume fraction, the diameter of the reinforcement phase, its arrangement and homogeneity. The component values of K_s can be measured by permeability experiments, using, for example water as a fluid [(114)].

There is no direct way to measure the relative preform permeability K_r. It is generally back-calculated from infiltration experiments or from calculations based on simplified porous preform geometries such as capillary tubes. A general form with two empirical parameters A and B can be given [(113)] as:

$$K_r = A \cdot S^B$$ Equation 27

with S the saturation of the porous body. The evaluation of modelling results showed best agreement with A and B both equal to 1. The saturation S is defined as the ratio of filled void space to initial void space as follows:

$$S = \frac{\theta_l}{1-\theta_c}$$ Equation 28

where θ_l is the volume fraction of the intruded liquid and θ_c the volume fraction of the ceramic phase. The saturation is expressed, in general, in soil mechanics as a function of pressure. The functional relationship is measured by establishing a drainage curve for the considered system, which represents the degree of saturation either of the wetting or of the

non-wetting fluid, as a function of the applied pressure P_{appl}. The curves obtained can be fitted to phenomenological equations, introducing a threshold pressure (P_0) which must be overcome to initiate infiltration, and a shape parameter α [115,113]:

$$S = 1 - \frac{1}{\sqrt{1 + \alpha^2 \cdot (P_{appl} - P_0)^2}} \qquad \text{Equation 29}$$

This equation is valid for $P_{appl} > P_0$. The curve shape described by the shape parameter value varies with the pore size distribution, the size and type of reinforcement and with the wetting behaviour of the matrix on the reinforcement. Dopler *et al.* [113] proposed an equation for modelling the infiltration behaviour of Saffil™ fibre preforms:

$$(1 - \theta_f) \cdot \frac{dS}{dp} \cdot \frac{\partial p}{\partial t} - \nabla\left(\frac{K_s \cdot K_r}{\mu} \cdot \nabla P \right) = 0 \qquad \text{Equation 30}$$

In most metal melt / ceramic preform systems, only the volume fraction θ_f and the dynamic viscosity μ are known. Thus the following terms need to be determined experimentally:

1. the drainage curve S(p) using the parameter P_0 and α
2. the relative permeability K_r.
3. the specific permeability tensor K_s.

Dopler *et al.* [113] investigated fibre preform infiltration using constant pressure both experimentally and by the aforementioned model. The system parameters 1 to 3 were determined and the function P(x,t) could be found by solving the non-linear partial differential equation (Equation 30) with given initial and boundary conditions. The results of the two-dimensional numerical analysis were in good agreement with the experiments, both in terms of infiltration kinetics and porosity distribution.

2.4. Preform fabrication

Composites of aluminium and its alloys with Al_2O_3 have the advantage of complete thermodynamic compatibility and exhibit no solubility of one phase in the other which may result in strong interfacial bonding [64]. As a result, most of the published work on oxide ceramic preforms used for MMC fabrication is based on alumina. Mainly fibres, like Saffil™ and others, were infiltrated with aluminium melts. Due to the multiple processing steps of fibre fabrication, the preforms made of chopped fibres are 30 to 50 times more expensive than particulate preforms.

2.4.1. Fibre preforms

The fibre material contains usually about 3- 4 wt.% silica which serves to stabilize a fine grain structure with grain sizes of around 50 nm and to inhibit coarsening of the crystallites [116]. This silica is dispersed throughout the fibre section, but also tends to become slightly concentrated at grain boundaries and free surfaces. On excessive heating, small crystallites of mullite ($3Al_2O_3 \cdot 2SiO_2$) may appear.

For preform fabrication, the bulk fibre material is dispersed in a fluid, usually water, containing an inorganic binder of the silicate type and an organic binder (e.g. starch). After thorough mixing the fibres are allowed to settle and excess water is decanted [117]. Vacuum forming over a fine mesh followed by the application of pressure results in the required preform density. The resulting green body is dried and fired at a temperature ranging from 800 to 1000°C. The amount of fibres in typical preforms is limited to a volume fraction of 0.08 to 0.30. At the lower level it is difficult to produce a coherent structure, whilst above 0.30 excessive fibre cracking may results in a significant reduction in aspect ratio and thus in reinforcing properties.

Figure 2.13 shows an Al-Saffil™ MMC with a surface layer (S) of the binder on the Saffil™ fibre (F). The mechanical properties of the final preform depend upon the volume fraction of fibres and the amount of inorganic binder used. Binder levels vary between 1 and 10% by weight. The higher the binder contents the stiffer the final preform [118]. In contrast, a high binder content is detrimental to MMC properties. With increased binder content, the preform exhibits brittle behaviour which is not favourable during infiltration. Furthermore, in the MMC, excessive binder-metal reactions led to brittle phases [119].

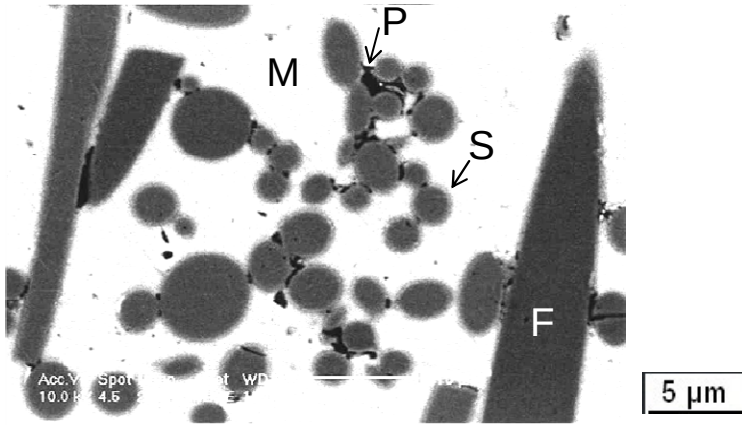

Figure 2.13 SEM microstructure of Saffil™ fibre MMC: pure Al matrix (M), fibres (F) , porosity (P) and silicate binder (S) surrounding the fibres [113].

The fibres in the preforms have an average diameter below 10 µm and a length of 200-500 µm [30,119]. Due to the processing of the fibres, which is in general based on a sol-gel process, large particles in the range of 200-800 µm with low aspect ratio are present in the bulk material. The amount of the large ceramic particles, the so-called shot content, determines the quality of the final MMC. The lower the shot content, the higher the MMC quality and reliability. Large shot concentrations in loaded MMCs result in significant lowering of the fatigue properties due to crack initiation on the surface of the particles [120]. Thus low shot contents should be the intent. Starting from an initial shot weight content of 4 %. An intensive washing procedure can lead to a reduction to less than 0.01 % [119].

According to Kniewallner [51] even at this low fraction, shots were observed in the microstructure as shown in Figure 2.14.

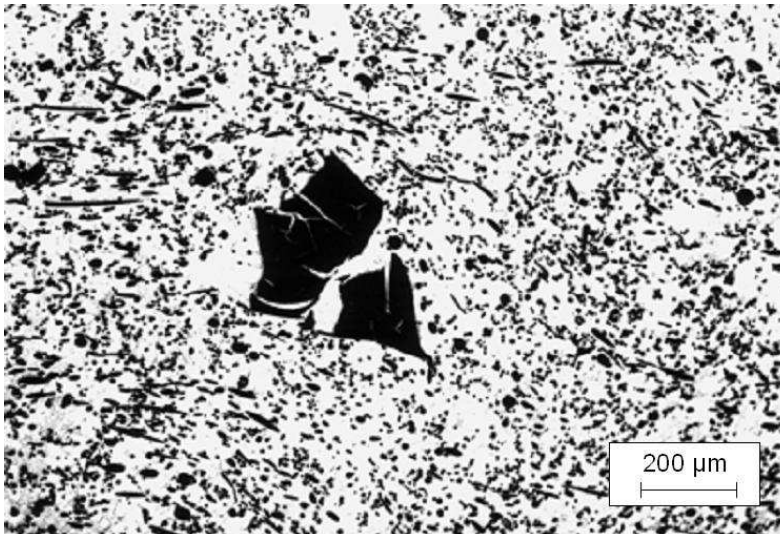

Figure 2.14 Microstructure of a Saffil™ fibre reinforced Al alloy with an Al_2O_3 inclusion [51].

The fabrication route leads to an anisotropic fibre distribution where the fibres are predominantly orientated perpendicular to the pressing axis, leading to a two-dimensional random distribution. This anisotropic structure is also represented by different permeabilities in different directions. Mortensen *et al.* [112] proposed a model to estimate the K_s of fibre preforms in the different directions. For flow parallel to the fibre axis, it can be calculated as:

$$K_{s_{||}} = \frac{0.427 r^2_{sf}}{V_{sf}} \left[1 - \sqrt{\frac{2V_{sf}}{\Pi}}\right]^4 \cdot \left[1 + 0.473\left(\sqrt{\frac{\Pi}{2V_{sf}}} - 1\right)\right] \qquad \text{Equation 31}$$

where r_{sf} is the radius of the fibre and V_{sf} is its volume fraction. For flow perpendicular to the fibre axis, the K_s can be calculated as:

$$K_{s\perp} = \frac{2\sqrt{2r^2_{sf}}}{9V_{sf}} \left[1 - \sqrt{\frac{4V_{sf}}{\Pi}}\right]^{\frac{5}{2}} \qquad \text{Equation 32}$$

Apart from permeability, the specific surface area of a preform plays an important role in preform infiltration. As reported by Mortensen [121], S_i of Saffil™ fibre preforms, which is the area (m^2) per unit volume of porosity (m^3) in the preform, is given by:

$$S_i = 977800 + 22217 \cdot V_{sf} \qquad \text{Equation 33}$$

In a later publication of the same author [122], the estimated value of S_i was four times higher than that obtained by using Equation 33. The differences in S_i were not further discussed.

2.4.2. Sintered particle compacts

One of the most common ways to fabricate MMCs is to press ceramic particles into a cavity and infiltrate the packed bed with a molten metal. Due to the simplicity, several research groups have concentrated on this method [103]. If the particles are assumed to have a spherical shape with an average diameter D, S_i of the packed particles is calculated as:

$$S_i = \frac{6\lambda V_p}{D(1-V_p)} \qquad \text{Equation 34}$$

where V_p is the particle volume fraction and λ is a geometrical factor introduced to describe deviations from sphericity, but also takes account of surface roughness and of the actual particle size distribution. As no binder is added, removal of the pressed compact out from the pressing cavity can result in breakage. Thus preforms fabricated using this route are not consistent. To achieve consistent ceramic preforms which exhibit sufficient strength to withstand the subsequent infiltration step, the particles have to be sintered. This allows the total porosity to be influenced to some extent by changing the powder compaction and sintering temperature, although it is very difficult to achieve porosities above 50%. It is possible to alter the metal ligament diameter to some small extent by changing the size of the particles [52, 68]. With this simple fabrication route it is not possible to influence the pore structure independent of the ceramic microstructure.

2.4.3. Foamed preforms

Another interesting approach to produce fully interpenetrating networks has been suggested by Lange *et al.* [123] who slip cast a ceramic suspension into a reticulated polymeric foam. After drying, burnout of the polymer and sintering, this leaves a negative replica of the foam with fully open porosity. By varying the polymeric foam, a variety of ligament diameters was achieved. The ceramic structure was not independent from the cell size of the foam and hence ceramic volume fraction of this method was limited to about 0.10.

A related technique has been reported by Cichocki *et al.* [124] who compressed thermoplastic polymer foams and fixed this state by heating to 200 °C with subsequent cooling. By cutting the foams into, for example, wedge shapes prior to compression to a uniform thickness, porosity gradients could be achieved. Subsequent slip casting, burnout and sintering as above led to interpenetrating, functionally graded networks with open porosity that were successfully infiltrated with aluminium melts. Preform porosities between approximately 5% and 25% were possible with this method.

Another foam-based approach has been reported by Peng *et al.* [125] who used a direct foaming and reticulation technique on suspensions of alumina powder and short Saffil™ alumina fibres. This led to an open-celled ceramic foam of approximately 94% porosity. In other work Peng *et al.* [54] synthesized bi-continuous MMCs using direct-foamed preforms with higher ceramic contents in the porosity range of 94% to 78%. By lowering the porosity level, the channels connecting the large cavities (the so-called “windows” as shown in Figure 2.15) were reduced in size.

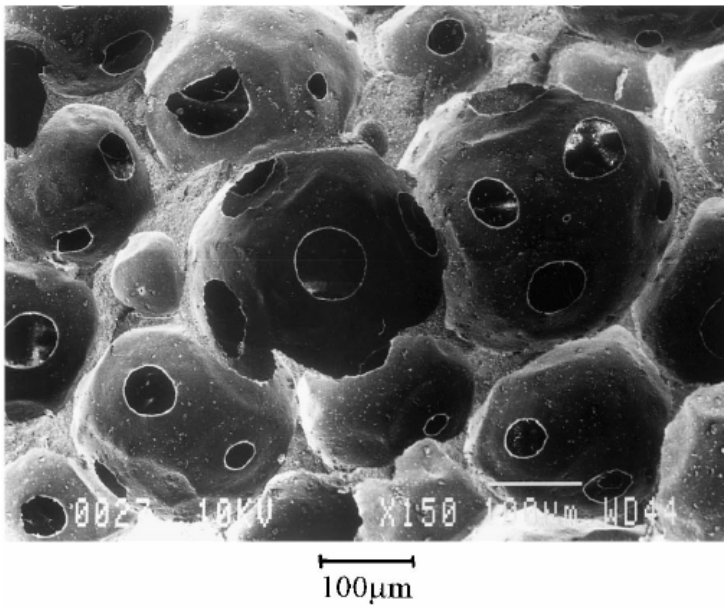

Figure 2.15 Microstructure of ceramic foam with a relative density of 17% [125].

At 91% porosity the medium window diameter was 80 µm compared to 20 µm at 78% porosity. The ratio of window size to cell size k could be predicted within less than 10% deviation by using:

$$V_{po} = \frac{\Pi}{\sqrt{2}}\left[\frac{3}{1-k^2} - \frac{5}{3}\left(\frac{1}{\sqrt{1-k^2}}\right)^3 - 1\right] \qquad \text{Equation 35}$$

where V_{po} was the pore volume fraction. According to this, a critical pore volume fraction is reached at V_{po} of 0.74, above which a sudden transition from an open to a closed cell foam occurs. It is evident that closed cell foams cannot be infiltrated to form an MMC.

2.4.4. Pore formation with pyrolysable additives

The usage of sacrificial pore forming agents (PFA) is a very flexible method to achieve porous ceramic parts. With this method pyrolysable organic agents are added to a slurry of the ceramic powder. After pressing and heat treatment, this organic agent pyrolyses and forms volatile products, forming pores of corresponding shape and size between the ceramic

structure. This is shown schematically in Figure 2.16. Due to simplification reasons, here the sintering shrinkage of the ceramic network was neglected.

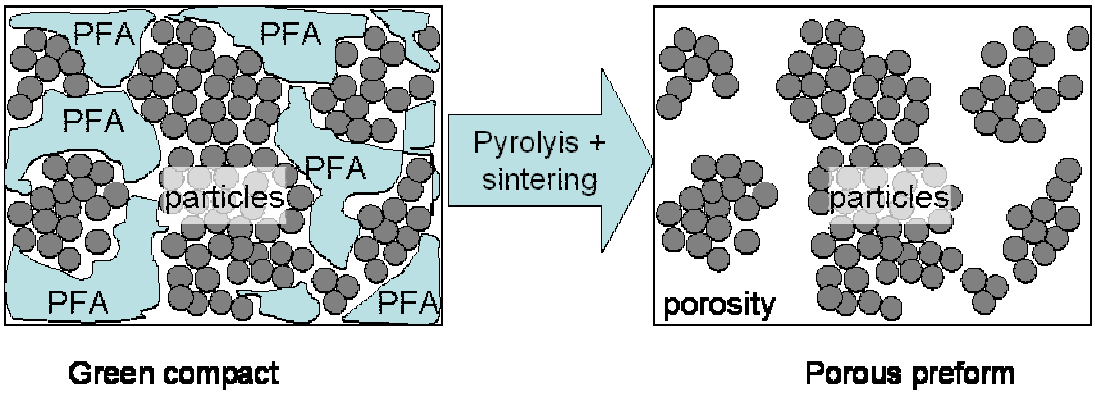

Figure 2.16 Schematic of pore formation using a PFA between the ceramic particles.

A large variety of PFAs has been reported in previous work, among them carbon fibres [(123)], flakes [(126)] and starch [(127)]. The method is very flexible as the porosity can be controlled in the range of 0 to approximately 80% by the amount of PFA added, depending on densification behaviour of the initial particles. By default, the porosity created is not open, especially at low PFA additions. Percolation thresholds are in the range of 15–30%, depending on PFA size, shape and homogeneity of distribution leading to an interpenetrating network.

The green compact consolidation can be either dry-pressing or suspension-based processes which allow a further influence on the microstructure. Alignment of non-spherical particles in a suspension flow is possible, as well as the creation of functional porosity gradients by using a special pressure filtration technique [(128)].

2.5. Pressure assisted infiltration methods

Apart from special systems such as the Lanxide process [(16)] and metallization of ceramic particles with copper or nickel [(129)], the non-wetting nature of aluminium prevents spontaneous infiltration of the metal melt into the preforms below processing temperatures of 1000°C. Thus a differential pressure between the inside of the capillaries and the metal melt

has to be applied. In general, infiltration methods are subdivided into the two methods of liquid transport: the constant pressure (CP) and the constant flux (CF) methods. The former is widely used in gas pressure infiltration of particulate compacts and is the single method published to determine dynamic wetting angles, as reviewed by Garcia-Cordovilla *et al.* [103]. The infiltration times vary in the range from 30 seconds to several minutes. In the CF infiltration mode, experimentally performed using direct squeeze casting and high pressure die casting set-ups, the molten metal is forced into the ceramic network within relatively short times of less than 10 seconds [130].

In all published infiltration experiments, the preforms were preheated to temperatures up to 1000°C. Nagata and Matsuda [131] suggested a critical minimum preheating temperature (T_{pct}) which is independent of size, morphology of the reinforcement and melt temperature and pressure (Equation 36).

$$T_{pct} = T_m - \frac{0.233 \cdot \rho_M \cdot H_M}{V_f \cdot \rho_f \cdot c_{pf}} \qquad \text{Equation 36}$$

The influencing factors are those of the melt (liquidus temperature T_M, melt density ρ_M and heat of fusion of the melt H_M) as well those of the fibre preform (volume fraction V_f, ρ_f and its specific heat capacity c_{pf}).

The critical preheating temperature is important in CF infiltration, where the temperature is usually below the liquidus temperature of the infiltration alloy which is a result of the handling of the preform and the infiltration temperatures. In contrast, in gas pressure infiltration, the preform is heated at the same time in the same cavity as the melt, thus the temperature of the porous media is normally the same temperature as the melt.

2.5.1. Gas pressure infiltration (GPI)

For continuous fibre preforms, GPI is the predominant way to produce MMCs. This is mainly attributed to the possibility of using low pressurization rates which are necessary to prevent fibre breakage and destruction of the preforms [103]. The process is performed in an autoclave within which the alloy and the preform is placed. To prevent gas inclusion in the preform, it has to be evacuated prior to infiltration. The alloy and usually the preform are heated up subsequently. After melting of the alloy, the autoclave is pressurized using an inert gas like Ar or He up to a maximum pressure, P, of 15 MPa [132]. This is the upper threshold for safety reasons. When P reaches P_0, the melt starts to infiltrate the preform. Garcia-Cordovilla *et al.* [103] used a unidirectional setup to infiltrate particulate compacts which were enclosed in tubes. The experiments were performed using relatively long contact times of the order of minutes. In reactive systems, this period exceeds the incubation time which is in general necessary to initiate thermodynamically preferred reactions. The reaction products sometimes block the preform entrance, preventing further infiltration [133]. To ensure that the cavities remain saturated with metal during solidification, the shrinkage has to be directed toward the unreinforced region. Therefore infiltration experiments were carried out using a chill in the furnace to impose directional solidification [132,134].

Knechtel *et al.* [68] infiltrated Al_2O_3 particle beds with pure Al using 15 MPa gas pressure and high processing temperatures of 1110°C. The fracture surface of the resulting Al_2O_3-Al composites exhibited a transgranular fracture of Al_2O_3 and no debonding of the metal phase. Even though the processing was done under extreme conditions, the interfacial reaction layer was only a few monolayers thick. Apart from Al-Al_2O_3 systems, a few carbide systems were also investigated [103], but no other Al-oxide ceramic systems were investigated in the pertinent literature.

2.5.2. Squeeze casting infiltration

In a review of squeeze casting, Ghomashchi and Vikhrov [135] showed that the process involves three essential steps. A specified amount of molten metal is poured into a die, the die is closed and the liquid metal is pressurized as quickly as possible to prevent premature solidification. Afterwards, the pressure is held on the metal until solidification is completed.

The application of pressure during solidification has an influence on the solidification behaviour and the resulting microstructure. In accordance to the Clausius-Clapeyron equation, the high metallostatic pressure, which can rise up to 200 MPa, leads to an increase in the melting point of the metal [136]. Further, as proposed by Epanchistov [137], the eutectic point in the aluminium-silicon system moves to higher silicon contents.

Depending on the gating system, squeeze casting is divided into direct and indirect squeeze casting. In the direct mode, there is no gating system at all. The metal melt is poured directly into the die cavity, which is subsequently closed and pressurized [6,135,138]. In the direct mode, just simple geometries without undercuts are realizable. In contrast, in indirect squeeze casting, the die is filled and pressurized through a gating system. The filling velocities in direct and indirect mode are below the threshold of turbulent flow, preventing entrapment of oxide films in film-forming liquid metals [6].

The pressure provides close contact of the melt with the die material, resulting in large heat transfer to the colder die. The fast cooling rate and solidification are reflected in fine-grained structures with a low secondary dendrite arm spacing [139]. Furthermore, the pressure application reduces gas porosity size and compensates feeding defects, thus reducing voids in the microstructure.

Cappleman *et al.* [116] were the first to publish work about squeeze cast infiltration of Saffil™ fibre preforms with Al alloys. The work was concerned with the fibre/matrix interface of

MMCs infiltrated with an Al-9Mg or Al-11Si (wt-%). They did not observe any intermediate phase between the fibres and the matrix, although a Mg-enriched layer about 0.17 nm thick could be detected in the case of the AlMg alloy. The enrichment of elemental Si on the surface of the fibre in the composite infiltrated with an AlSi alloy was probably a result of silicon precipitates nucleating preferentially on the fibre surface. They concluded that there is no chemical reaction in the composites due to the rapid cooling of the melt when using the squeeze casting infiltration process and therefore bonding between matrix and reinforcement is only the result of intimate physical contact. In contrast, observations of Levi *et al.* [140] showed that there was massive formation of spinel $MgAl_2O_4$ on Al_2O_3 fibres which were immersed in a Al-3Mg alloy (wt-%) for several minutes.

Another interesting aspect of the fast infiltration process is the suppression of Al_2O_3 formation on the Al melt surface. As the melt have an extraordinarily high affinity for oxygen, a thin oxide layer would be continually reforming at the infiltration front, as shown schematically in Figure 2.17. When assuming an outlet in front of the infiltration front which is connected to the atmosphere, the calculations by Cappleman *et al.* [116] showed that a monolayer oxide formation can keep pace with rapid infiltration up to a velocity of 10^{-2} to 10^{-1} m/s.

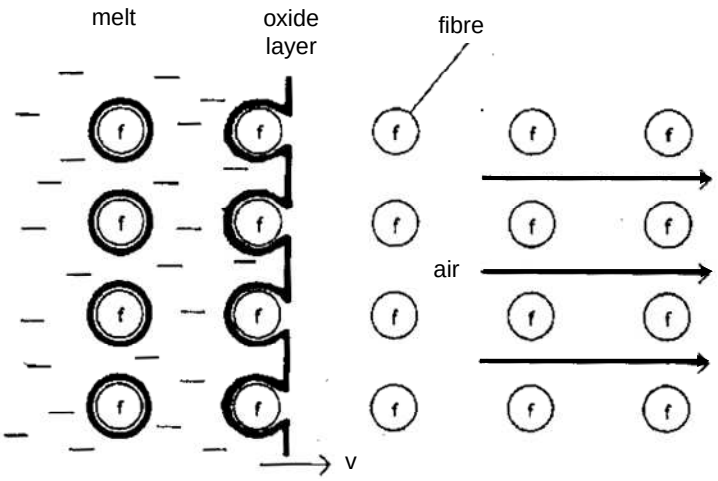

Figure 2.17 Schematic of oxide layer formation at the infiltration front in fibre (f) preform infiltration [116].

On the other hand, if the outlet of the preform is closed or the preform is enveloped within the melt pool prior to infiltration, the entrapped air determines whether an oxide film between the matrix alloy and reinforcement is formed or not. Depending on the specific surface area of the reinforcing phase, the calculations showed that, in preforms composed of more than about 50% by volume of fibres, oxide monolayers cannot be formed on all fibre surfaces.

2.5.3. High pressure die casting infiltration

The main benefit of high pressure die casting (HPDC) is to obtain components with accurate near net-shape geometry due to the use of a high precision metal die. HPDC was found to have excellent performance with regard to control of casting dimensions, making it the most accurate casting method for light metal components [(141)]. The filling pressures in HPDC machines are high and commonly operate at metallic pressures of up to 100 MPa. Such pressures will force the liquid into radii of only 10^{-8} m which is approaching atomic dimensions [(6)]. In the standard HPDC process, the high pressures are thus not needed to fill the cavity but to reduce the volume of the entrapped air. The air originates from turbulent filling of the die. In casting of film-forming metals, the turbulent filling process leads to formation of double oxide films [(6)]. These films decrease the mechanical properties, as they act as cracks inside the castings. A parameter to evaluate the turbulence is represented by the dimensionless Weber number We:

$$We = \frac{V^2 r \rho}{\gamma} \qquad \text{Equation 37}$$

where V is the velocity of the liquid, ρ is the density of the liquid, r is the radius of the section thickness the liquid has to pass and γ is the surface tension of the liquid. As reported by Campbell [(6)], if We ranges between 0.2 and 0.8, flow conditions free from surface turbulence might be assumed. If the Weber number reaches 100, surface turbulence can form double

layer oxide films. The Weber number in high pressure die castings can rise up to 100,000 which means that conditions are closer to atomisation than to fluid flow [6].

Fine grain microstructures of HPDC components result from rapid solidification. Nevertheless the material generally gives moderate strength and poor deformability. This is attributed to the large amount of internal defects [142] and the presence of iron in HPDC alloys. Iron is added to commercial HPDC alloys to prevent sticking of the metal to the uncoated die and results therefore in increased die life [143]. Iron is detrimental to material properties [144] as it forms an increased amount of iron-rich intermetallics of the Al_xFe_y or the $Al_xFe_ySi_z(Mn)$ [145] type which provoke crack initiation.

Even though HPDC is widely used for large scale manufacturing of light metal components, it has not been used extensively for preform infiltration. The main reason is probably the lack of suitable preforms which endure the high dynamic pressure. The plunger velocities in standard HPDC are in the range of 1 to 5 m/s. Due to low ratios of gate area to plunger area, gate velocities are as high as 50 m/s. The dynamic pressure often leads to intensive deformation and cracking of the reinforcement. A measure of this deformation behaviour is the compression which is defined as the ratio of the MMC volume after infiltration to the initial overall preform volume, comprised of reinforcing phase plus porosity. The compression in the published HPDC infiltration experiments reaches 30% [50,51]. In compressed areas, the local volume fraction of reinforcing phase is increased by the factor of compression.

Michaud *et al.* [122] investigated the preform compression behaviour when infiltrating fibre preforms with pure Al. Fluid flow starts only above the threshold pressure P_0, which leads to compressive strain in the preform which is usually purely elastic. Assuming no premature solidification after full infiltration of the preform, complete relaxation is possible leaving no

measurable compression in the resulting composite material. If solidification occurs prior to full infiltration, the relaxation is hindered and compression is observed.

Fibre-based reinforcements in combination with aluminium alloy matrices were the only systems investigated using HPDC infiltration. Just a few groups have published work on this subject. Generally the plunger velocity was lower and the gate area was larger than in standard HPDC. Thus, the casting processes are closer to indirect squeeze casting conditions [135] than HPDC conditions. The reason for this may lay in the suggestions by Long *et al.* [50] who introduced pre-requisites for high quality Al-MMC casting via pressurised infiltration techniques. They recommended that preforms should be preheated to a temperature significantly above the minimum limit suggested by Nagata *et al.* [131], in the range of 750°C to 800°C. If the preform temperature was too low, high deformation and inhomogeneous microstructures were obtained, as shown in Figure 2.18. A low preform temperature of 400°C resulted in compression and residual porosity whereas a homogenous fully infiltrated microstructure could be achieved with a preform temperature of 800°C.

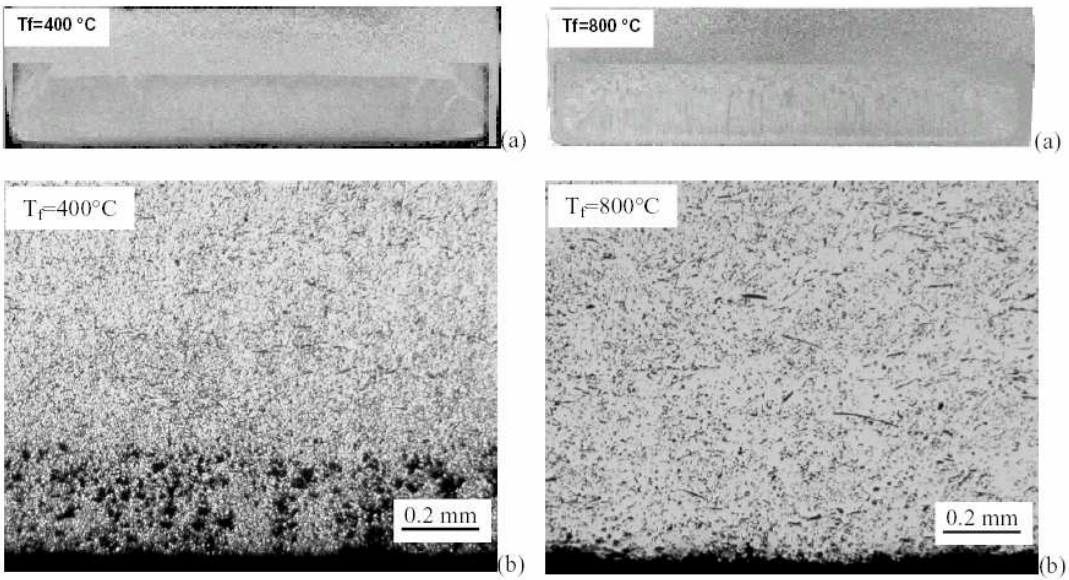

Figure 2.18 Influence of preform preheating temperature on MMC microstructure [50].

Long *et al.* [50] suggested that v_0 should be below 0.1 m/s to prevent crushing of the preform. Another requirement to attain homogeneity in the MMC is a large cross-sectional area of the gate to ensure feeding of the MMC to prevent solidification shrinkage.

Rasmussen *et al.* [146] infiltrated Al_2O_3 preforms with Al-Si and Al-Mg alloys using HPDC. In contrast to Cappleman *et al.* [116] who could infiltrate Al_2O_3 fibre preforms without any visible reactions, the infiltration with an AlMg alloy was unsuccessful due to reactions and blocking of the capillary entrances. Due to the configuration used in the experiment, where the melt was in extended contact with the reinforcement prior to infiltration, this behaviour may be a result of extensive melt-matrix reactions and thus might not be a result of the HPDC infiltration process itself.

Kang *et al.* [117] infiltrated fibre preforms using a broad range of plunger velocities from 0.1 m/s to 3.6 m/s. A velocity of 0.6 m/s was considered to be the optimum in terms of MMC homogeneity. At higher velocities, massive preform deformation and cracking occurred, making the MMC useless.

2.6. Aims and Objectives

Particulate preforms as a basis for preform MMCs are promising due to their advantages regarding cost, availability and knowledge of processing routes. Nevertheless, few papers have been published on infiltration of Al alloy melts into Al_2O_3 and TiO_2 and none into MgO preforms. The ceramic volume fraction range between the upper limit of chopped Al_2O_3 fibres (0.25) and the lower limit of metal toughened ceramics (0.60) has not been investigated, yet it is suggested MMCs within this range might offer improved tribological and mechanical properties. This study is aimed at investigating the properties of MMCs with a ceramic volume fraction between 0.30 and 0.40 in order to get sufficient strengthening and keep the ductility as high as possible.

As it was found that there is a lack of knowledge of the influencing factors on preform infiltration, the study of the preform infiltration behaviour was a further objective of the present study. As reported, the infiltration process is subdivided into two steps: initiation of the flow into the capillaries, characterised by the wetting behaviour, and further flow to fill the pores. Below process temperatures of 1000°C, fully non-wetting conditions ($\theta = 180°$) were proposed for most Al-ceramic systems [53,114]. A question of current interest is whether reactions influence the infiltration performance. The data found in the literature for different reactive melt-ceramic systems, either in static or dynamic wetting experiments, indicated that reactions do not improve the infiltration process. Even though for further pore filling commonly the slug-flow assumption was proposed, in recent publications some inconsistencies of this model could be better explained using the Richards model, originating from soil sciences, which assumes unsaturated flow. Both reactive wetting and further filling of the preform are of interest and to be investigated in the constant pressure and the constant flux modes.

3. EXPERIMENTAL PROCEDURE

The influence of reactivity between the metal melt and the ceramic reinforcement on infiltration behaviour was investigated. Thermodynamic calculations were undertaken to determine the equilibrium standard free energies of different aluminium alloy-oxide ceramic systems. From this analysis, promising systems were chosen for experimental investigation of static and dynamic wetting. The contact angles were determined using sessile drop experiments, whereas the dynamic contact angles and the fluid flow behaviour were evaluated during infiltration of the porous preforms with the selected aluminium alloys. The procedure of preform preparation and characterisation and their infiltration using gas pressure (GP), direct squeeze casting (DSQC) and high pressure die casting processes (HPDC) are presented. The resulting MMC materials were characterised using non-destructive X-ray methods as well as destructive metallographic methods. The Young's modulus, strength and fracture toughness of the MMCs and their tribological behaviour were measured. Details of these experimental methods are given in this chapter.

3.1. Thermodynamic calculations

The standard free energies of formation for different liquid aluminium alloy-oxide ceramic systems were calculated using the commercial thermodynamic modelling software FACTSAGE of GTT Technologies in Herzogenrath, Germany. The calculations were performed using the module 'Equilib' which is based on minimizing the Gibbs energy G by the method of complex system-equilibria as introduced by Eriksson and Hack [147] and given by the relation:

$$G = \sum \nu_i \mu_i = \min \qquad \text{Equation 38}$$

where ν_i is the stoichiometric coefficient and μ_i the chemical potential of a given system. Chemical equilibrium calculations can be made for a system which has been uniquely defined with respect to temperature, pressure and composition. The FACT database was used to provide data for the calculations. The software was used to calculate the concentrations of chemical species when specified elements or compounds react or partially react to reach a state of chemical equilibrium.

3.2. Contact angle

3.2.1. Sessile drop substrates

To obtain dense substrates, fine grained powders of different oxide ceramics were used. The properties of the initial Al_2O_3, TiO_2, MgO powders, the sintering conditions and the theoretical densities of the fully dense material are listed in Table 3.1. To ensure full dispersion and de-agglomeration, the powders were milled with water using a Fritsch Pulverisette ball mill with 12 mm diameter balls for 5 min. The container and the balls were made of ZrO_2. Subsequently 2 wt.% of the binder Mowiol 8-88, a partially hydrolysed polyvinyl alcohol, was added to enable uniaxial pressing of the final powders. Then the slurry was poured into aluminium alloy dishes and placed in a freezer adjusted to -24°C and stored there for 24 h. The dishes were placed in a Christ Alpha 1-4 freeze-drying unit and the slurry dried at 256 Pa for a minimum of 8 h. The dried powders were then passed through a 250 µm mesh sieve to produce a granulated powder. To make the powder pressable, the binder was activated with 2 wt.% of water dispersed into the powder. This was performed by spreading 20g of powder on a sheet of A4-size paper and atomising water above this bed until the mass of the bed increased by the required value. It then was stored for 24 h and subsequently pressed uniaxially to a pressure of 100 MPa to produce green compacts with a diameter of 30 mm and a height of 4 mm. The organic agents in the green compacts were pyrolysed with a low heating rate of 20°C/h up to 500°C and subsequently heated at a rate of 300°C/h to be

sintered at 1550°C, which represents the maximum temperature of the tube furnace used. In order to achieve near full densification, the Al_2O_3 (AF) and MgO (MO) specimens were sintered again in a custom-made industrial furnace at AAflow in Aalen, Germany, at 1730°C for 4 h. In all cases, the sintering resulted in less than 5% of residual porosity.

Table 3.1 Sessile drop substrate fabrication: powder materials, sintering conditions and resulting density. Data of purity, and grain size were provided by the suppliers. Other parameters were evaluated in this study.

Designation		**AF**	**TF**	**MO**
Ceramic type		Al_2O_3 corundum	TiO_2 rutile	MgO
Powder supplier /type		Sasol HPA0.5	Kronos 1001	Magnifin AM B21
Purity	%	99.95	≥99	99.5
Average grain size d_{50}	µm	0.47	0.35	0.8
Sintering temperature	℃	1730	1550	1730
Sintering time	h	4	2	4
Theoretical density	kg/m³	3950	4260	3580
Relative density	% td	97.2 ± 1.2	95.1 ± 1.5	98.1 ± 1.3

For surface finishing, the ceramic discs were mounted in a polymer resin. To obtain a smooth surface, the samples were ground and polished using metallographic equipment and consumables. The final diamond polishing step was continued until the surface roughness parameter R_a was less than 0.5 µm. The polished discs were removed from the polymer and cleaned of organics by heating at a rate of 20°C/h to 1000°C in air. Subsequently the discs were cooled to room temperature at 20 C/h. After the treatment, the surface of the samples were examined visually and found to be smooth without thermal etching effects.

3.2.2. Metal alloys

Two commercial aluminium high pressure die casting alloys to BS EN 1706 [(148)] were used for the contact angle measurements and the preform infiltrations. One was a near-eutectic Al-

Si alloy of the type EN AC-AlSi12Fe. In the following discussions this alloy is designated as IS. The other was an Al-Mg alloy of the type EN AC-AlMg9, designated as IM. Both alloys were purchased from VAW Imco, Germany. As shown in Table 3.2, the atomic fractions of the main alloying elements, silicon and magnesium, were 10.77% and 10.25% respectively.

Table 3.2 Chemical compositions of the alloys used for sessile drop tests and MMC fabrication in accordance to the suppliers certificates.

Alloy	Code	Si	Fe	Cu	Mn	Mg	Ti	Sr	Na	Be	Al
				weight-%				weight-ppm			
EN AC-Al Si12(Fe)	IS	11.10	0.76	0.05	0.20	0.01	0.044	<5	<5	<3	balance
EN AC-Al Mg9	IM	0.89	0.39	0.01	0.38	9.29	0.025	<5	<5	32	balance
				atomic-%				atomic-ppm			
EN AC-Al Si12(Fe)	IS	10.77	0.37	0.02	0.10	0.01	0.025	<5	<5	<3	balance
EN AC-Al Mg9	IM	0.85	0.19	0.01	0.19	10.25	0.014	<5	<5	49	balance

Both alloys contained iron to prevent sticking of the metal to the uncoated die walls and is always required in high pressure die casting alloys. The IM alloy contained beryllium which was pre-alloyed in order to inhibit oxidation of magnesium in the liquid alloy. The solidus and liquidus temperatures of the alloys were measured by thermal analysis using a crucible based on the Tec-Tip system by Leeds-Northrup Ltd, UK. These temperatures were evaluated in order to estimate the fraction of premature solidified aluminium during preform infiltration.

3.2.3. Sessile drop measurement

The experiments were carried out in a custom made cold-wall vacuum furnace fitted with a resistance heating coil as shown schematically in Figure 3.1. The inside of the furnace was illuminated using a halogen bulb. For gettering of gaseous contaminants, 80-100 g of Ti sponge, with a measured specific surface area of 0.82 m^2/g, were fitted to the heating coil of the furnace, as shown schematically in the detail view in Figure 3.1. For additional gettering, the innermost of five shielding cylinders which surrounded the heating coil was made out of a Ti alloy (TiAl6V4). The shape of the droplet was recorded through the observation hole by

using a AVT-Horn (Aalen, Germany) macro-zoom objective was connected to a Nikon Coolpix 990 digital camera. The resolution of the image of the droplet was measured to be 0.01 mm/pixel.

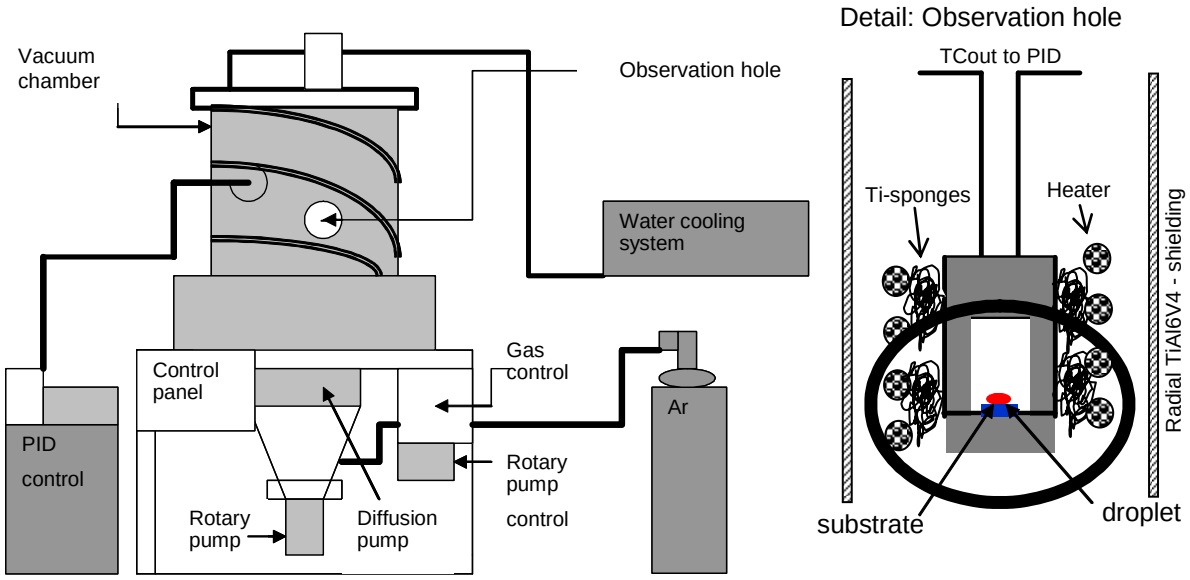

Figure 3.1 Sketch of the vacuum furnace unit and detail view through the observation window: holder with thermocouples (TC) close to the substrate.

Prior to the test, the substrates were cleaned using high purity ethanol. Cubes of the Al alloy with an edge length of 4 mm were ground and cleaned with ethanol. The first measurements were performed by contact heating of the alloy sample directly on the substrate as shown schematically in Figure 3.2 a). To enable cleaning of the liquid metal surface prior to the sessile drop test, a more refined set-up was adapted. The cube of the Al alloy was clamped in an Al_2O_3 tube, which was fixed to the substrate holder at an elevated position. At the lower end of the tube a sharp-edged Al_2O_3 sheet material was introduced into the interior of the tube. The sheet covered about 25% of the internal cross-sectional area. At 750°C the liquid metal in the tube was forced towards the substrate by an mechanical impulse applied to the holder as shown schematically in Figure 3.2 b).

a) contact heating

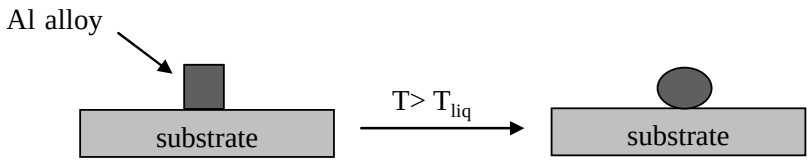

b) heating in tube

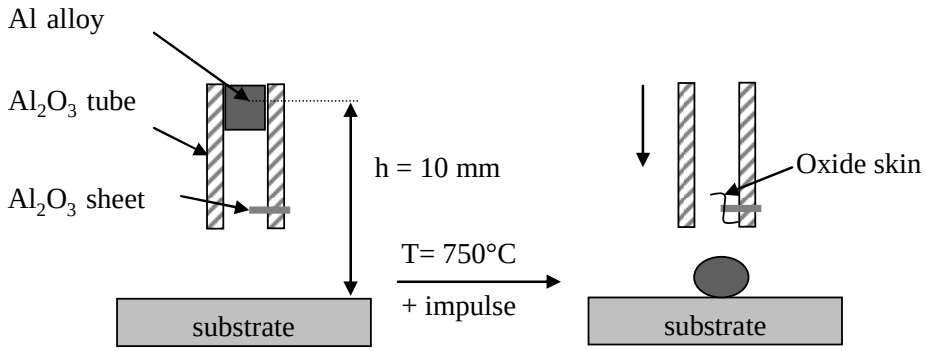

Figure 3.2 Schematic of the different set-ups of droplet generation in the sessile drop apparatus. a) contact heating method and b) heating and melting in a tube prior to contact with the substrate.

Temperature was measured using thermocouples directly mounted to the top of the substrate. The thermocouples were also used for control of heating intensity fitted with a PID-controller. The furnace was heated to 200°C prior to the test. After evacuation to a pressure lower than 10^{-4} Pa, the inside of the furnace was flushed with 99.9995% purity argon (BOC 2311470) with a typical oxygen and moisture contents of less than 1 volume part per million (vpm). This procedure was repeated three times. Once completed, the chamber was evacuated to the minimum pressure attainable, which was in the range of $2 \cdot 10^{-5}$ Pa to $7 \cdot 10^{-5}$ Pa. The system was heated to the measuring temperature of 750°C at a rate of 600°C/h. Once the droplet formed, it was held for 30 minutes during which a sequence of 10 images was recorded.

The images were processed using image analyzing software (ImageAccess of Imagic Bildverarbeitung AG, Glattbrugg/ Switzerland). The droplet profile was digitized and a binary image was generated. The coordinates of the boundary in the region of the triple point were calculated as shown schematically in Figure 3.3. The line which was fitted using the least-

squares fit function within the MAPLE (Waterloo Maple Inc., Canada) mathematical software to a cubic function:

$$y = a + bx + dx^3 \qquad \text{Equation 39}$$

The inflection point and the slope of the tangent at this point were calculated to evaluate the quasi-static contact angle θ_{st} . After the tests, cross-sections through the centre of the droplet were prepared metallographically to investigate the microstructure of the areas near the interface.

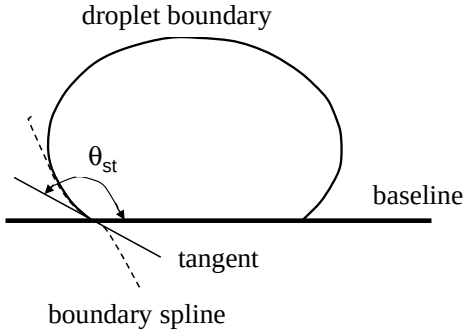

Figure 3.3 Schematic of the contact angle measurement extracted from digital images. The dashed line represents the spline in the vicinity of the triple line.

3.3. MMC constituents

In the preparation of preform-MMCs, a liquid metal is forced under pressure into a porous ceramic preform. The chemical compositions of the alloy were presented in Table 3.2. The target ceramic volume fraction in the preforms was between 0.30 and 40. The preform fabrication can be subdivided into three steps: liquid powder processing, drying and shaping, and finally preform sintering. The resulting pore structures and permeabilities as well as the compressibility of the preforms were evaluated. For reference purposes, two types of preforms were purchased. The fabrication route of preforms and their constituents as well as the properties of the purchased preforms are outlined in the following sections.

3.3.1. Preform ceramics

The seleced ceramic powders of Al_2O_3, TiO_2, MgO used for preform fabrication along with their properties are listed in Table 3.3.

Table 3.3 Properties of dense oxide ceramic materials. Density and coefficient of thermal expansion (CTE) and Young's modulus [149],heat capacity c_p [150], thermal conductivity λ [151], micro hardness [152].

	Temperature (℃)		Al_2O_3	TiO_2	MgO
Density ρ	25	kg/m³	3980	4260	3580
Thermal conductivity λ	700	W/m·K	7,5	1,6	9,1
CTE	20..1000	10^{-6} 1/K	7,4	9,0	13,5
Heat capacity c_p	100..1000	J/g·K	1,13	0,89	1,19
Elastic modulus E	25	GPa	410	270	317
Micro hardness HV	25	N/mm²	1860	1230	700

In contrast to the fabrication of the substrates for the sessile drop tests, where fine grained powders exhibiting median grain sizes below 1 µm were used, the particles used for preforms were coarser. This was to promote intragranular pore dimensions when sintering at relatively low temperatures. The properties of the powders used for preform preparation are listed in Table 3.4.

Table 3.4 Designation used in this work and product specific data provided by the suppliers of the powders, which were used for preform fabrication.

Designation code		AO	TO	MO
Ceramic type		Al_2O_3 corundum	TiO_2 rutile	MgO
Powder supplier /type		Alcoa CL2500	Kronos 3025	Magnifin AM B21
Purity	%	99.8	>99.0	99.5
Median grain size d_{50}	µm	1.8- 2.4	1.4- 1.8	0.8

The particle size distribution of the powder materials were measured at the University of Karlsruhe using a Sympatec Helos laser scattering (LS) particle analyser. The specific surface

areas, S_{sBET} ,of the powders were measured by the nitrogen adsorption method using a Micromeritics ASAP 2010 system [153].

One type of preform, designated as AG, was fabricated by bonding the particles of the powder AO with a glassy binder in order to get preform chemical conditions close to that of Saffil™ preforms, where Al_2O_3 fibres are bonded together with a 2-5% by volume of a silicate binder [119]. The binder type 90263, which was purchased from DMC² (Germany), consisted of SiO_2 with traces of Na_2O and K_2O. The starting point of softening was specified to be 570°C [154]. The ratio of binder to alumina particles was in accordance with that reported for Saffil™-fibre preforms [119]. The composition of the AG replicated that used by Staudenecker [155] and thus no optimisation steps toward the target porosity range were required.

3.3.2. Pore forming agents (PFA)

As the target ceramic volume fraction of 0.30 to 0.40 could not be reached solely by partial sintering of powder compacts, pore formers had to be added. Two types of organic agents, as specified in Table 3.5, were considered as suitable to form irregular or elongated pores. For irregular geometries, cellulose particles (PC) were used. For tubular pores, carbon fibres (PF) were added. In the as-purchased state, the carbon fibres were agglomerated and they could not be dispersed in the slurry. Thus the fibres had to be chopped by milling in a ball mill with zirconia balls using the same milling equipment as described in section 3.2.1. Different milling times were applied in order to reach the optimum compromise between dispersion in the slurry and fibre aspect ratio. The fibre length distributions were evaluated using a Zeiss Axioplan microscope equipped with an XYZ-stage and the Zeiss KS 400 image analyser. The particle size distribution of the cellulose particles was measured at the University of Karlsruhe using a Sympatec Helos laser scattering particle analyser.

Table 3.5 Specified properties of the pore forming additives (PFA) used for preform fabrication in accordance to the data sheets of the suppliers [156,157].

		PC	PF
Type		cellulose	carbon fibre
Main chemical constituents		$C_6H_{12}O_6$	C
Supplier		JRS	SGL Carbon
Type		Arbocell P290	C10 M350UNS
Purity	%	n.a.	≥99
Average particle diameter d_{50}	µm	150	n.a.
Fibre diameter	µm	n.a.	8 ± 0.5
Theoretical density	kg/m³	1500	1750 ± 50

Since it was important for the pore formers to crack and oxidise during the subsequent pyrolysis of the green parts, their pyrolysis properties were investigated in the 20 -800°C temperature range using a Mettler-Toledo DSC12E thermogravimetric analysis unit. The decomposition was performed in oxidising (air) and argon atmospheres heated at 10°C/min.

3.3.3. Powder preparation

The volume of PFA, the green compaction pressures and the sintering temperatures were optimised by studying the range of compositions shown in Table 3.6. The target was to produce preforms with ceramic volume fractions in the range of 0.30 to 0.40 with sufficient strength that they could be handled. The formulations were also fabricated without PFA to enable the fraction of PFA-formed porosity Φ_{PFA} of the total porosity Φ_{tot} to be determined.

The powder processing was undertaken following the procedure described in 3.2.1, except that the PFA was added prior to freezing, by stirring it into the slurry until visual homogeneity was reached. The powder type TOPC10 was fabricated using a large scale production unit at Alpha-Ceramics in Aachen (Germany). The ready-to-press powder was shaped using selected pressures from 10 MPa to 100 MPa by uniaxial pressing in a steel die to give green compacts

with dimensions of 65 mm x 46 mm x 8 mm. For TOPC10, the same powder preparation was applied apart from the drying procedure, which took place in a spray drying unit which led to near spherical grains as shown in Figure 3.4.

Table 3.6 Designation, composition, compaction pressures and sintering temperatures used for the fabricated preforms.

	PFA addition	Comp. pressure	Ceramics in preform				Sintering temp.
	wt-%	MPa	mass fraction				°C
			Al_2O_3	TiO_2	MgO	Frit	
AO	0	60	1				1600
AOPC	10, 20, 30, 40	20, 60, 100	1				1450, 1500, 1600
AOPF	10, 20, 30, 40, 50	100	1				1500
AG	0	100	0.94			0.06	1000
AGPC	15	100	0.94			0.06	1000
TO	0	100		1			1100
TOPC	10, 20, 30	10, 20, 40, 60, 100		1			1050, 1100, 1150
MO	0	100			1		1300
MOPC	0, 10, 20	100			1		800, 900, 1000, 1100, 1200, 1300

The designation of the preforms denotes the ceramics phase, the pore former type and its mass content. For example, MOPC20 is a MgO preform where the pores were formed using 20% of the cellulose particles.

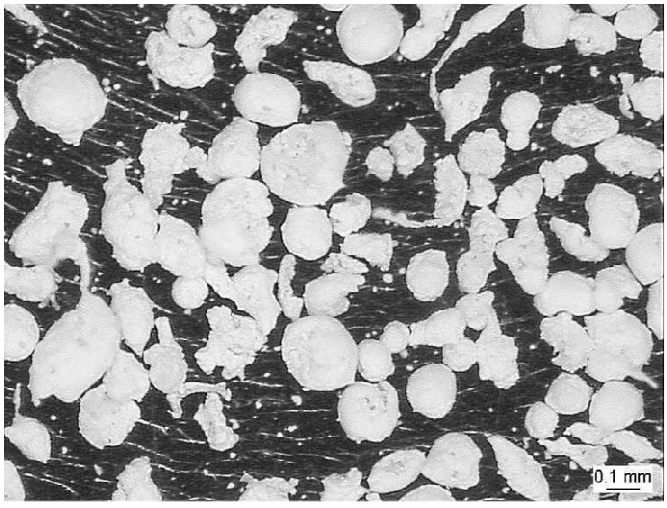

Figure 3.4 Morphology of the spray dried powder granules (white).

3.3.4. Sintering

Sintering of the green parts was performed in a Gero HTRH (Gero GmbH, Germany) alumina lined tube furnace with an inner diameter of 60 mm. A low initial heating rate was used to ensure that the organic compounds in the green parts were removed progressively. Thus a rate of 5°C/h was used up to 475°C with an air flow rate of 20 l/h inside the tube. Subsequently a rate of 300°C/h was applied under similar dynamic atmosphere. All preforms were sintered for 2 hours at the given temperatures (Table 3.6).

Due to preform cracking during sintering in an oxidizing atmosphere, all preforms with PFA content of 20 wt.% or more, apart from magnesia preforms and those with PF as the pore former, had to be heat treated in an inert atmosphere prior to the oxidising sintering cycle in order to crack the cellulose. The two stage sintering process shown in Figure 3.5 was adopted. In the first stage heating took place at 5°C/h to 800°C with a flow of 5 l/h Ar (Figure 3.5 a). Figure 3.5 b) shows the heating profile in air.

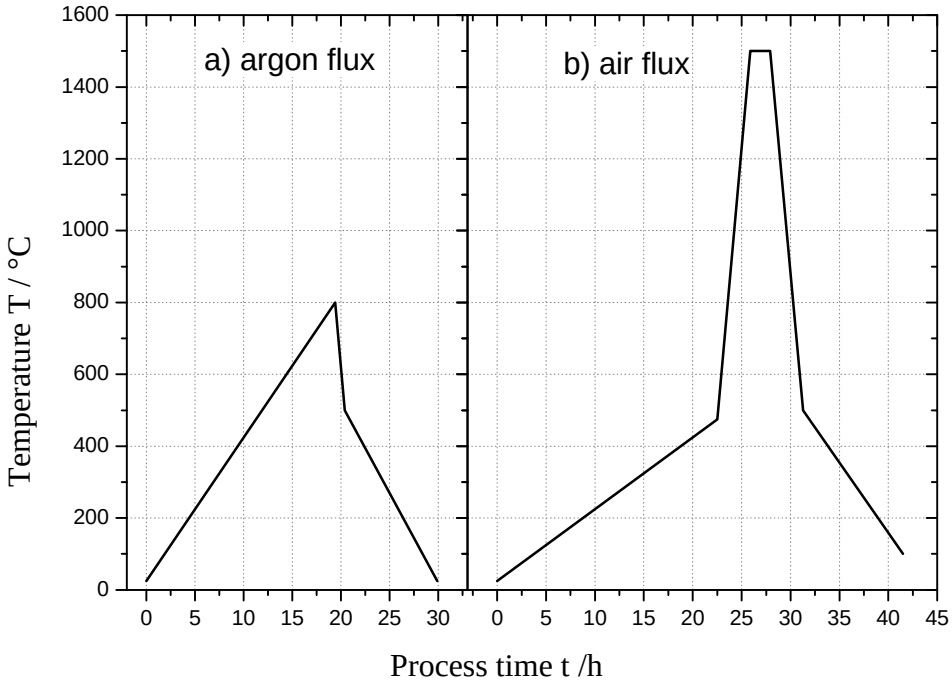

Figure 3.5 Pyrolysis and exemplary sintering cycle: a) pyrolysis in inert atmosphere. b) oxidation of organics and sintering.

The preform sintering process was optimised in accordance with the findings of earlier work [158]. The sintered preforms, which showed low sintering shrinkage, were ground to a standard size of 61 mm x 42 mm x 8 mm.

3.3.5. Porosity fractions

After sintering, the specimen dimensions and weight were measured. The total porosity Φ_{tot} was calculated using the theoretical density of the ceramics. Further, the preform types with sufficient strength for handling and porosity were measured using Archimedes´ principle to determine the fraction of open-cell porosity in accordance to DIN 51918 [159]. The sample was first dried in an oven at 100°C for 1 h and then weighed (m_0). It was then evacuated down to 50 mbar and immersed in distilled water. Following that, atmospheric pressure was applied for 30 min so that water fully entered the open pores of the preform and then reweighed immersed in water (m_2). Ethanol was used instead of distilled water for the measurements on the magnesia preforms. Finally, the sample was taken out of the water, drops of the liquid were removed from its surface and then it was reweighed (m_1). The apparent density ρ_r and the fraction of open porosity Φ_{op} in the preform were calculated from the following equation:

$$\rho_r = \frac{m_0}{m_1 - m_2}\rho_f \qquad \text{Equation 40}$$

where ρ_f was the density of the fluid used at test temperature. The values were taken from tables given by Lide [160]. The open cell porosity Φ_{op} is given by:

$$\Phi_{op} = \frac{m_1 - m_0}{m_1 - m_2} \qquad \text{Equation 41}$$

The closed cell porosity Φ_C was calculated as the difference between the total porosity Φ_{tot} and the open cell porosity Φ_{op}.

3.3.6. Pore structure

The pore size distribution measurements were carried out using the mercury intrusion method on an Autopore III-9400 system (Micromeritics, USA). Specimens of size 6 mm x 6 mm x 6 mm were first dried for at least 24 h at 95°C. Subsequently, they were placed into a quartz glass penetrometer, which is shown schematically in Figure 3.6 b). The penetrometer was then evacuated to a pressure of 6.7 Pa. The mercury was added and the low pressure measurement programme performed to a maximum pressure of 0.26 MPa. Subsequently the high pressure analysis was performed in the high pressure chamber in the range of 0.26 MPa to 227 MPa. The equilibration time for each pressure increment, which is shown as a single data point in the pressure-time schedule in Figure 3.6 a), was 10 s after which the volume of intruded mercury was measured.

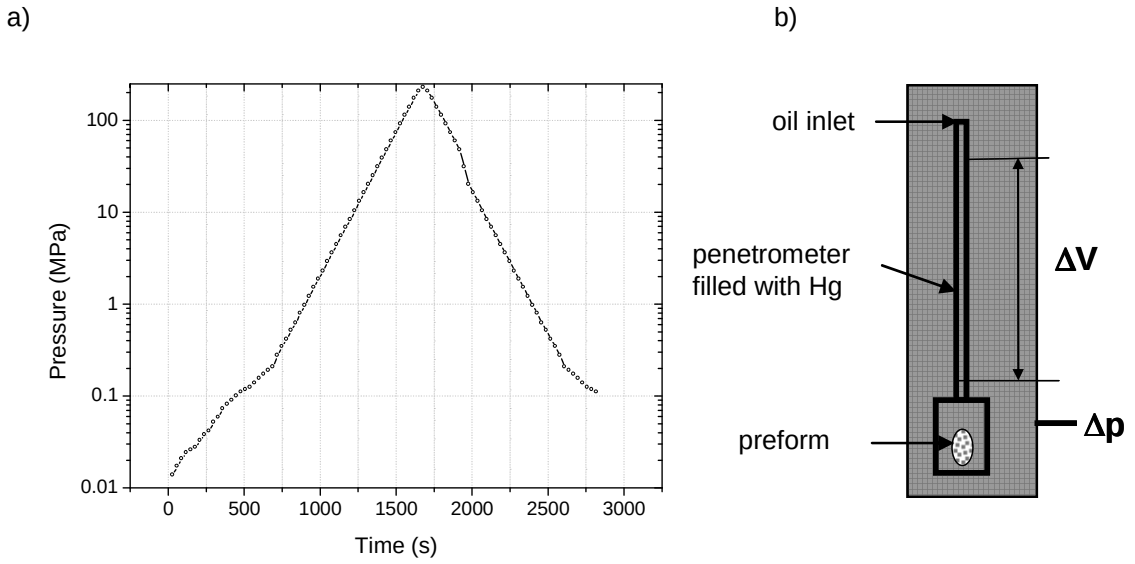

Figure 3.6 a) time-pressure schedule of pressurization in the porosimeter.
b) schematic of the penetrometer set-up fitted in the pressurization chamber fitted with a preform sample.

To determine the fraction of bottle-neck shaped pores, the pressure was decreased incrementally after the highest pressure was reached to give the extrusion curve. The lower limit in the high pressure chamber was ambient pressure. For safety reasons, low pressure extrusion analysis could not be used after the high pressure analysis due to the drastic increase

in the evaporation of mercury at low pressure. The pore fraction still intruded after the extrusion programme was assessed as the residual porosity after extrusion Φ_{ext}. The difference between the geometrically measured Φ_{tot} and the porosity intruded by mercury, Φ_{Hg}, at the maximum pressure was calculated in order to determine the sum of the closed cell porosity and the compression of the sample. The median pore diameter d_{Hg} was determined on the basis of the intrusion curve and represents the diameter at which 50% of the total porosity was intruded.

$$S_{iHg} = \frac{S_{sHg}\,\rho(1-\phi_{tot})}{\phi_{tot}} \qquad \text{Equation 42}$$

The specific surface area per unit mass S_{sHg} was calculated in accordance to Equation 22. The specific surface area per unit volume of porosity S_{iHg} was calculated using Equation 42:

3.3.7. Permeability

The permeability of the preforms was measured along and perpendicular to the uniaxial pressing direction of the initial green compacts. This was carried out as anisotropic permeability was expected in accordance to the work on uniaxial formed fibre preforms by Mortensen *et al.* [112].

For measurements along the pressing direction, disk-shaped samples 30 mm in diameter and 7 mm high were machined from the standard preform geometries. The perpendicular direction was measured applying a cross-sectional cut as shown in Figure 3.7 a). The samples were bonded into aluminium rings using a high viscosity hot-melt adhesive to prevent infiltration. Prior to testing, the samples were evacuated and immersed in water for 12 h to completely fill the open porosity. When measuring magnesia preforms, ethanol was used instead of water to prevent hydroxide formation. For measurement, the ring was mounted to the end of a vertical tube. The tube was filled with the fluid and a controlled gas pressure was applied in the range

of 0.05 to 0.25 MPa to determine the influence of differential pressure ΔP on permeability. The optimized pressure of 0.1 MPa, which was a compromise between measuring time and preform fracturing, was then used for further measurements and the temperature of the fluid was recorded. A schematic of the apparatus used is shown in Figure 3.7 b).

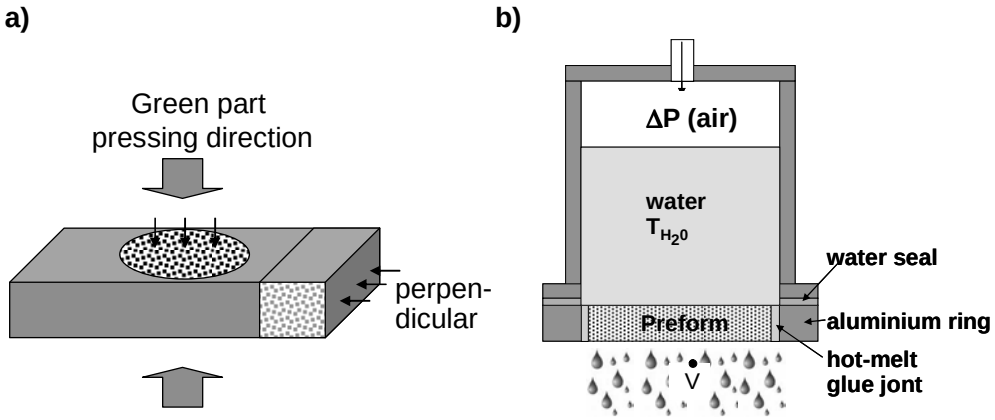

Figure 3.7 Schematic: a) pressing direction and location of the samples used for permeability measurements. b) apparatus for preform permeability measurements, exemplarily when using water as a fluid.

The mass of water was weighed continuously with a Mettler-Toledo PG-5002 SA balance with a resolution of 10 mg. The flow rate v_l of water was calculated by using the density of the fluid at test temperature. The data for density and viscosity η of the fluids were taken from tables [160]. The specific permeability K_S of the preform was calculated as:

$$K_S = \frac{\eta L v_l}{A \Delta P} \qquad \text{Equation 43}$$

where L was the thickness of the preform in the direction of the fluid flow, A the projected area and ΔP the gas pressure applied to the fluid.

3.3.8. Compressibility

The compressibility of the preforms was characterised using two different methods. The first was a compression test on rectangular samples loaded uniaxially between two parallel plates. The second was an isostatic compression test.

The compressive strength, σ_c, of the preforms was determined on an Instron 1362 universal testing machine at the University of Karlsruhe using samples of dimensions 16 mm x 16 mm x 8 mm according to European Standard ENV 658-2 [161]. Six samples of each type of preform were tested.

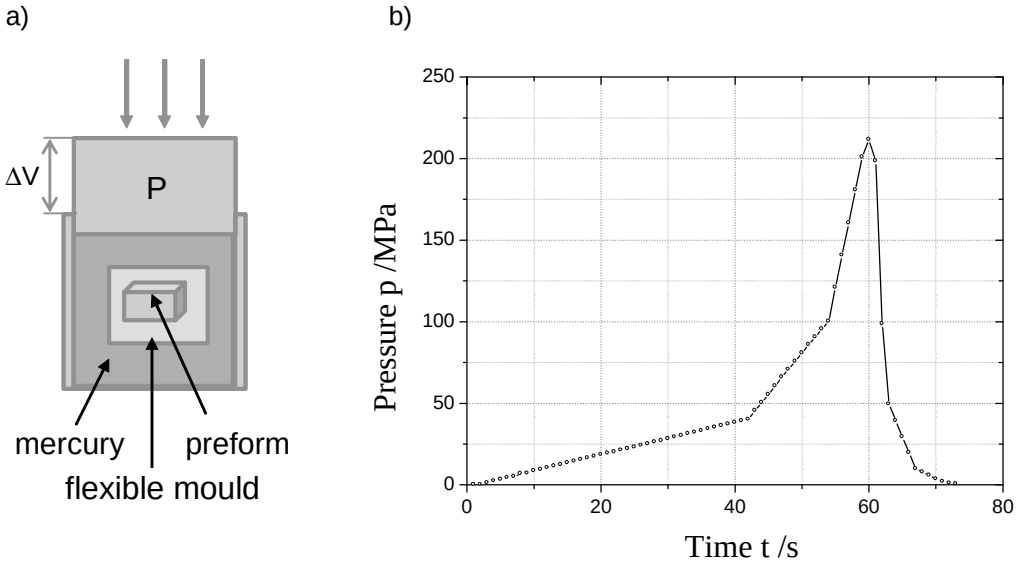

Figure 3.8 a) Schematic of the set-up used for isostatic compression tests on preforms performed on a mercury porosimeter. b) Time-pressure schedule

The isostatic compression tests were conducted on a mercury intrusion porosimeter as described in 3.3.6. The preform samples which measured 6 mm x 4 mm x 3 mm were cut out of the preforms and ground to produce smooth surfaces and round edges. Each sample was canned in a latex finger from a latex glove which was evacuated down to 0.01 mbar and hermetically sealed by applying a knot to its open end. The sample was set into the cavity of a porosimeter as shown schematically in Figure 3.8 a).

Compared to the pore size measurements, a relatively fast incremental pressurization programme was applied, leading to circumstances as close as possible to preform infiltration. The pressurization curve is given in Figure 3.8 b). The volumetric change, ΔV, at each pressure point was recorded. The volume changes at pressures below 0.1 MPa were neglected, since it was assumed that these represented intrusion and compression of the latex and not

preform compression. The relative volumetric compression c_{iso} was calculated as the ratio of volume change ΔV to the initial preform volume. The volumetric stiffness of the preform E_{iso} was calculated as the slope of the linear regression of the pressure- compression curve in the pressure range of 0.1 to 10 MPa. After reaching the maximum pressure, it was reduced stepwise to ambient pressure while measuring volume change to evaluate the permanent compression $c_{iso,per}$ after pressure release.

3.3.9. Reference preforms

Two routes were used in preparation of the reference preforms: a foaming method developed by Dytech Corporation Ltd (Sheffield, UK) and a slurry vacuum filtration route for preforms supplied by Saffil Japan Ltd. These preform types were chosen as they represent the most important fabrication routes reported in the literature and because they were the only commercial preforms within the target ceramic per cent volume content range of 0.30 to 0.40.

The processing of the foamed alumina preform was in accordance with the patent of Sambrook [(162)]. The target ceramic volume fraction of 0.30 could be reached by sintering the green part at 1550°C. The preforms were cut from plates to get the preferred geometry for infiltration which is 61 mm x 42 mm x 8 mm. The designation of this preform type was AODY30 which represents the alumina ceramics (AO), the supplier (DY) and the volume fraction of the ceramic phase (0.30).

As reported by Hegeler *et al.* [(119)], the ceramic volume fraction in chopped Saffil™ fibre preforms is limited to 0.25 by volume. Thus, to reach the target volume fraction of 0.30- 0.40, hybrid preforms made from Saffil™ RF fibres in combination with ceramic particles in a volumetric ratio of 1:1 were purchased. Initially, a chemically inert preform consisting of δ-alumina fibres and α-alumina particles was preferred. This type (Saffil™ designation RFX50AX-301) contained nominally a ceramic volume fraction of 0.30 but could not be used

as the measured mean value 0.23. The producer confirmed problems in processing, resulting in lower values.

As a substitute a hybrid preform type was selected with the designation RF50TD-301, in the following designated as FATO. This consisted of Saffil™ chopped alumina fibres with titania particles having a mean ceramic volume fraction 0.29, which was close to the target range. The delivered preforms were 300mm x 300mm x 8mm and were then cut into standard size samples. The properties of the reference preforms are listed in Table 3.7.

Table 3.7 Properties of purchased reference preforms, manufacturers data with exeption of density and ceramic volume fraction which were determined using procedures described in 3.3.5.

		AODY30	FATO
Type		α-alumina particles	50% δ-alumina fibre RF + 50% TiO_2 particles
Pore formation		Slurry foamed	Vacuum filtration
Supplier		Dytech LTD UK	Saffil Japan LTD
Suppliers designation		POR-AL30	RF50TD-301
Theoretical density	kg/m³	3920	3830
Number of preforms		40	10
Density	kg/m³	1226 ± 59	1096 ± 22
Ceramics elastic modulus	GPa	410	300
Ceramic volume fraction		0.31 ± 0.02	0.29 ± 0.01

3.3.10. Microstructural investigations

SEM examinations were carried out on powder materials by spreading the powder on an adhesive carbon pad. The preform structures were investigated on sawn cross sections. For increased electrical conductivity, the samples were sputter coated with a gold-palladium alloy.

3.4. Infiltration

Different infiltration modes were used to fill the pores of the preform. A constant pressure was applied using gas pressurization. In infiltrations using squeeze casting and high pressure

die casting methods, a constant flow rate infiltration mode was adopted. The infiltration experiments were performed with melts of IS and IM alloys for which the chemical compositions are shown in Table 3.2.

3.4.1. Constant pressure infiltration (CPI)

In this method liquid metal was forced to infiltrate the preforms by means of pressurized argon where the applied pressure, P_{appl}, the difference between absolute pressure P_{abs} and ambient pressure, P_{amb}, could be adjusted in the range of 0.01 MPa to 2.5 MPa. The pressurization was performed in a tool built up of three parts: a lower punch (LP), an upper punch (UP) and a die (DI) as shown in Figure 3.9. All parts were made of H13 hot working steel, with a thermal conductivity of 22 W/m K at 25°C [53]. The die and the lower punch formed a rectangular-shaped cavity of dimensions 65 mm x 46 mm x 35 mm. Prior to the infiltration tests, the cavity and the upper punch were coated with a very thin layer of graphite using a spray (ESD 33, Kontaktchemie, Germany) and then preheated to 450°C in a TP 400 (Fontjine Ltd, The Netherlands) laboratory platen press. The preforms were preheated in a muffle furnace at a rate of 300 °C/h to 800°C to prevent thermally-induced cracking. The gas pressure infiltration comprised the following:

The preform was set into the cavity. The metal melt was transferred from a crucible holding furnace, set to a temperature of 800°C, to the die using a preheated boron nitride coated ladle loaded with 100 ± 10 g of melt. The dross on the surface of the melt was removed and the cleaned melt was poured directly onto the preform. The upper punch, which was fitted with a copper sealing ring, was set onto the die cavity and the die was closed and pressed between the platens of the press to ensure sealing between DI and UP. The gas pressure was applied within 1 s to the chosen value. The gas in the preform which was replaced by the melt volume could flow through the air gap between the bottom punch and the die. The pressure was held

for 90 s to ensure complete solidification of the metal melt. After the test, the pressure was reduced to atmospheric pressure.

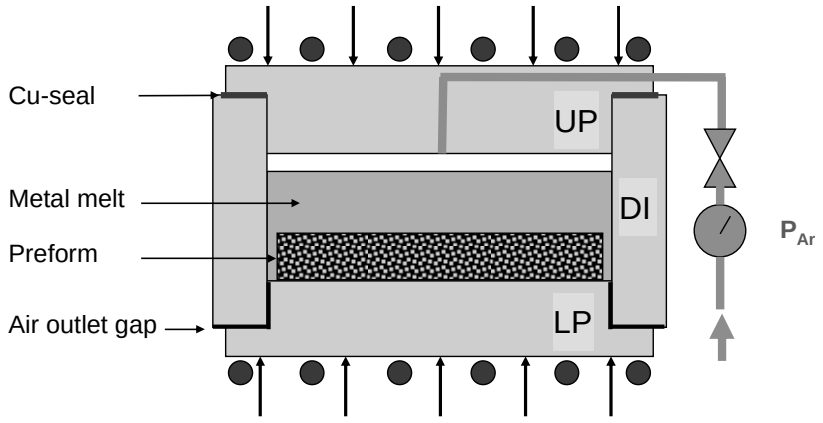

Figure 3.9 Schematic cross-sectional view through the closed gas pressure infiltration set-up. The punches (LP and UP) were heated in the platen press.

The gas pressure infiltrated castings were cut through the centre along the longitudinal axis. As the infiltration behaviour could be shown to be symmetrical, only one half of the casting was mounted in polymer for metallographic preparation. By using a vacuum polymer infiltration technique, the residual pores could be filled, thereby enabling the sample to be polished without scratches being formed by particles originating from non-infiltrated preform regions.

3.4.2. Direct Squeeze-Casting (DSQC)

The die was prepared in a similar way to that used for the gas pressure infiltration except the upper punch geometry was changed to a rectangular block with a height larger than the depth of the cavity. The preform was set into the cavity and the melt was added in the same manner as described in the previous section and the mould was then closed and the press lower platen moved up at an average velocity of 0.017 m/s to a maximum load-controlled pressure in the die cavity of 100 MPa. The time between placing the preform and the end of pressurization was in the range of 10 to 12 s.

After solidification under pressure, the samples were ejected. The process parameters were applied in accordance to Schneele [163] who showed that in the current system the infiltration took place through the four sides and the top of the preform, resulting in a calculated entrance area of $5 \cdot 10^{-3}$ m² for the standard preform geometry (61 mm x 42 mm x 8 mm). Figure 3.10 schematically shows the steps in direct squeeze casting infiltration of a preform. As a reference, samples made of the matrix alloy were fabricated without preforms using identical process parameters. A data acquisition system was used to record the pressure increase with time and the displacement of the punch during squeeze casting infiltration. The compliance of the press was taken into account. The true pressure was calculated as the ratio of the force to the cross sectional area of the die cavity and the infiltration ratio as the ratio of volume reduction in the die due to plunger displacement to the nominal preform porosity volume.

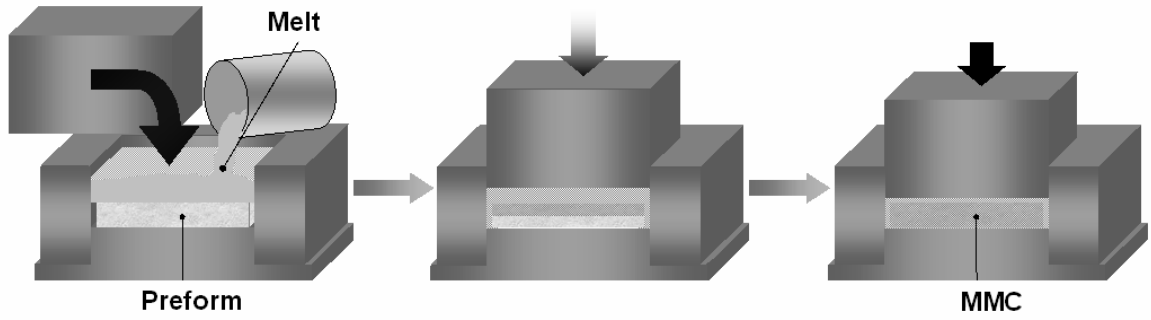

Figure 3.10 Schematic overview of direct squeeze casting (DSQC) preform infiltration process steps.

In order to vary the heat flow, the die was modified by the introduction of an inner cylinder to the centre area of the bottom punch. The cylinder was made from a copper alloy (CuCr1Zr) of 15 mm in diameter with a thermal conductivity of 335 W/mK at 25°C [143].

During infiltration the temperatures inside the die cavity and the preform were recorded using NiCr-Ni thermocouples (Type K) with a diameter of 0.5 mm. The nominal response time of the temperature measurement setup was 30 ms. The thermocouples were fixed by brazing with an silver alloy into the bottom punch so the tip of each thermocouple was close to the

bottom punch surface. The temperature near the edge of a magnesia preform set into the die cavity was recorded in order to investigate its cooling behaviour prior to infiltration.

3.4.3. High pressure die casting infiltration technique

Preform infiltrations were performed using the high pressure die casting technique. The technique is in general characterised by high filling velocities combined with small gating areas and low die temperatures, which were 250°C in the present experiments. The gating areas were varied to investigate the influence of turbulence on preform infiltration behaviour. First, a comparatively large gate area of 18 mm x 50 mm was selected to be close to the indirect squeeze casting (ISQC) geometries described in the literature [50, 135]. In contrast, a tool with a small gate of 62 mm x 1.5 mm was also used for high pressure die casting infiltration (HPDC). The schematic views of the infiltration geometries cast in the studies and the gate structures are shown in Figure 3.11. The diameters of the plunger connections of the tools were 60 mm for ISQC and 45 mm for HPDC.

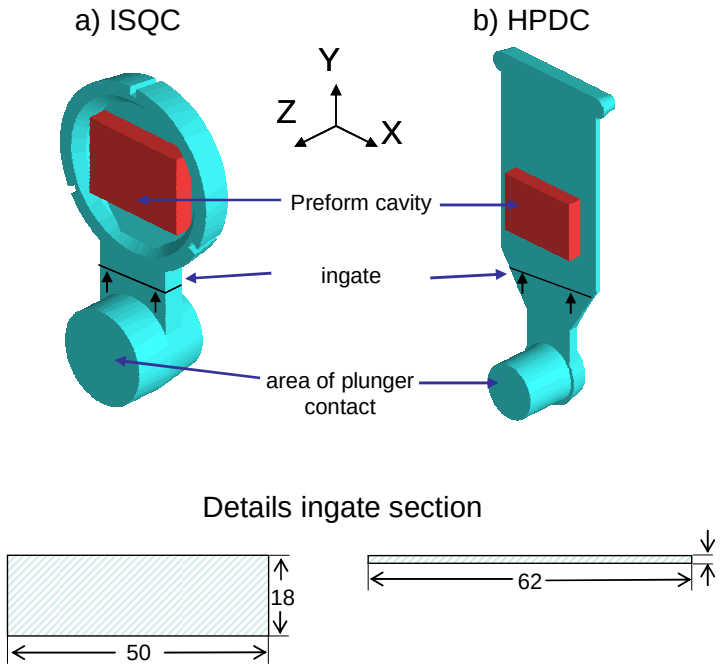

Figure 3.11 Schematic of the die casting components and position of the preform. a) large gate for indirect squeeze casting infiltration (ISQC).b) small gate for high pressure die casting infiltration (HPDC).

The plunger velocity of the die casting machine was varied within the range from 0.4 m/s to 4.5 m/s in order to investigate its influence on preform compression behaviour and infiltration quality. At a given velocity, the flow rate was calculated assuming that the melt covered the whole are of the plunger in the shot sleeve. The gate velocity v_{gate} was calculated as:

$$v_{gate} = \frac{A_{pl}}{A_{gate}} v_{pl} \qquad \text{Equation 44}$$

Where A_{pl} is the surface area of the plunger, A_{gate} the gate cross-sectional area and v_{pl} the velocity of the plunger. In the present system, the preform was infiltrated isostatically from all outer surfaces. Thus the sum of the outer surface areas was used as the infiltration area for calculation of v_0 which is defined in 2.3.2.

The outer surface area was calculated to be 7.6×10^{-3} m² for the standard geometry of 61 mm x 42 mm x 8 mm. The Weber number was calculated using Equation 37, with the surface tension calculated using Equation 1 at a temperature of 700°C, which was the temperature of the melt at the gate during infiltration as predicted by computer simulations [158]. The plunger velocity and the calculated velocities, flow rate and calculated Weber numbers are given in Table 3.8.

Table 3.8 Designation and preform infiltration parameters using direct (DSQC), indirect squeeze casting (ISQC) and high pressure die casting (HPDC) at different velocities.

		DSQC	**ISQC**				**HPDC**			
			05	10	20	40	04	09	18	36
Plunger velocity v_{pl}	(m/s)	0.017	0.5	1.0	2.0	4.0	0.4	0.9	1.8	3.6
Flow rate dV/dt	(10^{-3}m³/s)	$5 \cdot 10^{-5}$	1.4	2.8	5.7	11.3	0.6	1.4	2.8	5.7
Gate velocity v_{gate}	(m/s)	n.a.	1.6	3.1	6.3	12.6	6.0	15.4	30.8	61.6
Superficial velocity v_o	(m/s)	0.02	0.18	0.36	0.72	1.44	0.07	0.18	0.36	0.72
Weber number We	()	n.a.	63	252	1008	4030	76	504	2015	8061

A graphic presentation of the relationship between the plunger velocity, v_{pl}, and the Weber number, We, is given in Figure 3.12 a).

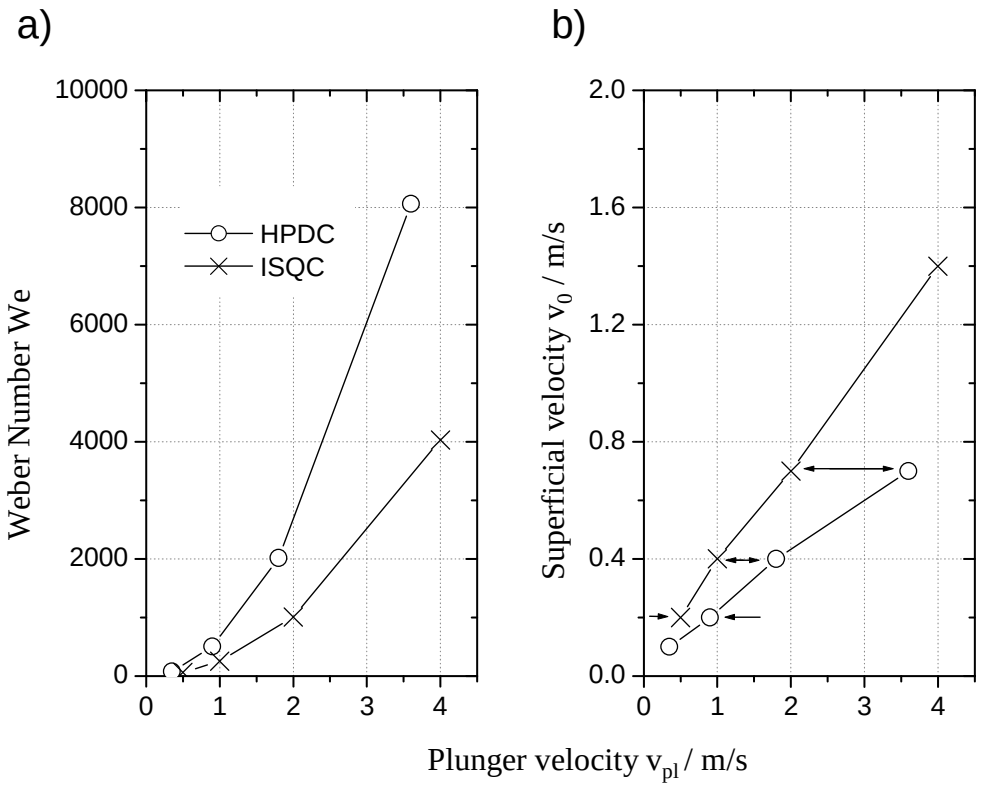

Figure 3.12 Weber number and superficial velocity as a function of plunger velocity in ISQC and HPDC infiltration mode: a) relation between Weber number and plunger velocity b) relation between superficial velocity and plunger velocity. Corresponding superficial velocities are marked with arrows.

The superficial velocity was adapted in such a way that it would be equal in both infiltration modes, ISQC and HPDC. As the plunger velocities were limited, this target could be reached with only three plunger velocities in the different infiltration modes, as shown in Figure 3.12 b), namely ISQC05 and HPDC09, ISQC10 and HPDC18, and ISQC20 and HPDC36.

3.5. MMC characterisation

3.5.1. Differential thermal analysis

Reactions of the final MMC materials after infiltration with alloy IS was investigated by qualifying the calorimetric thermal characteristics using simultaneous thermal differential method (SDTA) (DSC 12E of Mettler-Toledo, Switzerland). In SDTA measurements, the

temperature difference between a reference sample at T_{ref} and the sample (T_{sample}) was recorded. Reference and sample were under the same atmosphere conditions.

The reference sample of the current measurements consisted of a 20 mg alumina block. In the range of 100°C to 800°C, the test was run at a heating rate of 20°C/min using samples of 20 mg. The samples were placed in an alumina crucible and the test was run using a dynamic nitrogen atmosphere achieved by a constant flux of 50 ml/min of high purity nitrogen (>99.9999% N_2). The microstructures of the MMC after the SDTA were investigated using an optical microscope.

3.5.2. Non-destructive testing

The MMC bodies were non-destructively tested using a Wällischmiller Rayscan 200 3D-X-ray computer tomography system shown schematically in Figure 3.13. The procedure has previously been described by Nagel *et al.* [164].

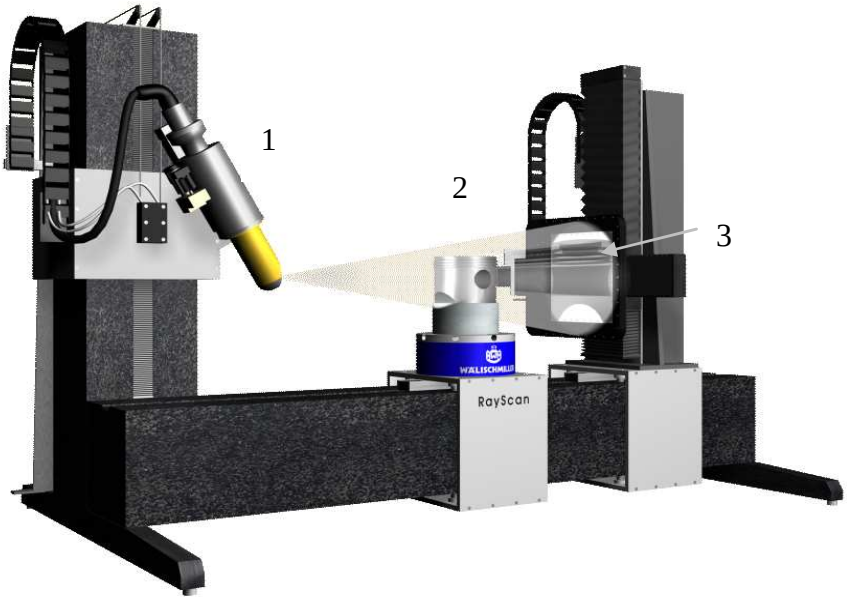

Figure 3.13 Wällischmiller Rayscan 200 3-D CT X-ray scanning system: The micro-focus X-ray-tube (1), component to be tested (2), and area detector (3) [164].

The infiltrated bodies were fixed onto the manipulator (2) and scanned with a resolution of 53 µm edge lengths per cubic volume-pixel (voxel) and therefore only macro pores could be

detected. This operation took approximately 80 min using a microfocus X-ray source (1). An area detector (3) with a 1024x1024 pixel matrix was used. The subsequent 20 minute reconstruction step led to a 3D-database which was used for making the virtual 2D-cuts.

3.5.3. Compression of preforms during infiltration

For determination of the preform compression, MMC samples were cut along the longitudinal axis and fine ground in several stages using graded SiC papers down to a 1200 grit size. The cross-sectional area of the MMC was measured using digital images. The borderline of the MMC was detected by using a grey value threshold and the area was evaluated using image analysis software. A reproducibility test on one sample showed a scatter of 0.2 mm² for a typical area of 400 mm². The relative preform compression, c_{pr}, was calculated as the ratio of the MMC cross-sectional area to the initial cross-sectional area of the preform. When using the die casting technique for preform infiltration, a minimum of three samples per parameter set were measured.

3.5.4. Microstructure and Detailed Image Analysis

Metallographic preparation of the composite samples was achieved by grinding and polishing on a Struers Planopol automatic polisher. Qualitative and detailed image analyses were performed using a Zeiss Axiophot optical microscope fitted with a computer-controlled XYZ-stage. For determination of local saturation of the preform with metal, Zeiss KS400 image analysis software in combination with the macro presented by Bernthaler *et al.* [165] were used. High resolution microstructures were captured using a LEO Gemini 1525 SEM.

3.5.5. Mechanical properties

The elastic modulus, bending strength and fracture toughness, K_{IC}, of the alloy IS and the MMCS were determined using bend test bars of dimensions 42 mm x 4 mm x 3 mm. The elastic modulus was calculated from the first resonant frequency of the bar in accordance with ASTM-E 1876-99 [166]. The bending strength was measured in the four-point mode taking into

account the compliance of the test system. The support distances were 20 mm and 40 mm in accordance with EN 843-1 [167]. The probability of failure, P_f, of the single fracture stresses σ was assumed to follow the two parameter Weibull distribution as:

$$P_f = 1 - \exp\left(-\left(\frac{\sigma}{\sigma_o}\right)^m\right) \qquad \text{Equation 45}$$

where σ_0 is the characteristic stress at which 1/exp of specimens survived, and m the Weibull modulus. The latter is a measure of the distribution of flaws. It is a dimensionless number corresponding to the variability in measured strength and reflects the distribution of flaws in the material. A high Weibull modulus indicates little variation from sample to sample. Both m and σ_0 were calculated using the maximum likelihood method in accordance with EN 843-5 [168]. The fracture toughness was evaluated using single edge V-notched bars (SEVNB) as described by Kübler *et al.* [169]. The mechanical tests were conducted by the Fraunhofer Institut für Werkstoffmechanik in Freiburg, Germany.

3.5.6. Tribological test

The model system investigated for tribological wear consisted of sliding a hardened steel cylinder (r_c=6 mm, l_c=22 mm) on a polished MMC sample with a diameter of 24 mm and a thickness of 7.9 mm. Standard motor oil (SAE 15-W40) was chosen as the tribological medium between the two materials. The translational-reverse movement of the cylinder was conducted on a SRV III-Optimol tribometer. A schematic of the test set-up is shown in Figure 3.14 b).

$$P_H = 0.418\sqrt{\frac{F_N\, E}{r_c\, l_c}} \qquad \text{Equation 46}$$

The normal force F_N was kept constant at 100 N resulting in an initial Hertzian pressure P_H of 100 MPa in accordance to Equation 46 [170]. The calculations were based on the elastic

modulus E_{dyn} of the unreinforced alloy IS, which was reported to be 73 GPa [(1)]. The amplitude of the 30 minute test was 2 mm at a frequency of 20 Hz and a test sample temperature of 150°C.

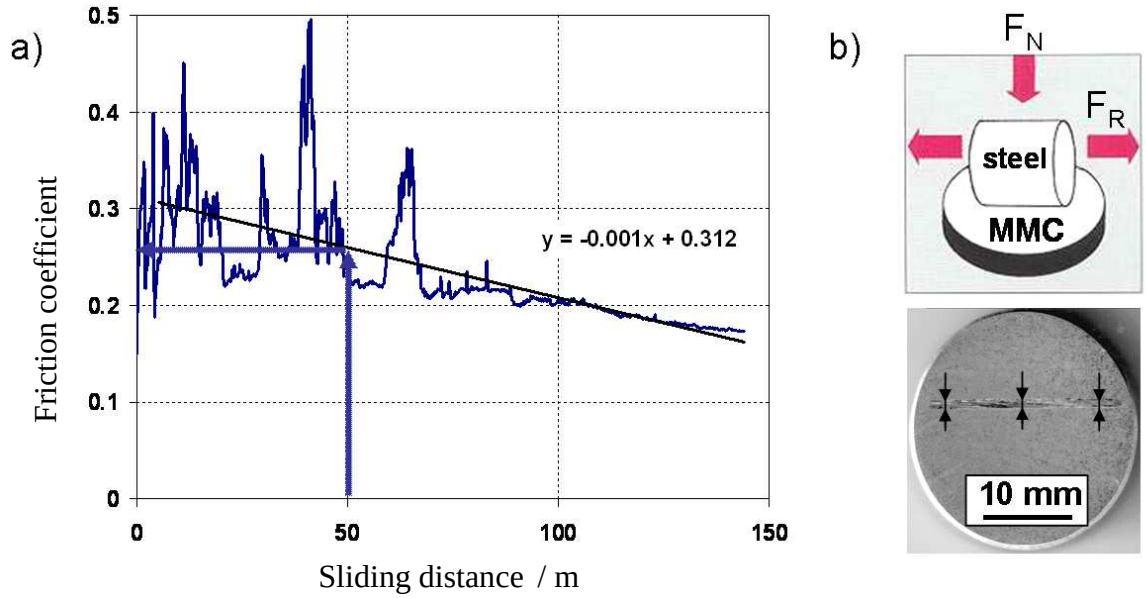

Figure 3.14 a) Typical graph of friction coefficient as a function of sliding distance. b) Schematic of friction piaring and wear path width on MMC sample.

The friction coefficient was calculated as the ratio between the normal force F_N and the friction force F_R. It was recorded continuously as shown in the graph in Figure 3.14 a). The characteristic friction coefficient, f_{50m}, was calculated as the friction coefficient of linear regression at 50m sliding distance. As a single parameter of wear, the mean width of the wear path, w_w, was measured with an optical microscope. The wear path microstructures were investigated using a LEO Gemini 1525 SEM.

4. RESULTS

4.1. Thermodynamic calculations

One aim of the research reported here was to investigate whether chemical reactivity between the ceramic reinforcement and the molten alloy during the MMC processing influences the infiltration behaviour and the properties of the resulting material. A negative heat of reaction is presumed to be a necessary conditions for reactivity. Values were calculated on the basis of the MMC target volume fraction (0.35 ceramic, 0.65 metal alloy) and the infiltration with pure Al at 750°C.

4.1.1. Standard free energy of formation

The Ellingham-Richardson-Jeffes diagram [89] given in Figure 2.11 shows that oxide ceramics may be divided into a group exhibiting higher energies of formation than Al_2O_3, for example Y_2O_3, CaO and MgO, and a group with lower free energies such as ZrO_2, TiO_2 and SiO_2.

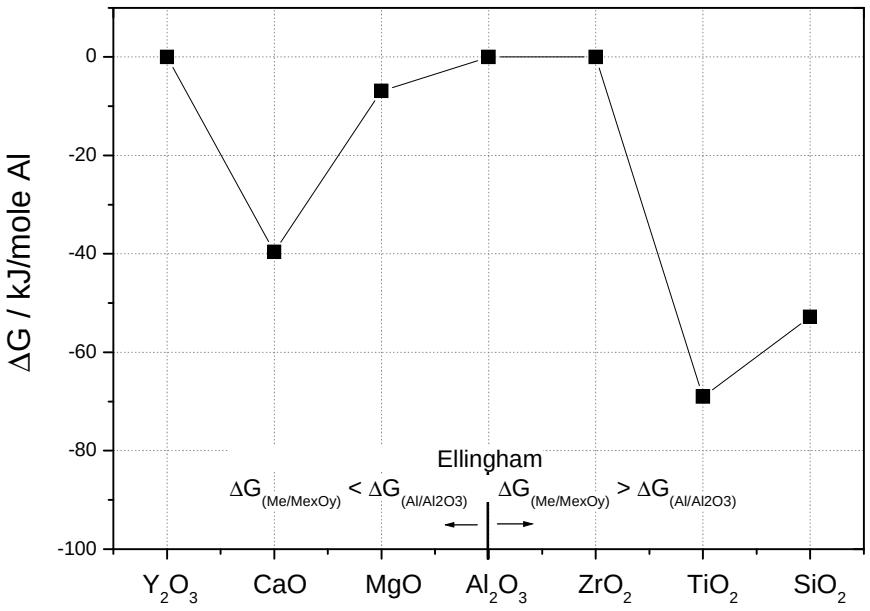

Figure 4.1 Free energy of formation standardized to 1 mole of pure Al of liquid aluminium-oxide ceramic systems at 750°C. Ceramic volume fraction of 0.35.

The latter are reactive systems when in contact with Al whereas the others may be regarded as non-reactive systems. The free energies of formation ΔG for these systems at 750°C were

calculated using the methods outlined in 3.1 and were normalized to one mole of Al. The resulting free energies of formation are shown in Figure 4.1.

The calculation shows that the free energies of CaO, MgO, TiO_2 and SiO_2 are smaller than that of the Al-Al_2O_3 system. Even though CaO and MgO were assumed to be non-reactive systems, free energies of -39 kJ/mole Al and -8 kJ/mole Al, respectively, were calculated. This is attributed to the predicted formation of intermetallics and ternary phases, which are not taken into account in the data for the Ellingham-Richardson-Jeffes diagram, which is only based on the reaction of metal to the metal oxide. Greater values of ΔG were calculated for the reactive systems Al-TiO_2 and Al-SiO_2 (-68 and -52 kJ/mole Al) respectively. The calculations predicted no reaction of liquid Al with Y_2O_3, Al_2O_3 and ZrO_2, as indicated by zero values for ΔG.

4.1.2. Most stable product phases

Knowing the free energy of the system it was possible to calculate the composition at equilibrium. The composite density and the density changes were calculated based on data of Gmelin [171]. In contrast to the pure ceramics, the densities as a function of temperature were not available for all solid solution compounds. Thus the calculations were based on room temperature values of the density. The predicted volume fractions of the product phases brought to equilibrium at 750°C are shown in Figure 4.2. The thermodynamic calculations of Y_2O_3, Al_2O_3 and ZrO_2 showed no change from the initial composition already indicated in the previous section by zero ΔG values.

In the system with CaO, the entire ceramic phase reacted with the aluminium to form the more stable phases of alumina and an intermetallic compound $AlCa_2$, in combination with a low volume fraction of the initial liquid aluminium. As no density data for $AlCa_2$ could be found in the literature and the Gmelin [171] database, the density of the mechanical mixture of

calcium and aluminium in the stoichiometric composition of $AlCa_2$, which was calculated to be 2320 kg/m³, was used for the volumetric calculations.

The predicted phases after reaction of liquid aluminium with MgO were a small amount of the spinel phase $MgAl_2O_4$, the initial ceramic MgO and a solution of magnesium in aluminium. As indicated, the calculated equilibrium was reached before all the MgO reacted to form the ternary $MgAl_2O_4$ phase.

In the Al-TiO_2 system, it was predicted that Al would react completely to result in a composite containing Al_2O_3, titanium suboxides and titanium aluminides. The titanium suboxides were mainly TiO and Ti_2O_3 and the aluminide phases were predominantly $TiAl_3$ and a minor fraction of TiAl. In the system with SiO_2, the ceramic was reduced completely to give a composite of Al_2O_3 and a solution of Si in liquid Al.

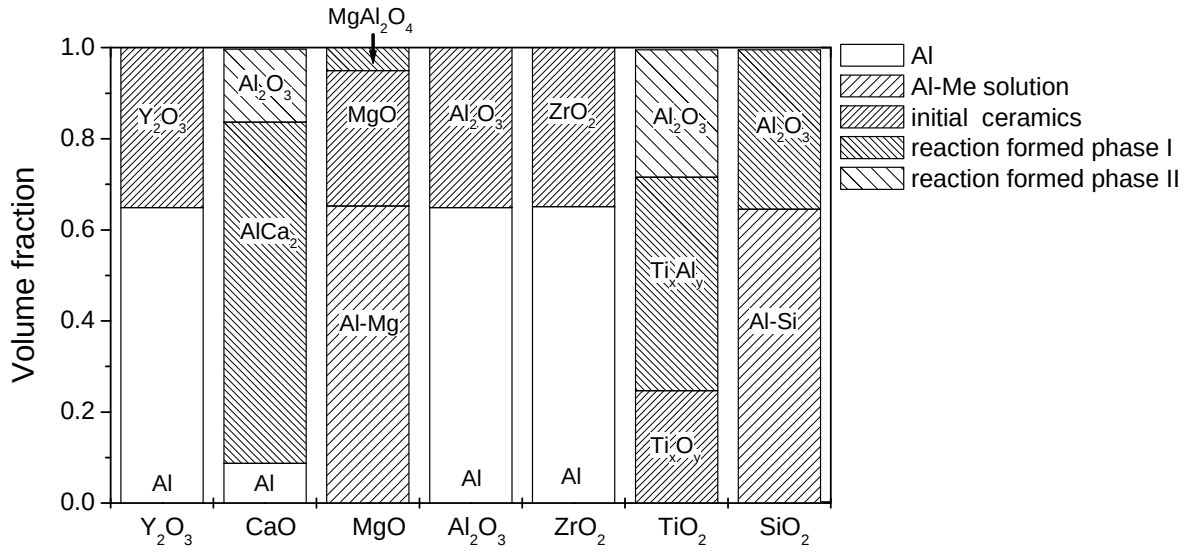

Figure 4.2 Equilibrium composition of different liquid aluminium-oxide ceramic systems.

The relative volume changes between the reactants and the reaction products (i.e. thermodynamically most stable phases as shown in Figure 4.2) were calculated and the results are shown in Figure 4.3. No reaction was predicted in the systems with Y_2O_3, Al_2O_3 and ZrO_2 and thus the density was a result of the mechanical mixture of the ceramic phase with Al.

Positive volume changes were predicted for the Al-CaO and Al-MgO systems. The formation of the $CaAl_2$ intermetallic resulted in a volumetric increase of 10%. A marginal positive volume change of 3% was calculated for the MgO system. According to Gmelin [171], the density of $MgAl_2O_4$ is the same as that of magnesia MgO. Therefore the volume change is a result of the formation of the solid solution of Mg in Al, which results in a density reduction of the alloy. According to Quested *et al.* [172], the density of the solid solution of Mg in Al is accurately given by calculating that of the mechanical mixture of both elements.

Negative volume changes were calculated for the Al-TiO_2 and Al-SiO_2 systems. The formation of the ceramic-intermetallic composite by reaction in the Al-TiO_2 system resulted in a relative volume change of -10%. The largest volume change of -15% was in the Al-SiO_2 system, due to the formation of a solid solution of Si in Al and Al_2O_3 by reduction of SiO_2 with Al. The highest densities of more than 3500 kg/m³ were obtained when combining Al with Y_2O_3, ZrO_2 and TiO_2.

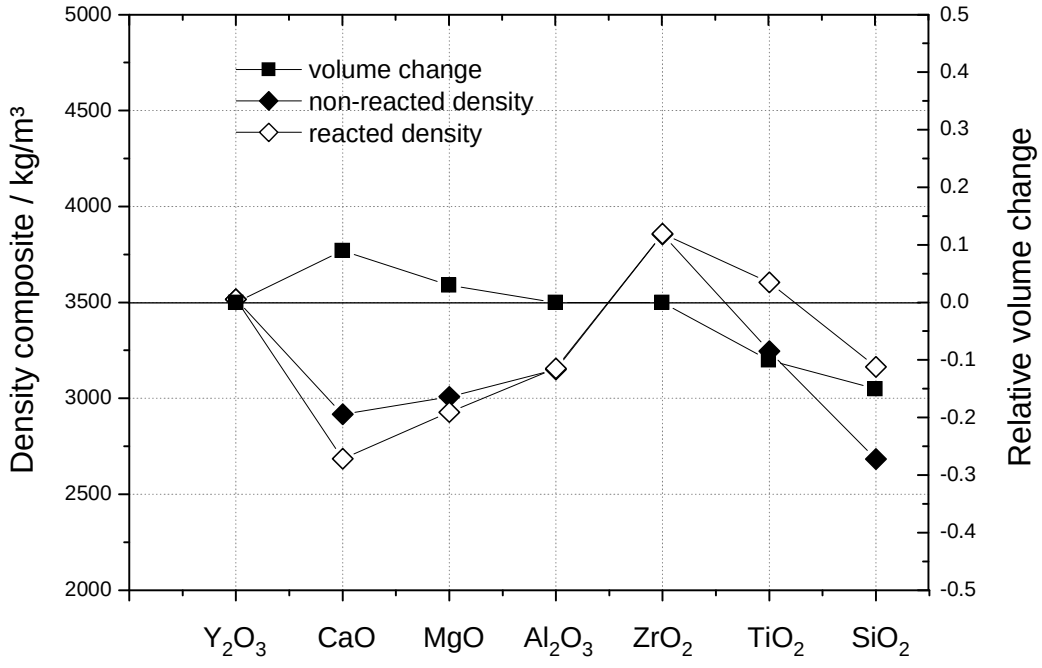

Figure 4.3 Theoretical density of the non-reacted and reacted composite materials at 25°C and the resulting relative volume change from non-reacted to reacted composite material.

4.2. Contact angle

4.2.1 Influence of heating method on droplet formation

Various heating methods for the metal were examined in order to obtain an optimized droplet shape and minimum surface oxidation. First the metal sample was heated directly on the substrate as presented in Figure 4.4 a) but the surface of the metal oxidized during heating to the testing temperature and a skull of oxide prevented the formation of a droplet.

With the AlMg9 alloy, which is referred to as IM in the following, and by using a method which consisted of heating the metal in a tube above the substrate and dropping the molten metal onto the substrate, a droplet with a shiny surface was obtained as shown in Figure 4.4 b). Prior to the impact, the surface oxide was removed by shearing the melt along an alumina sheet located inside the tube, as explained in 3.2.3.

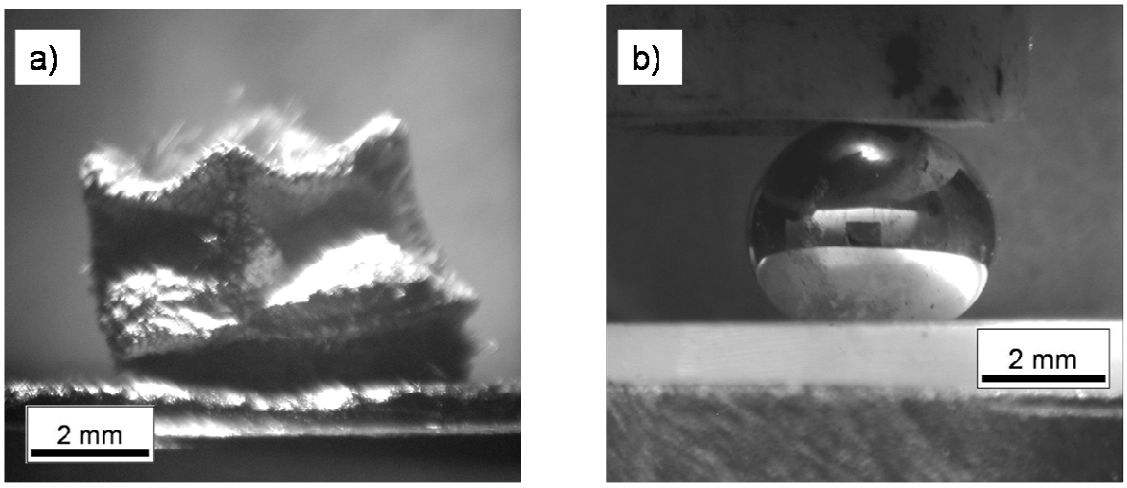

Figure 4.4 a) contact heating of IM cubic sample on substrate at liquidus temperature. b) droplet of IM instantaneously after impact.

In contrast to IM, when the dropping method was applied to the AlSi12Fe alloy (IS) regular spherical droplets were not achieved. A typical example with non metallic lustre is shown in Figure 4.5. The shape of the droplet could not be used for contact angle measurements. No solution was found to prevent the oxidation of the IS alloy during droplet preparation. This restricted the measurements to IM in contact with alumina (AF), titania (TF) and magnesia substrates (MO).

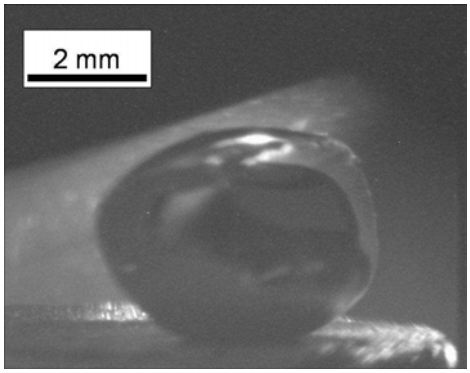

Figure 4.5 Droplet formation of the melt of alloy IS with oxide skin removal prior to impact of melt on substrate.

4.2.2 Wetting kinetics

The time dependency of the static contact angle θ_{st} was measured for a maximum holding time of 1800 s. The error in contact angle measurement was estimated to be ± 5° based on three measurements of each droplet image of the same sample.

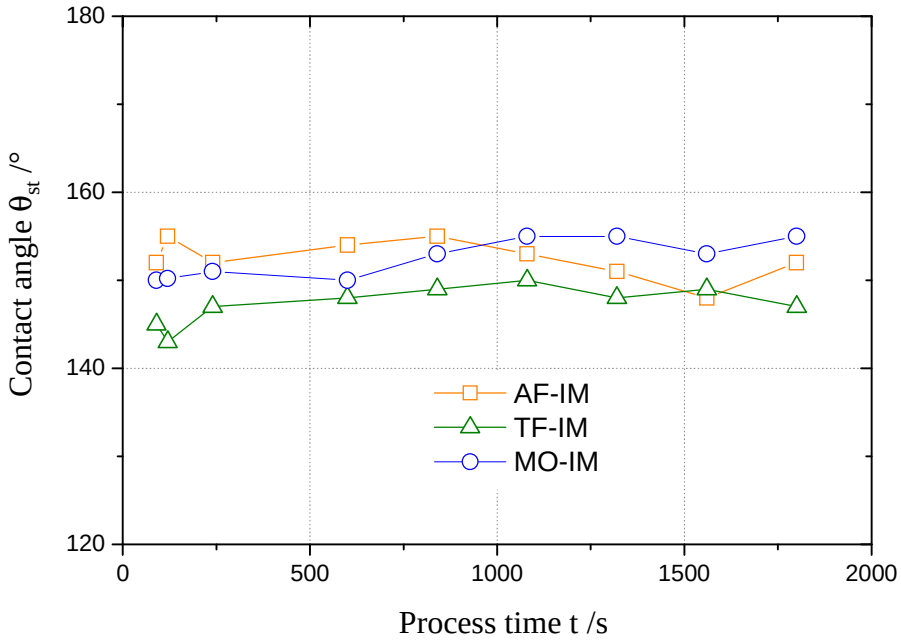

Figure 4.6 Time dependence of wetting angle of the aluminium-magnesium alloy IM on alumina (AF), titania (TF) and magnesia (MO) substrates.

As shown in Figure 4.6, the wetting angle of IM on AF ranged from 148° to 155° with no significant trend over the holding period. Indicating a non-wetting behaviour. The same behaviour was observed in the systems of IM on titania TF and magnesia MO where the wetting angles θ_{st} ranged from 143° to 150° and 150° to 155°, respectively. Taking into

account the error in contact angle measurements, the wetting angles in all three systems were similar with no significant variations within the holding time.

The reliability of the measurement of the wetting angle θ_{st} during the holding time was demonstrated when the wetting angle measured on the liquid droplet in situ was compared with that measured on a section cut through the centre of the solidified droplet. This measurement, as shown in Figure 4.7, was performed using the spline method similar to that used for the in-process measurements. The wetting angle of IM on MO was 154° in both cases, indicating good agreement between the two methods.

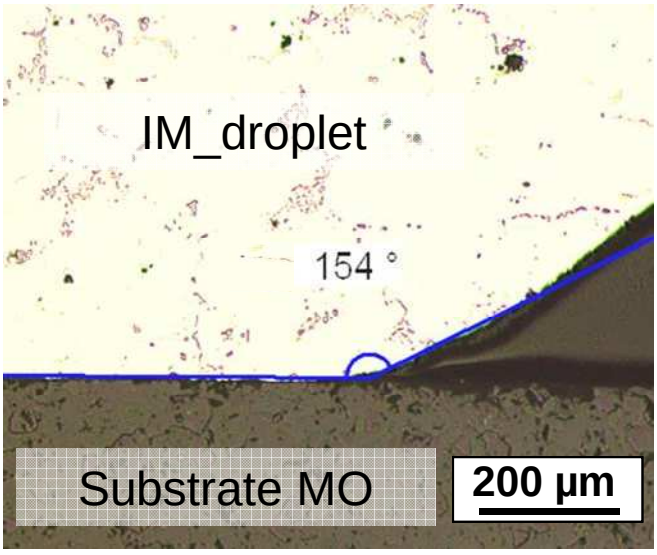

Figure 4.7 Contact angle of IM on MO determined using a micrograph at the triple point on a cross-section through the centre of the solidified droplet.

4.2.3 Influence of substrate on interface formation

Apart from the contact angle measurements, the microstructure of the contact area between the substrate and the metal alloy was investigated in order to detect interfacial reaction phases and irregularities.

The ceramic substrates could not be made totally dense and contained residual closed porosity which was opened to the surface during the substrate polishing process. In metal-ceramic substrate couples, the bottle-neck shaped microporosity on the substrate surface was filled

with the metal alloy IM: examples are given in Figure 4.8 a) to c). The cavity inlet diameter was measured to be below 1.3 µm in titania (TF) and alumina (AF) substrates. Examination of the magnesia substrates showed that the main pore inlets had a diameter of about 3 µm. These pores and the smaller pore branches leading off them had inlet diameters in the sub-micron range and were generally filled with the metal phase, as shown in Figure 4.8 c).

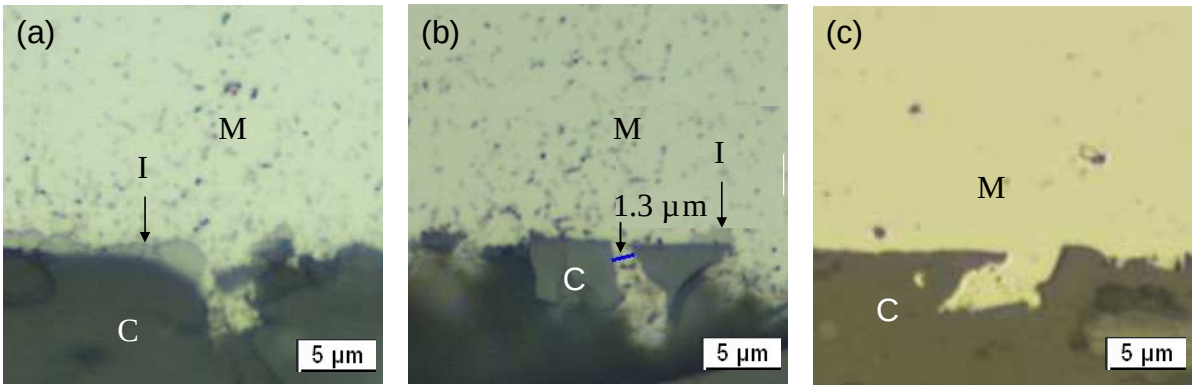

Figure 4.8 Optical micrographs of the interface after sessile drop test a) IM-AF; b) IM-TF and c) IM-MO. Light phase: metal (M), dark phase on the bottom: ceramic substrate (C) and an interfacial phase in IM-AF (I).

Infiltration of the porous structure was further investigated by replacing the low porosity MO substrate with the porous preform MOPC20. After 1800 s, the metal could be easily removed from the substrate, indicating no significant infiltration of the open porosity. This was further confirmed as the surface of the substrate was flat, even after removal of the metal.

The metal had similar microstructures when comparing IM-TF with IM-AF. The finely dispersed grey magnesium-rich phase in the metal alloy (M) in Figure 4.8 a) could not be detected clearly at the IM-MO interface. This was attributed to the over exposure necessary to visualize the ceramic phase. Without over exposure, the distribution of the alloying element in the metal region M of MO-IM was similar to that of AF-IM and TF-IM.

In the case of TF and AF, a coarse plate-shaped phase developed at the metal-substrate interface. This phase and the interfacial delamination behaviour were investigated by

removing the droplet of the IM-AF couple from the substrate and examining a cross-section using SEM and EDS, as shown in Figure 4.9.

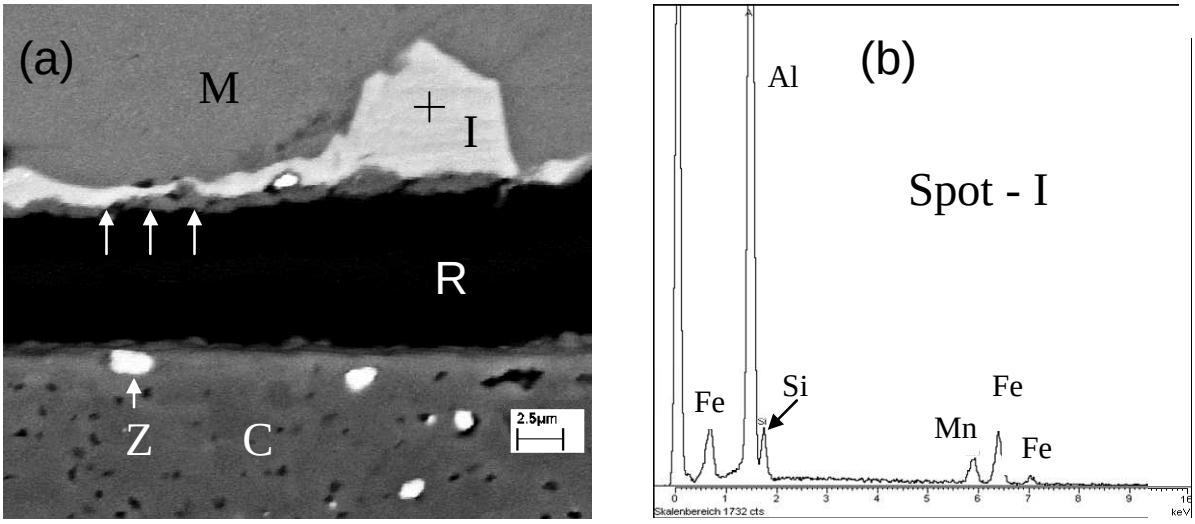

Figure 4.9 (a) Interface of AF-IM after droplet pull-off. M: alloy, I: Fe-rich interfacial phase, R: resin which fills the gap between ceramic substrate (C) with inclusions of zirconia (Z). (b) EDS spectrum of the spot analysis of phase I.

Bright areas in the SEM backscatter image indicate phases with higher atomic weights. These were distributed in the substrate (C) and adjacent to the metal (M) and designated as an interfacial phase (I) and phase Z in Figure 4.9. The phase I was found to contain mainly Al with Fe and Mn and Si. The Fe originated from the commercial AlMg9 alloy (IM) where it was added in order to prevent sticking to the tool steel die walls during high pressure die casting. It accumulated on the substrate by gavity during the relatively long holding time.

The second bright phase, which was distributed in the substrate (C) and is marked with Z in Figure 4.9, was ZrO_2 which originated from the powder preparation step, where the powders were milled in a ZrO_2 container with ZrO_2 balls. The abrasive properties of Al_2O_3 appear to be the cause of this contamination. The comparatively lower hardness of TiO_2 and MgO prevented abrasion of ZrO_2 during powder processing and therefore no zirconia debris was found in the TF and MO substrates.

As shown in Figure 4.9, apart from the ZrO_2 debris in the ceramic phase, there was a particle embedded in the iron-rich phase which was covered with a small layer of the substrate AF. As the metal droplet was pulled off prior to metallographic preparation, the weakest link in the metal-ceramic couple appears to be the first few microns of the ceramic substrate.

4.3. Ceramic powders

4.3.1 Powder particle size

The particle size measurements of all powders were carried out in the as-purchased state. In addition, AO was sized after a milling process used during the preform processing. The particle size distributions of TO and MO were not specified in the data sheets of the supplier.

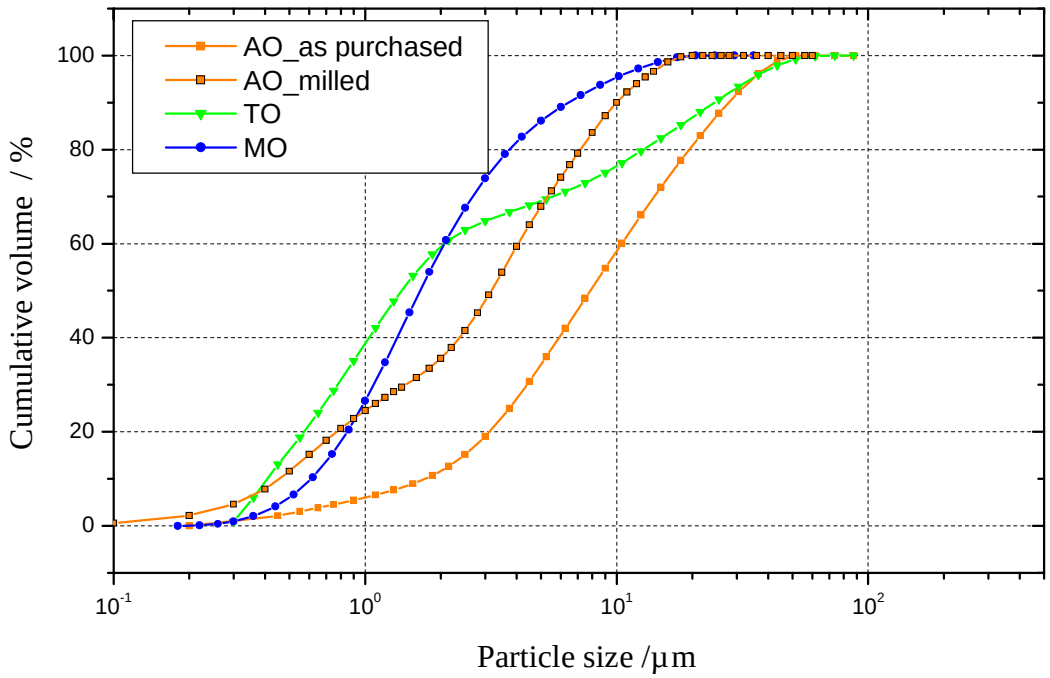

Figure 4.10 Cumulative particle size distributions of the initial ceramic powders AO, TO and MO in the as-purchased state and AO after a milling step.

The characteristic median particle size d_{50} shown in Figure 4.10 was measured to be 1.3 µm and 1.5 µm for TO and MO, respectively. The distribution of TO was significantly broader than that of MO. The unmilled AO and MO powders both showed an S-shaped curve on the log-normal plot in Figure 4.10. The unmilled TO powder was bimodal as indicated by the

shoulder between 60 and 70% cumulative volume. The milled AO powder was also bimodal with a shoulder in the distribution curve between 30% and 40%. Milling reduced the d_{50} of the powder from 8 µm to 3.2 µm. Both values were larger than the d_{50} of 1.8 to 2.4 µm specified by the supplier.

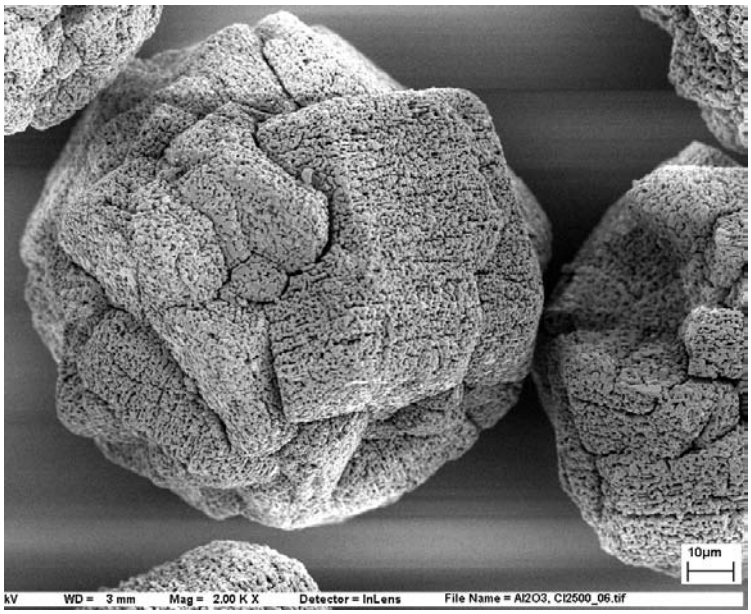

Figure 4.11 Microstructure of AO in the as-purchased condition.

The non-milled AO powder was examined by SEM to determine the source of the deviation between the nominal and measured particle sizes. As shown in Figure 4.11, relatively large spherical agglomerates with diameters exceeding 100 µm were dominant. This diameter was larger than that evaluated by the laser-scattering method. Some breakdown occurred in sample preparation where the powders were suspended in water by ultrasonic agitation, resulting in a lowering of the median particle size to 8 µm. With the introduction of a de-agglomeration step, further crushing occurred resulting in the further lowering of d_{50}. Nevertheless the particle size suggested by the manufacturer could not be achieved even after the de-agglomeration. Therefore, it is evident that the specified median particle size range of 1.8 to 3.2 µm is that of the single particles which were agglomerated in the as-delivered condition.

4.3.2 Powder specific surface area

The specific surface area $S_{s\,BET}$ of TO, MO and AO in the as-purchased state was determined with the nitrogen adsorption method. That of MO was performed additionally on powder aged for 12 months in standard atmospheric conditions and that of AO after milling. A reproducibility test showed that the scatter in $S_{s\,BET}$ was within 5% for the same sample.

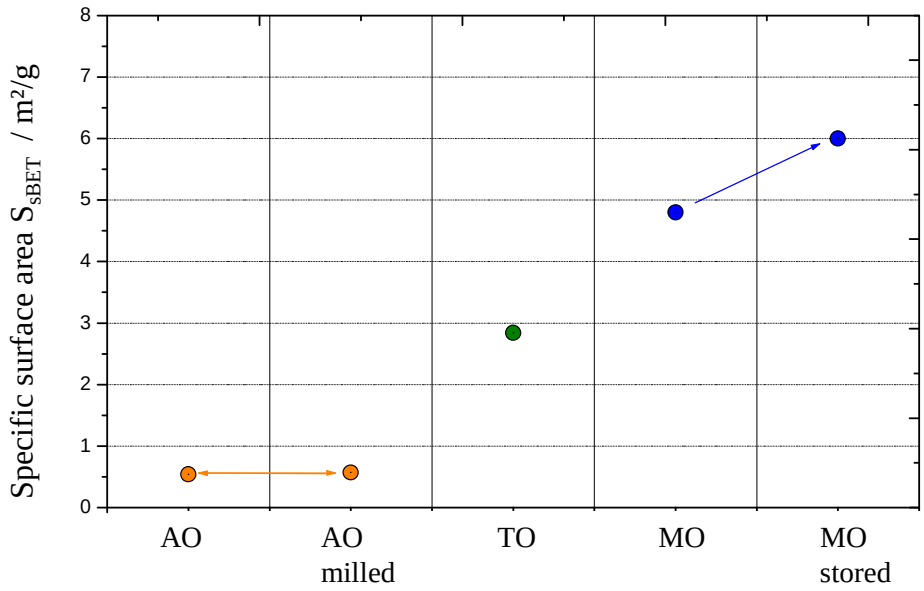

Figure 4.12 Specific surface area S_{sBET} of ceramic powders. AO in the initial and de-agglomerated state. MO before and after storage for 12 months.

As shown in Figure 4.12, the powder AO showed a specific surface area of 0.57 m²/g in the initial state and a marginal reduction to 0.54 m²/g after milling which was within the scatter of the method. Therefore milling did not increase the specific surface area of AO as a result of the relatively short milling time of 300 s within which no new surface could be generated.

The surface area of TO was 2.84 m²/g and that of MO was 4.8 m²/g. The latter met the specified value of 4 - 5 m²/g. The surface area increased to 6.0 m²/g when the powder was stored for 12 months. At the same time, the loss of ignition (LOI) increased from 1.78% to 3.49%. This indicates that further hydration of MgO occurred during storage and led to an increase in its surface area.

4.3.3 Microstructure

Figure 4.13 a) to c) shows the microstructures of the milled AO powder and TO and MO in the as-purchased condition. The microstructure of MO powder was after storage for 12 months in a normal climate.

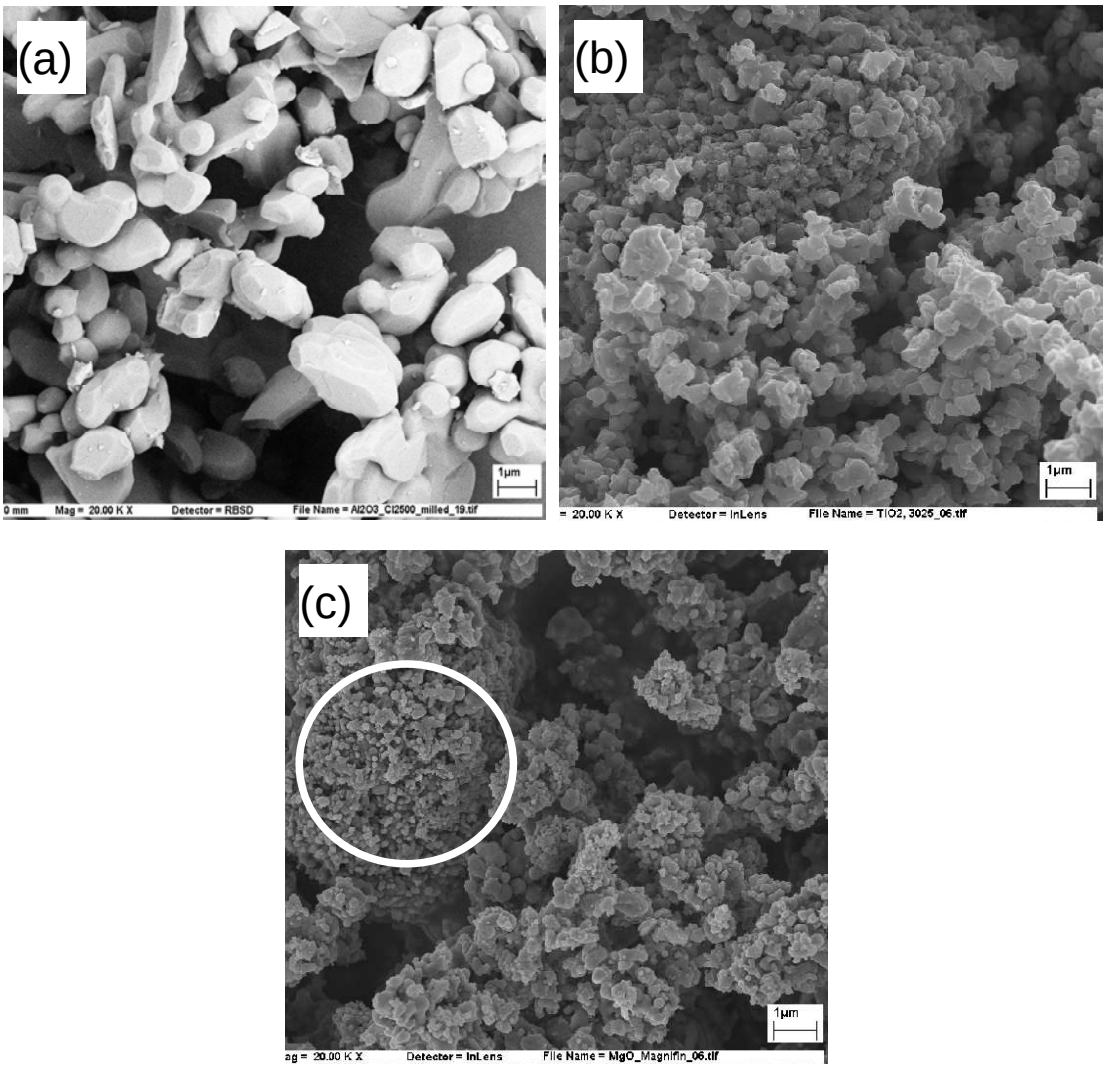

Figure 4.13 Microstructures of the powders used for preform fabrication. a) AO in the milled condition. b) TO in the as-purchased condition. c) MO after storage.

The low magnification image of the as-purchased AO powder in Figure 4.11 shows a rounded structure. The higher magnification image of the milled structure in Figure 4.13 a) shows small tabular grains with an aspect ratio significantly lower than unity as a result of milling which broke down the spherical agglomerates to the primary grains.

The particles of TO and MO were distinctively smaller and had a platelet morphology. On the surface of some agglomerates of MO, there were regions with very small round particles; one area is circled in Figure 4.13 c).

4.4. Pore forming additives (PFA)

4.4.1 Particle size distribution

Two pore forming agents (PFA) were used: carbon fibres (PF) and cellulose particles (PC). The PF were ball milled to produce a fibre length which was dispersible in the aqueous ceramic slurry. The optimum milling time, which was a compromise between the maximum aspect ratio to keep the fibrous shape and the ability to be dispersed in the slurry, was found to be 1 minute [173]. The lengths and diameters of 1200 fibres were measured after milling.

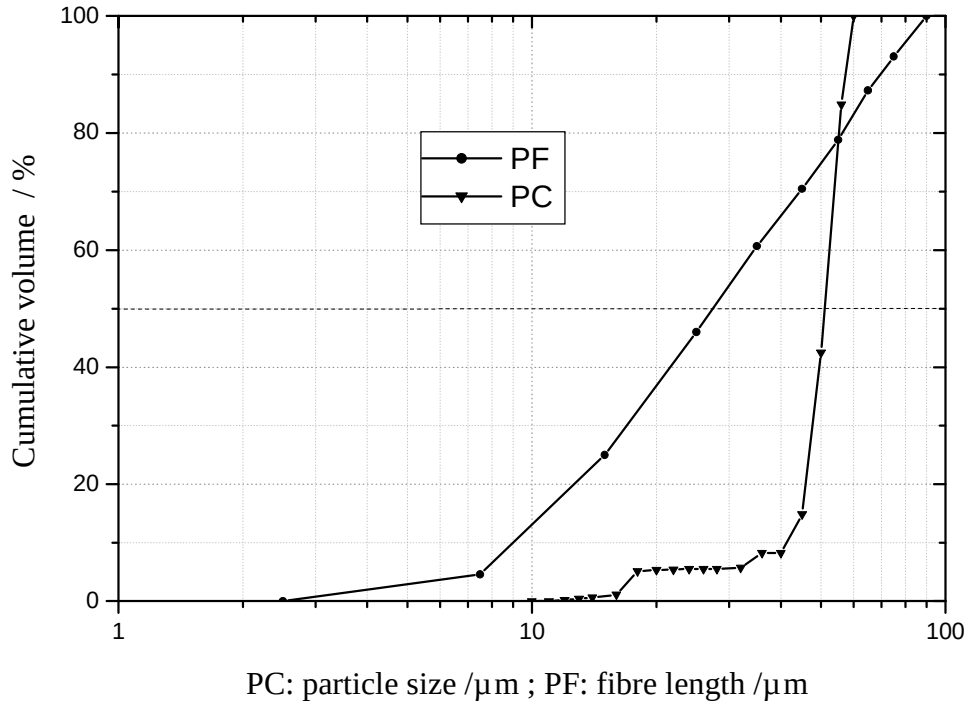

Figure 4.14 Size of the pore forming additives: Particle size of the cellulose (PC) and length distribution of the carbon fibre (PF).

The mean diameter was 8 µm, with all measured fibres falling in the range between 7.5 and 8.5 µm. The volume fractions per fibre length class were calculated assuming the fibres to exhibit a cylindrical geometry with a diameter of 8 µm. This allowed the cumulative volume

fraction to be calculated as shown in Figure 4.14. The median fibre length was 28 µm. As shown in Figure 4.15 a), the diameter was consistent at the specified value of about 8 µm therefore the median aspect ratio of PF was 3.5.

The results of the particle size distribution of PC, which was measured using a laser scattering technique, are shown for comparison in Figure 4.14. The median particle size d_{50} of PC was 51 µm. More than 90% of the particles were between 40 and 60 µm. Figure 4.15 b) shows a macrograph of the cellulose particles which exhibited an irregular shape. Most of the particles were flat and elongated with an estimated aspect ratio between 2 and 4.

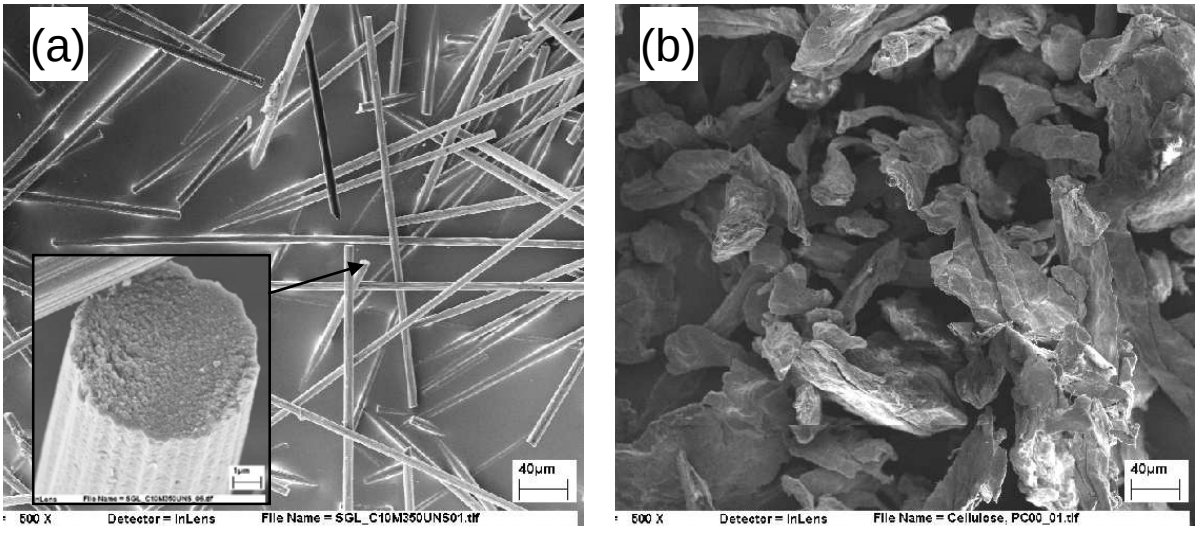

Figure 4.15 Microstructure of the pore formers (a) carbon fibre PF and (b) cellulose PC; both in the as-purchased state.

4.4.2 Influence of pore former chemistry on degradation properties

The pyrolysis behaviour of the pure pore formers, as well as that of a green part with MgO particles, was assessed using thermogravimetric analysis over the temperature range 20°C to 800°C. The relative residue as a function of temperature, shown in Figure 4.16, was calculated as the ratio of the mass at the respective temperature to the initial mass. The pore formers were pyrolysed in inert and oxidizing atmospheres. In the inert atmosphere up to the maximum pyrolysis temperature, the initial mass of the carbon fibre PF was reduced by only 2%. In contrast, about 10% of the mass of PC was transformed into gaseous products between

room temperature and 270°C, with a further 70% lost rapidly as the temperature was raised to 350°C. At 800°C, the residue reduced to 4%.

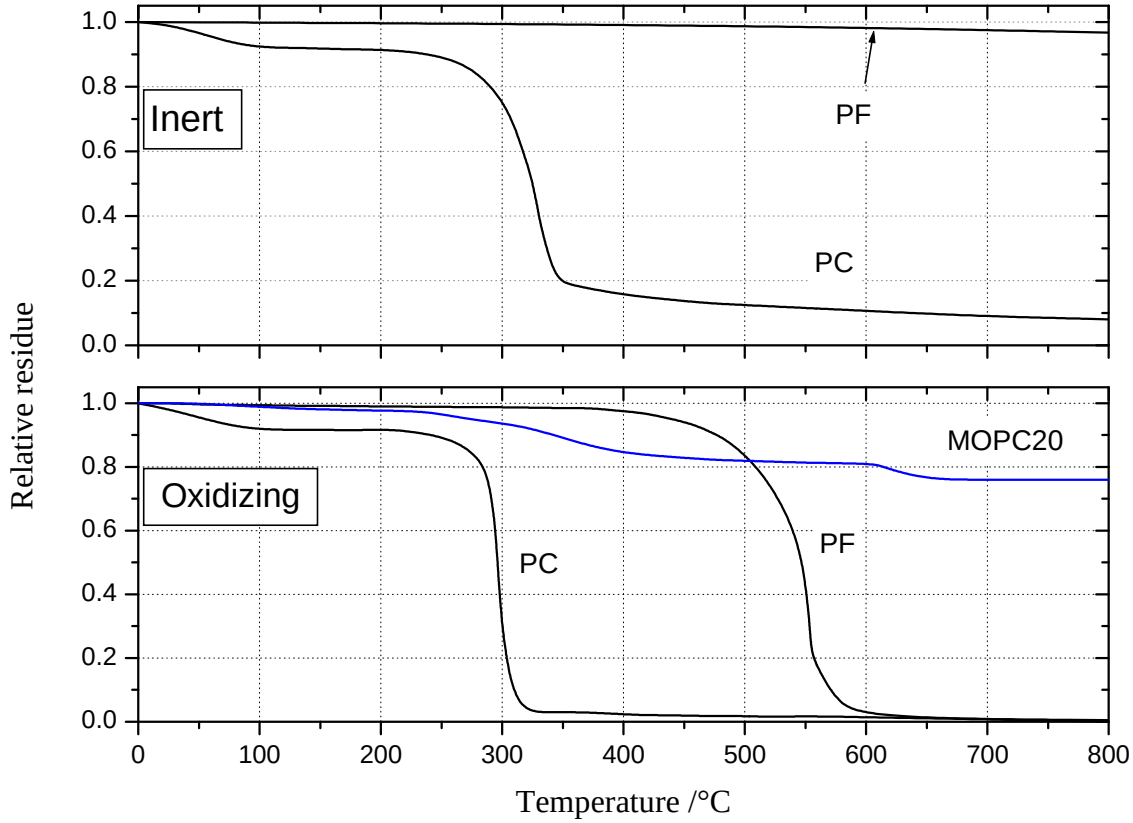

Figure 4.16 Decomposition behaviour of the pore formers PC and PF in inert and oxidizing atmospheres and of the green MOPC20 preform in an oxidizing atmosphere.

The behaviour in an oxidizing atmosphere was different. The carbon fibre PF started to degrade at 400°C which was followed by a steep decrease at about 500°C which led to less than 1% of residue above 600°C. All the carbon fibre had transformed to gas when the maximum temperature was reached.

The decomposition behaviour of PC up to 270°C in an oxidizing atmosphere was similar to that in an inert atmosphere. As the temperature was increased up to 320°C, a steep decrease in the residue took place to less than 3%. The residue was reduced to zero at 800°C.

In the green part of magnesia with 20 wt-% of the pore former PC (MOPC20), the first main gas formation started at about 200°C and ended at 400°C. At 620°C, another mass loss took

place which was attributed to the calcination of $Mg(OH)_2$, which was assumed to be the reaction product when MgO was in contact with water during processing. A residue of 76% was measured at the end of the test. This mass corresponded to the nominal amount of magnesia ceramic particulates in the green as apart from 20% of PFA an organic binder and water, each 2 % by weight, were initially added to powder.

4.5. Preform processing

The processing parameters such as the amount of pore forming agent (PFA), green sintering temperature and green pressing pressure were varied in order to reach the target total porosity of 60% to 70% in the final preform. As shown in the literature review, this preform volume fraction has been rarely and incompletely investigated for preforms of particulate ceramics. The challenge was to obtain sufficient preform strength at this relatively low ceramic volume fraction to withstand the metal infiltration process.

4.5.1 Influence of PFA content

Figure 4.17 shows the correlations between the relative mass of pore former added to the ceramic particles and the resulting porosity. The sintering temperature, the atmosphere (which consisted of air throughout the whole investigation), the sintering time of 2 h and the green compaction pressure of 100 MPa were kept constant. The sintering temperature T_{sint} was kept relatively low aiming for residual porosity between the ceramic particles in order to achieve preforms with low solid fractions. The initial sintering temperatures were taken from previous studies, for example that of Staudenecker [155] for Al_2O_3 preforms with a glassy frit (type AGPC), and Schneele [163] for TiO_2 preforms. The sintering temperatures for AO and MO preforms were based on supplier's recommendations.

For preforms comprising pure alumina AO with the pore former PF, the minimum sintering temperature was found to be 1500°C. When the pore former was PC it was only possible to

obtain usable products when they were sintered at 1600°C. Below 1600°C, the edge strengths were too low for handling. The sintering temperature of the Al_2O_3 preform with the glassy frit binder (AG) was 1000°C, as suggested by Staudenecker [155]. The sintering activity of the Al_2O_3 particles was very low at this temperature and the resulting strength of the preforms has to be attributed to the glassy frit binder which nominally softens at 570°C [155].

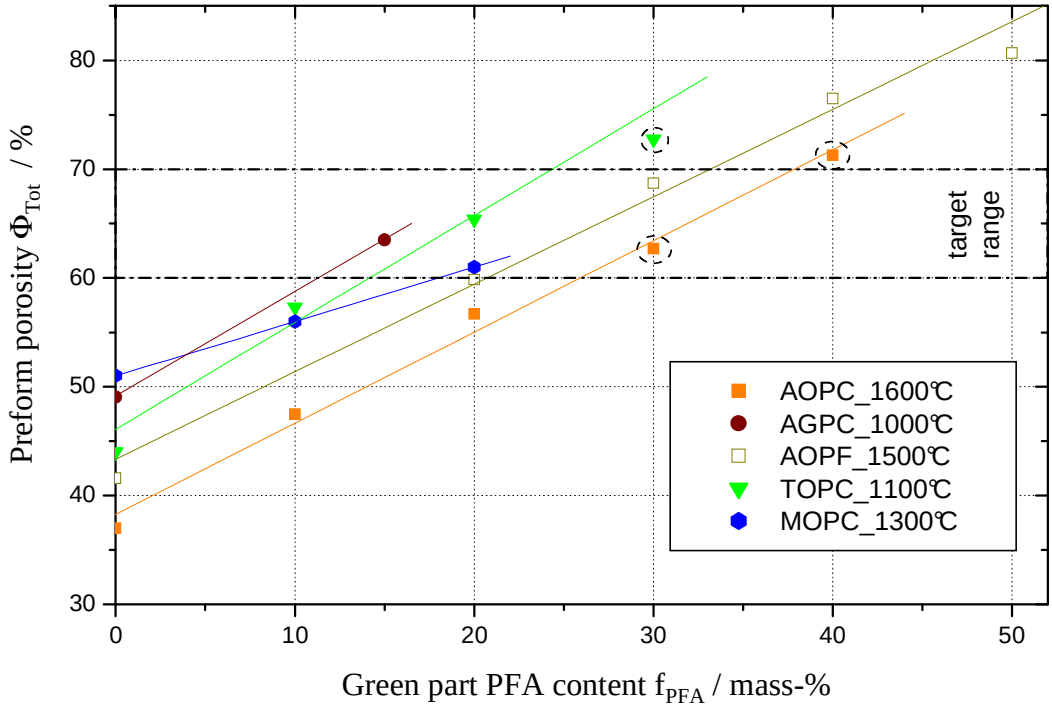

Figure 4.17 PFA addition and resulting total preform porosity Φ_{tot} . Data points in circles indicate parameters leading to insufficient edge strength or cracking of the preform after sintering.

From the literature [53] the sintering temperature of TO preforms was initially fixed at 1100°C and that of magnesia MO at 1300°C. The latter was suggested by the supplier to be the minimum temperature to get acceptable volume diffusion in order to get sintering bridges between the particles, a prerequisite condition for obtaining sufficient preform strength for particulate preforms without binder additions.

As shown in Figure 4.17, the total porosity Φ_{tot} of preforms without pore former addition was in the range of 37% to 50%, i.e. all below the target pore fraction. Pore formers were added to increase the porosity. However, increasing the porosity resulted in lower strength and a

compromise had to be found, where there was sufficient porosity (60 to 70%) and strength as indicated by low edge fracture during handling.

The processing parameters for AG with PC were previously investigated by Staudenecker [155]. The optimum PC fraction was found to be 15% giving a final porosity of 65%. Thus AGPC15 preforms were used for further characterisation and MMC processing.

Linear regression of the data shown in Figure 4.17 indicates that AGPC, AOPC and TOPC exhibit similar gradients. The gradient for MOPC was significantly lower, indicating a different behaviour of the pore former PC in the MO preforms. Even though PF had a higher density (1750 kg/m³) than PC (1500kg/m³) AOPF showed similar gradient as AOPC in Figure 4.18, which has to be attributed to higher efficiency of the pore formation with PF. More detailed work may be performed in future to investigate the differences between PF and PC.

Cellulose (PC) or carbon fibres (PF) were used in the AO preforms in order to investigate the influence of the pore former geometry and chemistry. For PC additions, the porosity was raised from 35% (AO) to 72% for AOPC40. Those with the highest values (AOPC30 and AOPC40) had low strength after sintering, making them unsuitable for further processing (circled data points in Figure 4.17).

The AO preforms with PF could be fabricated with sufficient edge strength up to the maximum PFA addition investigated of 50%. The resulting total porosity was 79%. The porosity of AO in the AOPC curve was lower than that in the AOPF curve. This was due to a lower sintering temperature of 1500°C being used for AOPF. Therefore the remaining intragranular porosity fraction was higher.

The porosity of TO preforms was 44% and therefore higher than that of AO sintered at 1500°C and 1600°C. For TOPC with 30 wt-% of pore former the preforms had inadequate

strengths, whereas with 10 and 20 wt-% PC the preforms had sufficient strength and 57% and 65% porosity respectively.

The highest total porosity of 50% without PFA additions was found in the MO-preforms. The additions of PFA showed less effect in MOPC than in the other ceramics. The addition of 20 wt-% of PC resulted in an increase of 28% total porosity in AOPC compared to 12% for MOPC20. As TOPC did not show this behaviour, it has to be attributed to the chemistry of the preform.

By altering the PFA content, the AOPF20 and TOPC20 preforms as well as AGPC15, provided materials in the target porosity range and therefore were taken forward for further characterisation and composite processing. It was wished to increase the porosity of MOPC20 from 62% to 65% (the centre of the range) by a reduction in sintering temperature which is presented in 4.5.3. In order to reach the target range with AOPC, other process parameters such as green compaction pressure and sintering temperature were varied, as presented in 4.5.2 and 4.5.3 respectively. The same variations were applied to the TOPC10 preforms. For the TO preforms, the influence of the pore structure on the preform infiltration behaviour was investigated. The pore former fractions influenced the ratio between the PFA-formed and intragranular porosities, thus giving different ratios of coarse and fine pores with the same total pore volume. The target was to get equal total porosity at two different pore former fractions.

4.5.2 Influence of green part compaction pressure

The influence of the green compaction pressure on the porosity of AOPC20 and TOPC10 at sintering temperatures of 1600 and 1100°C respectively is presented in Figure 4.18. By reducing the compaction pressure from 100 MPa to 60 MPa, the AOPC20 preform could be

fabricated in the target porosity range. A compaction pressure of 20 MPa resulted in preforms with too low edge strength.

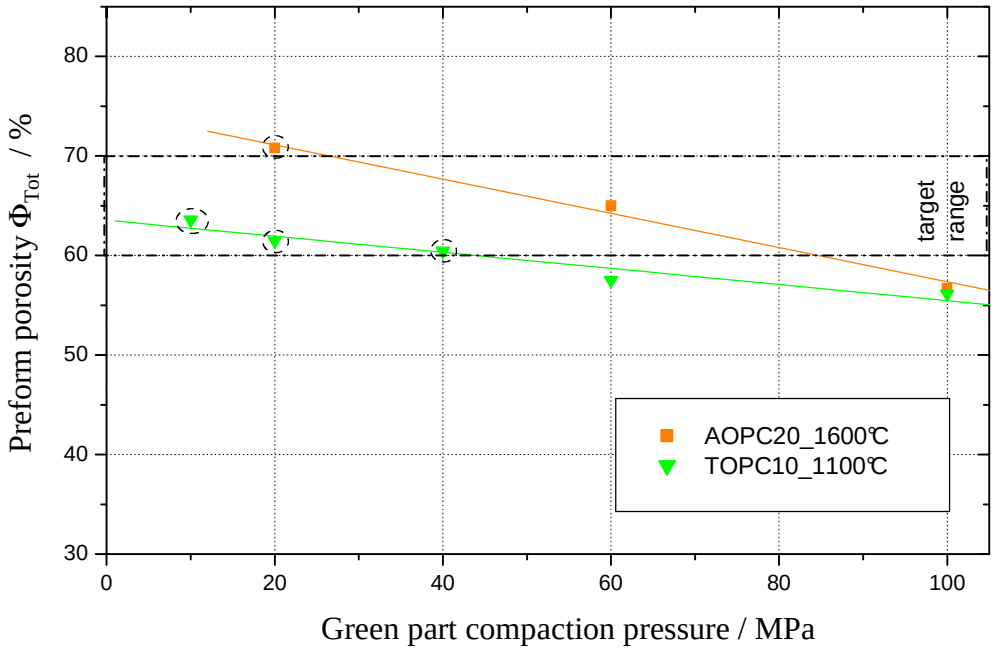

Figure 4.18 Total porosity Φ_{tot} of preforms as a function of the powder compaction pressure. The points in circles indicate parameters leading to insufficient edge strength or cracking.

A reduction in the compaction pressure of TOPC10 to 40 MPa resulted in preforms with the target porosity but the strength was insufficient and cracks were observed after sintering. A possible solution to this issue was to change the sintering profile, which is reviewed in section 4.5.3.

4.5.3 Influence of sintering temperature

The influence of the sintering temperature on the total preform porosity is shown in Figure 4.19. The porosity of the TOPC10 titania preform reached the target range when the temperature was lowered to 1050°C. The sintering temperature was also increased to 1150°C in order to investigate the correlations. The regression shows a negative slope.

In contrast, there was no significant change in the total porosity values when the sintering temperature of MOPC20 was reduced to 800°C. The subjective assessment of preform

strength showed no significant difference between the lowest and the highest sintering temperatures. The preforms used for further processing were sintered at 1300°C as suggested by the supplier. For comparison of MMC microstructures, one preform sintered at 800°C was also infiltrated and characterised.

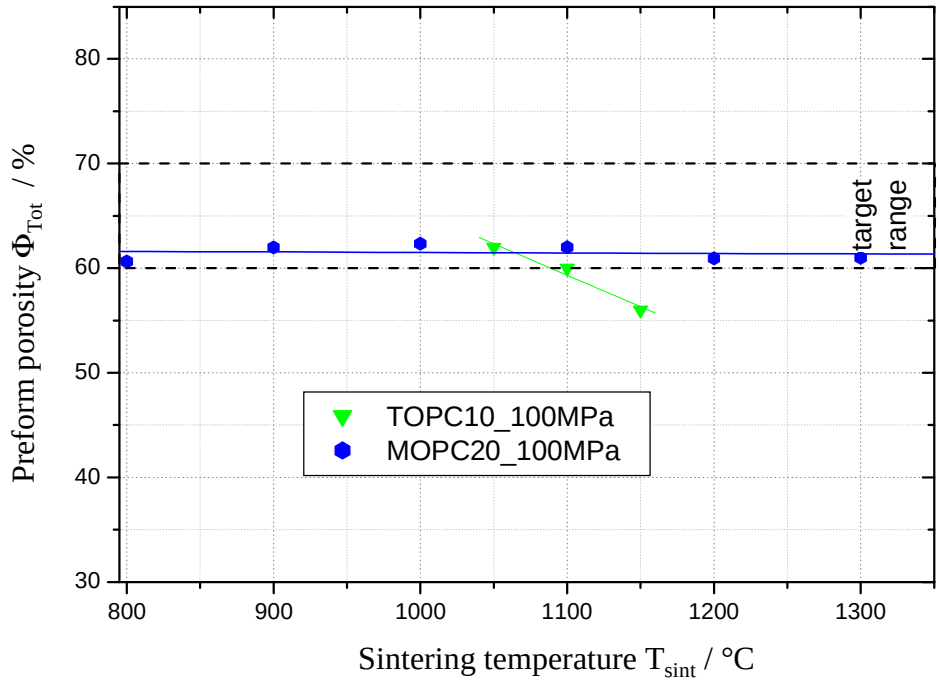

Figure 4.19 Final total porosity Φ_{tot} as a function of the sintering temperature.

As with all preform types, the target porosity range was reached by varying the PFA content, compaction pressure or the sintering temperature. These optimized parameter combinations were used to produce further preforms which were used to investigate the structure and infiltration behaviour.

The manufacturing parameters and properties of each preform type are listed in Table 4.1. The pore former concentration is given as both weight and volume fraction. The latter was calculated using the densities of the pore former given in Table 3.5. The resulting total, closed cell and open cell porosities are shown, as well as the porosity attributed to the pore forming additive, Φ_{PFA}, which was calculated taking into account the porosity of the preforms without PFA. It was found that the the closed cell porosity, Φ_c, ranged from 0.2% (AOPC20) to 2%

(AGPC15). That of MOPC20 could not be measured due to hydrolysis of magnesia in contact with water. As an alternative, ethanol was used but these measurements were not successful, as the mass of the saturated preform (m_1 in Equation 40) could not be evaluated accurately due to the evaporation of ethanol.

Table 4.1 Fabrication parameters and the measured resulting porosities of the preforms used for further composite processing.

	PFA addition		Compaction pressure	Sintering temperature	Porosity			
			$P_{comp.}$	T_{sint}	total	closed cell	open cell	PFA formed
	wt-%	vol-%	MPa	°C	Φ_{tot}	Φ_c	Φ_{op}	Φ_{PFA}
AOPC20	20	40	60	1600	65%	0,2%	65%	46%
AOPF20	20	36	100	1500	60%	0,3%	60%	32%
AGPC15	15	32	100	1000	65%	2,0%	63%	27%
TOPC10	10	21	100	1050	62%	1,4%	61%	22%
TOPC20	20	42	100	1100	65%	1,8%	63%	40%
MOPC20	20	37	100	1300	62%	n.a.	62%	24%

4.5.4 Dimensional change during sintering

The relative change in dimensions along the three axes of preform type was evaluated and the results are shown in Figure 4.20. It was similar along the x- and y-axes (s_x and s_y) and in the range 0% to 7.5% for all preforms. The lowest value was achieved with AGPC15 and the highest with TOPC20. In the z-direction (s_z) the change in dimension was significantly different to s_x and s_y. AOPF20, TOPC10 and MOPC20 showed a reduction in the height of the preform whereas AOPC20, AGPC15 and TOPC20 showed an increase in the height. The shrinkage of AOPC20 and AGPC15 was similar (-7.5%) whereas that of TOPC20 was lower (-4.5%).

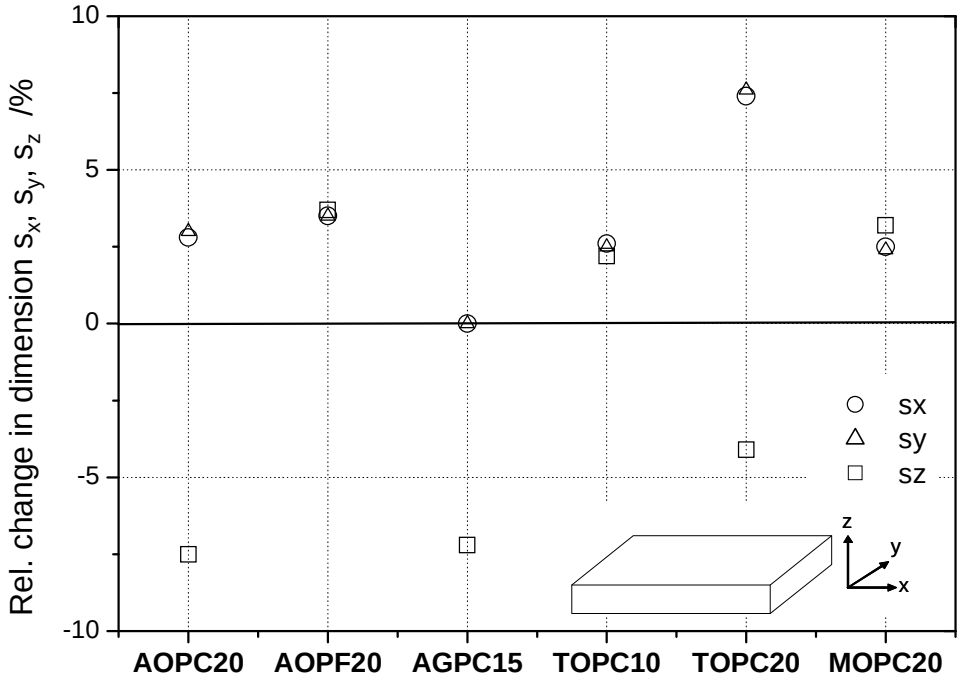

Figure 4.20 Dimensional change due to sintering of the preforms in the three normal directions.

4.6. Preform characteristics

4.6.1 Preform microstructure

Pyrolysis of the pore formers left cavities in the preform. The influence of the pore former geometry on the coarse porosity in the preform microstructure is shown in Figure 4.21.

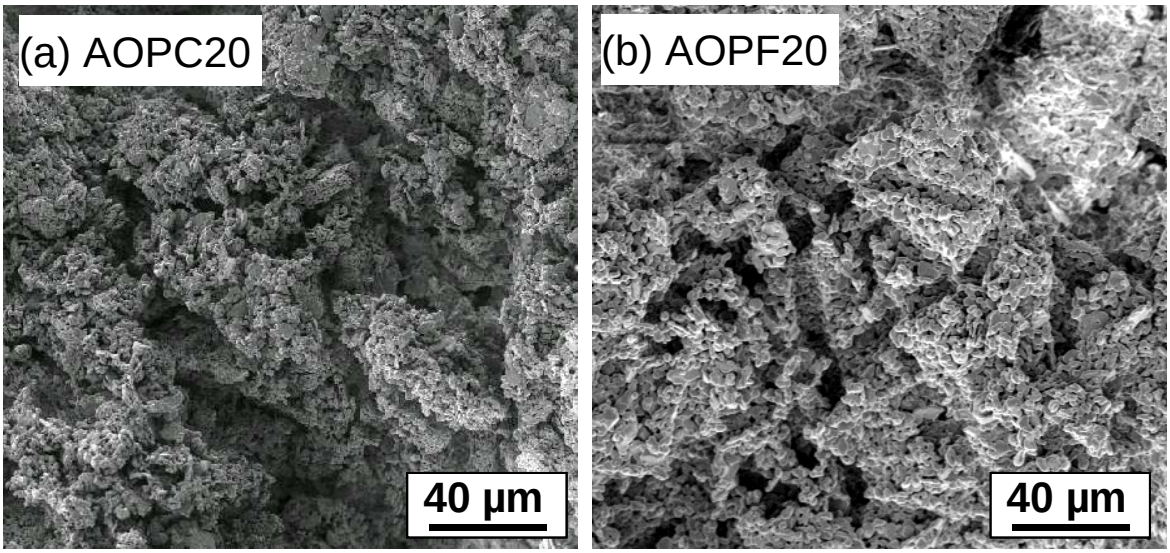

Figure 4.21 SEM images of the preform microstructures: a) AOPC20 and b) AOPF20.

As shown in Figure 4.21 a), the cavities had an irregular shape when cellulose (PC) was used. The pore openings of AOPC20 were up to 30 µm in size. In contrast, Figure 4.21 b) shows that the pore diameters and cavities were more distinct in AOPF20 where carbon fibres were pyrolysed. The cavities were aligned with a diameter of about 10 µm which was slightly larger than the nominal fibre diameter of 8 µm.

Apart from the coarse pores generated by pyrolysis of the pore formers, the regions between the large cavities comprised particles which were just lightly sintered. These areas were investigated at progressively higher magnifications. The structures of 4 preforms are shown in Figure 4.22.

The tabular nature of the starting powder is reflected in the AO preforms AOPC20 and AGPC15. A greater portion was observed in AGPC15 compared to AOPC20. Most of these particles had an aspect ratio larger than 3. The glassy binder in AGPC15 could be clearly seen to bridge between some particles, as marked with an arrow in Figure 4.22 b).

In contrast to the pure Al_2O_3 preform AOPC20, the sinter bridges in TOPC10 and MOPC20 were more distinctive and the particles were finer and more spherical. They were significantly finer in the TOPC10 titania preform than in AOPC20 and MOPC20, as can be seen by comparing Figure 4.22 c) with b) and a). Some particles were less than 1 µm in diameter.

The sintering in the MOPC20 was more extensive than in the other preforms, as shown by the neck plane areas in Figure 4.22 d) indicated with an arrow. The plane faces result from the removal of particles during preparation of the preform sample for the SEM investigations.

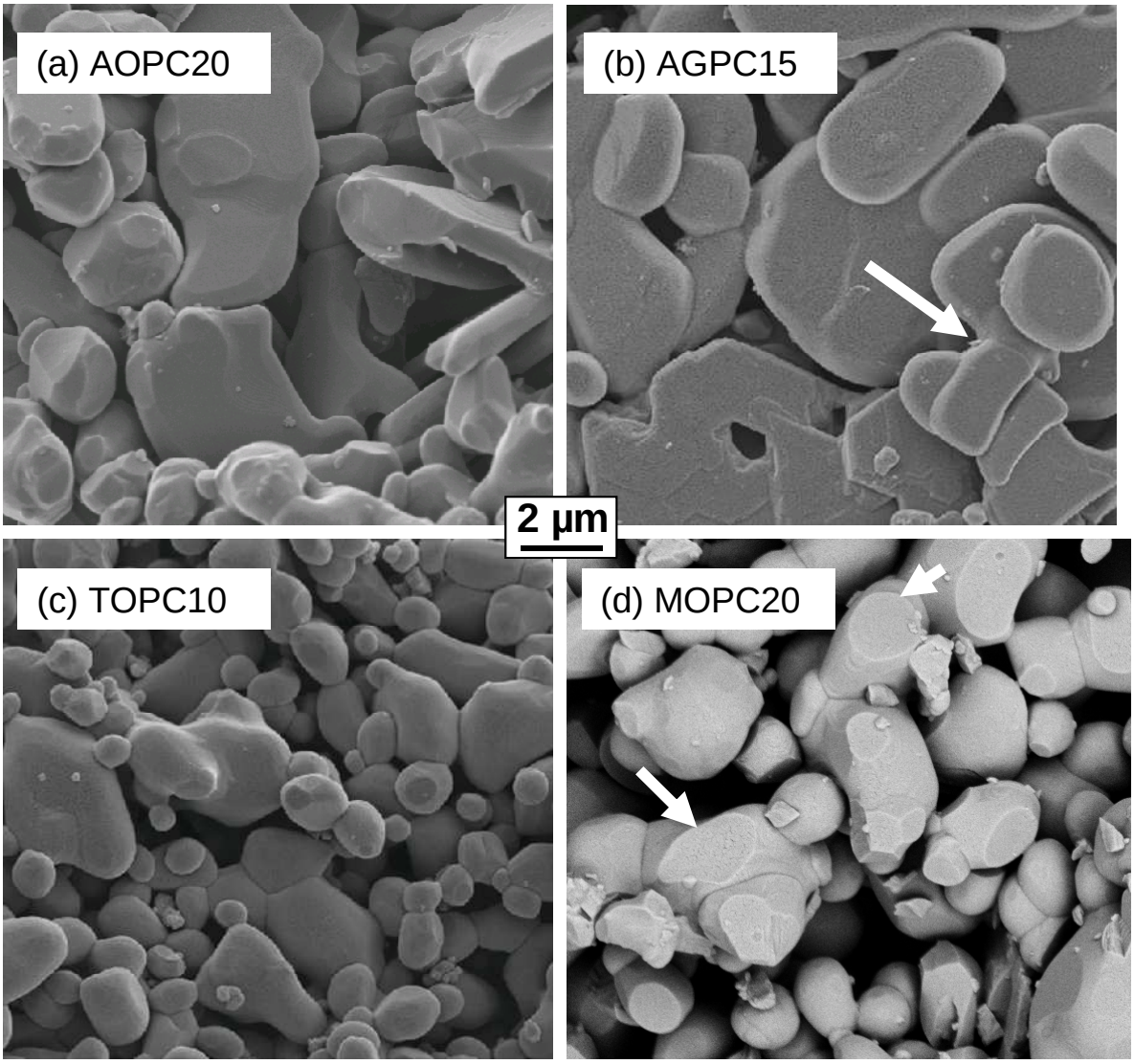

Figure 4.22 SEM images of the microstructures of the preforms in the intragranular region of a) AOPC20, b) AGPC15, c) TOPC10 and d) MOPC20.

The microstructures of the procured preforms are presented in Figure 4.23 for AODY30 and Figure 4.24 for FATO. The AODY30 preforms produced by Dytech Corporation [(162)] using a foaming route showed relatively large spherical pores with a diameter of about 120 µm in cut sections as shown in Figure 4.23 a). The preform was cut prior to the SEM investigations in order to eliminate edge effects. The spherical shape was a result gas bubbles in he initial ceramic slurry. In the final preform, the bubbles were interconnected by passages (windows) indicated by arrows in Figure 4.23 a) which were about 10 µm in diameter. The struts between the bubbles exhibited high density as shown in the high magnification image, Figure

4.23 b). The immediate border of the window was about 2 µm wide and had a thickness equal to the diameter of one to three particles. Because grain growth has occurred during the sintering process is was probable that the starting powder was smaller than one micron.

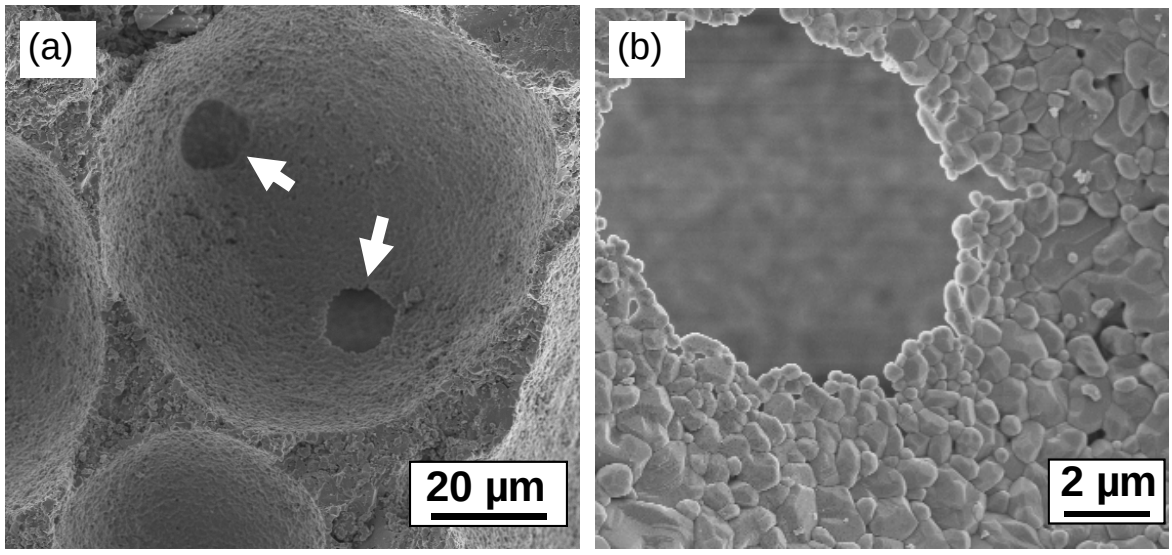

Figure 4.23 Microstructure of the purchased AODY30 preforms: (a) overview with the single windows marked and (b) detail of a window connecting the cavities.

In the FATO preforms, built up of Saffil™ fibres and TiO_2 particles, the two phases were clearly visible, Figure 4.24 a). The fibres were embedded into the fine particles. Between the clusters of particles and fibres, there were large pores 15-20 µm wide and more than 200 µm long.

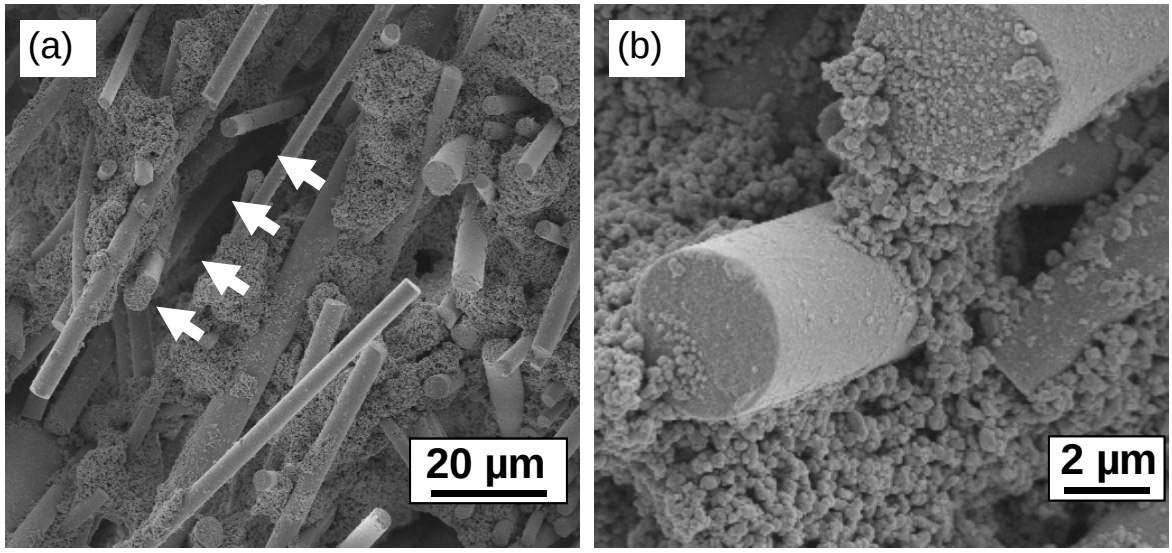

Figure 4.24 Microstructure of the FATO preform. Arrows indicate an extended pore.

At higher magnification, Figure 4.24 b) shows the alumina fibre diameter to be about 4 µm and the titania particles to be sub-micron. The loose particles on the fibre sections cut during specimen preparation suggests a weak interparticle bonding.

4.6.2 Pore size distribution

The incremental and cumulative graphs of the relative pore volume of two alumina preforms, AO and AOPC20, as a function of pore diameter are shown in Figure 4.25 a) and b) respectively. The incremental plot is often easier to interpret in terms of fraction per pore size diameter class and was therefore used for further presentations of the pore size distributions. Intrusions below 0.25 µm pore diameter were not observed in any of the preforms made with pore forming additives. Therefore the pore size distribution plots of all preforms, apart from AODY30 and FATO, were limited to a minimum of 0.1 µm.

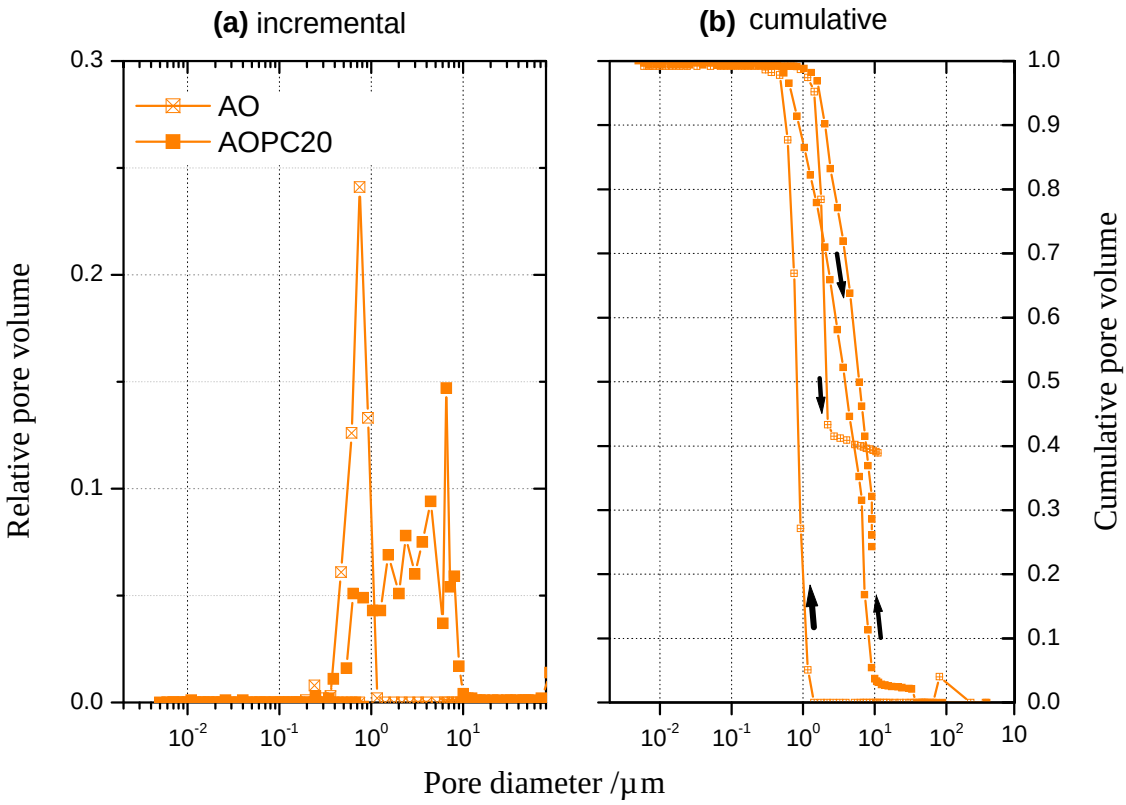

Figure 4.25 Pore size distribution curves of AO and AOPC20. a) incremental and b) cumulative outline.

Compared to the incremental diagram, the cumulative expresses better the intrusion-extrusion behaviour. The intrusion-extrusion experiments are indicated by the pointers in Figure 4.25 b). The residual intruded porosity is referred to as the residual porosity after extrusion $\Phi_{ext.}$. In the AO preforms without a pore former, the Φ_{ext} was 39% whereas about 25% still remained in the preform when a pore former was used (AOPC20).

The incremental size distribution of AO showed a single distinct peak between pore diameters of 0.25 µm and 1.1 µm. In contrast, the pore size distribution of AOPC20 was broader, starting at 8 µm and going down to a minimum pore size of 0.25 µm. The maximum incremental value of 14.5% was at a pore diameter of 7.5µm.

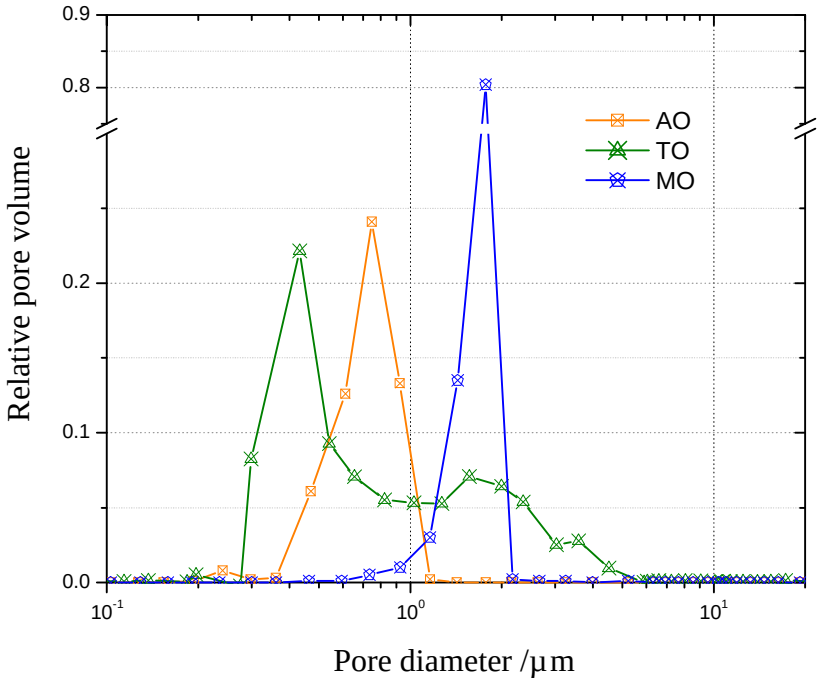

Figure 4.26 Pore size distribution of the preforms without pore former additions: AO, TO and MO.

The pore size distributions of the particulate preforms of different chemical compositions without pore forming additions (AO, TO and MO) are shown in Figure 4.26. As already shown in Figure 4.25 a), AO exhibited a distinct peak at a pore diameter of 0.8 µm. The MO preform had a distinctive peak with the highest relative incremental intrusion of 0.81 at a larger pore diameter of 1.8 µm. In contrast, TO exhibited a broader distribution: the first

intrusions started at 4 µm and ended at 0.2 µm. One distinct peak at 0.2 µm was obvious and a second was indicated at 1.5 µm therefore indicating a bimodal pore size distribution.

The pore size distribution curves of the preforms of different chemical composition fabricated with PC as pore forming additive are presented in Figure 4.27. The broad pore size distribution of AOPC20 in the range of 10 µm to 0.25 µm was also found with the AGPC15 and TOPC20 preforms. The distribution curve of AGPC15 started at lower diameters and exhibited a significantly increased fraction of small pores. The distribution of TOPC20 was similar to that of AOPC20. In contrast, MOPC20 showed a bimodal pore size distribution with a peak at a pore diameter of about 7 µm, attributed to the pore forming additive, and one peak at 0.9 µm representing the intergranular pores.

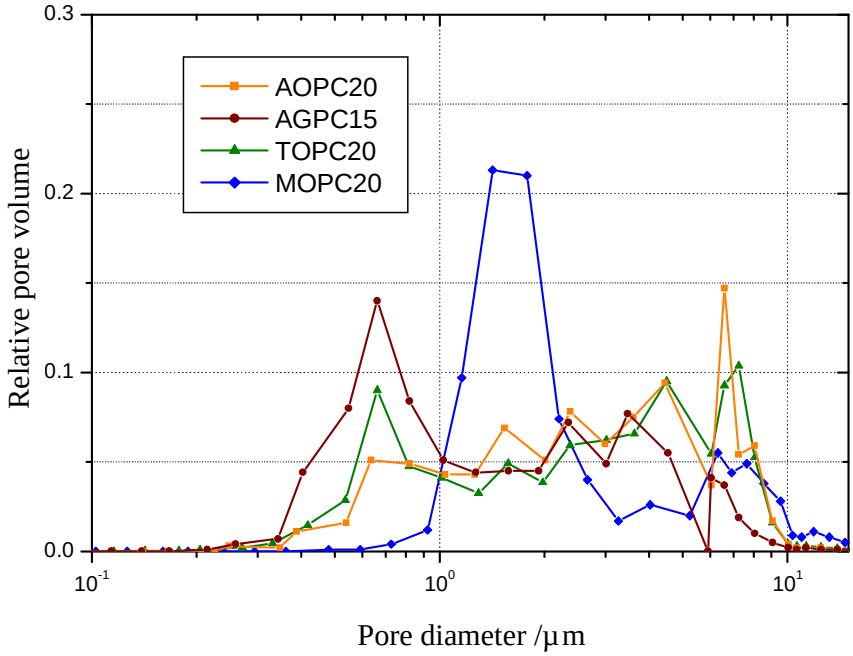

Figure 4.27 Pore size distributions of AOPC20, AGPC15, TOPC20 and MOPC20.

Figure 4.28 shows the pore size distributions of TOPC10 and TOPC20. In TOPC10 the coarsest pores were about 2.5 µm in diameter and the main concentration of pores had a diameter of 0.3 µm. In contrast, the higher PFA fraction in TOPC20 resulted in a larger

fraction of coarse pores. The alteration of the sintering temperature from 1100°C for TOPC20 to 1050°C for TOPC10 resulted in smaller intragranular pores in the latter.

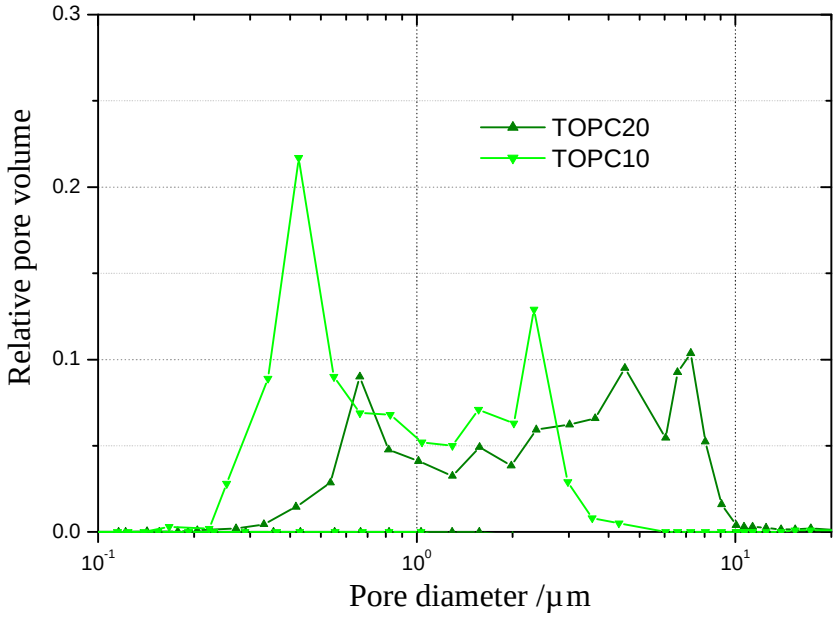

Figure 4.28 Incremental pore size distribution of TOPC10 and TOPC20.

The composition and geometry of the pore former influenced the pore size distribution. The carbon fibre pore formation in AOPF20 led to a distinct peak at a diameter of about 8 µm as shown in Figure 4.29 which represents exactly the carbon fibre diameter.

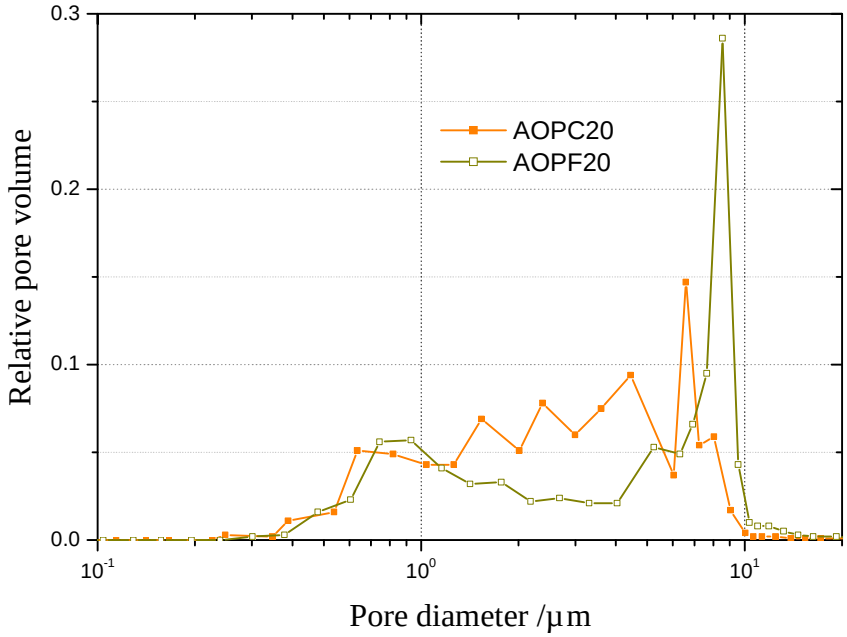

Figure 4.29 Incremental pore size distributions of AOPC20 and AOPF20.

As shown in Figure 4.27, the pore size distribution of the magnesia preform MOPC20 sintered at 1300°C was significantly different from that of the other ceramic preforms with the same PFA. In the metal infiltration experiments, an equal pore size distribution was targeted in order to minimize the effect of differing pore size distributions on the comparative study.

In order to increase the fraction of finer pores in MOPC20, the sintering temperature was reduced to 800°C with a constant holding time of 2 h. As shown in Figure 4.30, the preform sintered at 800°C shifted the pores to finer sizes while maintaining the bimodal profile. The coarse peak reduced from around 8 µm to about 2 µm and the fine peak reduced from 1.5 to 0.2 µm. The target to reduce the small pore size and to leave the coarse pores as they were, could not be achieved as the coarse pores shifted to smaller sizes when the sintering temperature was reduced.

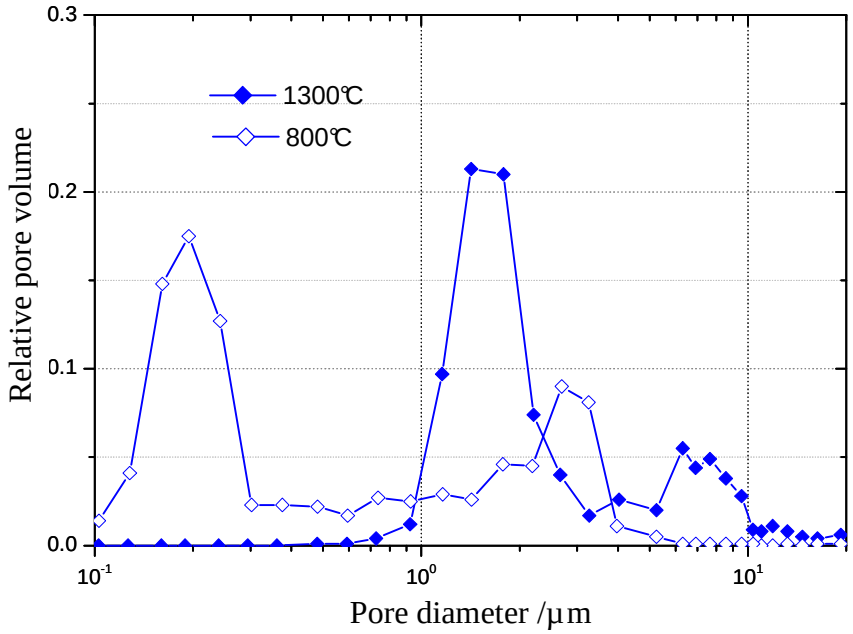

Figure 4.30 Influence of sintering temperature on pore size distribution of MOPC20.

The influence of the sintering temperature on the median pore diameter, d_{Hg}, and the specific surface area, S_{sHg}, of the MOPC20 preforms is shown in Figure 4.31. As the sintering temperature was lowered from 1300°C to 1200°C, the median pore diameter reduced from 1.50 µm to 0.25 µm and the specific surface area increased from 0.70 m²/g to 3.78 m²/g.

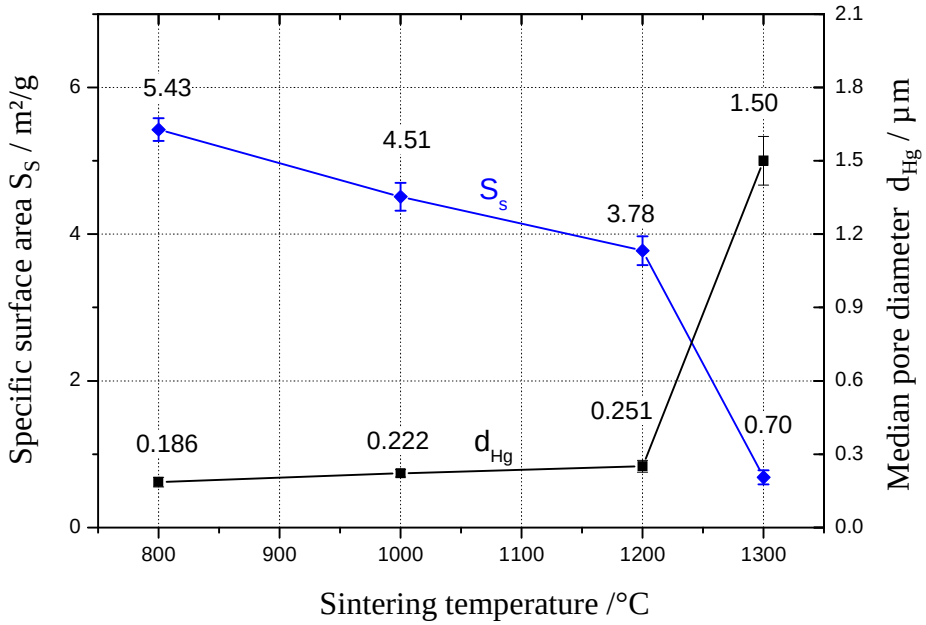

Figure 4.31 Influence of sintering temperature on specific surface area S_{sHg} and median pore diameter of preform MOPC20.

The pore size distributions of FATO and AODY30 are shown in Figure 4.32. The foam-based AODY30 exhibited two peaks, one at a pore size of about 20 µm and another more distinct at about 8 µm, which showed the largest incremental pore fraction of 0.42. The FATO hybrid preform had a wide range of pore sizes from 20 µm to 0.05 µm. There were two main peaks, one at a pore diameter of 18 µm and the other at 0.2 µm.

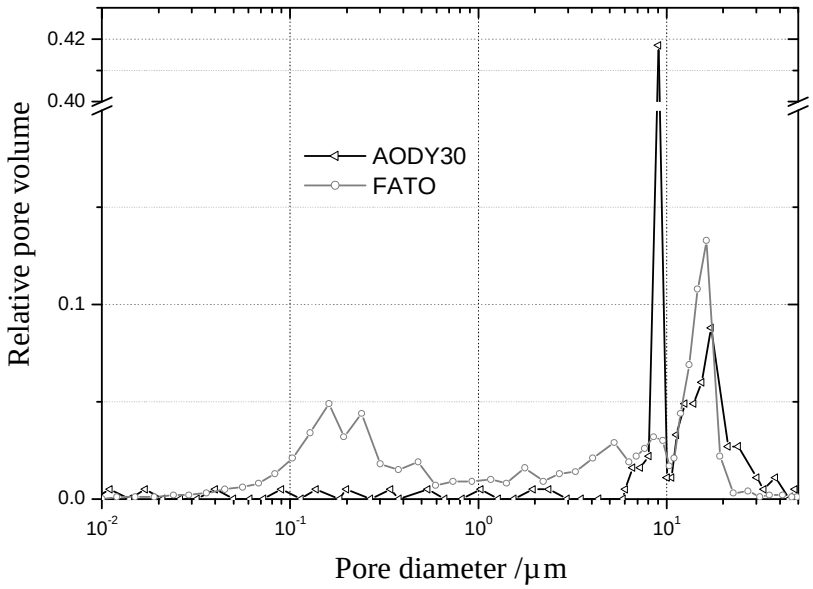

Figure 4.32 Incremental pore size distribution of the purchased preforms FATO and AODY30.

An overview of the specific values derived from the pore size distribution curves is shown in Table 4.2. Most of the preforms exhibited differences between the total porosity Φ_{tot} calculated on the basis of the measured preform volume and the theoretical density, and the total porosity measured using the mercury intrusion method Φ_{Hg}. These differences represent the closed cell porosity of the preform. No difference was observed with the TO and MO preforms and small differences of 3% were found with AO, AODY30 and FATO preforms. Larger differences were observed when cellulose (PC) was used as a pore forming agent. Here AOPC20 showed the smallest difference of 7%, whereas TOPC10 and AGPC15 showed the maximum differences (9%) of all the preforms investigated.

The median pore diameter d_{Hg} varied significantly over the range of 0.77 µm to 9.05 µm. The titania and alumina preforms AO and TO exhibited the smallest diameter which was below 1 µm. In contrast MO showed a median diameter of 1.84 µm which was larger than 1.50 µm for the MOPC20, where cellulose was used as PFA. This behaviour was unique to the magnesia system. In all other preform types where a pore former was used, the median pore diameters ranged between 1.06 µm (TOPC10) and 4.98 µm (TOPC20) and therefore were larger than that of the respective preforms without PFA additions. The alumina based preforms AGPC15 and AOPC20 showed median pore diameters of 2.77 µm and 3.48 µm respectively. Larger values were achieved with AOPF20, where the carbon fibre was used as a pore former. The largest values of the entire project were reached with the purchased preforms FATO and AODY30 with 8.53 µm and 9.05 µm, respectively.

Table 4.2 shows the specific surface area per unit mass (S_{sHg}), normalized per unit of preform volume (S_{pHg}), and the inner surface area per porosity volume (S_{iHg}) which were calculated using Equation 22 and Equation 42 respectively. The S_{sHg} values of the preforms ranged between 0.69 and 5.85 m^2/g for AOPF20 and FATO respectively. The high value of the latter

is attributed to the relatively large fraction of very fine porosity in this hybrid preform of Saffil™ fibres and fine-grained titania powder.

Table 4.2 Overview of the mercury intrusion porosimetry results of the preforms.

	Total porosity Φ_{tot}	MIP porosity Φ_{Hg}	Deviation $\Phi_{Hg} - \Phi_{tot}$	Median pore dia. d_{Hg}	Specific surface area per unit mass S_{sHg}	volume preform S_{pHg}	volume porosity S_{iHg}	Extrusion residual Φ_{ext}
				µm	m^2/g	$10^6 \cdot m^2/m^3$		
AO	37%	34%	-3%	0.77	1.51	3.80	10.37	0.39
AOPC20	65%	58%	-7%	3.48	0.86	1.20	1.84	0.18
AOPF20	60%	56%	-4%	7.00	0.69	1.10	1.83	0.69
AGPC15	66%	57%	-9%	2.77	1.49	2.00	3.04	0.14
TO	44%	44%	0%	0.86	1.47	3.51	7.97	0.23
TOPC10	62%	53%	-9%	1.06	2.30	3.72	6.01	0.20
TOPC20	65%	57%	-8%	4.98	0.76	1.13	1.74	0.55
MO	50%	50%	0%	1.84	0.75	1.34	2.69	0.06
MOPC20	62%	56%	-6%	1.50	0.78	1.05	1.68	0.13
AODY30	68%	67%	-1%	9.05	2.41	3.02	4.45	0.97
FATO	71%	68%	-3%	8.53	5.85	6.50	9.15	0.47

The inhouse fabricated preforms with PFA exhibited S_{sHg} values between 0.69 m^2/g and 2.30 m^2/g. The latter value (TOPC10 sintered at 1050°C) resulted from the relatively low sintering temperature when compared to TOPC20, the preform fabricated with similar ceramic powder but higher PFA content and sintered at a higher temperature 1100°C.

When the specific surface area per unit volume (S_{iHg}) is compared to that per unit mass (S_{sHg}), the preforms fabricated without PFA (namely AO, TO and MO) showed a significant difference between the two values. This was a result of the lower total porosity and therefore the larger preform volume necessary to obtain an equal surface area to that in the highly porous preforms, where PFA was used to form coarse porosity. The specific surface areas per unit pore volume of AOPC20, AOPF20, TOPC20 and MOPC20 were in the range of

1.71 to 1.98·10^6 m²/m³. The similar values enabled direct comparison in the infiltration experiments.

The AGPC15 preform was sintered with the aid of a glassy frit at a relatively low temperature of 1000°C. As the Al_2O_3 powder showed no significant sintering activity at this temperature, the initial grain size of the AO powder was presumably maintained. Therefore a comparatively large surface area of 3.05 m²/m³ could be achieved compared to that of the Al_2O_3 preform without frit additions (AOPC20) sintered at significantly higher temperatures. The reference preforms, AODY30 and FATO, exhibited larger S_{iHg} values of 4.45 m²/m³ and 9.15 m²/m³ respectively, attributed to the comparatively high fraction of small pores.

The relative residual non-extruded porosity Φ_{ext} describes the relative volume still intruded when an ambient pressure of 0.101 MPa is reached which corresponds to a pore diameter of 11 µm using Washburn´s equation (Equation 21). It was shown that Φ_{ext} ranged between 0.06 and 0.97. The lower value for the MO preform indicates that 6% of the total mercury volume was still trapped in the preform after the extrusion procedure. In contrast, the highest value was that of the AODY30 preform, which indicates that about 97% of the mercury remained in pores with an entrance diameter of more than 11 µm. This indicates that the characteristic window connections between the larger spherical cavities predominantly had diameters smaller than 11 µm.

4.6.3 Compressibility

The quasi-static compression behaviour of the preforms was investigated using two testing conditions. In the first, the preform samples were loaded between two platens such that the sample could yield laterally in the x- and y-directions. The specific compression strength σ_c was the ratio of the maximum load to the initial loading area. In the second, samples were loaded isostatically and the pressure dependent volumetric compression, c_{iso}, recorded.

As shown in Figure 4.33, the uniaxial compression strength of the preforms ranged between 1.1 MPa (TOPC10) and 245 MPa for the foamed preform AODY30. The compression strength of the AGPC15 with the glassy frit binder was lower than that of the AOPC20. The FATO hybrid reference preform had a strength of 7.0 MPa.

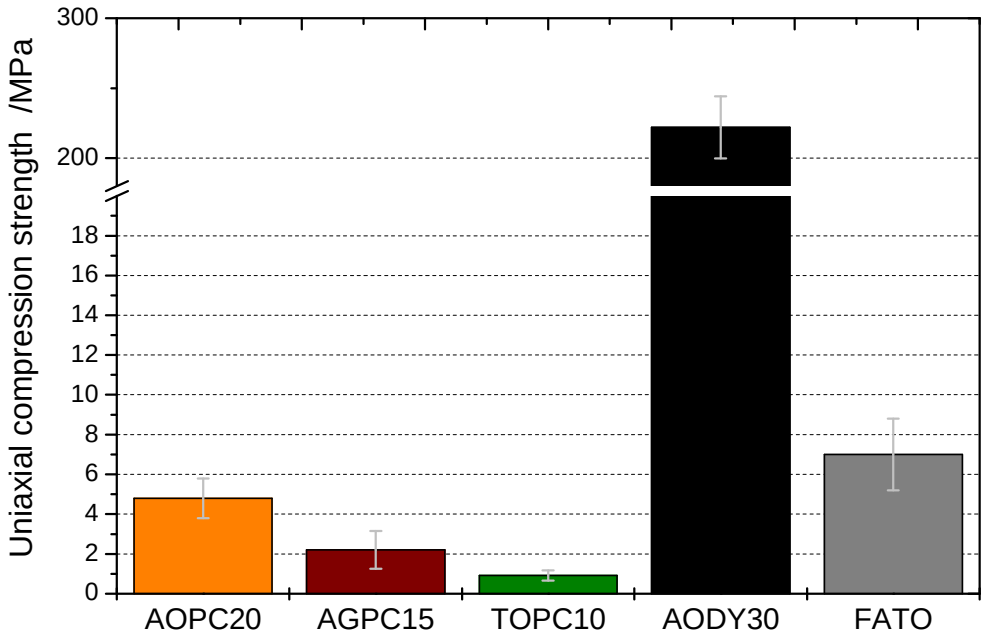

Figure 4.33 Uniaxial compression strength σ_c of the preforms.

The isostatic compression test was used in order to reproduce the conditions in the squeeze cast infiltration experiments. As the compression strength σ_c of the AODY30 preform was above the maximum pressure of the porosimeter, the isostatic testing method was omitted for this preform.

The relative compressions c_{iso} of the preforms made with pore forming additives as a function of the applied mercury pressure are presented in Figure 4.34. As an incremental pressurisation programme was used, the curves show a step-like form. The results may be categorized into two groups. The first group consisted of the AOPC20 and TOPC20 preforms which exhibited marginal compression up to 1 MPa and subsequently a steep increase in the degree of compression. Up to the maximum applied pressure, the curves described a close to

logarithmic compression behaviour, leading to relative volumetric compressions of 0.32 and 0.33 for AOPC20 and TOPC20, respectively. After pressure release to an ambient pressure of 0.1 MPa, a spring back to a constant compression of 0.27 occurred.

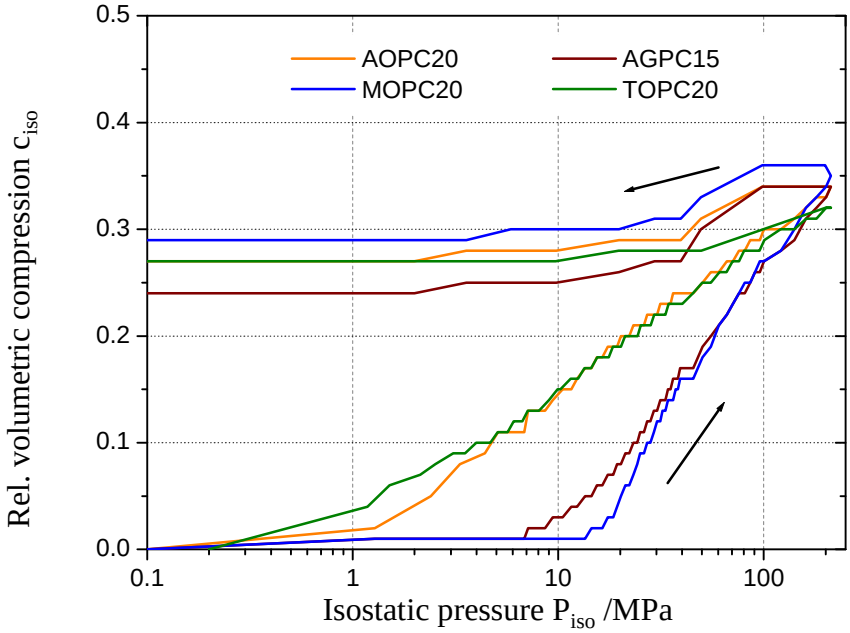

Figure 4.34 Isostatic compression and pressure relief behaviour of the AOPC20, AGPC15, MOPC20 and TOPC20 preforms.

The second group consisted of the MOPC20 and AGPC15 preforms with no significant compression up to 10 MPa. After that pressure, a steep increase in the degree of compression occurred. Compression reached similar levels to AOPC20 and TOPC20 at an applied pressure of 100 MPa. After pressure release, a spring back to 0.26 and 0.29 was measured for AGPC15 and MOPC20 respectively. Similar to the compression behaviour of AOPC20 and TOPC20, the TOPC10 preform and the FATO hybrid preform started to compress after reaching an isostatic pressure of about 1 MPa, as shown in Figure 4.35. FATO showed the greatest compression of all the preforms which was 0.45 at the maximum load of 212 MPa. After pressure relief, a spring back to 0.40 took place.

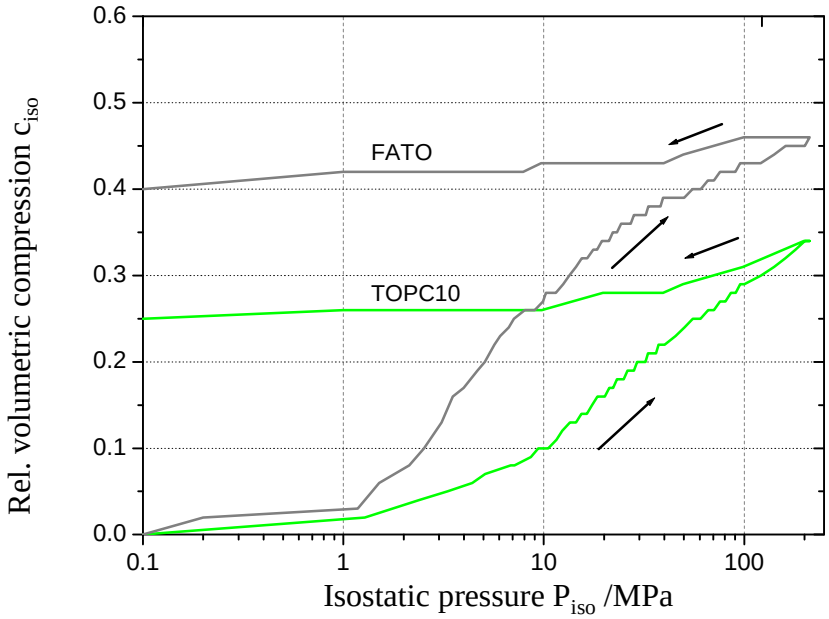

Figure 4.35 Isostatic compression of the TOPC10 and FATO preforms.

The TOPC10 preform with the lowest compression strength σ_c in the uniaxial test (0.7 MPa) started to compress significantly in the isostatic test at a pressure of 1 MPa. At the maximum load, the compression reached 0.34 and after pressure release to ambient, a constant compression of 0.25 was measured.

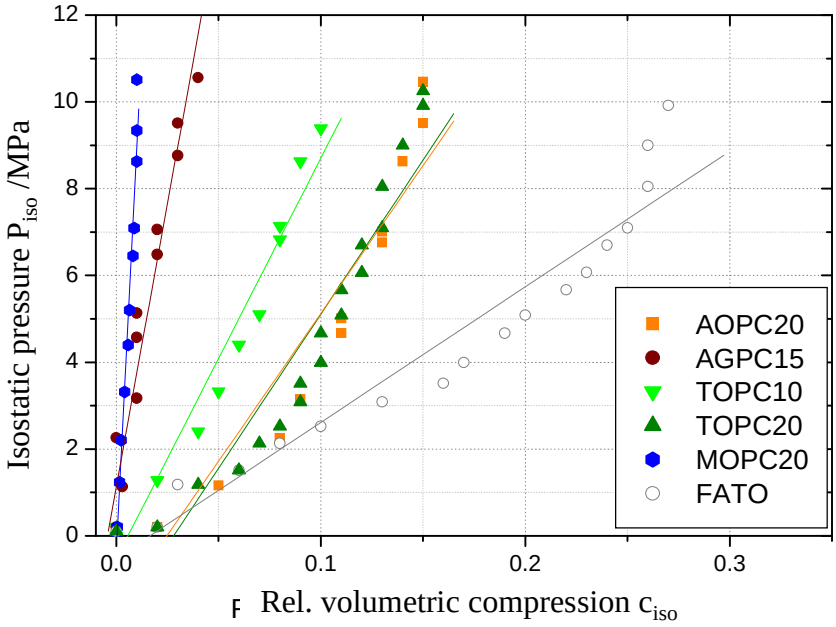

Figure 4.36 Isostatic pressure as a function of the compression in the range of 0.1 MPa to 10 MPa.

The volumetric stiffness E_{iso} of the preforms in the isostatic compression mode was evaluated as the slope of the linear region in the pressure range of 0.1 to 10 MPa, Figure 4.36.

Table 4.3 Characteristic parameters of isostatic compression test of preforms.

	Volumetric stiffness E_{iso} MPa	**Compression at 100 MPa $c_{iso,100}$**	**Maximum compression $c_{iso,max}$**	**Permanent compression $c_{iso,per}$**
AOPC20	68	0.30	0.34	0.27
AGPC15	261	0.28	0.34	0.24
TOPC10	92	0.29	0.34	0.25
TOPC20	71	0.26	0.32	0.27
MOPC20	921	0.28	0.36	0.29
FATO	31	0.40	0.46	0.42

The slopes of the curves were calculated and the values are presented in Table 4.3. The lowest value was that of FATO (31 MPa) whereas MOPC20 exhibited a stiffness of 921 MPa. That of TOPC20 and AOPC20 were similar to each other and are between the stiffness of TOPC10 and FATO. The values of the compression $c_{iso,max}$ reached at the maximum isostatic pressure of 212 MPa are listed in Table 4.3. The permanent compressions after pressure release ($c_{iso,per}$) and the compressions at 100 MPa ($c_{iso,100}$) are reported. The pressure of 100 MPa was the maximum isostatic melt pressure applied in the constant flux metal melt infiltration experiments.

4.6.4 Preform permeability

The permeability of the preforms was measured by passing pressurized water through them and the influence of water pressure assessed by varying the pressure in the range of 0.05 MPa to 0.25 MPa. The maximum deviation of a series of 3 measurements at each pressure point was ± 5%. The test at the highest pressure (0.25 MPa) resulted in fracture of the TOPC10 preforms, indicating that the maximum shear strength of the wet sample had been reached.

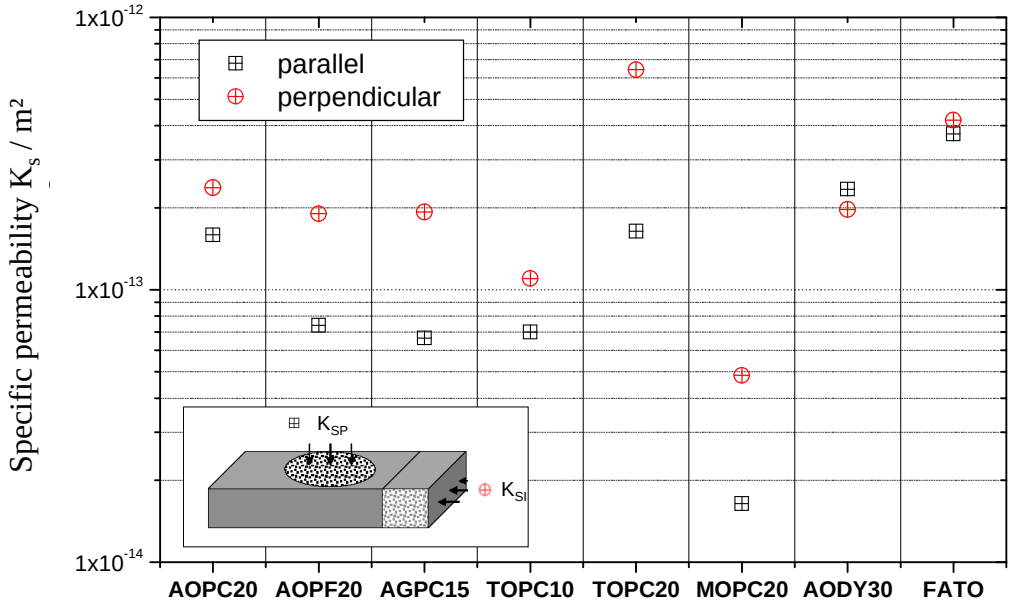

Figure 4.37 Permeability of the preforms parallel (K_{SP}) and perpendicular (K_{SI}) to the pressing direction of the initial green part, respectively.

The following permeability measurements were performed using a water pressure of 0.1 MPa, as this was a compromise between keeping preform integrity and a high volume flow, enabling short measuring times. The specific permeability of the preforms was measured perpendicular (K_{SI}) and parallel (K_{SP}) to the green part pressing direction.

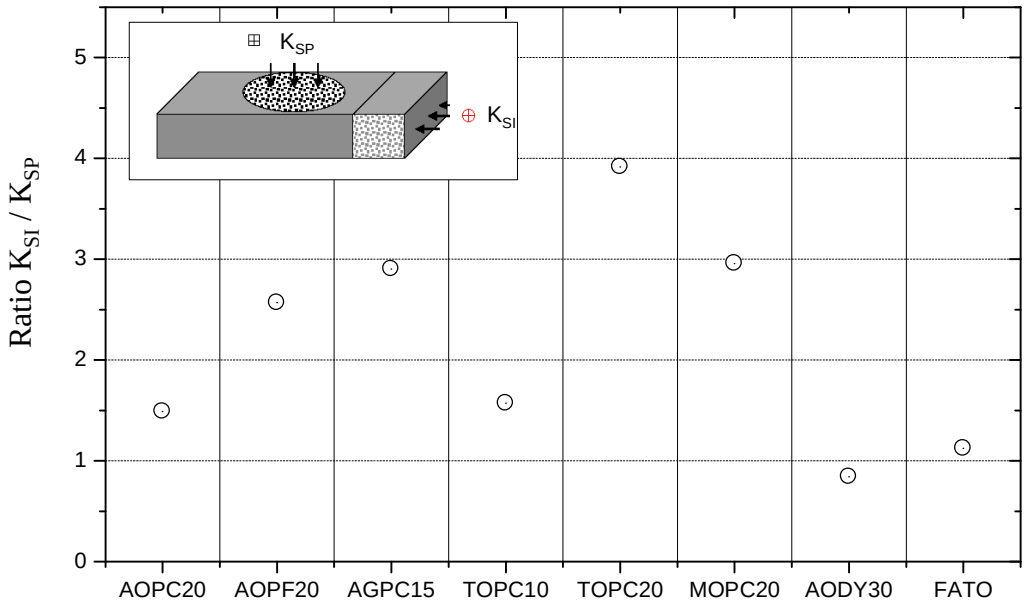

Figure 4.38 Ratio of specific permeabilities in the preforms.

Figure 4.37 shows that the TOPC20 preform showed the highest permeability ($6.4x10^{-13}$ m²) which was in the perpendicular direction, and the MOPC20 preform the lowest ($1.6x10^{-14}$ m²), which was in the parallel direction. Apart from the procured preforms AODY30 and FATO, all the preforms tested were made using pore forming additives (PFA) and all had a higher permeability in the perpendicular direction than in the parallel direction.

The anisotropy in permeability was calculated as the ratio K_{SI} to K_{SP} and values are shown in Figure 4.38. The ratios for the preforms fabricated with PFA lay between 1.5 for AOPC20 (low anisotropy) and 4 for TOPC20 (high anisotropy).

The permeability of AODY30 and FATO lay between $2.0 \cdot 10^{-13}$ m² and $4.2 \cdot 10^{-13}$ m² which was similar to the values reported for AOPC20 and TOPC20. In contrast to the preforms formed with PFA, there was no significant anisotropy, as indicated by ratio values close to unity in Figure 4.38. Table 4.4 gives an overview of the specific permeability of the preforms in the different directions and the ratio between them.

Table 4.4 Evaluated preform permeability parameters K_{SI} and K_{sp} and their ratios.

	Permeability		**Ratio**
	K_{SI}	**K_{SP}**	**K_{SI}/K_{SP}**
	10^{-14} m²	**10^{-14} m²**	
AOPC20	23.7	15.9	1.5
AOPF20	19.0	7.4	2.6
AGPC15	19.3	6.7	2.9
TOPC10	13.1	7.0	1.9
TOPC20	64.2	16.4	3.9
MOPC20	4.8	1.6	3.0
AODY30	19.7	23.4	0.8
FATO	41.9	37.3	1.1

4.7. Constant pressure infiltration

Efforts to determine the progress of infiltration in one of the constant flux infiltration setups by prematurely stopping the infiltration process were not successful as the preforms were either not infiltrated or fully infiltrated as result of the relatively short infiltration period. Even at the slowest velocity (0.07 m/s in DSQC), complete infiltration took less than 1 s. The preform was infiltrated within 1 ms at the highest infiltration velocity used in the current investigations at a plunger velocity of 4.0 m/s in the ISQC mode (Table 3.8). Instead of the constant flux infiltration, a constant pressure infiltration using gas pressure was developed to investigate the first steps of preform infiltration.

The infiltration of preforms in the constant pressure mode was performed using a die similar to that used for the DSQC except a lid was used as an upper plunger which could be closed immediately after the metal was poured into the die cavity. After closing, the pre-selected gas pressure was applied immediately onto the top surface of the metal melt. In order to investigate only the effects of pressure, without reaction between the ceramics and the metal, the inert system consisting of an AOPC20 preform infiltrated with the alloy IS was studied.

In order to prevent gas flow from the pressurized volume on the top towards the bottom and the inside of the preform, a self sealing effect of the metal melt was used. Initially the gas pressure forced the liquid metal into the gap between the die and the preform. Intimate contact of the melt on the die wall was achieved by using a coating of graphite and K_2ZrF_6. The latter was used to promote wetting of the die wall by the melt [6,21]. As the melt reached the bottom punch, the metal solidified partially in the edge between the lower punch and die wall, as shown by the curvature of the solidified metal towards the bottom punch, indicated by an arrow in Figure 4.39 a). The solidification shrinkage of the metal resulted in a gap formation. Therefore, the air which was displaced by the melt which infiltrated the preform could escape

unhindered through the gap between the bottom punch and the die walls. As a result, the metal could flow from the top and the side walls into the preform. In Figure 4.39 a) the macrograph of the preform infiltrated at 0.40 MPa shows minor metal intrusions on one side towards the melt reservoir on the top of the preform.

Metal could be maintained in the molten condition directly on top of the solidified region as the preform and metal were both heated to 800°C. At an infiltration pressure of 0.80 MPa, the liquid metal entered the preform from the side walls as well as from the top as shown in Figure 4.39 b). The infiltration depth on the top and outer sides reached 3 and 13 mm respectively. The centre line along the y-axis showed axisymmetric intrusion behaviour. The macrostructure consisted of adjacent grey and white phases in the infiltrated regions.

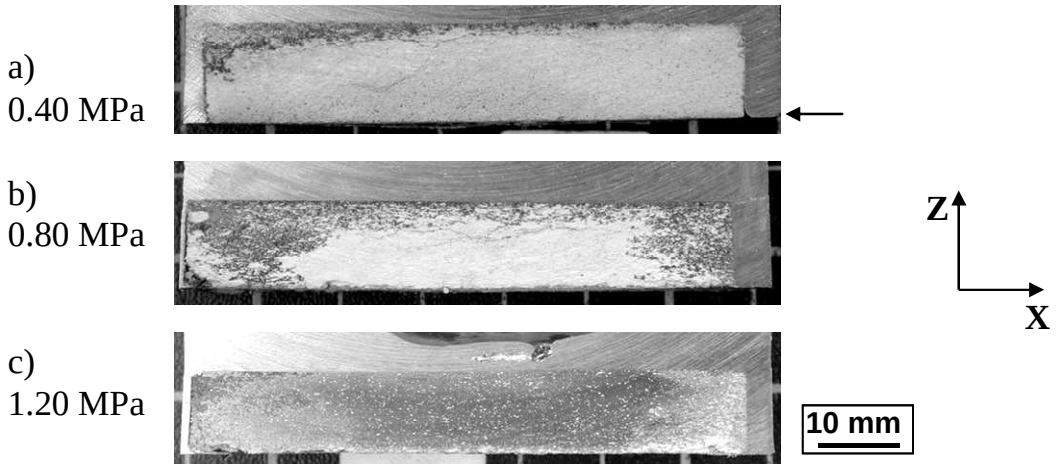

Figure 4.39 Macrographs of cuts through the xz-plane of AOPC20 preforms infiltrated with the alloy IS at constant gas pressures of 0.40, 0.80 and 1.20 MPa.

As shown in Figure 4.39 c), at an infiltration pressure of 1.20 MPa, the metal reached all other regions, apart from an area near the bottom of the preform. Some white spots are visible. Similar to the sample infiltrated at 0.80 MPa, an axisymmetric arrangement of the metal intrusions was found. Therefore the subsequent metallographic investigations were performed on a half preform in the X-Z plane. The microstructures of the AOPC20 preforms infiltrated at 0.80 MPa and 1.20 MPa and the visualisation of the pore saturation profiles are shown in Figure 4.40 and 4.41, respectively.

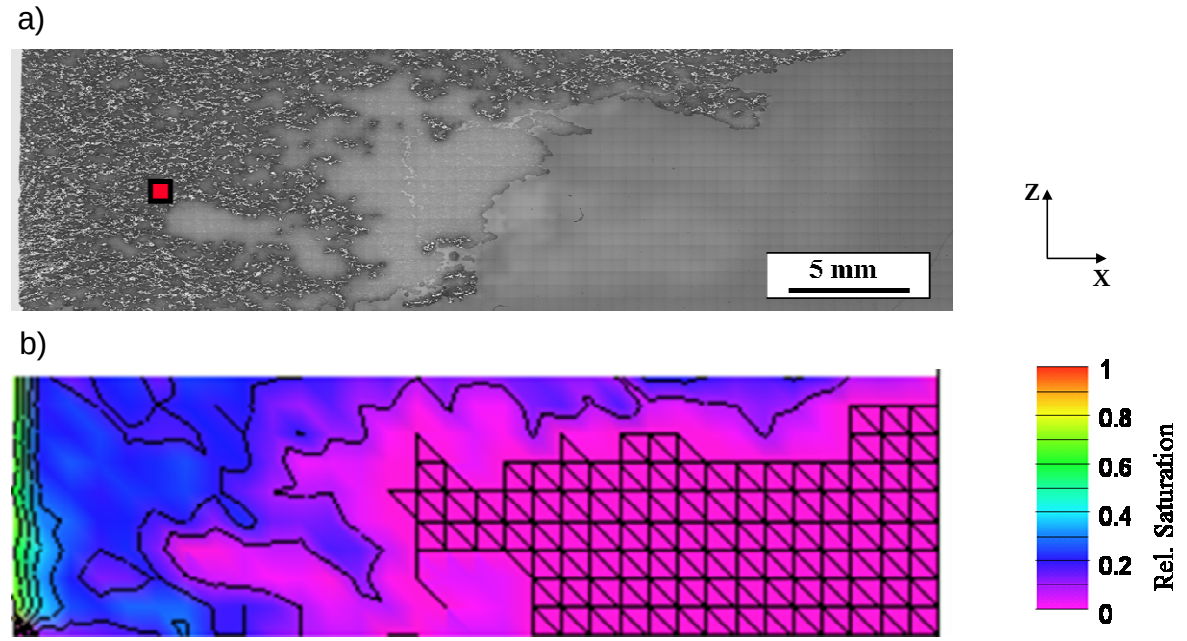

Figure 4.40 Cross sectional macrograph of AOPC20 infiltrated at 0.80 MPa: a) Reflected light grey scale image with metal (white), alumina and the residual porosities (dark). The frame in the microstructure indicates the position of the detailed view in Figure 4.42 b) Quantification of the relative saturation of a).

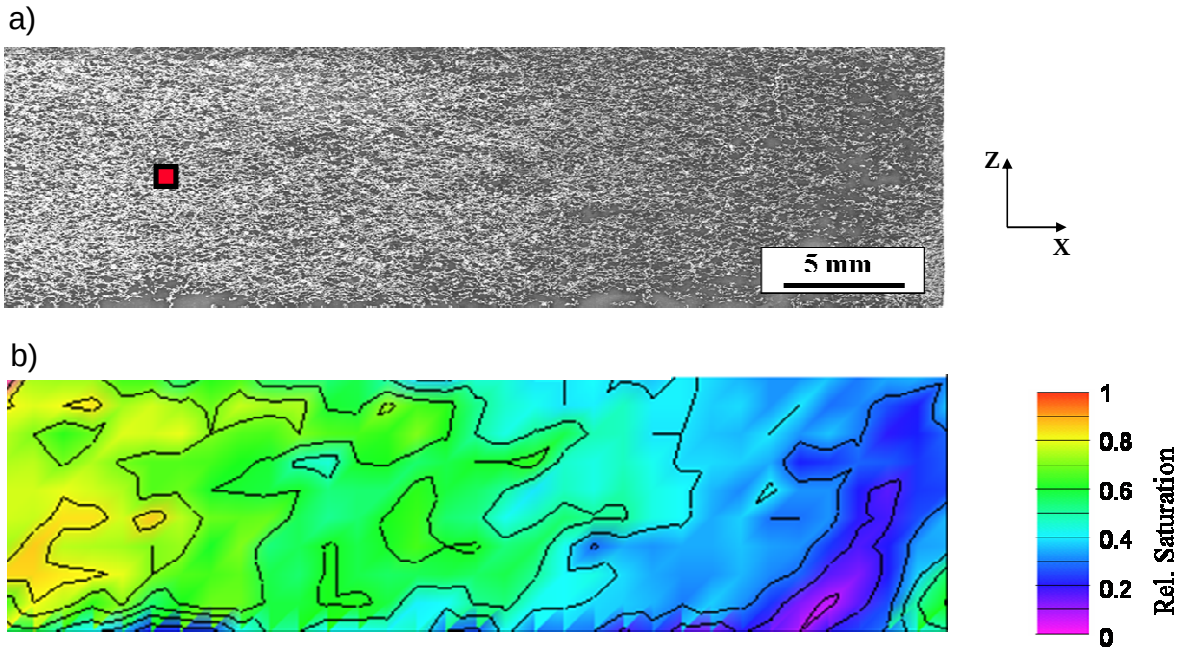

Figure 4.41 Cross sectional macrograph of AOPC20 infiltrated at 1.20 MPa: a) Reflected light grey scale image: frame indicates the position of the detailed view in Figure 4.42 b) Quantification of the relative saturation of a).

The preform infiltrated at 0.80 MPa had metal ligaments concentrated towards the side and the top areas of the preform. About 35% of the overall area of the preform showed metal

intrusions and the other areas were free of metal. The saturation reached 0.4 on the outer edge and the top of the preform and about 0.2 towards the centre.

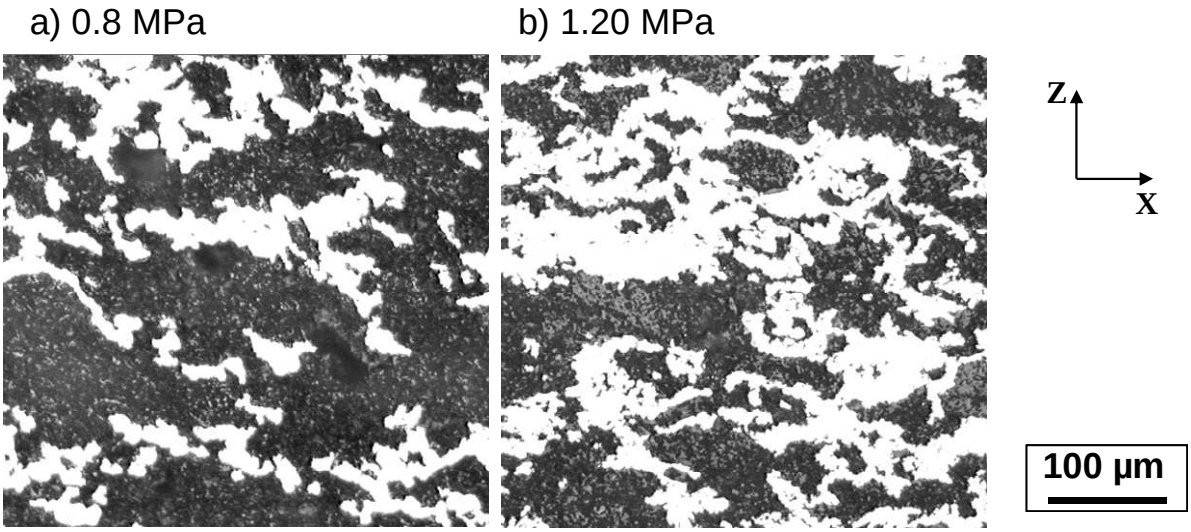

Figure 4.42 Microstructure of preforms AOPC20 infiltrated at constant pressures of a) 0.8 MPa and b) 1.20 MPa. Dark phase: residual porosity; grey phase: Al_2O_3 ceramic; light: alloy.

In contrast, comparatively larger saturations were observed in the preform infiltrated at 1.20 MPa, as shown in Figure 4.41. Apart from a small area on the upper corner of the infiltrated preform, no other regions were fully infiltrated. Similar to the preform infiltrated at 0.80 MPa, the areas toward the outer edge had saturation values between 0.7 and 0.8. In the central area, the saturation reduced to 0.2 to 0.3 with a significant negative saturation gradient along the positive x-axis, from the outside to the centre of the preform.

The microstructures at defined position (5 mm from the outside border along the x-axis and in the centre of the y-direction of the preform and marked with a square in Figure 4.40 a) and Figure 4.41 b) are shown in Figure 4.42 a) and b). At the lower pressure of 0.80 MPa, the coarse porosity resulting from the pyrolysis of PFA was filled while the pores between the finer particles remained empty. In contrast, at 1.20 MPa, the fine porosity between the particles was at least filled partly. This is in agreement with the overall saturation data.

The mean saturation along the x-axis calculated as the arithmetic mean of pore saturation along the z-direction is presented in Figure 4.43 for the AOPC20 preform. In general, the saturation decreased from the edge towards the centre of the preform. After infiltration at a constant pressure of 0.80 MPa, the saturation on the edge was 0.27 but this dropped to close to zero at a depth beyond about 12.5 mm.

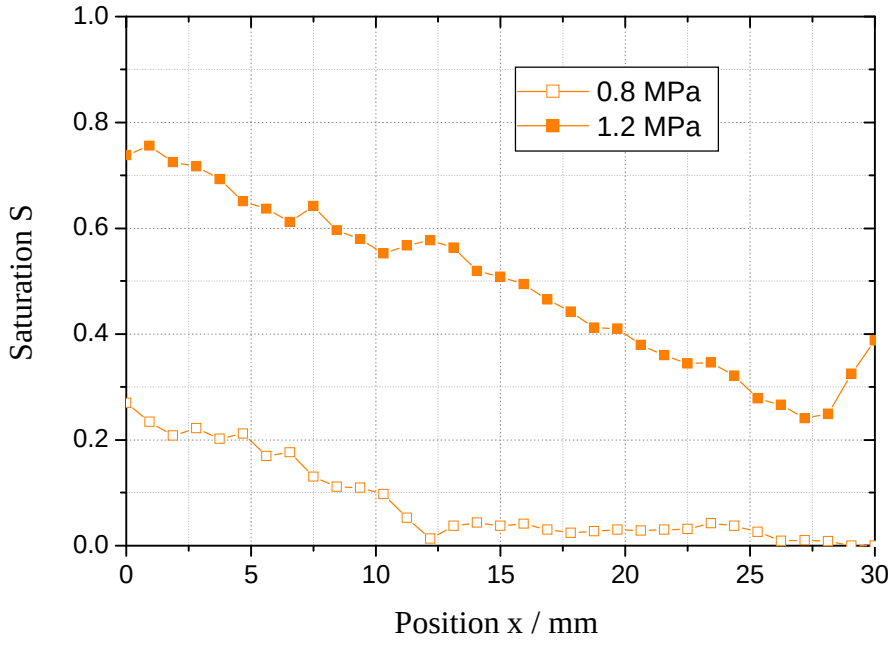

Figure 4.43 Mean saturation along x-axis in AOPC20 infiltrated at constant gas pressures of 0.80 MPa and 1.20 MPa.

At 1.20 MPa, the saturation on the outer edge was 0.77 and decreased to 0.22 close to the centre of the preform. The curve showed unsteady behaviour towards the centre. Starting from an infiltration depth of 26 mm, the saturation increased again to 0.39 in the centre at the x-position of 30 mm.

4.8. Squeeze cast preform infiltration

The non-reinforced infiltration alloys were characterised in terms of their microstructure, thermal behaviour whilst cooling, and the thermal conditions during an infiltration cycle.

4.8.1 Unreinforced matrix properties

The microstructures of the non-reinforced infiltration alloys are shown in Figure 4.44 a) and b) for squeeze cast specimens processed using same conditions as used for infiltration. The microstructure of IM (AlMg9) consisted of discontinuous chain-shaped precipitates in a light matrix as shown in Figure 4.44 a). According to the binary phase diagram of Al-Mg, Figure 2.2, the precipitates consisted of the β-phase, Al_3Mg_2.

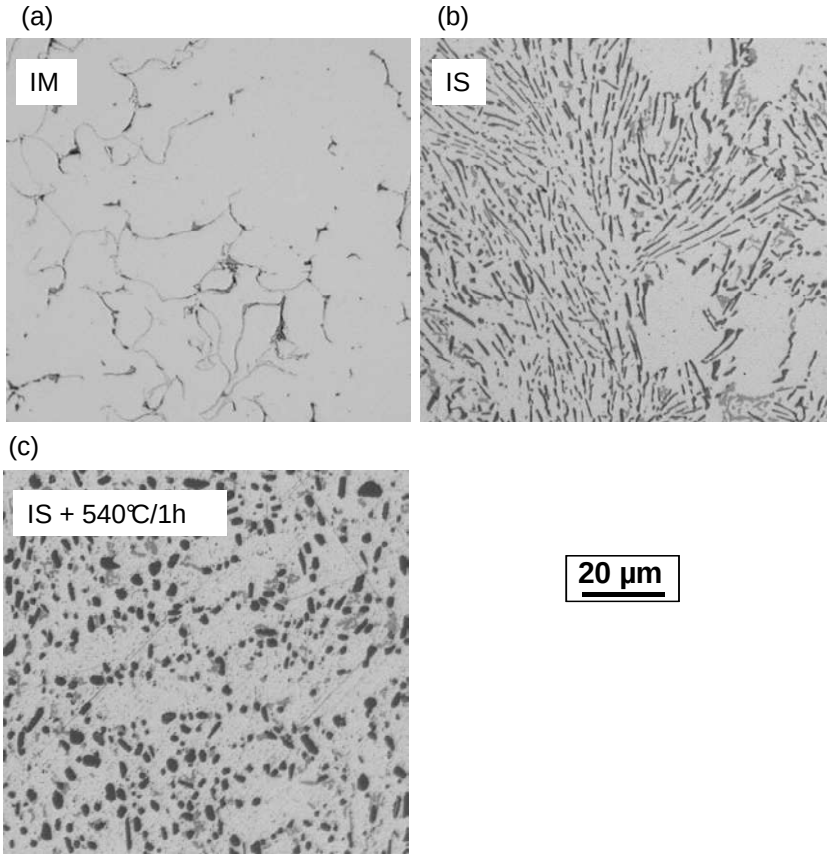

Figure 4.44 Microstructure of the unreinforced matrix alloys a) Al-Mg IM ; b) Al-Si IS and c) IS heat treated at 540°C for 1 h.

The AlSi12Fe alloy (IS) was examined in the as-cast condition (Figure 4.44 b) and after heat treatment at 540°C for 1h (Figure 4.44 c). In the as-cast condition, acicular precipitates and small Chinese-character shaped light grey precipitates were observed. The binary phase diagram of the Al-Si system in Figure 2.4 indicates no room temperature solubility of silicon in aluminium. Therefore the acicular precipitates consisted of pure silicon whereas the light

grey areas consisted of an intermetallic of the Al-Fe-Si type as reported by Schumann [174]. Both types of precipitates were spherodized by the heat treatment.

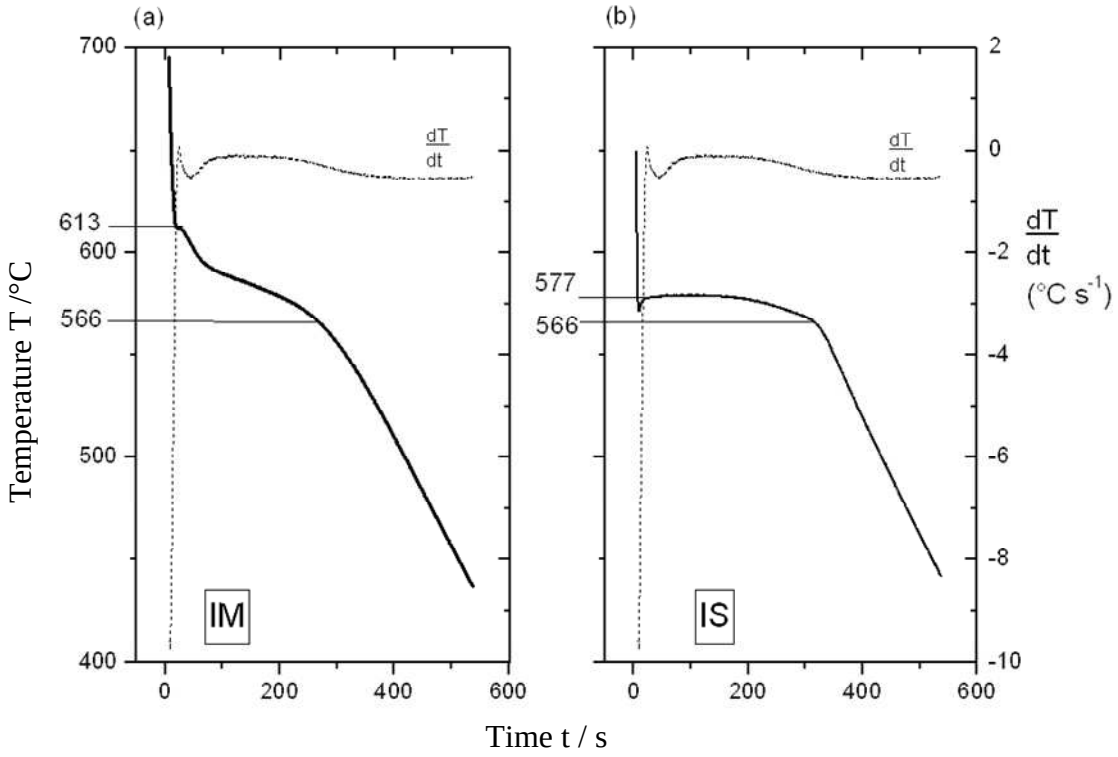

Figure 4.45 Thermal analysis of the infiltration alloys a) IM and b) IS.

The thermal analysis curves of the infiltration alloys are shown in Figure 4.45 a) and b). To ensure infiltration in the fully molten condition, the temperatures of the melt and the preform were maintained above the liquidus temperatures of the alloys. The liquidus temperature of IM was measured to be 613°C and that of IS, 577°C. The solidus temperatures of both alloys were evaluated to be 566°C.

4.8.2 Thermal properties during infiltration

The temperatures $T_{preform}$, T_{edge}, T_{centre}, the displacement of the upper punch $s_{plunger}$ and the metallic pressure P_{met} were measured during the first 15 s of an infiltration cycle and are given in Figure 4.46 for MOPC20. The $T_{preform}$ curve corresponds to the temperature in the preform close to its edge (p. 82) whereas T_{centre} and T_{edge} represent the temperatures close to the bottom punch surface in the centre and the edge respectively. As the melt temperature in the

die, $T_{melt,die}$, could not be recorded during the infiltration process, it was assessed in a prematurely terminated cycle to be 665°C.

The measurements were performed with the MOPC20 preform as magnesia exhibited the highest thermal conductivity of the dense sintered materials at a given temperature, Table 3.3. Therefore the thermal flux has to be assumed to be the highest of all the preforms and thus the sample would exhibit the lowest preform temperature prior to infiltration.

Zero time in Figure 4.46 corresponds to the first movement of the upper punch. Approximately 20 s prior to this event, the preform was transferred from the preheating furnace held at 800°C into the infiltration die cavity held at 450°C. As shown in Figure 4.46, the contact between the preform and the bottom punch resulted in an intitial punch temperature rise from 450°C to 470°C. The temperature signal at the edge of the preform was interrupted at an early stage of infiltration, as the leads to the thermocouple were sheared in the gap between the die and the upper punch. Prior to that, the preform cooled from 800°C to 750°C.

The pressure P_{met} increased steadily as the plunger moved until the preset ultimate pressure of 100 MPa was reached. The main plunger movement took place in the first second of the infiltration cycle at a mean velocity of 0.017 m/s. After the steep increase in the pressure, no significant change in displacement was observed.

The pressure P_{met} increased steeply up to 15 MPa and subsequently a smooth pressure increase occurred. This resulted from the infiltration press control system which switched at 15 MPa to the high pressure mode with a low hydraulic fluid volume displacement. The maximum pressure in the die was reached 7.5 seconds after the start of the infiltration cycle. As the maximum pressure was reached, the hydraulic system of the press switched off and

restarted when the pressure dropped below 95 MPa, leading to the stepped curve of P_{met} in Figure 4.46.

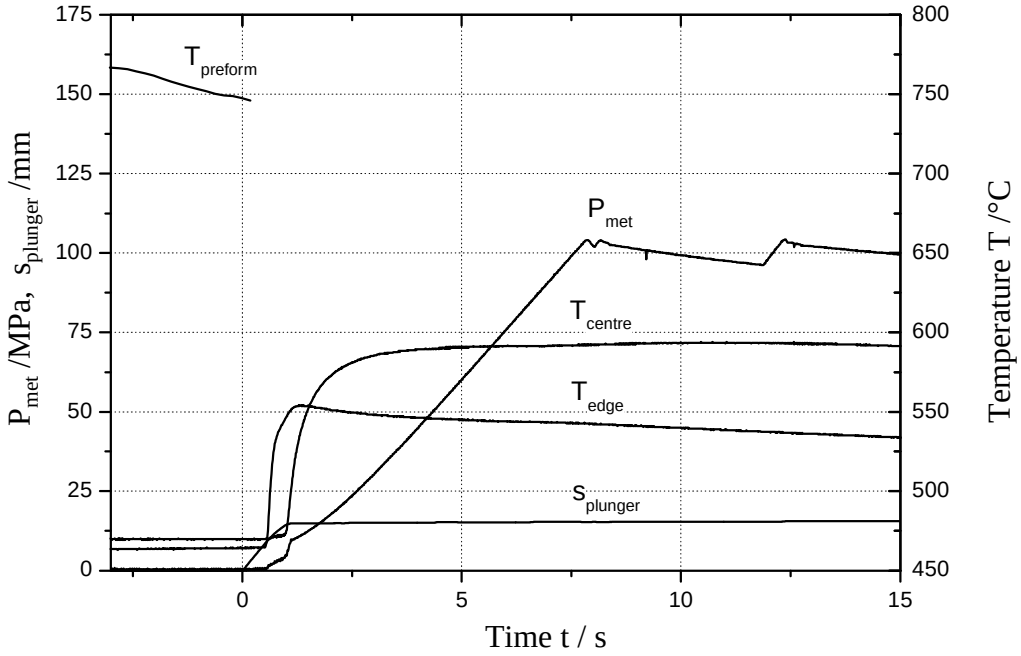

Figure 4.46 Process parameters during preform infiltration with melt IS. Metal pressure P_{met} , plunger displacement $s_{plunger}$ and temperatures in the vicinity of the surface of the bottom punch (T_{centre}, T_{edge}) and in the preform ($T_{preform}$) are shown.

The temperature in the bottom punch varied with position as shown by T_{centre} and T_{edge}. At the edge, the temperature increased to a maximum of 555°C within the first 1.5 seconds and then cooled to 535°C at the end of recording. As the maximum of T_{edge} was reached, the temperature in the centre T_{centre} increased steeply to 585°C with no further significant change until the end of the recording period. The temperature increase in the centre occurred as the main movement of the plunger terminated, whereas the temperature at the edge reached its maximum at about half of the maximum plunger displacement.

4.8.3 Evaluation of infiltration behaviour

The first 2 seconds of the infiltration process were investigated more precisely in order to compare the preform-specific infiltration behaviours. To allow comparison, all infiltration parameters were kept constant and only the preform type was changed. The infiltration

pressure was recorded as a function of the preform saturation curves were recorded and examples are given in Figure 4.47 for TOPC10 and AOPC20 preforms infiltrated with IS.

The saturation point was taken to be the point at which the maximum pressure of 100 MPa was first reached and then the volume intruded calculated by displacement. Displacements above this point came from solidification shrinkage and were about 6% by volume for IS [(1)].

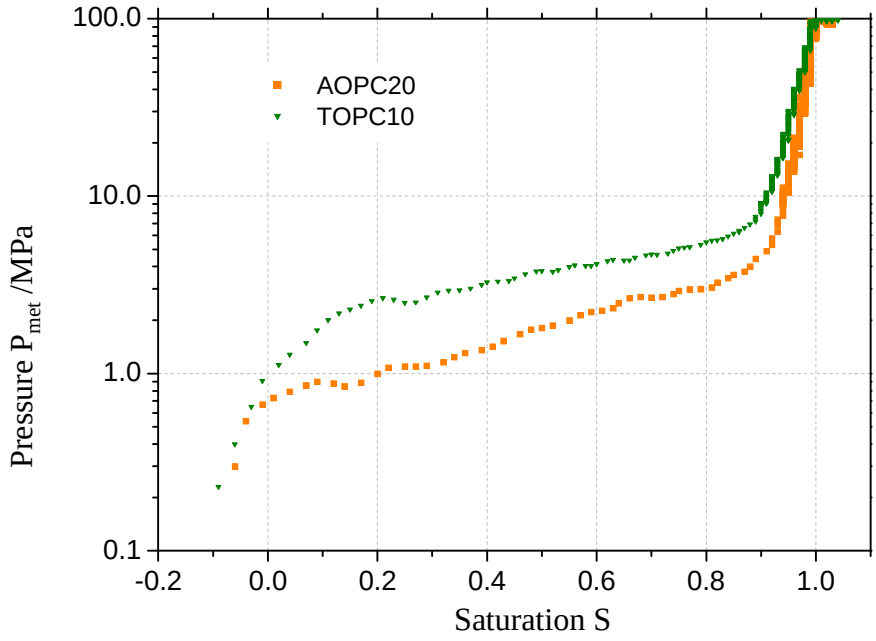

Figure 4.47 Infiltration curves of the preforms AOPC20 and TOPC10 when infiltrating with molten IS alloy.

After the point of complete saturation was determined, the melt volume necessary for full infiltration was subtracted, leading to the zero point equivalent to no saturation. This point corresponded to the starting point of melt intrusion into the preform. This procedure was applied to the data determined during infiltration of AOPC20 and TOPC10 with the IS alloy.

The infiltration curves in Figure 4.47 showed two regions of unsteady filling. The first region was below the saturation of 0.1 where a steep increase was observed up to a pressure of about 1 and 2 MPa for AOPC20 and TOPC10 preforms respectively. A second region in which the

gradient of the curve changed was observed above a saturation of approximately 0.8. Here a steep pressure increase occurred up to the maximum present infiltration pressure of 100 MPa.

The investigations showed that infiltration curves may be subdivided into three stages:

1. Initiation of infiltration up to a saturation of 0.1

2. Steady increase in pressure over the saturation range of 0.1 to 0.8

3. Steep increase in pressure towards full saturation of 1.0

The analysis of the infiltration curves was therefore subdivided into these three stages.

4.8.4 Initiation of preform infiltration with Al-Si alloy IS

The first step of the preform infiltration was characterised by the pressure to initiate filling, designated as the threshold pressure P_0. In order to determine this parameter, the first 2 to 5.7 mm of infiltration depth was plotted as a function of the applied pressure as presented in Figure 4.48. The depth calculations were based on the assumption of infiltration on five sides of the preform, as was found in the constant pressure experiments (section 4.7).

In accordance to Darcy´s law [103], the infiltration depth is a square root function of the applied metal pressure P_{met}. Therefore a linear behaviour was expected in plots of L^2 against P_{met}. The data were fitted to a linear equation with a slope of a and an intercept on the pressure axis of P_0. As shown in Figure 4.48, the behaviour was close to linear with the exception of AGPC15 and TOPC10, where a transient behaviour was observed.

The preform type affected the pressure axis intercept and the slope of the fitted lines. The values of the slope a and the threshold pressure P_0 are summarized in Table 4.5. The lowest threshold pressure of 0.65 MPa and the steepest curve were found for AODY30. The slopes of

the linear fits for AOPC20, TOPC20 and FATO were similar but the intercept increased in the same order from 0.72 to 0.94 MPa.

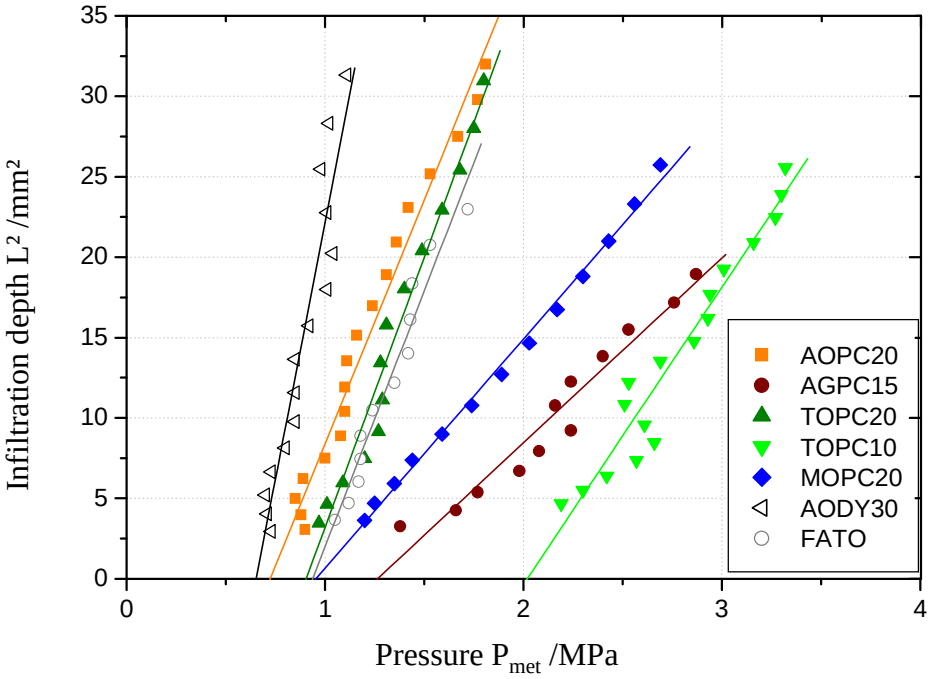

Figure 4.48 Square of infiltration depth of different preform types as a function of the melt pressure (alloy IS). Linear regression of the infiltration curve in the range of 2 mm to 5 mm infiltration depth.

The MOPC20, AGPC15 and TOPC10 preforms exhibited comparatively lower gradients and higher threshold pressures. The TOPC10 preform exhibited the highest threshold pressure of 2.02 MPa and a steeper gradient than MOPC20 and AGPC15.

Table 4.5 Results of infiltration curve regression analysis when infiltrating with IS. Gradient a and threshold infiltration pressure P_0.

	a **mm² / MPa**	**P_0 (at L^2=0)** **MPa**
AOPC20	30.4	0.72
AGPC15	11.5	1.27
TOPC20	33.6	0.91
TOPC10	18.5	2.02
MOPC20	14.3	0.95
AODY30	63.8	0.65
FATO	31.9	0.94

4.8.5 Advancing infiltration with alloy Al-Si alloy IS

In order to determine the shape factor α, defined by Equation 29, the infiltration curves of the self-fabricated preforms with the lowest and the highest threshold pressures P_0 (namely AOPC20 and TOPC10) were investigated until the point of complete saturation was reached. The infiltration curves up to a pressure of 10 MPa are shown in Figure 4.49. The curves were fitted to a function of the type given in Equation 29 by taking the threshold pressure given in Table 4.5 and varying the shape factor α in the range of 0.1 to 10 MPa^{-1}.

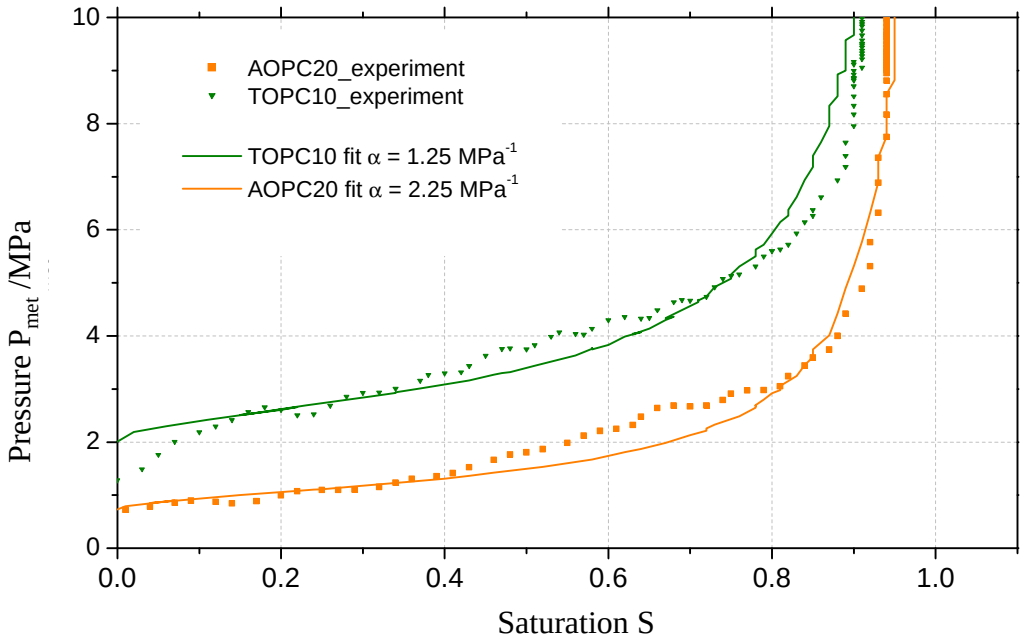

Figure 4.49 Infiltration curves of AOPC20 and TOPC10 and fitted functions in accordance with Equation 29 to determine the shape factor α.

The best fit for the TOPC10 preform was attained by using α =1.25 MPa^{-1}. A higher α of 2.25 MPa^{-1} was required for the best fit function for the AOPC20 preform. The least squares fit curve of AOPC20 with the best fit parameters showed deviations from the experimental data points in the saturation range between 0.4 and 0.8. Deviations from the infiltration curve for TOPC10 were evident in the saturation range above 0.8.

4.8.6 Non destructive testing of MMC infiltrated with alloy IS

Non-destructive X-ray computer tomography was conducted on the infiltrated MMC samples to detect defects resulting from processing. In order to determine the MMC properties with minimum influence of internal defects, the aim was to have a structure as homogenous as possible.

As an example, virtual cross-sectional views in the X-Y and Y-Z planes, which were generally taken from the respective centre planes of the MMC, were extracted from the three dimensional computer tomography data and are shown for the TOPC20IS MMC in Figure 4.50 and Figure 4.51 for different infiltration tool set-ups. The light areas represent the infiltrated preform and the darker areas the pure infiltration Al-Si alloy IS. The central linear discontinuity in the X-Y plane of Figure 4.51 was an artefact resulting from the reconstruction algorithms, and was visible to a greater extent in Figure 4.51 than in Figure 4.50.

In the MMC infiltration process, the preform was initially placed on the bottom punch. It remained in this position throughout infiltration. Even though it had to be assumed that the preform floated as a result of differences between its bulk density and the melt density partial premature solidification at the edge between the bottom punch and the die wall, as indicated in the temperature measurements in 4.8.2, prevented the melt flowing under the preform and therefore floating was impeded. The right hand side of the Y-Z plane views of the virtual cuts in Figures 4.50 and 4.51 represent the X-Y plane of the preform which was initially in contact with the bottom punch.

In the first infiltration tool, the bottom punch was completely made of tool steel as shown schematically in Figure 4.50. In the X-Y plane, darker areas were visible in the region close to the centre of the MMC, indicating material with lower X-ray absorption. Metallographic characterisation attributed the inhomogeneities to non-infiltrated coarse pores formed by the

organic additive in the preform processing. The depth of the porosity field could be visualized in the central cut in the Y-Z plane of Figure 4.50. The porosity was situated towards the upper central volume of the preform.

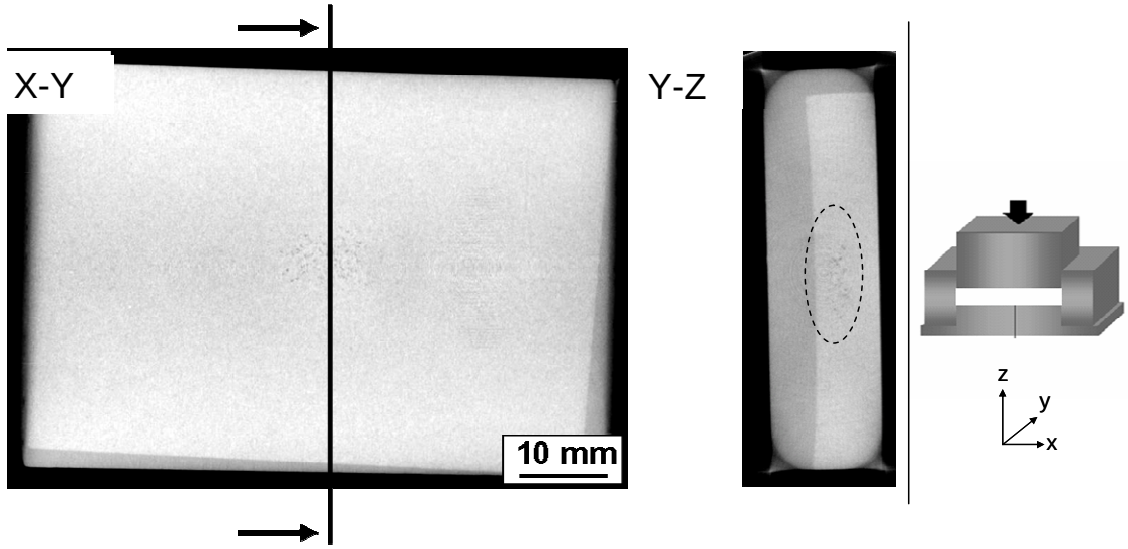

Figure 4.50 Virtual cross-sectional cut through the MMC TOPC20IS in the X-Y and the Y-Z planes (pore field circled).

In order to improve the homogeneity of the MMC, the thermal conduction in the die was altered to achieve directional solidification from the bottom punch through the preform to the melt pool on top of the preform. As a first step, ceramic coatings generally used for thermal management in gravity die casting were applied to the upper punch and the die walls. As the upper punch slid along the die walls during infiltration, the ceramic coating resulted in extensive abrasive wear in the gap, making further movement and infiltration impossible.

The application of the ceramic coating solely to the upper punch did not prevent inhomogeneities in the MMC, as the coating was penetrated at an early stage of infiltration and therefore thermal conduction toward the upper punch was not significantly reduced. Therefore measures were taken to improve thermal conduction toward the bottom punch and to preserve conditions on the die walls and the upper punch.

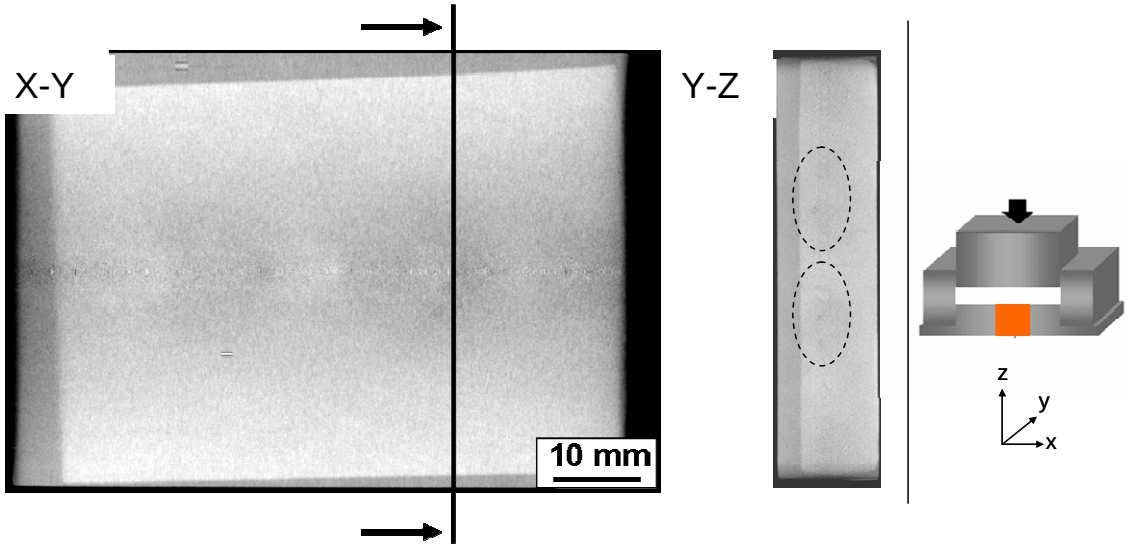

Figure 4.51 Virtual cross-sectional cut through the MMC TOPC20IS in the X-Y and the Y-Z planes (pore fields circled). Schematic cut through the infiltration tool with an integrated chill.

When an insert made of high heat conducting material (a copper alloy) was integrated into the bottom punch, the porosity in the centre of the MMC was reduced. The effect is shown when comparing the pore field intensities in Figure 4.50 and Figure 4.51. Two fields of minor porosity were detected outside the central area, as shown in the cut of the X-Z plane in Figure 4.51. These fields were of significantly lower intensity than that detected in the MMC made without a copper chill, Figure 4.50. All MMCs characterized in the following sections were fabricated using a bottom punch with a central copper chill.

4.8.7 Microstructure of MMCs with Al-Si alloy matrix

The light phase in the micrographs represents the metal and the darker phase the ceramic. The micrographs are presented at low magnifications in order to show the coarse metal ligaments originating from the filled PFA-formed porosity and higher magnification micrographs show the intragranular metal ligaments between the ceramic particles. All images were taken from the central area of the MMCs cut in the X-Z plane. Therefore, the horizontal and the vertical axes of the images correspond to the X- and Y-axes of the MMC respectively.

The low magnification micrographs of the alumina-reinforced MMCs AOPC20IS, AOPF20IS and AGPC15IS in Figure 4.52 a), b) and c) respectively show an apparently predominant fraction of the ceramic phase. The large metallic areas developed from the filling of the coarse pores in the preforms derived from the pyrolysed pore forming additive. In AOPF20IS, where carbon fibres were used to form the coarse porosity, the elongated shape of this PFA is clearly shown in the circled area in Figure 4.52 b). Additionally, the metal phase areas were larger and more distinct compared to AOPC20IS (a) and AGPC15IS (c), indicating that the initial green part contained carbon fibre agglomerates (arrows).

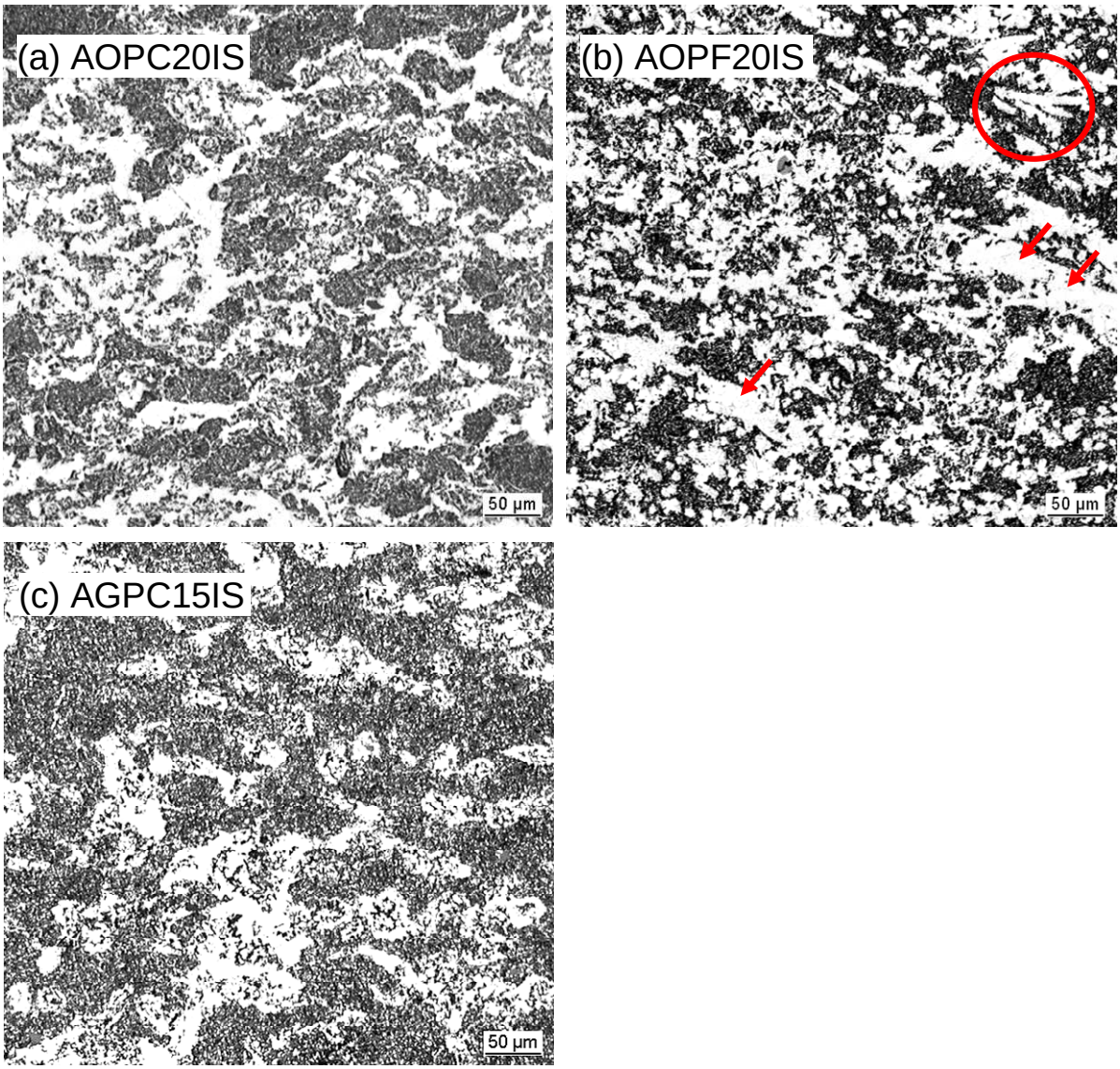

Figure 4.52 Optical micrographs (low magnification) of the MMC materials based on alumina preforms: AOPC20IS, AOPF20IS and AGPC15IS.

The metal filling the intragranular regions was visible at higher magnifications as shown in Figure 4.53 a) to c). Furthermore, the Si precipitates as well as the grey Fe-containing phases were resolved. The finest Si-precipitates were found in AGPC15IS where they were round and sub-micron in size. Here the interstices between the ceramic particles were relatively small in the sub-micron range and had a fuzzy appearance. It is presumed that the larger transparent areas were agglomerates of the glassy binder added to the ceramic slurry to bond the particles in this preform. The metal phase in the interstices of AOPF20IS (Figure 4.53 b) and AOPC20IS (Figure 4.53 a) was more distinct and the interstices were larger compared to AGPC15IS.

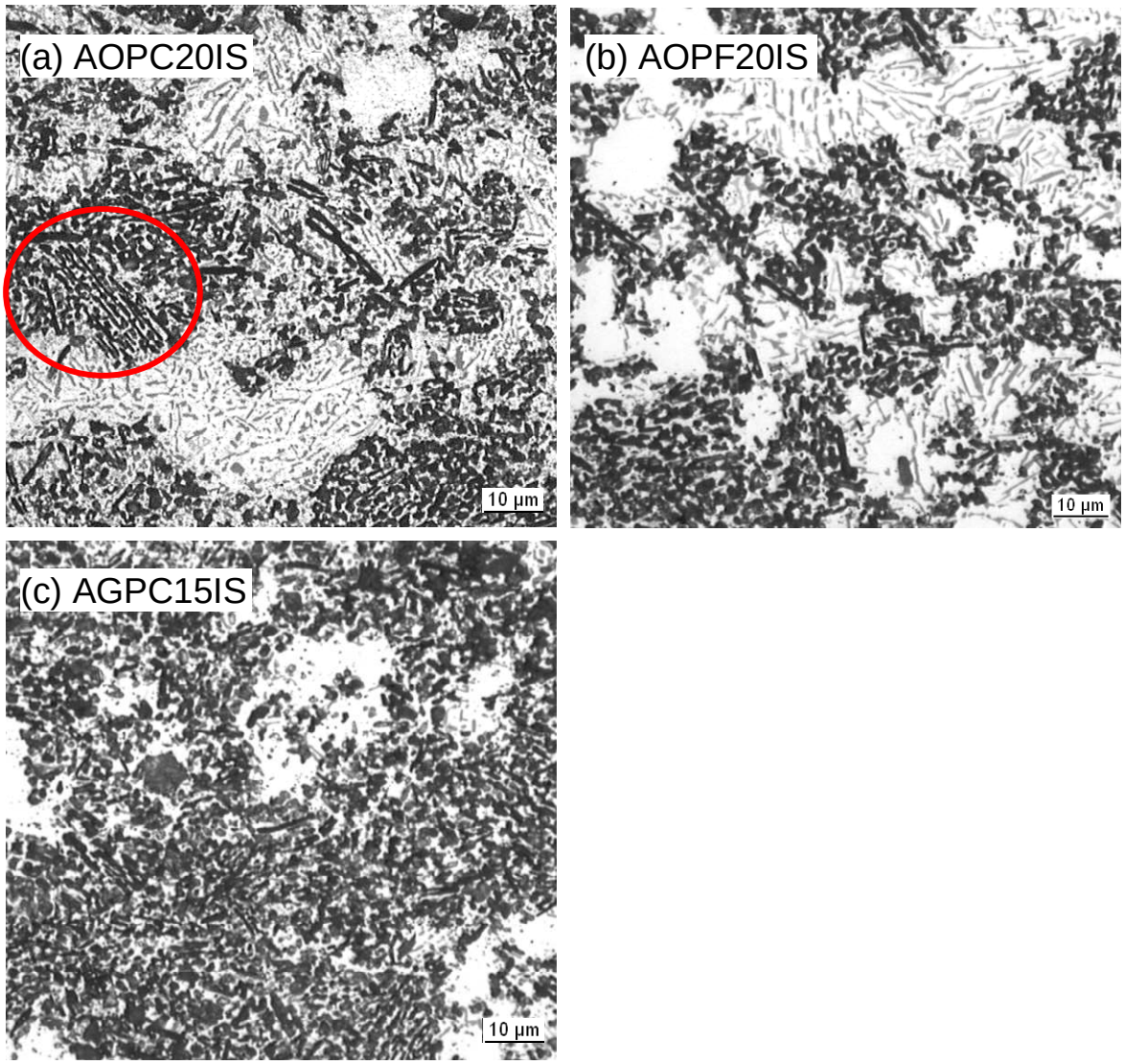

Figure 4.53 Optical micrographs (high magnification) of the MMC materials based on alumina preforms: AOPC20IS, AOPF20IS and AGPC15IS.

The bimodal porosity in the preforms generated by the pyrolysis route was completely filled with the metal during infiltration. Therefore a bimodal metal ligament distribution was developed with the large metal regions visible at lower resolution and fine metal ligaments between the particles visible at higher magnifications This is a characteristic feature of this type of MMC.

The grains in AOPC20IS exhibited a significant fraction with an aligned elongated structure which can be seen in the circled area of AOPC20IS in Figure 4.53 a). This structure was not apparent in the micrograph of AOPF20IS. Even though the sintering temperature of the latter preform type was 100°C less than that of AOPC20IS, the ceramic phase was apparently coarser. This was due to the pore former influencing the sintering kinetics of the alumina.

Similar to the alumina preforms, the intragranular metal fractions in the titania MMCs were not clearly defined in the low magnification micrographs of TOPC10IS and TOPC20IS as shown in Figure 4.54 a) and b) respectively. The intergranular metal fractions are apparent at this low magnification in MOPC20IS, Figure 4.54 c). There is a strong anisotropy with a preferred metal ligament orientation along the X-axis in TOPC20IS, Figure 4.54 b). Additionally, agglomerates of the ceramic particles are visible. Figure 4.55 shows the materials at higher magnifications. TOPC10IS (Figure 4.55 a) exhibited a finer ceramic structure than TOPC20IS (Figure 4.55 b) which resulted from the higher sintering temperature used for the latter. In comparison to the AO type MMCs shown in Figure 4.53, the ceramic phase was rather more continuous with distinct sintering bridges between the particles.

In the microstructure of TOPC20IS, sintering reached a stage where closed cell porosity was formed as indicated exemplarily by the arrows to the black features in Figure 4.54 b) which were non infiltrated porosity. In contrast to the titania-based MMCs, the interconnection of

the ceramic particles was not visible in the magnesia-based MMC MOPC20IS, Figure 4.55 c), where a granular structure of the ceramic phase was apparent.

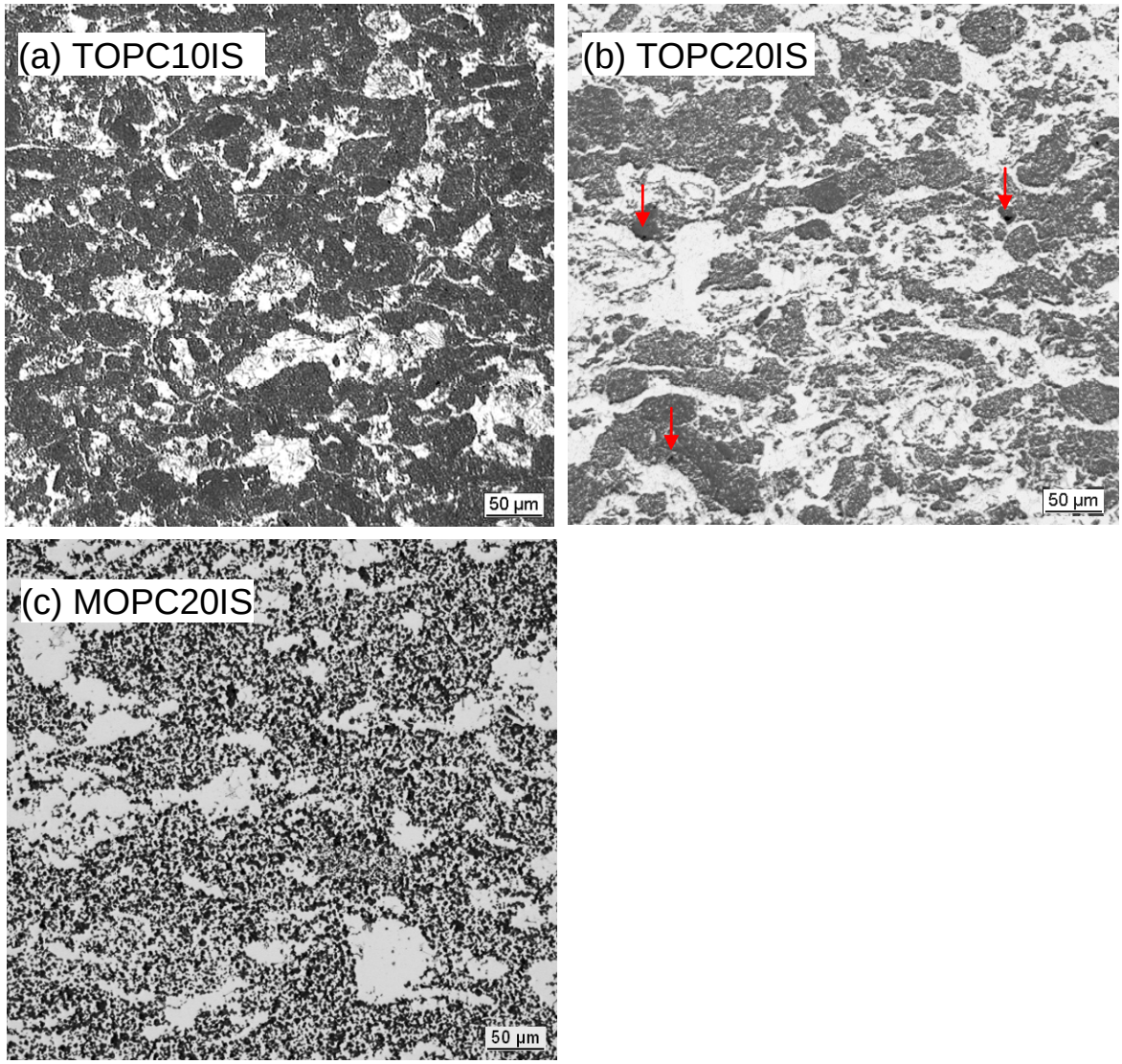

Figure 4.54 Optical micrographs of the MMCs based on reactive preforms: TOPC10IS, TOPC20IS and MOPC20IS.

Similar to the alumina-based MMCs, the Si precipitates in the alloy in the intergranular regions of the reactive MMCs shown in Figure 4.55 a) to c) were finer and more spherical compared to that of the pure alloy. The microstructure of MOPC20IS exhibited the finest Si precipitates of all MMCs investigated in the present research: the lengths of the individual precipitates were generally below 3 µm and their width sub-micron in scale.

The sintering temperatures of the MOPC20 preforms were varied. The MMC microstructures resulting from preforms sintered at the two extreme temperatures, namely 1300°C and 800°C, and infiltrated with the alloy IS are shown in Figure 4.56 a) and b). The microstructure in terms of the size and shape of the MgO ceramic phase differed significantly. The structure of the MOPC20IS made with a preform sintered at 1300°C in Figure 4.56 a) exhibited a coarse ceramic phase with particle diameters in the range of 2 to 10 µm.

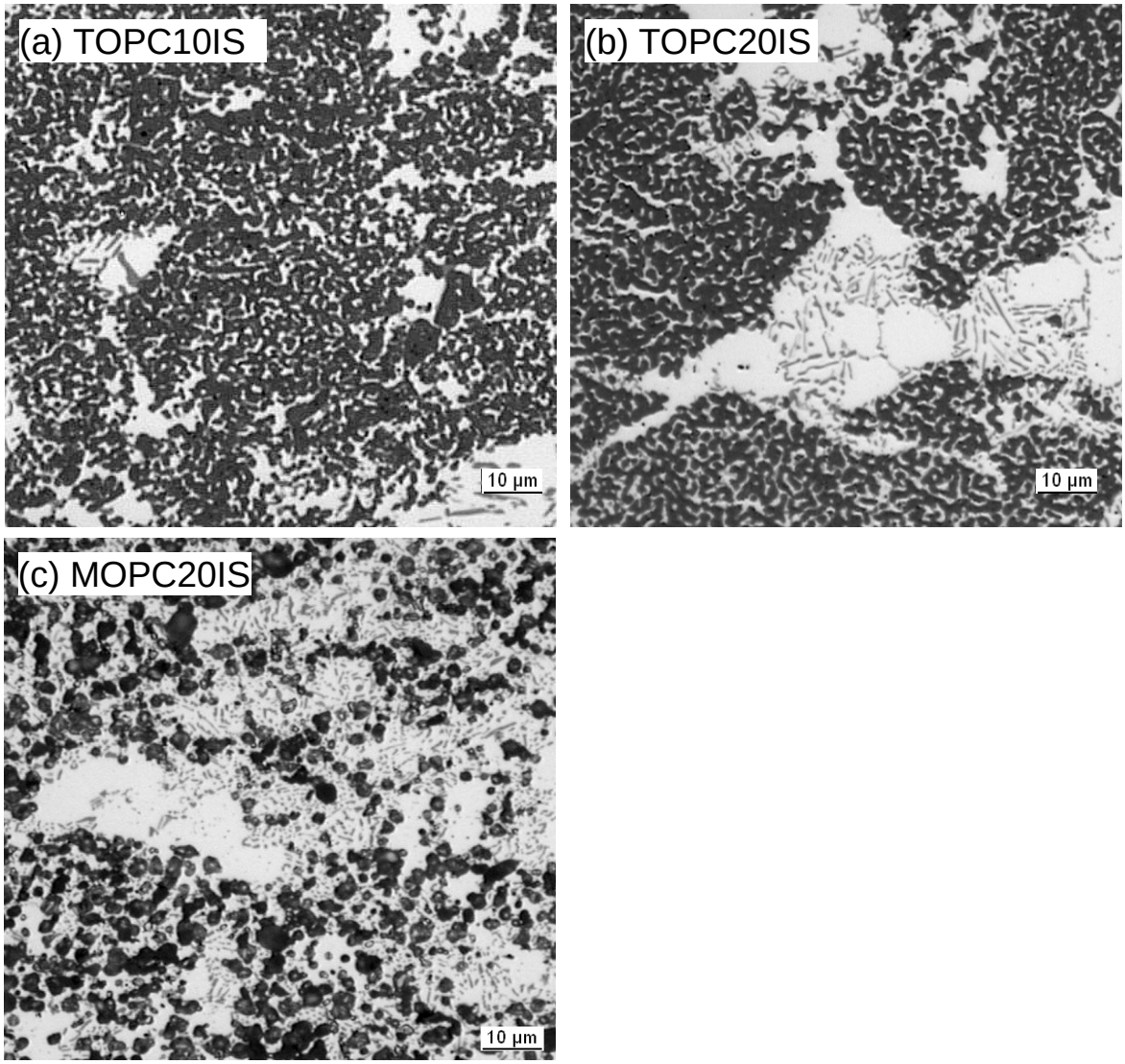

Figure 4.55 Optical micrographs of the MMCs based on reactive preforms: TOPC10IS, TOPC20IS and MOPC20IS.

In contrast, the MOPC20IS fabricated using a preform sintered at 800°C (Figure 4.56 b) had a significantly finer ceramic structure, with grain sizes in the sub-micron range. The intragranular region showed some areas where the light metal phase infiltrated the small pores

between the dark grey ceramic phases. However a significant portion of the porosity between the ceramic particles was not infiltrated, shown by the black regions. With the current infiltration set-up and parameters, the fine pores were not infiltrated, leaving residual porosity.

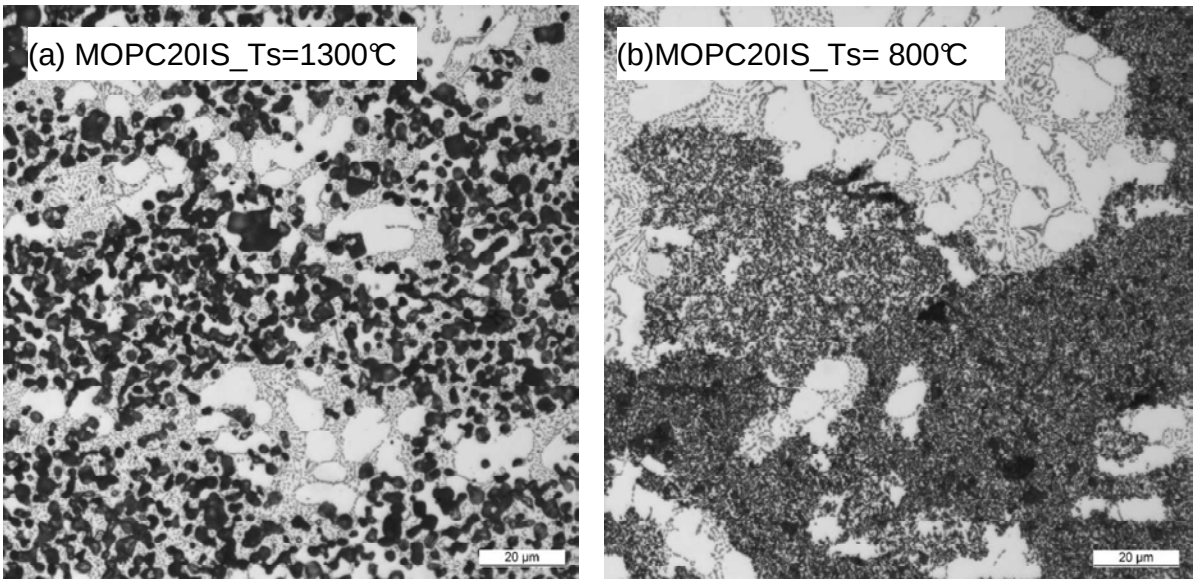

Figure 4.56 Optical micrograph of MOPC20IS with preforms sintered at a) 1300° and b) 800°C.

The MMC based on the FATO preform comprised alumina fibres (the black phase) embedded in titania particles (the dark grey phase) and the infiltration alloy with relatively coarse needle shaped Si precipitates in α-Al, Figure 4.57.

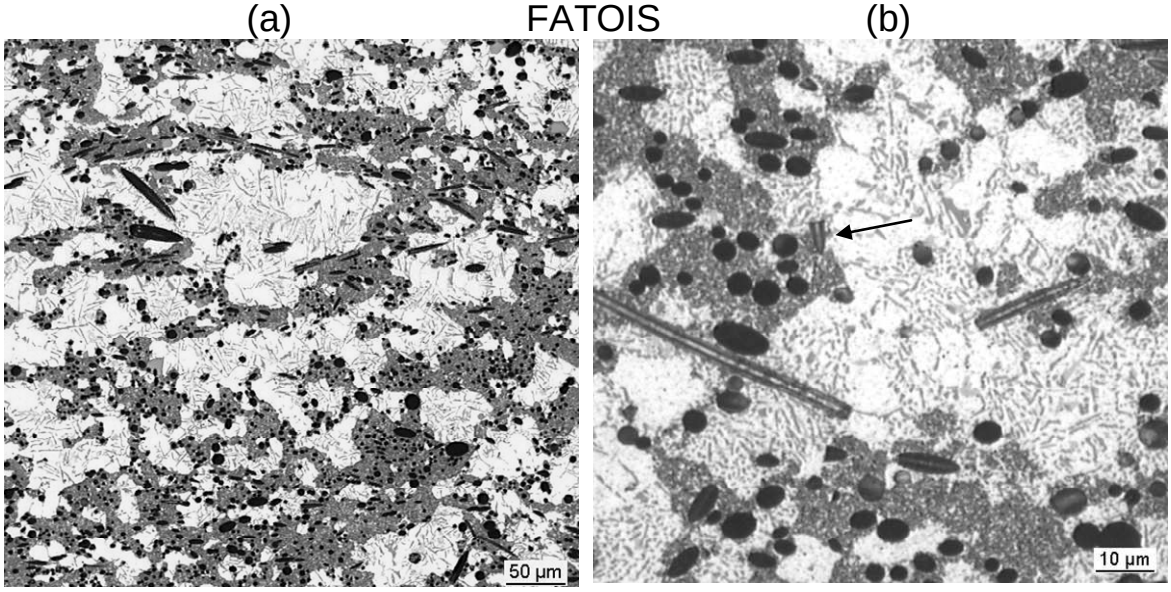

Figure 4.57 Optical micrographs of the FATOIS type MMC at low (a) and higher magnification (b).

Compared to the micrographs of the MMCs fabricated with preforms of the PFA pyrolysis route, e.g. the AOPC20IS in Figure 4.52, the alloy regions were significantly larger in the FATOIS. The length of the fibres aligned along the cutting plane of the micrograph varied in the range of 30 µm to 80 µm. At higher magnifications, fibre fragments shorter than 10 µm were visible. An example is marked with an arrow in Figure 4.57 b). The fibre diameter was in the range of 3 µm to 8 µm. The fibres at the polished surface were transparent allowing the sub-structure to be seen.

The MMC fabricated with the AODY30 preform exhibited a cellular ceramic structure, as shown in Figure 4.58. Here the dark phase is the relatively dense sintered alumina struts and the light phase the alloy IS. The bubbles in the ceramic slurry were filled with the alloy during infiltration. The Si precipitates were comparatively coarse and dendritic growth of α-Al can be seen in Figure 4.58 a). The areas of metal had diameters in the range from 10 µm to more than 300 µm, which represented the bubble diameters in the preform. The ceramic struts between the metal regions showed some residual porosity. The partial filling of the pores in the struts was apparent at high magnification in Figure 4.58 b). The residual porosity consisted of isolated, closed cell pores which could not be infiltrated.

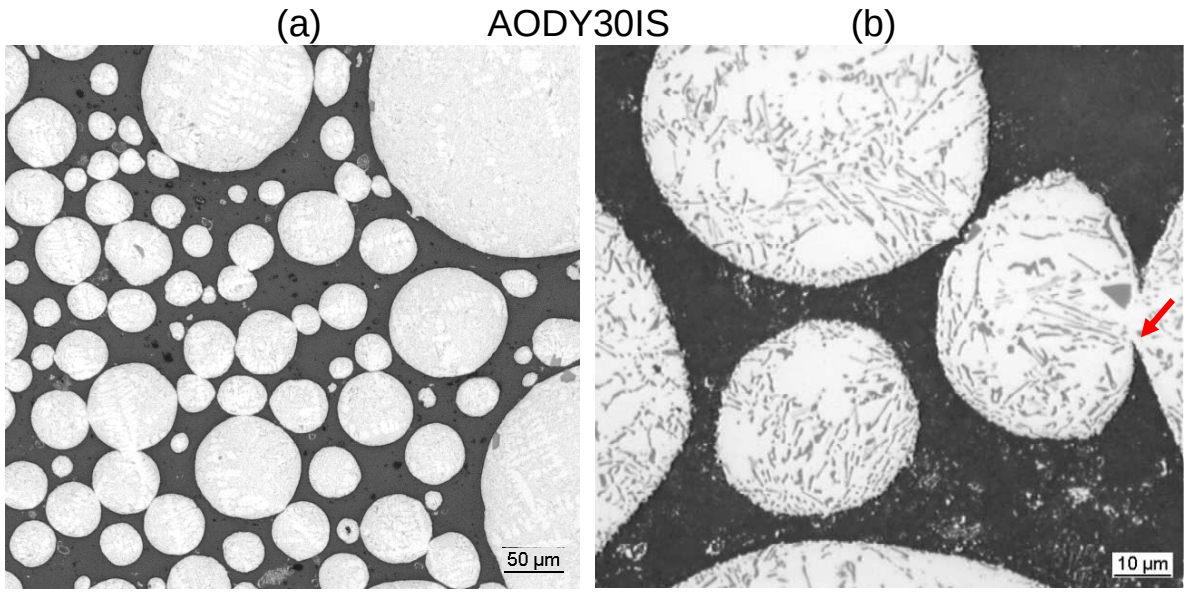

Figure 4.58 Optical micrographs AODY30IS type MMC.

The windows, one of which is marked in Figure 4.58 b), in foamed preforms were connecting paths between two single bubble-shaped cavities. The light phase inside the struts is the metal intruded into the sub-micron pores. Therefore a small portion of the preform porosity consisted of open cell pores in the struts. The Si phase in the alloy was marginally coarser than that in FATOIS, Figure 4.57 b), but significantly coarser than in the MMCs fabricated using PFA-formed pores in the preform shown in Figure 4.53.

4.8.8 Interfacial microstructure of MMC with alloy IS matrix

The interface between the unreinforced region on top of the MMC and the MMC itself was investigated in order to detect any oxide films originating from the alloy melt. These films might be prevented from entering the preform during infiltration as the preform inlets blocked the passing of solid particles into the body. This is the concept of metal filtration, where inclusions are collected at the surface of the ceramic.

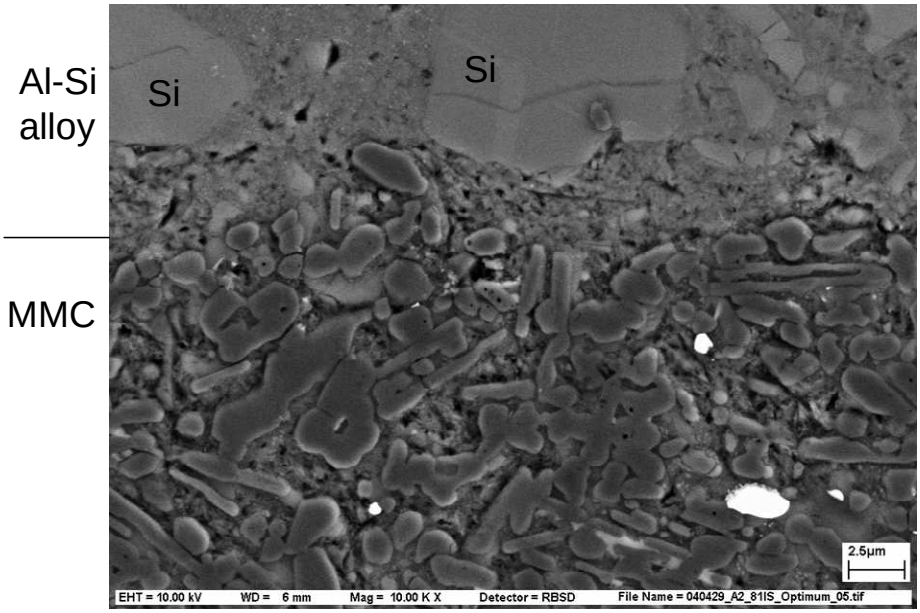

Figure 4.59 SEM micrograph (backscattered electron image) of the interface between MMC and unreinforced material on the top of the MMC type AOPC20IS.

The interface of the AOPC20IS MMC is presented in Figure 4.59. At the chosen magnification, there was no evidence of oxide film accumulation at the preform inlet. The silicon precipitates on top of the MMC exhibited some cracking. These cracks resulted from

shear stresses in this brittle phase caused by the thermal mismatch at the interface. A light phase with a high specific mass was visible in the MMC microstructure in Figure 4.59. As already detected in the Al_2O_3 substrates for the sessile drop test (Figure 4.9), the light phase was ZrO_2 which originated from debris of the milling vessel and balls worn during ceramic slurry preparation.

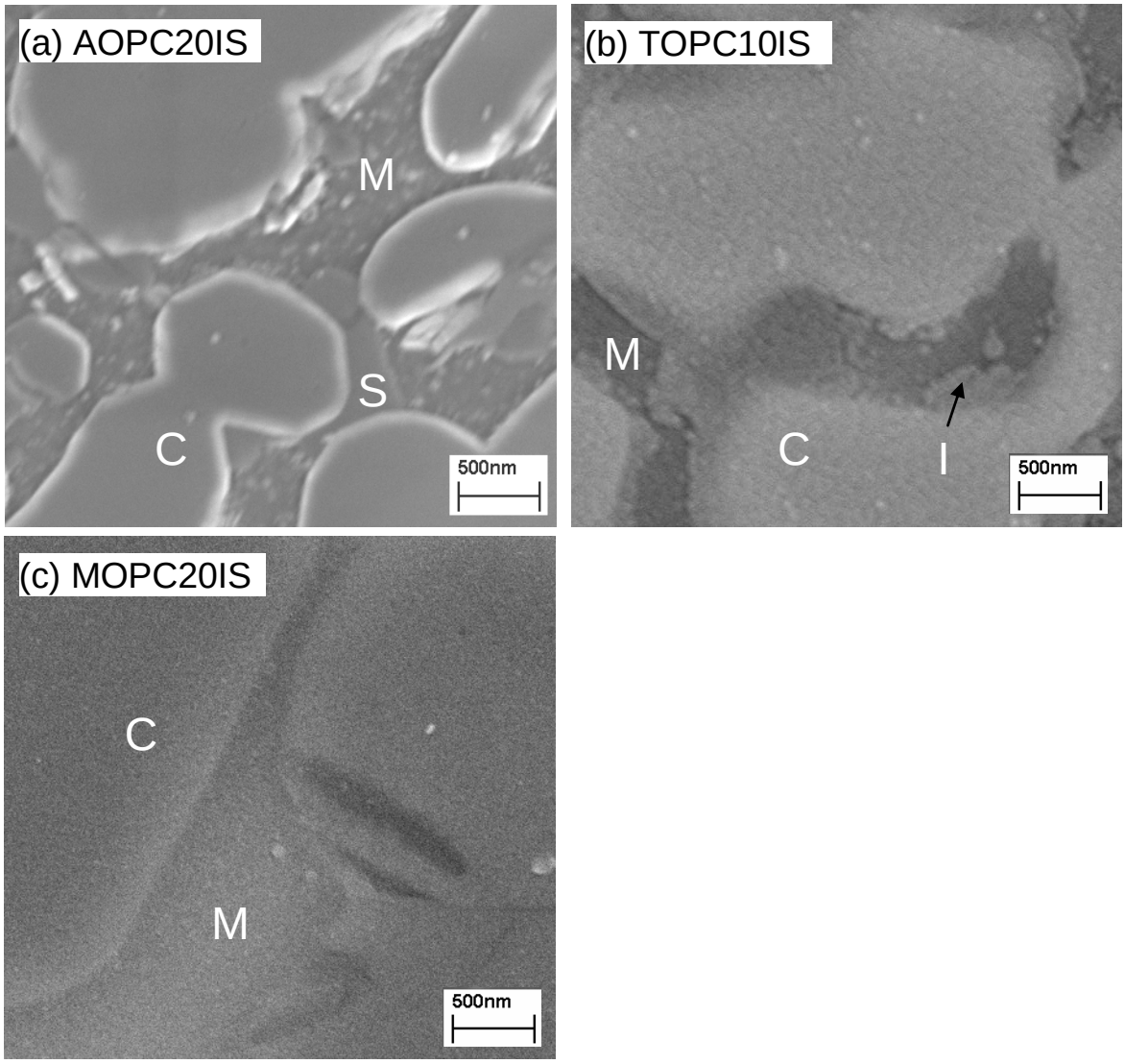

Figure 4.60 Backscattered electron micrographs of the metal-ceramic interfaces in the intragranular region of a) AOPC20IS b) TOPC10IS and c) MOPC20IS. Phase C, M and I: ceramic, metal alloy and interfacial phase, respectively.

No significant interfacial reactions were observed in the microstructures of the MMCs presented in the previous section. The thermodynamic calculations predicted reactions when Al is in contact with the reactive preforms containing TiO_2 or MgO. In order to detect

potential interfacial reactions, the microstructures close to the ceramic phases were investigated at high magnification using an SEM.

At the resolution limit of the SEM employed, Figure 4.60 a) and c) show that no reaction products were observed on the inner surfaces of the alumina and magnesia MMCs, AOPC20IS and MOPC20IS. In the matrix alloy (M) of AOPC20IS, silicon precipitates (S) were observed as well as some debris resulting from metallographic preparation. Due to the significant hardness differences between alumina and the infiltration alloy, metallographic preparation led to preferential removal of the metal and alumina debris being embedded into the matrix alloy, as shown in the micrograph of AOPC20IS in Figure 4.60 a). In contrast, magnesia is comparatively soft and Figure 4.60 c) shows that the polishing results were significantly improved, indicated by the lack of debris in the metal areas. An intensive effort to optimize the SEM image quality was not successful, leading to a `fuzzy´ appearance of the microstructure. No reaction layer phase could be detected at the interface of MOPC20IS.

The microstructure of the titania-reinforced MMC TOPC10IS is shown in Figure 4.60 b). The surface of the ceramic phase was covered with an interfacial layer with a thickness of 50 to 100 nm. The entrance to the bottle-neck shaped pore in the centre of the micrograph was entirely filled with the reaction product. As the micrograph was taken in the backscattered electron mode, the grey value of the interfacial phase indicates that its atomic mass was between that of the matrix alloy and titania.

4.8.9 Differential thermal analysis on MMCs with alloy IS matrix

In order to investigate whether the predicted reactions could occur in the MMC, thermal analysis was performed on the final MMC in the temperature range between 100 and 800°C. Under these conditions the infiltrated alloy would remelt. Figure 4.61 shows the differential temperatures between sample and reference over the temperature range applied. Endothermic

reactions in the MMC samples are indicated by positive peaks and negative peaks indicate exothermic reactions. The condition of equilibration of the system could not be fulfilled as a rather fast heating rate of 20 K/min was chosen. Therefore the SDTA investigations represented a comparative study between the different preform types only.

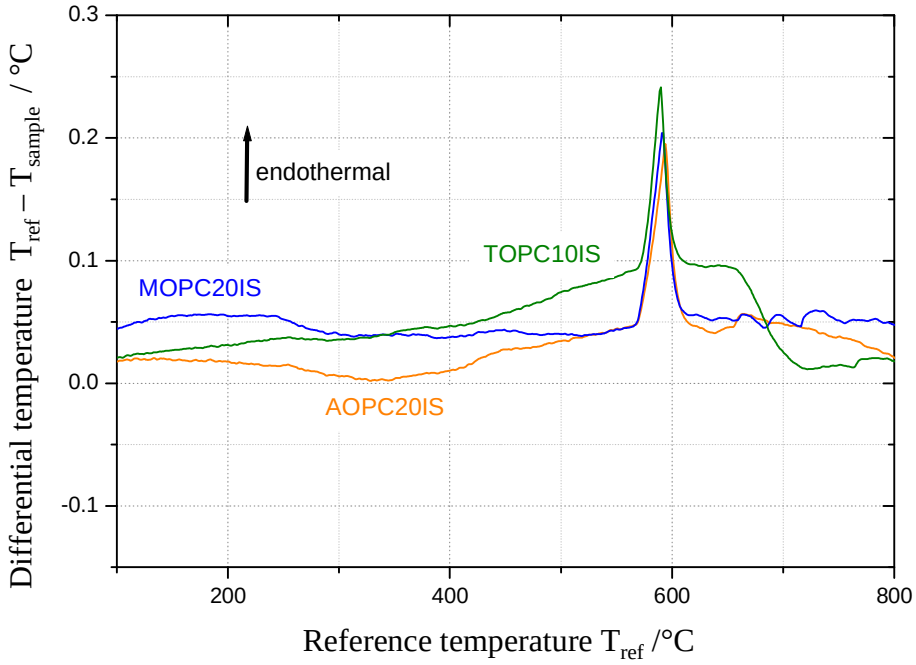

Figure 4.61 Differential thermal analysis on MMCs. Differential temperature as a function of reference temperature.

The curve of AOPC20IS MMC showed minor fluctuations in ΔT between 100°C and 575°C which were assumed to be within the range of the scatter of the measuring system. A sharp positive peak, indicating the endothermic melting of the alloy, occurred above 575°C.

The curve for MOPC20IS exhibited a marginal endothermic reaction between 100°C and 300°C, which was attributed to the decomposition of magnesium hydroxide on the surface of the sample. The hydroxide resulted from the sample preparation which was wet ground and dried prior to the SDTA analysis. The fusion peak of the non-reactive AOPC20IS was reproduced and at higher temperatures no significant trend was observable. After the fusion peak TOPC10IS showed a significant exothermic reaction starting at 650°C and finishing at 720°C. After that point, no significant reactions were indicated.

In order to determine the effect of the SDTA thermal cycle on the microstructure of the MMC, the micrographs of the MMC samples were investigated as shown in Figure 4.62 a) and b) and in Figures 4.63 a) and b). Prior to the test the samples were ground and therefore the droplet on the edge of the sample of AOPC20IS must be a result of an extrusion of the alloy during remelting (Figure 4.62 a). This behaviour was not observed in the reactive MMCs TOPC10IS and MOPC20IS. The needle-like shape of the Si phase in the alloy was similar to that in the microstructure taken prior to the SDTA cycle presented in Figure 4.53. The coarse precipitates were a result of the rather slow cooling rate of 20°C/min after the test run was finished.

Figure 4.63 a) shows that after the SDTA test, TOPC10IS had a significantly different microstructure compared to the initial MMC in Figure 4.55 a). A significant fraction of porosity (black) was formed which quantitative metallography showed to be 15%. Furthermore, the colour of the former alloy areas changed from white to a light greyish colour and the former ceramic grains were subdivided into greyish and brownish phases.

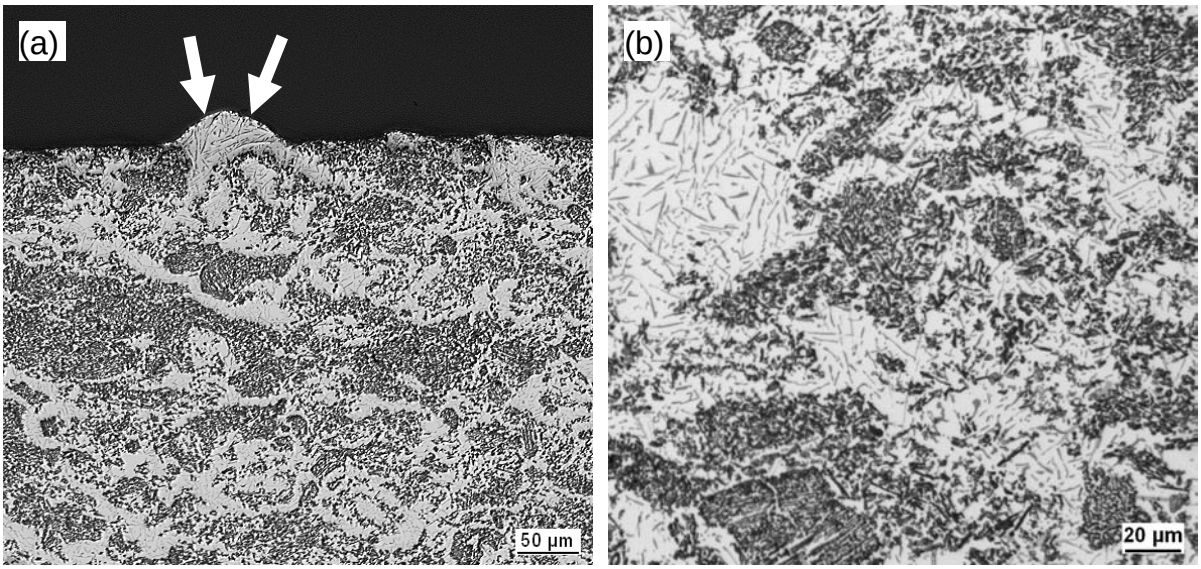

Figure 4.62 Microstructure of MMCs after thermal analysis. a) AOPC20IS overview near the edge and b) centre of the sample.

The microstructure after heat treatment of the AlSi-TiO_2-MMC shown in Figure 4.63 a) was similar to that resulting from the same preform infiltrated with the Al-Mg alloy IM. The investigations of the different phases are presented in 4.8.12.

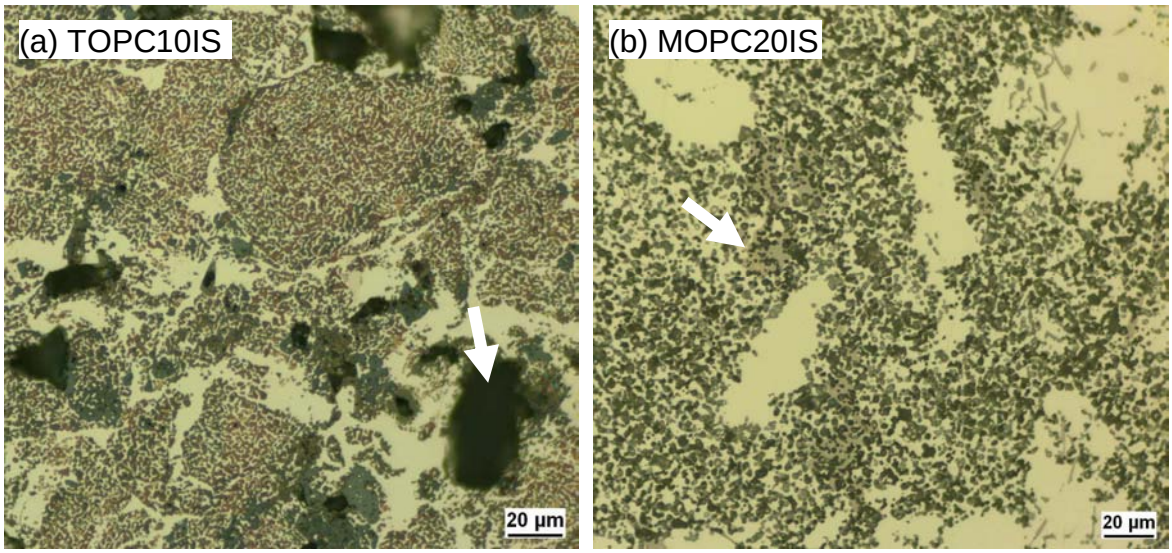

Figure 4.63 Microstructure of reactive MMCs after thermal analysis test. a) TOPC10IS and b) MOPC20IS.

In the micrograph of MOPC20IS in Figure 4.63 b), the amount of the Si phase in the intergranular coarse metal ligament areas was reduced significantly when compared with the micrograph prior to the SDTA cycle in Figure 4.55 c). The amount of the mid-grey phase in the intragranular region was increased. An EDX investigation confirmed the mid-grey phase to be pure Si from the alloy. Therefore, as already indicated by the differential thermal analysis, no reaction product was formed during the SDTA cycle of the MMC sample.

4.8.10 Infiltration behaviour with Al-Mg alloy IM

The infiltration alloy was changed from an Al-Si alloy (IS) to an Al-Mg alloy (IM) with an equivalent molar fraction of the main alloying element (Mg) as listed in Table 3.2. The influence of probable reactions on the infiltration behaviour of the reactive preforms TOPC10, MOPC20 and FATO was studied and the threshold pressure P_0 and the gradient of the infiltration curves were evaluated through linear regression.

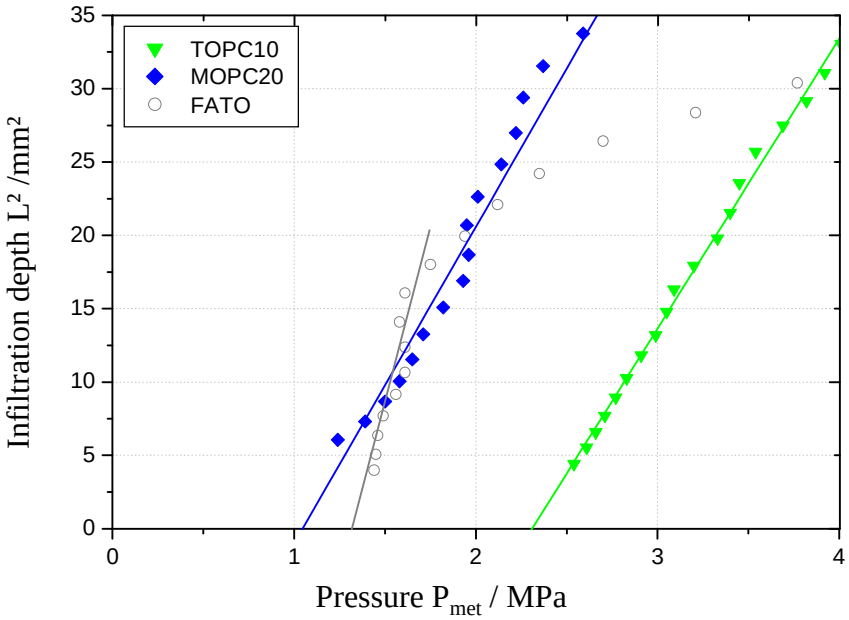

Figure 4.64 Square of infiltration depth as a function of the applied pressure infiltration with Al-Mg alloy IM. Linear regression in the range of 2 mm to 5 mm infiltration depth except FATO in the range of 2 mm to 4 mm.

In the same manner as presented in Figure 4.48 when infiltrating with the alloy IS, the square of the infiltration depth of the preforms is presented as a function of the applied pressure in Figure 4.64. Good linear fits were found for MOPC20IS and TOPC10IS. In contrast, the infiltration of FATO exhibited unsteady behaviour above an infiltration depth of 4 mm. Therefore the linear fit was limited to the infiltration depth below this point.

Table 4.6 Results of infiltration curve regression analysis when infiltrating with Al-Mg alloy IM. Gradient, a, and threshold pressure of infiltration, P_0.

	a **mm² / MPa**	**P_0 (at L^2=0)** **MPa**
TOPC10	19.77	2.31
MOPC20	21.58	1.05
FATO	50.92	1.35

Table 4.6 summarizes the threshold pressures P_0 for the three materials infiltrated. The gradient of the fitted line of TOPC10 was similar to that of MOPC20, whereas that of FATO was more than double.

4.8.11 Homogeneity of MMC infiltrated with alloy IM

The macrograph of the cross-section of the titania-reinforced MMC infiltrated with the Al-Si alloy (TOPC10IS) is compared to that infiltrated with an Al-Mg alloy (TOPC10IM) in Figure 4.65. The dark phase corresponds to the MMC and the light one to the unreinforced metal.

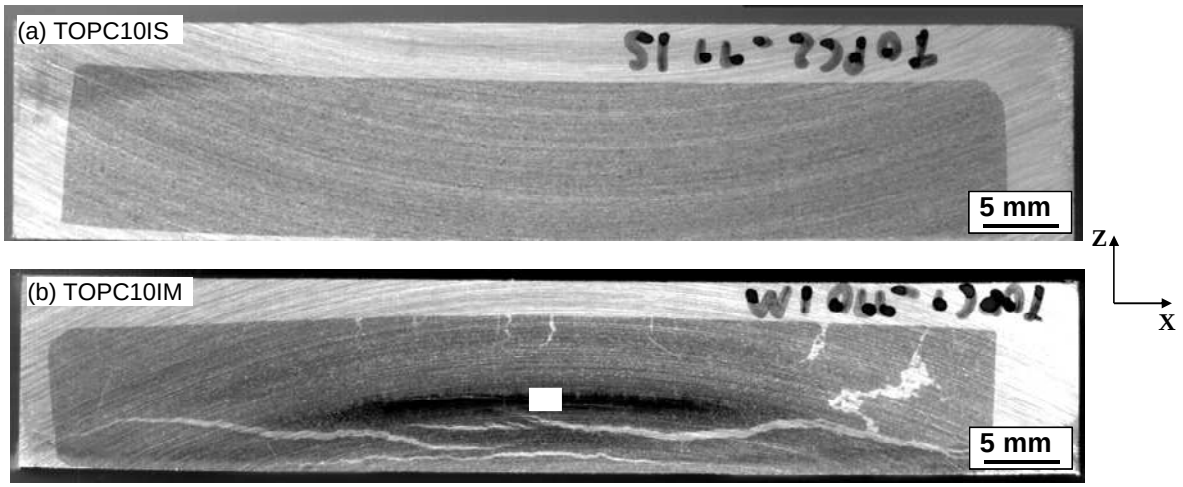

Figure 4.65 Cross section of titania MMCs infiltrated with Al-Si (TOPC10IS) and Al-Mg alloy (TOPC10IM). The rectangle in TOPC10IM shows the zone of detailed microstructural investigations.

When the preform was infiltrated with the Al-Si alloy (IS), the rectangular shape of the preform was reproduced in the MMC cross section, Figure 4.65 a). Under the same infiltration parameters, the Al-Mg alloy-infiltrated MMC exhibited large cracks filled with the matrix alloy. These cracks were located towards the bottom of the MMC along the x-axis, as shown in Figure 4.65 b). Further cracks occurred on top of the preform. A dark area was visible in the centre of the MMC where the characteristic macroscopic MMC colour changed to an optically different phase. A similar appearance was observed in the cross-section of the FATO hybrid preform infiltrated with the alloy IM. The microstructure in the dark area was investigated for both MMC types. For comparison, the microstructure of the MOPC20 preform infiltrated with the alloy IM was also investigated. Here the macroscopic structure appeared similar to that of the same preform type infiltrated with the alloy IS.

4.8.12 Microstructure of MMCs with Al-Mg alloy IM matrix

The microstructure in the central dark area of TOPC10IM of Figure 4.65 b) is presented in detail in Figure 4.66 a) and b). The microstructure changed significantly when compared with that of TOPC10IS shown in Figure 4.55 a). A minor fraction of the bright metal phase (IM) was left in the intergranular regions but it was predominantly replaced by a grey phase (I). The initial ceramic phase was replaced by a grey phase (G) and a brown phase (B).

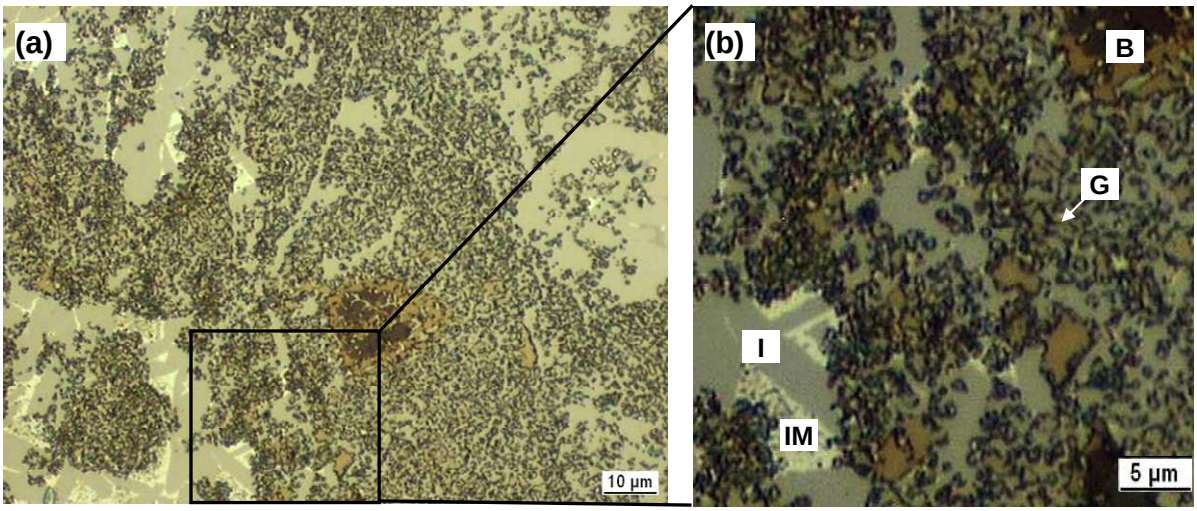

Figure 4.66 Optical micrograph of the dark areas marked in Figure 4.65 b). a) Overview and b) detail with designation of the different coloured phases.

The EDS analysis of the reacted MMC was performed in an area where residual matrix alloy IM was obvious. As shown in Figure 4.67, a spot analysis was carried out on the four optically different phases designated IM, I, G and B in Figure 4.66 b). The quantification of the spot analysis was limited to the main constituents, namely Mg, Al, Si, O and Ti, and the results are listed in Table 4.7.

The phase designated IM was confirmed to be the infiltration alloy IM, although this had different composition to the initial alloy see Table 3.2. The Mg mass content was reduced from 9.3% to 5.3% and that of Ti increased from 0.04% to 1.1%.

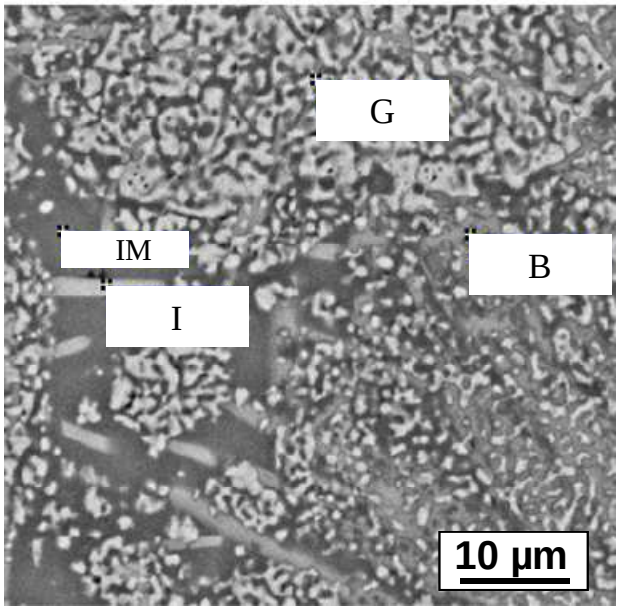

Figure 4.67 SEM micrograph of TOPC10IM in the reacted area and markers setting the location of the EDS spots IM, I, B and G.

The analysis at position I showed that the needle-shaped phase in Figure 4.66 consisted mainly of Al and Ti with minor fractions of Mg and Si. Based on the relative mass contents in Table 4.7, the molar ratio between Ti and Al was calculated to be 1:4. This indicates that this phase consisted of a titanium aluminide with minor fractions of Si and Mg. As predicted by the thermodynamic calculations and shown in the work of Beyer [53] the phase is $TiAl_3$ with traces of the main elements of the infiltration alloy Al, Mg and Si.

Table 4.7 Results of the EDS spot analysis performed on the phases shown in Figure 4.67.

	O	**Mg**	**Al**	**Si**	**Ti**
			mass-%		
IM	0.0	5.3	93.5	0.0	1.1
I	0.0	3.3	68.1	2.8	25.8
B	34.9	9.4	12.3	0.0	43.5
G	43.6	0.4	52.1	0.8	3.2

The EDS analysis at spot B in Figure 4.67 showed that the brown phase in Figure 4.66 b) consisted of predominantly Ti and O with minor fractions of Al and Mg. The molar ratio of the main phases was 1Ti : 2.4 O indicating a mixture of the initial reinforcement TiO_2 and a

minor fraction of suboxides with higher titanium contents, for example, TiO or Ti_2O_3. The Ti and Al concentrations in B may have been a result of the EDS spot size which was larger than the phase itself. Finally, the main elements in spot G were Al and O with traces of Mg and Si. The molar ratio of Al to O was 1 to 1.4 and therefore this phase was Al_2O_3 with traces of Mg and Si.

The EDS analysis and the optical microscope results of TOPC10IM enabled interpretation of the microstructure of the TOPC10IS MMC after thermal analysis, Figure 4.63. Based on their colours and shapes the mid-grey, brown and the light grey phases in the initial infiltration alloy areas can be attributed to Al_2O_3, TiO_2 in combination with titanium suboxides, and $TiAl_3$, respectively. During the SDTA cycle, TOPC10IS was kept at ambient pressure and therefore reactions in the MMC resulted in open porosity as no metal melt was intruded in the pores. In contrast, during squeeze casting, the porosity resulting from volume changes due to reaction of the preform material with the infiltration alloy was filled with molten metal, indicated by the light metal alloy shown in the MMC areas in Figure 4.66 a). Similarly the cracks were filled with metal.

Reactions between the metal and the ceramics led to changes in the microstructure of FATOIM, as shown in Figure 4.68, which should be compared with FATOIS infiltrated with alloy IS, Figure 4.57 b). A needle-shaped grey phase grew from the reinforcement into the alloy and EDS analysis confirmed it to be $TiAl_3$. The concentration of magnesium in the alloy was reduced from 9.3 to 7.5 %. In contrast to TOPC10IM, Al_2O_3 and titanium-suboxides could not be detected as distinctive phases in the ceramic-rich region of the MMC, which may be a result of the initial sub-micron scale of the initial titanium particles. The Saffil™-fibre reinforcement was not affected.

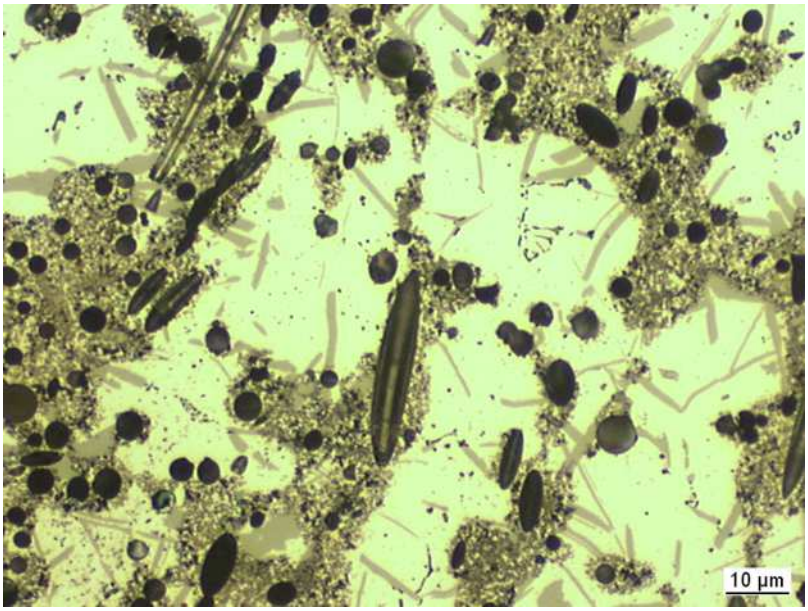

Figure 4.68 Optical micrograph taken from the centre of FATOIM.

There were no major differences in the ceramic phase when the MgO preform infiltrated with alloy IM, Figure 4.69, was compared to infiltration with IS (Figure 4.55 b). Therefore reactions between the reinforcement and the alloy were not evident. Light grey precipitates were found in the alloy areas of the MMC similar to those visible in the unreinforced alloy IM, Figure 4.44 a). The binary phase diagram in Figure 2.2 would suggest the precipitates in the alloy IM to be the intermetallic Al_3Mg_2.

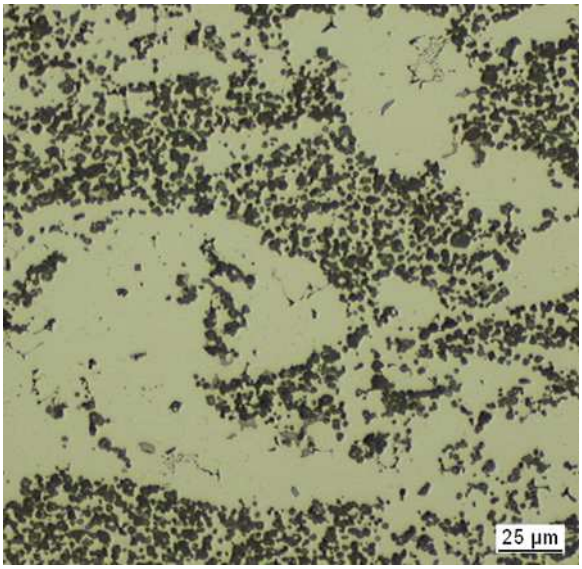

Figure 4.69 Optical micrograph of magnesia-reinforced MMC infiltrated with the aluminium-magnesium alloy IM (MOPC20IM).

4.9. High pressure die casting infiltration

As well as squeeze cast infiltration, some preforms were infiltrated using high pressure die casting. Two different infiltration modes were used which were characterised by significantly different metal flow velocities at the ingate: the indirect squeeze casting (ISQC) and the high pressure die casting (HPDC) mode. For each mode, four velocities were selected using a natural logarithmic velocity graduation shown in Table 3.8. The resulting MMCs were characterised in terms of their homogeneity and the relative compression of the preforms.

4.9.1 Homogeneity of MMC

The homogeneity of the MMCs was characterised using 3D X-ray computed tomography. In the resulting virtual cuts, the light areas were the MMC, the grey areas the non-reinforced metal alloy and the black areas were either porosity or the atmosphere surrounding the sample. Prior to the 3D analysis, approximately 2 mm were milled off the castings along the y-axis until the surface of the MMC was reached. As a result, no alloy coverage is visible on top of the MMC in the XZ-plane in the virtual cuts. Each figure shows the virtual cuts of the central layer in the MMC in all three cartesian coordinates, as defined in Figure 3.11.

The virtual cut in Figure 4.70 shows the internal structure of the AODY30 preform infiltrated in the ISQC mode using a velocity v_0 of 0.72 m/s. The parameter v_0 is defined by Equation 24. In each plane, significant fractions of porosity and multiple cracking were detected in the MMC. There was also porosity in the unreinforced alloy on top of the MMC.

Examination of the X-Y plane reveals the porosity in the MMC was predominantly concentrated in a rectangular area 6 mm from the edges of the preform. The porosity was subdivided into round pores with a diameter of up to 1.5 mm and pore agglomerations exhibiting a cellular arrangement. The cracking of the preform was most obvious in this plane.

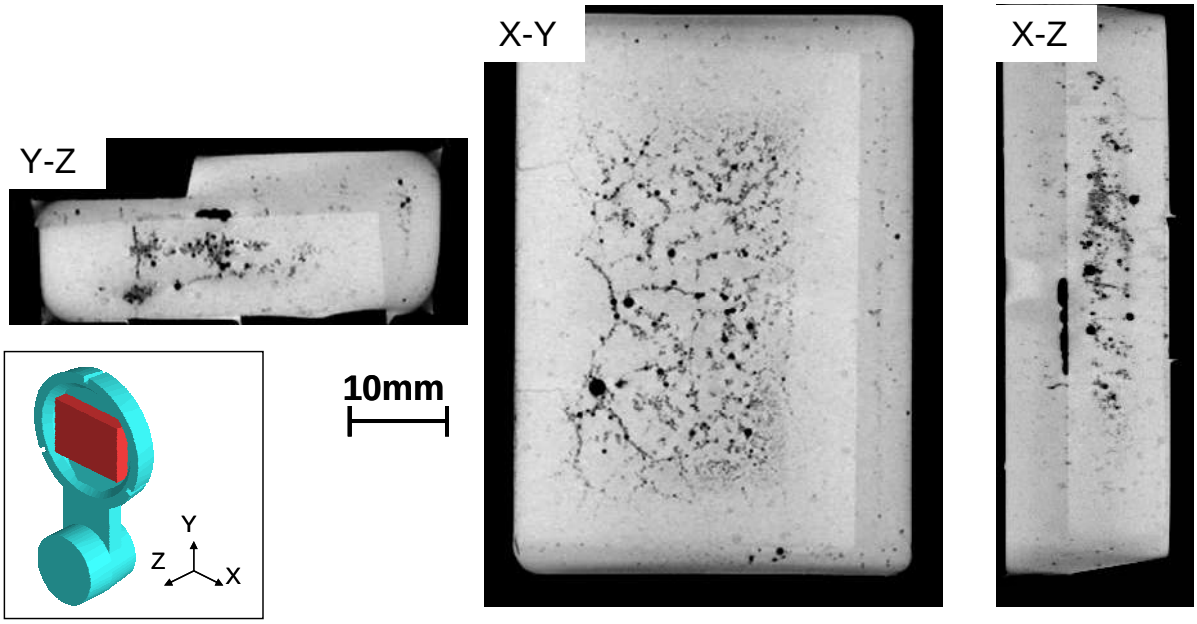

Figure 4.70 Virtual cuts through the central layer of the Y-Z, X-Y and X-Z planes of AODY30IS infiltrated in the ISQC20 mode at v_0 = 0.72 m/s.

When comparing the Y-Z plane view of AODY30IS (Figure 4.70) with that of AOPC20IS (Figure 4.71) the deformation of the preform as a result of the infiltration process is apparent. The preform before infiltration had an rectangular cross-sectional shape which was preserved during infiltration of AODY30IS. Here a maximum compression, assessed as the reduction of the cross-sectional area in the X-Z plane, was 3% compared to 27% in AOPC20IS.

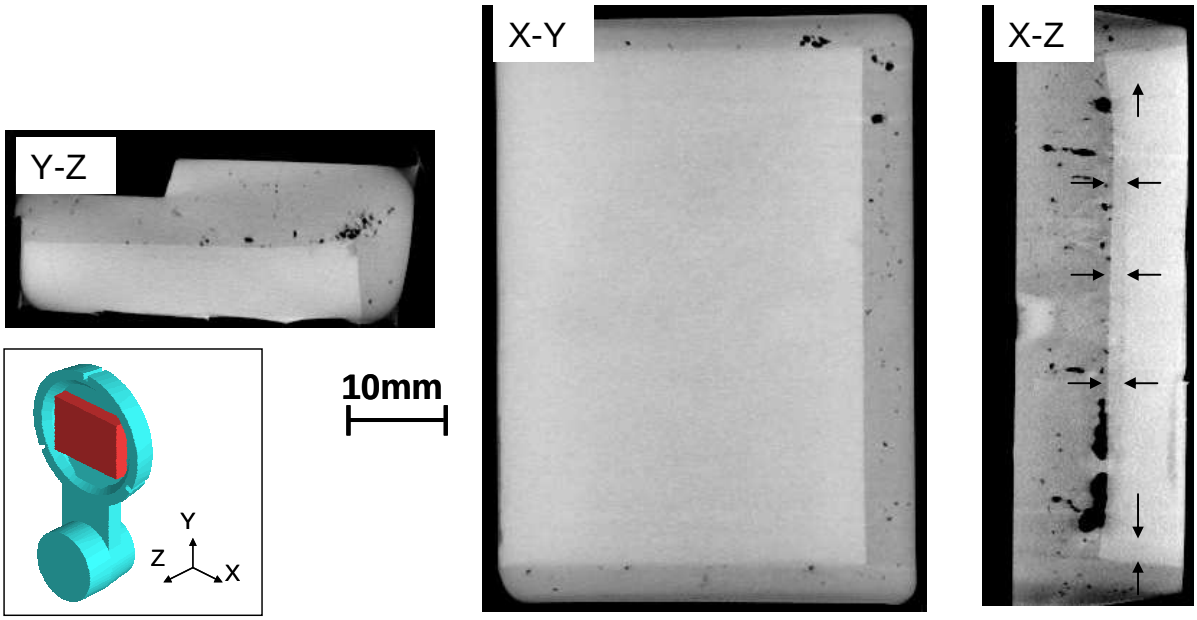

Figure 4.71 Virtual cuts through the central layer of the Y-Z, X-Y and X-Z plane of AOPC20IS infiltrated in the ISQC20 mode at v_0 = 0.72 m/s.

In the Y-Z plane section in Figure 4.71 there was an increased fraction of porosity in the pure infiltration alloy on top of the MMC compared to that in AODY30IS in Figure 4.70 and it was mainly concentrated on and close to the surface of the MMC. The porosity originated from shrinkage of the metal due to reduced metal flow during feeding after solidification started. The voxel resolution of the 3D-CT was 64 µm and so finer porosity could not be detected by this method. The MMC appeared uniform at this resolution.

Brightness was reduced in the outer volumes of the MMC since this material absorbed less X-ray radiation than the inner volumes. This layer is marked in the X-Z plane view in Figure 4.71. The depth of this layer ranged between 2 mm and 3 mm in the z-and the y-directions respectively. These layers are of different density and were found in all MMCs. They have been compressed by more than 15%.

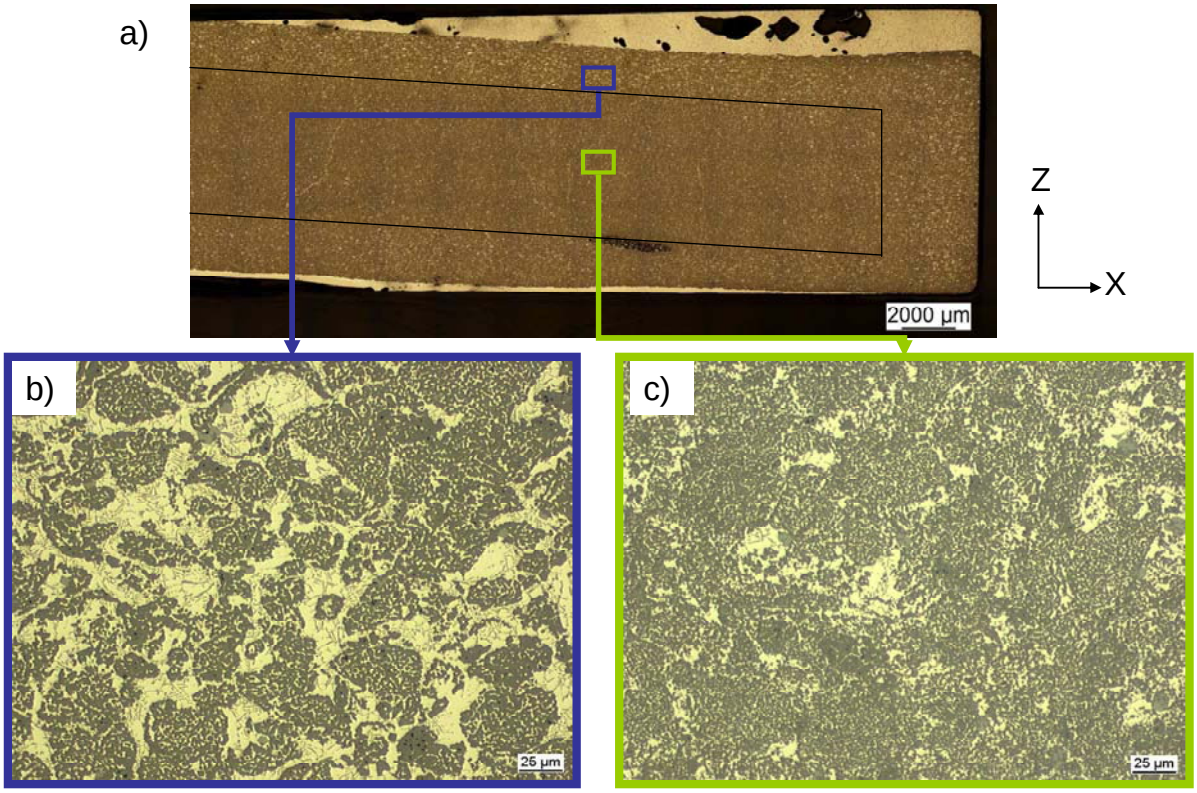

Figure 4.72 Micrographs of TOPC10IS infiltrated in ISQC at 0.72 m/s in the X-Z plane. a) Overview with markers defining the position of the higher magnification micrographs b) and c). The lines in a) mark roughly the borderline between lighter and darker MMC areas.

In order to determine the effects of this inhomogeneity on the microstructure, a titania-based TOPC10IS was investigated using metallography. Figure 4.72 shows TOPC10IS infiltrated in the ISQC mode at a velocity of 0.72 m/s. An overview of one half is shown, as they are axisymmetric. Due to the high velocity infiltration the preform was distorted.

In Figure 4.72 a) the border between the lighter and darker regions is indicated by the line. It highlights that the thickness of the lighter region varied in between the Z- and the X-direction from about 2.1 mm to 3.8 mm respectively. Figure 4.72 b) shows that the lighter appearance of the outer areas was due to the higher fraction of metal than in the inner area shown in Figure 4.72 c). This was mainly attributed to the relatively fewer larger-scale metal ligaments in the centre. The loss of intergranular metal ligaments is attributed to preform compression at the expense of the intergranular porosity in the preform during infiltration.

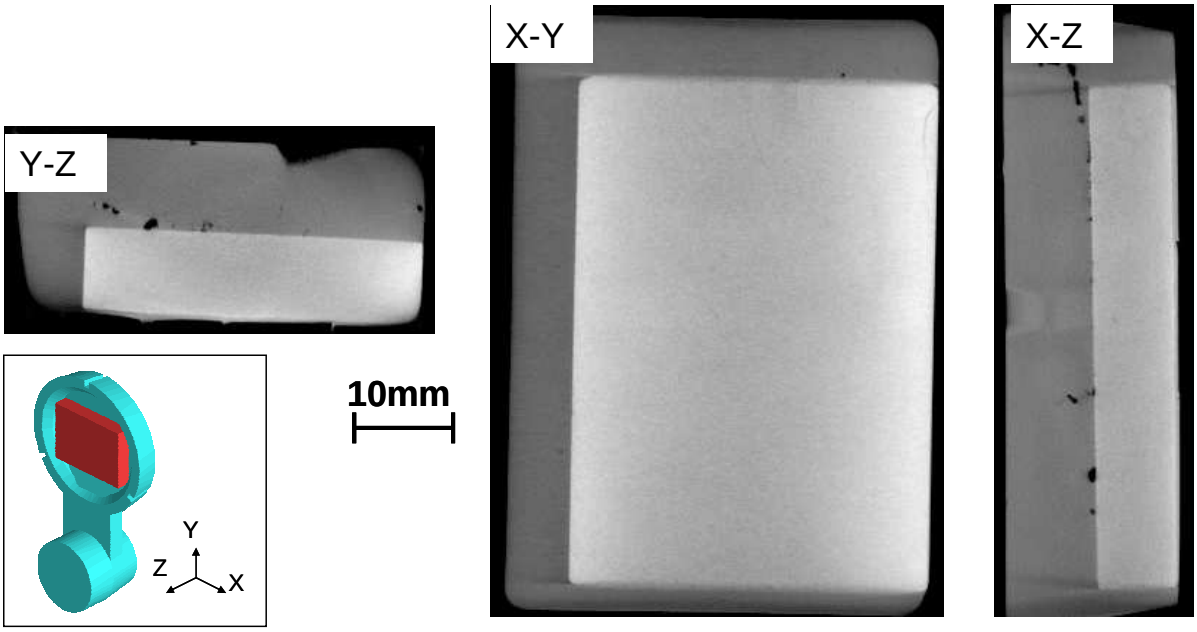

Figure 4.73 Virtual cuts through the central layer of the Y-Z, X-Y and X-Z plane of TOPC10IS infiltrated in the ISQC10 mode at v_0 = 0.36 m/s.

The only preform type with PFA formed pores which showed an intermediate decrease in compression was TOPC10IS (0.36 m/s - ISQC mode). Its virtual cut is shown in Figure 4.73. No compression and no porosity were visible inside the MMC.

4.9.2 Compression of preforms

The constant flux infiltration, where the liquid metal was driven by means of a plunger with constant velocity under pressure into the porous body, is subdivided into three modes: direct squeeze casting (DSQC), indirect squeeze casting (ISQC) and high pressure die casting infiltration (HPDC). The evaluation of the compression of the preforms of all constant flux infiltration modes is summarized in Table 4.8 and displayed in Figure 4.74 for the non-reactive Al_2O_3 preforms and in Figure 4.75 for the MgO or the TiO_2-containing preforms. The relative compression of the preform was evaluated using the parameter c_{pr}, which was defined as the relative reduction in the preform cross-sectional area in the x-z-plane as a result of the infiltration. Relatively slow infiltration at a velocity, v_0, of 0.018 m/s was achieved when using DSQC. The ISQC and the HPDC processes were performed on a high pressure die casting machine at significantly higher velocities v_0 in the range of 0.07 m/s to 1.44 m/s. The ISQC mode differed from the HPDC mode mainly in the geometry of the ingate area which influenced the ingate velocity.

Three of the four v_0 in ISQC and HPDC modes were equal. The two modes were used in order to determine the influence of the metal melt history, e.g. in terms of turbulence, on the compression behaviour of the preforms. As described in section 2.5.3, the minimum velocity, v_0, in HPDC and the maximum in ISQC represented the extremes which could be realized with the current high pressure die casting setup. Due to the unavailability of the MOPC20 and AODY30 preforms at the time of infiltration, these were not infiltrated in the ISQC or in the HPDC mode at a plunger velocity of 0.4 m/s (HPDC04), respectively. The designation system of the infiltration modes and velocities is listed in Table 3.8.

The mean compressions of the preforms are listed in Table 4.8. The scatter of each mean value is represented by the error bars in Figure 4.74 and Figure 4.75. In the DSQC mode, the

deviations were 0.01 whereas larger scatter was observed for ISQC and HPDC modes. Here the minimum scatter was 0.02 for the preforms exhibiting low compression such as AODY30, and 0.05 for the preforms with largest compression, which was that of the FATO hybrids at an infiltration velocity of 0.36 m/s in the HPDC mode. The preform geometry remained most consistent in DSQC, with compressions ranging from 0.01 to 0.04 for AODY30 and FATO preforms respectively. Taking into account the scatter, the preforms fabricated with a pore forming additive had similar compressions expressed by c_{pr} values of 0.02 for AOPC20 and MOPC20 to 0.03 for TOPC10 and AGPC15.

Table 4.8 Evaluated mean relative compression c_{pr} of preforms as a result of infiltration in DSQC, ISQC and HPDC modes and effect of the infiltration velocity.

	DSQC	**ISQC**				**HPDC**			
		05	10	20	40	04	09	18	36
Superficial velocity v_o (m/s)	0.018	0.18	0.36	0.72	1.44	0.07	0.18	0.36	0.72
	compression c_{pr} ()								
AOPC20IS	0.02	0.21	0.22	0.26	0.33	0.07	0.18	0.26	0.28
AGPC15IS	0.03	0.10	0.09	0.17	0.23	0.05	0.10	0.11	0.14
TOPC10IS	0.03	0.07	0.04	0.15	0.14	0.14	0.22	0.22	0.23
MOPC20IS	0.02	n.a.				0.04	0.11	0.14	0.17
FATOIS	0.04	0.12	0.17	0.23	0.29	0.08	0.31	0.40	0.39
AODY30IS	0.01	0.03	0.03	0.03	0.03	n.a.	0.05	0.05	0.05

In general, higher c_{pr} were obtained in ISQC than in DSQC and HPDC infiltration. The only exception was AODY30 which exhibited the lowest c_{pr} of 0.03, combined with no significant influence of infiltration velocity. This behaviour was attributed to the structure of the preform with strong, predominantly dense, sintered struts and good permeability. Apart from a discontinuity in TOPC10IS between 0.18 and 0.36 m/s in ISQC, all preforms showed a steady increase or constant compression with increasing infiltration velocity. At the maximum velocity of 1.44 m/s, AOPC20 and FATO showed maximum c_{pr} of 0.33 and 0.29 respectively.

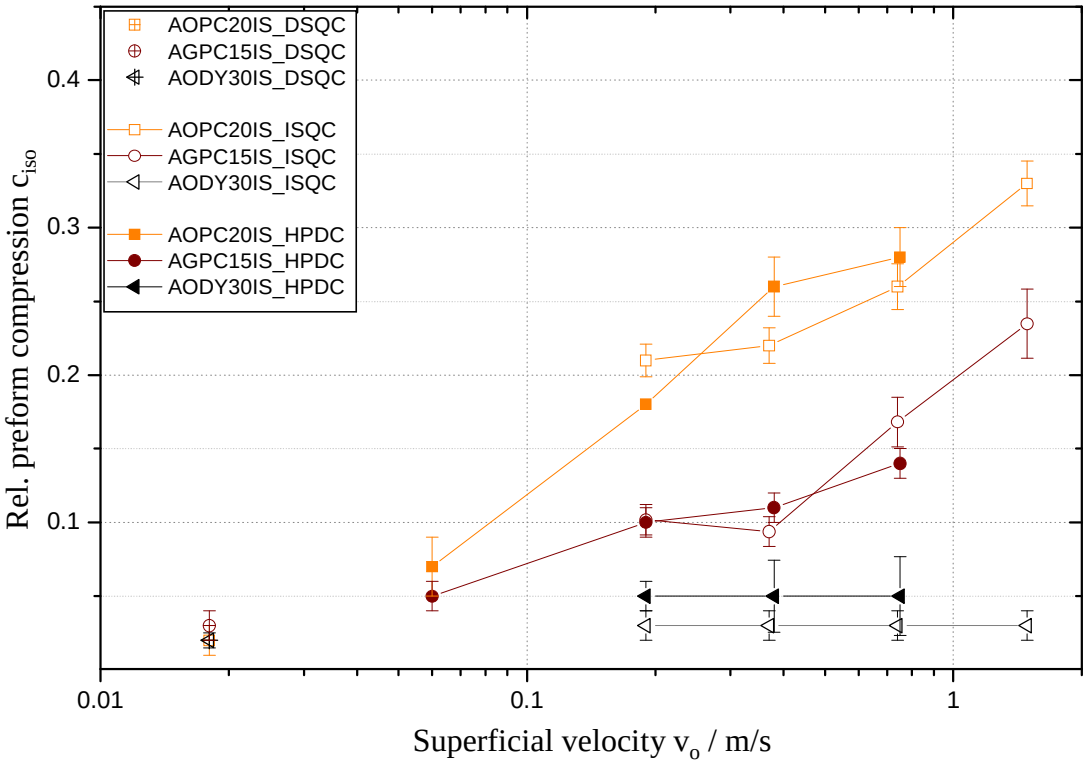

Figure 4.74 Compression of alumina preforms as a function of superficial velocity in the DSQC, ISQC and HPDC infiltration modes.

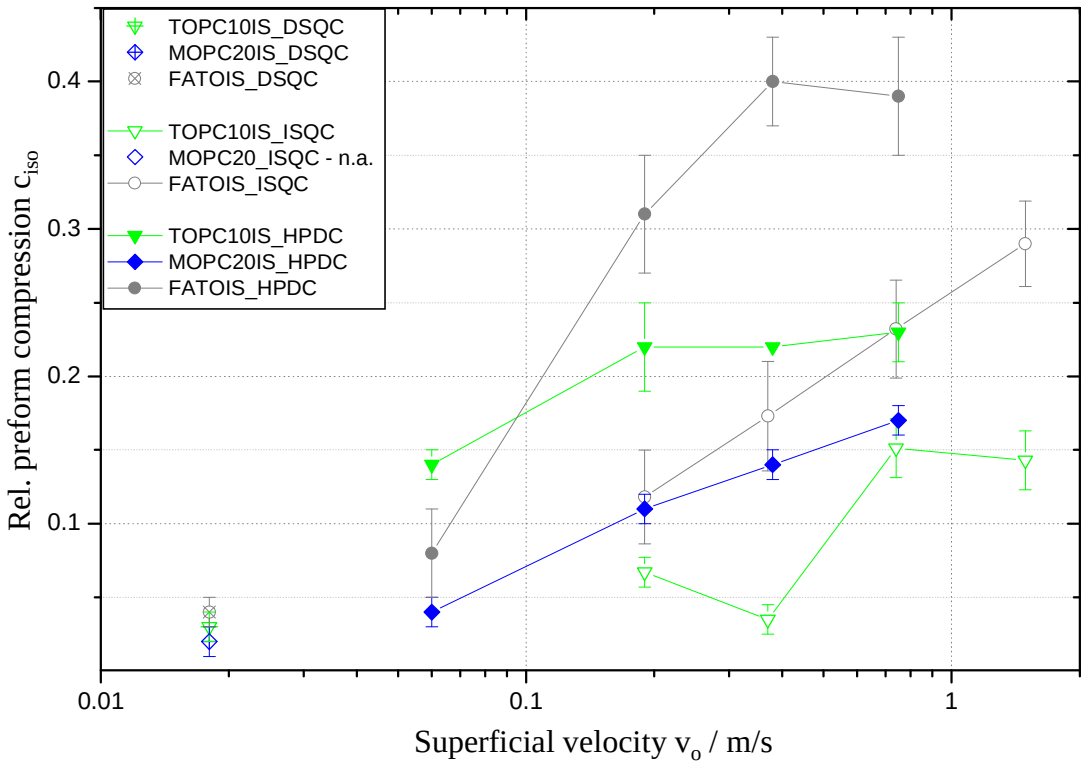

Figure 4.75 Compression of titania and magnesia-containing preforms as a function of superficial velocity. MOPC20 was not used in the ISQC mode.

There were minor differences in the compression of the Al_2O_3 preforms infiltrated in ISQC compared to those infiltrated in HPDC at the three equivalent infiltration velocities (0.18, 0.36 and 0.72 m/s). Marginally higher compressions were found in the HPDC mode, although the mean values lay in the scatter band of the compressions of ISQC. In contrast, the compression of the reactive preforms between the infiltration modes was different, as shown in Figure 4.75. For example, the FATO preform showed significantly different compressions in the three overlapping velocities of ISQC and HPDC. The compression in HPDC was more than double that in ISQC at given velocity.

A similar trend was visible with the TOPC10 preforms. In the ISQC mode, compressions of 0.04 to 0.14 were found, compared to 0.22 to 0.23 in the HPDC mode. The sudden drop to a low compression of 0.04 at a velocity 0.36 m/s in the ISQC mode did not occur in the HPDC mode. As aforementioned, MOPC20 preforms were only infiltrated in DSQC and HPDC. In the HPDC mode, this preform exhibited the lowest compression of all preforms fabricated using a pore forming agent.

4.10. MMC properties

The mechanical and the tribological properties of the MMCs with an Al-Si alloy matrix were assessed and compared to the properties of the pure alloy IS.

4.10.1 Influence of inhomogeneities on bending strength

The influence of inhomogeneities on the 4-point bending strength was investigated by comparing the local bending strength along the x-axis of MMCs produced with the standard infiltration tool with those produced using a copper chill insert in the bottom punch. The bending strength was determined as described in 3.5.5. Each data point in Figure 4.76 is the bending strength of a single bend test bar at the defined x-position. Both curves in Figure 4.76 showed a decrease in bending strength in the centre of the MMC but the extent of this

decrease depended on the tooling used. The MMC produced with an all-steel plunger exhibited a steep decrease in strength from 420 MPa at the lower x-axis to 305 MPa towards the centre position. In contrast, the strength did not fall below 375 MPa in the sample produced with the Cu insert on the bottom punch.

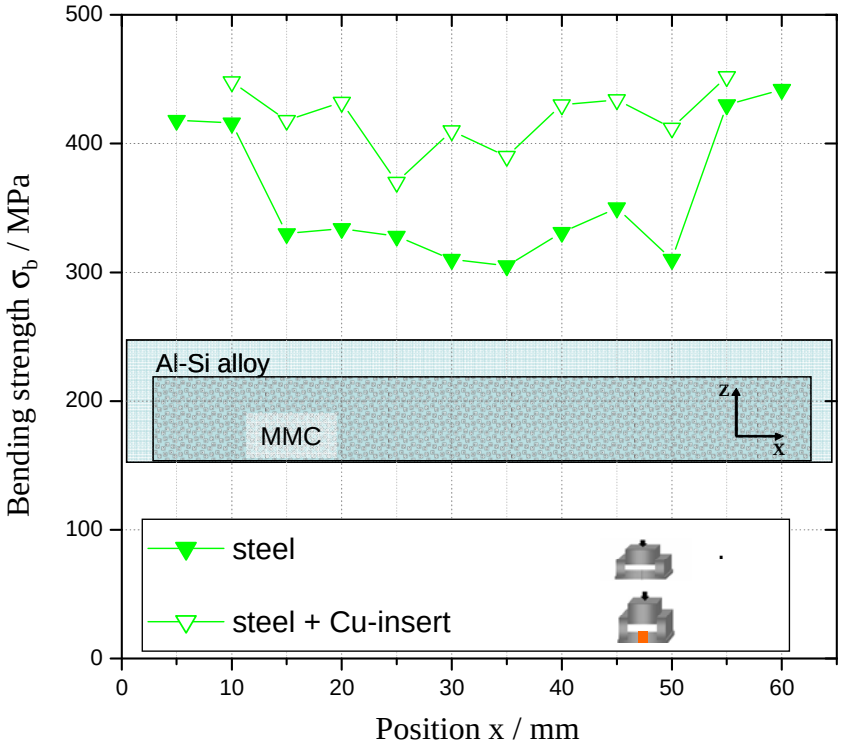

Figure 4.76 Bending strength along the x-axis of the TOPC10IS MMC with bottom plunger made of steel or steel with a central chill.

The cross-section of a TOPC10 preform infiltrated in a die with a steel bottom punch shown in Figure 4.77 a) shows that the porosity in the MMC was concentrated towards the centre in the x-direction and about 2.5 mm from the top of the preform in the z-direction. In the detailed view in Figure 4.77 b), the relative pore fraction was assessed to be 8.2% using image analysis. The predominant fraction of the porosity was interconnected with a maximum dimension of 250 µm. Therefore, it represented the coarse porosity of the preform whereas the fine pores between the particles of the preform were filled with metal.

In order to exclude the influence of porosity on the properties, the following results were taken from MMCs infiltrated using a bottom plunger with a central Cu chill. Furthermore, the

resulting MMCs were checked using non-destructive computed tomography (CT) and only those with negligible porosity were tested.

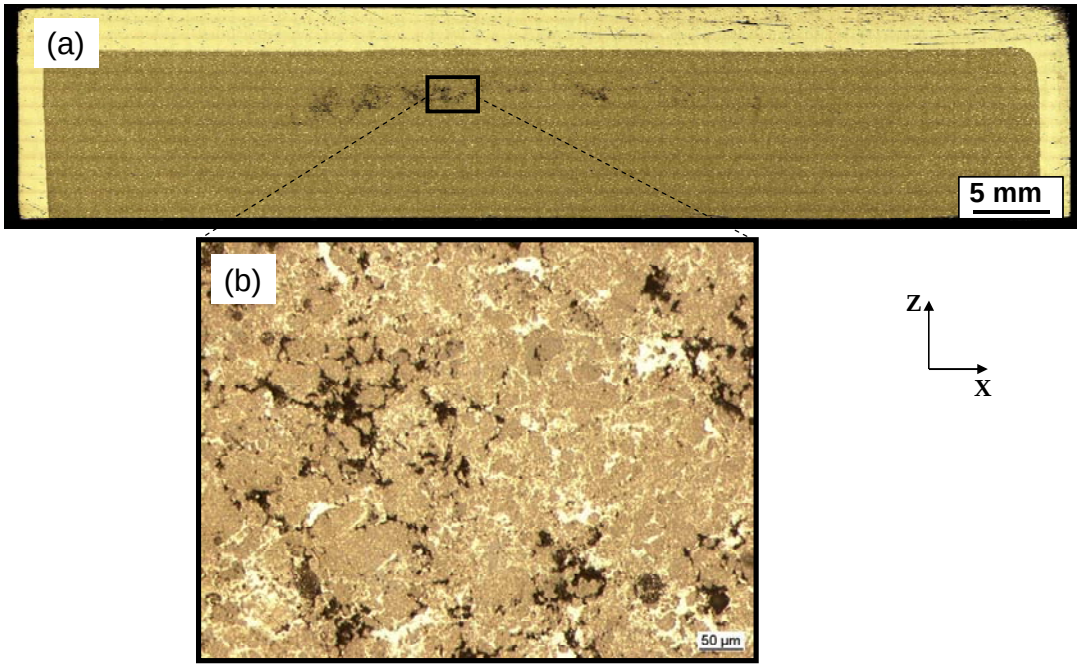

Figure 4.77 TOPC10IS infiltrated in a tool with a bottom plunger made of steel without chill: a) Overview macrograph. Light phase: alloy; darker phase: MMC. b) Detail view of the porous region.

4.10.2 Influence of reinforcement type on strength and elastic modulus

The bending strengths of the MMCs were compared with that of the pure alloy IS. The stress-deflection curves of IS and the AOPC20IS, are presented in Figure 4.78. The pure alloy IS exhibited a linear behaviour up to a bending stress of 110 MPa which represents the change from elastic to plastic deformation. The test was finished at a deflection of 1300 µm, the latter being the maximum deflection possible in the test which was designed for brittle materials. In the stress-deflection curve presented in Figure 4.78 the maximum deflection corresponded to a stress of 230 MPa.

In contrast to IS, the elastic portion of the curve for the AOPC20IS MMC was significantly steeper and was linear up to a stress of 130 MPa. Subsequently, the curve developed a steadily decreasing gradient up to the stress at fracture of 430 MPa, which corresponded to a deflection of 450 µm.

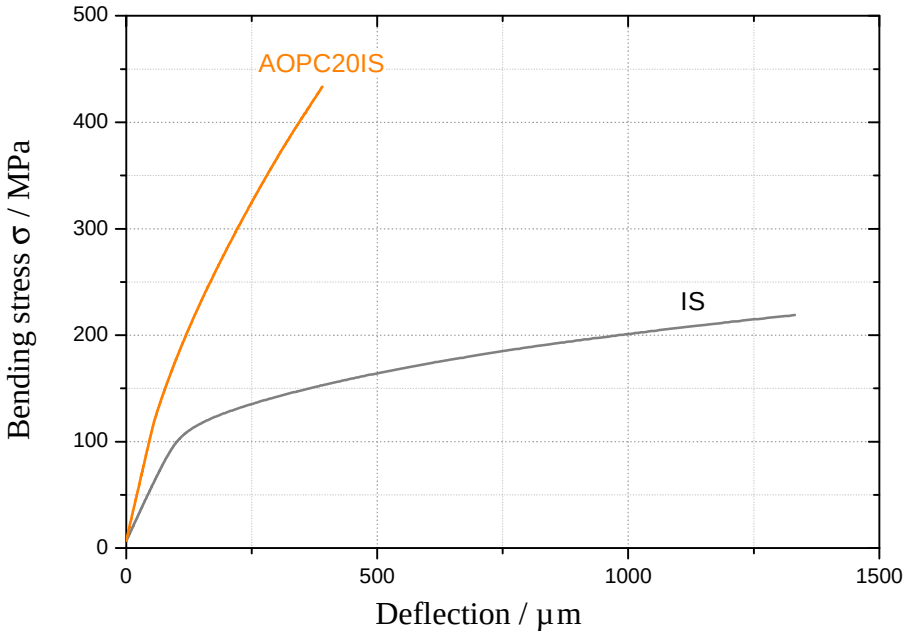

Figure 4.78 Comparison of bending stress - deflection curves of the pure alloy (IS) and the MMC (AOPC20IS).

As already indicated by the profile of the stress-deflection curves in Figure 4.78, the elastic moduli E_{dyn} of the MMCs were significantly higher than the value of 69 GPa for IS which is presented in Figure 4.79 a). The E_{dyn} values of the MMCs fabricated with PFA varied between 135 GPa for TOPC10IS and 148 GPa for AGPC15IS. In contrast, the MMCs fabricated with purchased preforms, AODY30IS and FATOIS, showed lower moduli of 119 GPa and 105 GPa, respectively. These values were still significantly higher than that of IS.

The characteristic stress σ_0 was based on the results of a minimum of 24 test bars. The σ_0 values in combination with the corresponding Weibull moduli are presented in Figure 4.79 b). They were calculated using Equation 45 presented in section 3.5.5. As aforementioned, the IS samples did not break at the maximum deflection and this deflection was constant. Therefore the calculated σ_0 value of IS does not represent the characteristic stress at fracture and it is higher than the value of 241 MPa. In contrast, as there was a deflection limit which led to smoothing of the maximum value, with 88 the m value is overestimated and not representative for an comparative study which was focussed in the present work.

AODY30IS showed the lowest σ_0 value of all materials (58 MPa). It was attributed to the coarse ceramic structure which fractured without influence of the metal phase. The hybridic reinforced FATOIS showed the lowest m value of 6.

Apart from AODY30IS, all MMCs showed higher strength than the pure alloy IS. The alumina-reinforced MMCs, AOPC20IS and AGPC15IS, showed the highest bending strengths of 443 MPa and 456 MPa respectively. The Weibull moduli of both were around 30 combined with around 80% higher strength compared to the Al-Si alloy. The MMCs reinforced with magnesia (MOPC20IS), titania (TOPC10IS) and the hybrid reinforced MMC (FATOIS) showed bending strength values in the range of 345 to 380 MPa which were about 80 to 100 MPa lower than that of the alumina-reinforced MMCs. The Weibull modulus of 6 for FATOIS was the lowest of all MMCs investigated.

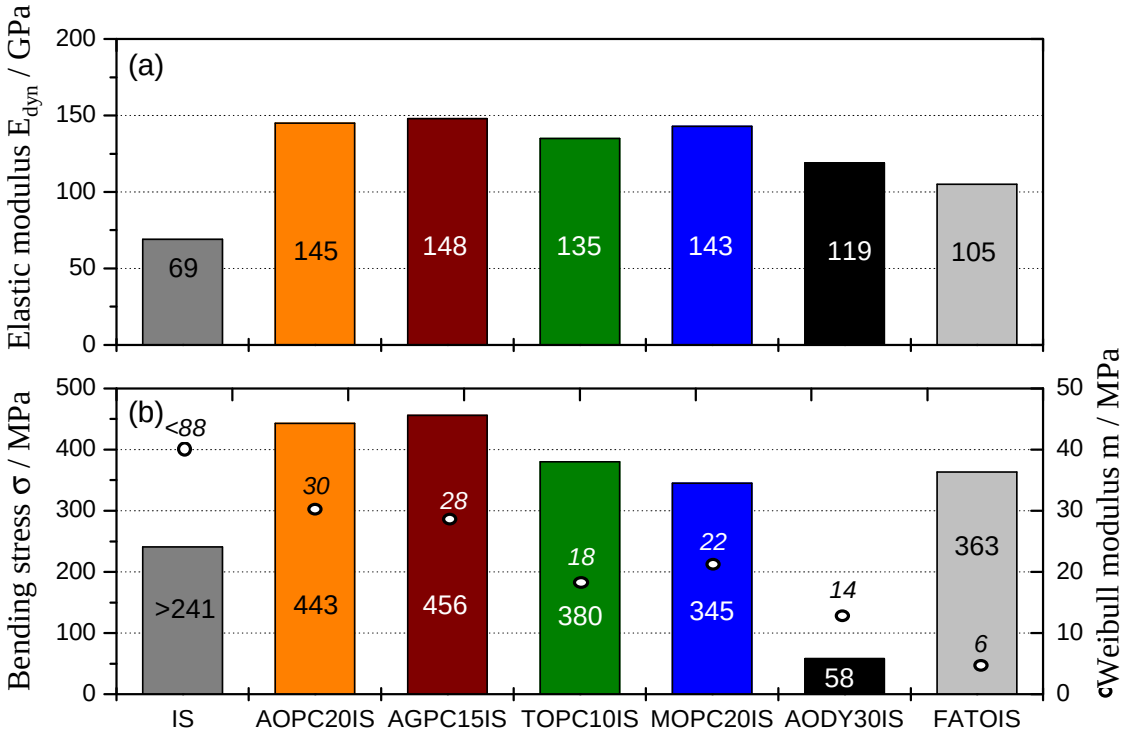

Figure 4.79 Mechanical properties of unreinforced Al-Si alloy IS and the MMCs: a) elastic modulus b) bending strength and Weibull moduli m (circles).

4.10.3 Influence of reinforcement type on fracture toughness

The fracture toughness of the MMCs was measured in bending using beam-shaped samples with a V-notch as described in 3.5.5. The mean fracture toughness K_{IC} of the MMCs varied between 7.2 and 9.5 MPa·m$^{1/2}$ except that of AODY30IS which was significantly lower, as shown in Figure 4.80. The value of the latter had to be estimated, as the samples broke prior to the end of the preloading phase of the test. The maximum preloading stress corresponded to a K_{IC} of 3.0 MPa·m$^{1/2}$ and therefore K_{IC} of AODY30IS was below this value.

In the unreinforced Al-Si alloy (IS), the required notch geometry could not be obtained using the chosen notching device, as this was designed for brittle materials but produced a U-shaped notch in the pure alloy. The general geometry criterion, where the notch root should have a radius of less than 50 µm to minimize the influence of notch radius on K_{IC}, could not be achieved. Therefore the K_{IC} values could not be evaluated for the pure alloy, whereas the MMCs had a satisfactory notch geometry.

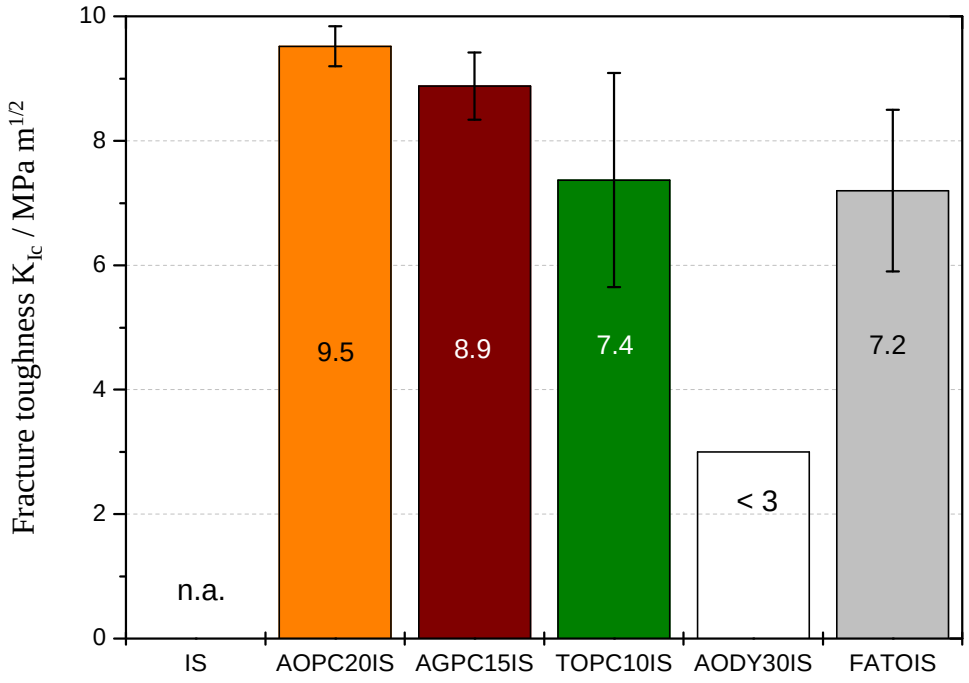

Figure 4.80 Fracture toughness K_{IC} of the MMCs.

With a K_{IC} of 9.5 MPa·m$^{1/2}$, AOPC20IS showed the highest mean K_{IC} combined with the lowest scatter of all MMCs. Marginally lower values were determined for AGPC15IS, where the preform was fabricated with a glassy binder. The TOPC10IS MMC and the hybrid-reinforced composite FATOIS showed comparatively lower mean K_{IC} values between 7.2 and 7.4 MPa·m$^{1/2}$ combined with a larger scatter.

The fracture surface of a tested sample of TOPC10IS was investigated using SEM. Figure 4.81 a) shows a typical optical micrograph of a similar MMC sample to represent the examined areas. These were the intergranular area with coarse metal ligaments (Figure 4.81 b) and the intragranular area with small ligaments between the single particles (Figure 4.81 c).

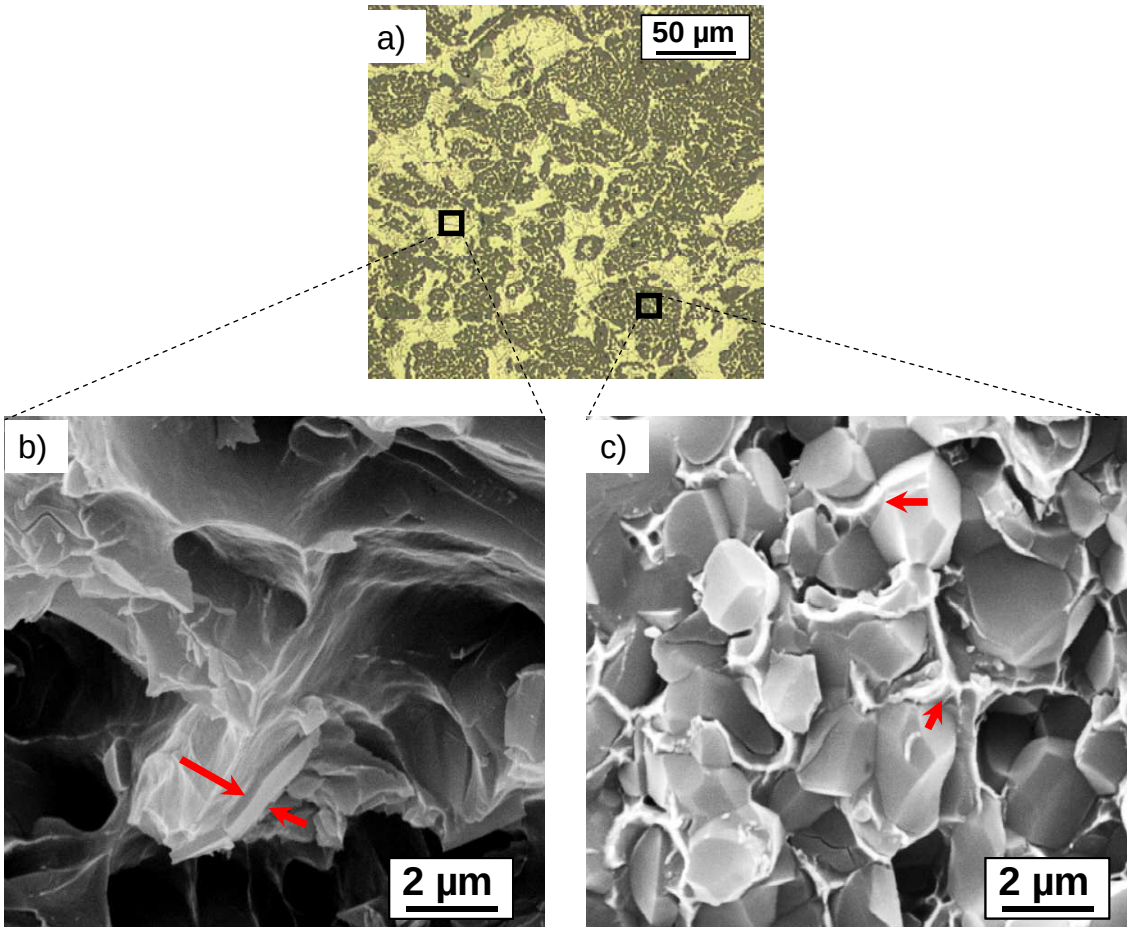

Figure 4.81 Fractographic microstructure of TOPC10IS. a) Representation of the regions examined in an optical micrograph. SEM of the fracture surfaces: b) Intergranular and c) intragranular region.

Significant deformation developed in the intergranular area prior to fracture, as indicated by the fissured surface with deep cleavages. A platelet-shaped phase was observed on the apex of a deformed alloy volume as indicated by the arrows. The plane fracture surface of this phase indicates brittle fracture. The position of it in the alloy, its shape and the brittle behaviour indicated that Si in the alloy acted as the focus for failure. As it was free of residual Al, low adhesion of the surrounding α-Al on the Si-grain is indicated.

The surfaces of the ceramic particles in the intragranular infiltration region were free of adhering alloy, Figure 4.81 c). The metal ligaments between the particles were fissured and are marked with an arrow. This indicated ductile fracture of the metal alloy. In contrast, the fracture surfaces of the ceramic particles were plane and therefore brittle fracture occurred but fracture was dominated by intergranular fracture across the grains.

4.10.4 Tribological properties

Tribological testing was carried out by sliding a steel cylinder on a disc of a fine polished surface of the MMC in reciprocative sliding contact with oil as a lubricating medium. The resulting time-friction coefficient curves were analysed as described in 3.5.6 to give the friction coefficient f_{50m}. After the test, the width of the sliding path was evaluated as a measure of the wear. The f_{50m} values and the width of the wear path w_w are presented in Figure 4.82 for the pure alloy IS and the MMCs. The maximum scatter in f_{50m} of three test runs was ±0.02. The lowest value of f_{50m} of 0.15 was measured for the AODY30IS. The MOPC20IS, AOPC20IS and AG15IS MMCs had intermediate f_{50m} values between 0.19 and 0.20. The pure alloy IS and the TOPC10IS MMC had similar friction coefficients of 0.24. The highest friction coefficient of 0.26 was found for FATOIS.

Apart from AODY30IS, w_w of the tested samples were between 250 µm and 670 µm as shown in Figure 4.82. The maximum wear (670 µm) was found for the pure alloy IS and the

w_w values of all MMCs were less than half that value. TOPC10IS had the highest wear of all MMCs. The Al_2O_3-reinforced MMCs (AOPC20IS and AGPC15IS) had similar w_w of around 300 µm. MOPC20IS and FATOIS had lower values of 260 µm and 250 µm respectively.

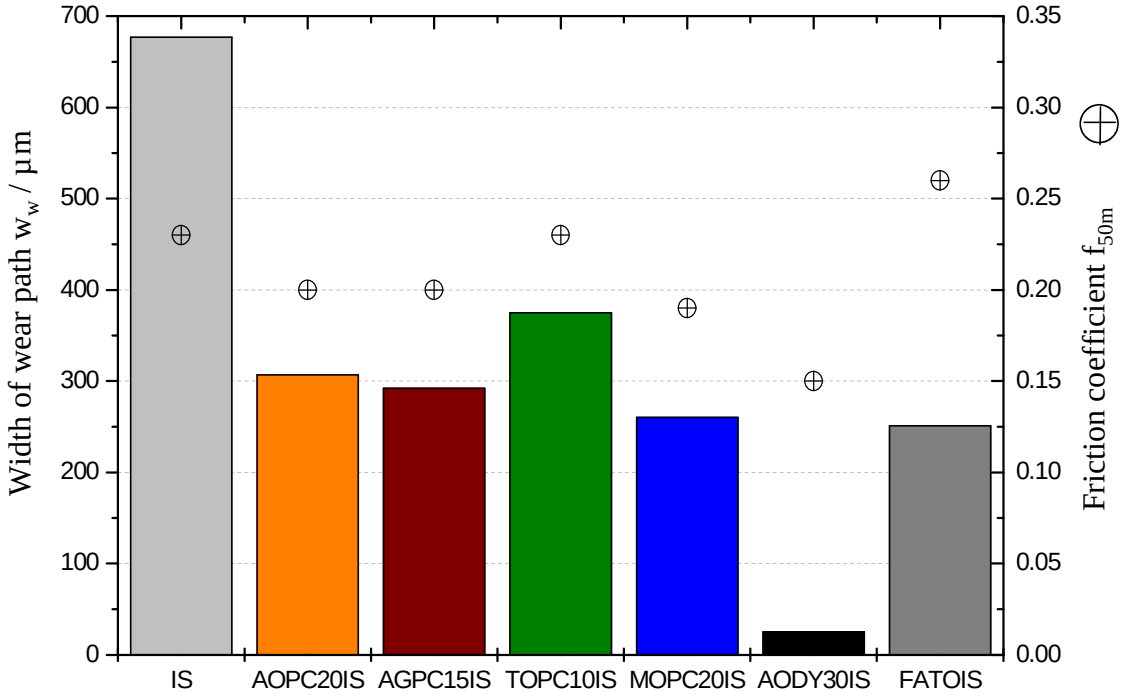

Figure 4.82 Characteristic friction coefficient f_{50m} and width of wear path w_w after wear test of unreinforced and MMC materials.

In contrast to AOPC20IS, AODY30IS showed no distinct wear path after the test. Only wear pits in the ceramic phase and some small local metallic regions about 25 µm wide, such as that on the left of Figure 4.83 b), were found. In the metal areas, no contact with the sliding cylinder was detected compared to the other MMCs. Therefore, the tribological pairing of AODY30IS with steel has to be assumed to between steel and pure alumina with the contact area interrupted by the circular metallic domains.

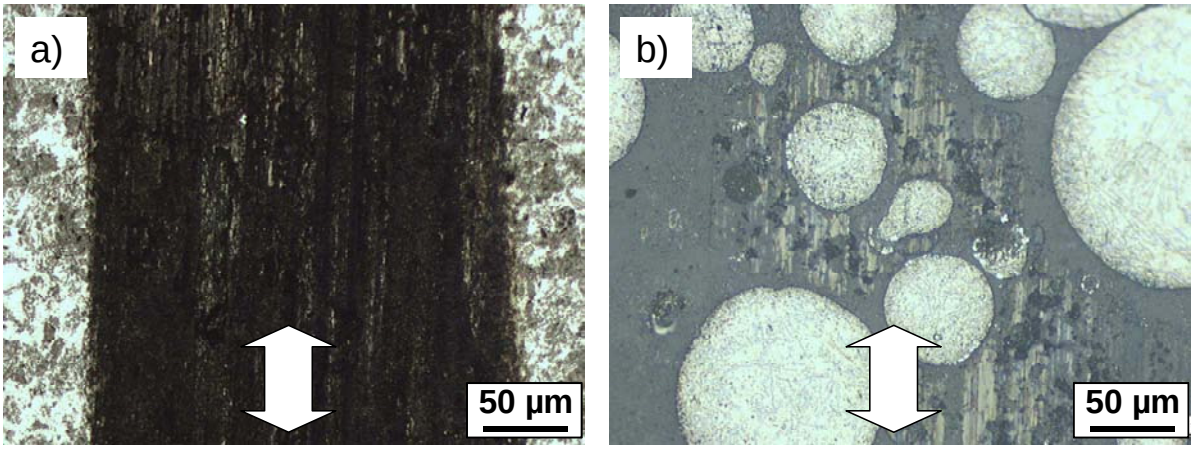

Figure 4.83 Structure of the wear path after tribological test run. a) AOPC20IS and b) AODY30IS.

In FATOIS, a phase with a higher density accumulated along the edge of the wear path as indicated by the light area in Figure 4.84 a) which EDS analysis showed to be an iron and chromium-rich phase shown in Figure 4.84 b). As a chromium-containing 100Cr6 bearing steel was used for the cylinder, the light phase was transferred from this to the MMC surface.

Figure 4.83 shows the wear paths of the AOPC20IS and AODY30IS alumina-reinforced composites. The structure of AOPC20IS had deep grooves which could not be resolved with the optical microscope. The groove wear was parallel to the sliding direction of the counterpart cylinder as indicated in Figure 4.83.

A light grey phase enclosed a darker fibre-shaped phase outside the wear path of Figure 4.84 b). The grey phase was the titania particles and the darker enclosed phase the alumina fibres. In Figure 4.84 b) an accumulation of worn steel is visible which enclosed a fragmented alumina fibre (circled). This had a larger diameter than the other fibres visible in the image and which had a nominal diameter of 3 µm. Furthermore, the small aspect ratio of less than 3 indicated that it was a fibre shot, a by-product of fibre fabrication. The accumulation of the steel debris in the vicinity of the shot has to be attributed to its increased abrasive effect compared to the normal fibres.

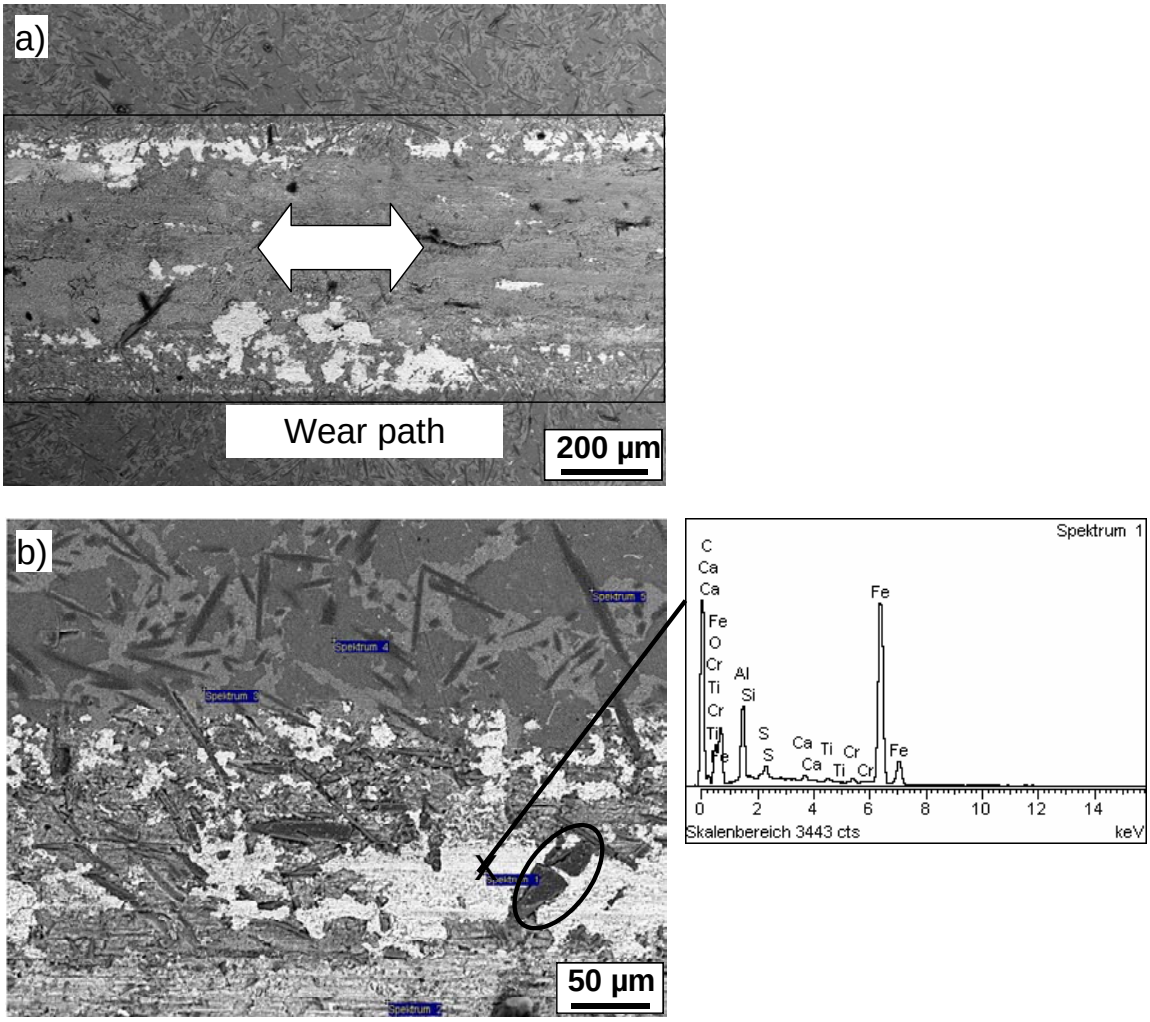

Figure 4.84 a) Microstructure and b) SEM micrograph with the EDS spot analysis of the wear path of FATOIS.

5. DISCUSSION

First the properties of the MMCs are discussed and compared with those of the pure infiltration alloy. Properties are influenced by the preform pore structure and its chemistry. Residual porosity influences the performance and preform saturation is important and is discussed. Finally, the results of preform infiltration experiments are compared to one dimensional infiltration models.

5.1. Tailoring properties of preform MMCs

The main task in composite research is to combine the desirable properties of the different phases. Even though high strength Al alloys are available for use up to a temperature of 150°C, above this point the mechanical properties reduce drastically. For MMCs consisting of an Al alloy matrix with ceramic particles and/or fibres, the target is increased elastic modulus, greater strength and wear resistance combined with sufficient failure tolerance at room and elevated temperatures combined with an economic material synthesis process. The drastic reduction is not observed in preform-based MMCs due to the interconnected phases. Kniewallner [51] demonstrated for Saffil™ fibre-reinforced Al alloy MMCs that, if the room temperature properties were superior to the pure alloy, the gap in properties is even larger at elevated temperatures. This behaviour was assumed to be applicable for the MMCs produced in the present research and therefore only room temperature properties were assessed.

5.1.1 Pure alloy properties

The chemical and mechanical properties of the pure alloy IS (EN AC-AlSi12Fe), a commercial high pressure die casting (HPDC) alloy, are specified in EN 1706 [148]. Here the minimum mean tensile strength of HPDC materials is higher (240 MPa) than that of gravity chill cast materials (150 MPa). The latter process is closest to direct squeeze casting

(DSQC) [135] which was applied in the present study for fabrication of the test samples. The differences in strength are a result of the lower cooling rates found in gravity chill cast material. A rate of 1°C/s was measured for DSQC (Figure 4.46), whereas 10 to 1000°C/s was reported for HPDC [143]. The higher cooling rates lead to finer microstructures and higher strengths [143]. The pure alloy IS had a calculated characteristic bending strength of 241 MPa. Due to the limited deflection of the bending test set-up and the relatively high ductility of IS the test bars did not break and therefore the calculated value did not represent σ_0 which calculation is based on the stress at fracture.

For an alloy similar to IS processed in indirect squeeze casting (ISQC) Kniewallner [51] measured in the tensile tests a mean UTS of 190 MPa (Table 2.1). Kniewallner found inhomogeneities such as oxides and gas inclusions in the fractured surface which led to reductions in strength. No such defects were found in IS in the present work leading to higher fracture strength values. Even though the actual σ_0 of IS is higher than the calculated value evaluated with limited deflection, the measured UTS [51] and the specified alloy values [148] indicate that it is legitimate to assume that the real σ_0 is higher but close to the value of 241 MPa and it was used for the comparative study. Nevertheless, in future work the bending test set-up will have to be improved in order to allow testing of materials with higher ductility.

The limited deflection in the bending test further reduced the scatter in maximum stress values of IS and therefore its Weibull modulus (m) of 88 is an overestimation and not representative. It was reported that m values for the tensile strength of Al alloy castings lie below 40 [6]. For the present comparative study, the maximum value (m = 40) was used as it represents a worst case regarding the comparison with m values of the MMCs, where all test bars fractured prior to the deflection limit being reached.

The measured elastic modulus, E_{dyn}, of IS of 69 GPa is marginally lower than recorded in the literature [166]. For metallic materials, E is usually measured in tensile tests. For example Kniewallner [51] found 75±3 GPa for an alloy similar to IS. The difference in modulus may be the result of using the dynamic method which was originally developed for ceramic materials, exhibiting higher moduli and lower damping. Nevertheless, the difference is acceptable and the method was successfully applied to Al-MMCs [175].

The fracture toughness, K_{IC}, of IS could not be measured using the single edge V-notch beam (SEVNB) method [169], which is a standard method used for ceramics [149], because the metallic character of the unreinforced alloy prevented the fabrication of an obligatory sharp notch. The compact tension test method (CT) is usually used for metals and precracking is performed using cyclic loading. No K_{IC} values for HPDC Al alloys were found in the literature. Using the CT method, Chan *et al.* [176] reported values in the range of 12.0 to 17.8 $MPa \cdot m^{1/2}$ for gravity cast Al-7%Si-Mg. The lower values were for the as-cast condition and the higher for the T6 condition. The solution heat treatment in the precipitation hardening process of Al-Si-Mg alloys consists of prolonged holding at temperatures about 30-50°C below the solidus. Here, not only solution of Mg takes place but also the morphology of Si is changed from needle-like to a spherical shape. This shape transformation is reported to be used to increase the elongation of casting alloys. As a result of this silicon spheroidization treatment (SST), the elongation of an A356 alloy increased by 70% [177]. The possibility of spheroidization of the IS alloy was investigated and Figure 4.44 shows that the needle-like shape was transformed into a globular one and therefore the K_{IC} of the as-cast alloy may be improved by heat treatment. However, as the target of the present work was a low cost composite, heat treatment was not applied.

From Figure 4.81 b) it appears that cracking initiates at the interface of the needle-like Si-precipitates. It can therefore be assumed that the K_{IC} of IS is similar to that reported for as-

cast A356 [178] (12 MPa·m$^{1/2}$). This is reasonable if other microstructural conditions were close to that of A356 mentioned by Chan *et al.* [176]. This may not be the case since the chemical composition is different: apart from Si, the A356 contained 0.097 wt.% Fe, whereas the infiltration alloy IS contained 0.76 wt.% Fe. Iron forms intermetallic phases which reduce the elongation and toughness [6]. Therefore IS may exhibit a K_{IC} lower than 12 MPa·m$^{1/2}$. However, the microstructure of IS made by DSQC is finer than that of the gravity cast alloys and so ultimately 12 MPa·m$^{1/2}$ was assumed.

As aforementioned, the fracture toughness of a metal is generally determined using the CT method. In this work, the SEVNB method was used to characterise MMCs with a metal per cent by volume of 60-70%. Kounga-Njiwaa *et al.* [179] have compared the K_{IC} of commercial lead zirconate titanate (PZT) ceramics measured using CT and SEVNB. They stated that the investigated PZT material, which was at the morphotropic phase boundary and doped with nickel and antimony, show a similar stress-strain behaviour to metals. Quasi-plasticity was found similar to that in the MMCs indicated by distinctive non-linear, quasi-plastic behaviour shown in the curve of AOPC20IS in Figure 4.78. Furthermore the authors found that for PZT the toughness calculated using the standard equations was 5% higher for the CT than in the SEVNB test. Therefore, the SEVNB method was rated as an applicable method for MMC characterisation which is comparable with K_{IC} values tested with the CT method.

5.1.2 MMC properties in relation to the pure alloy

Figure 5.1 presents the values of the relative MMC performance as a ratio of that of the MMC (P_{MMC}) to that of IS (P_{IS}). For the tribological properties, low wear and low friction coefficients are considered favourable and therefore reciprocal values of width of the wear path (w_w) and the friction coefficient (f_{50m}) were calculated and presented.

The MMCs showed similar wear with the exception of AODY30IS which had the largest metal and ceramic ligaments and showed no visible wear in the metal phase (Figure 4.83). This behaviour agrees with Clyne and Withers [31] who stated that large ceramic particles showed lower wear compared to finer ones at similar volume fractions. This also agrees with Long *et al.* [50] who found that the coarser the particles in a AlCu4Mg-SiC MMC, the lower the wear rate. Nevertheless, large particles embedded into finer ones, like the shot particle in FATOIS shown in Figure 4.84, seem to be detrimental to friction properties, indicated by the highest f_{50m} of all MMCs tested (Figure 4.82).

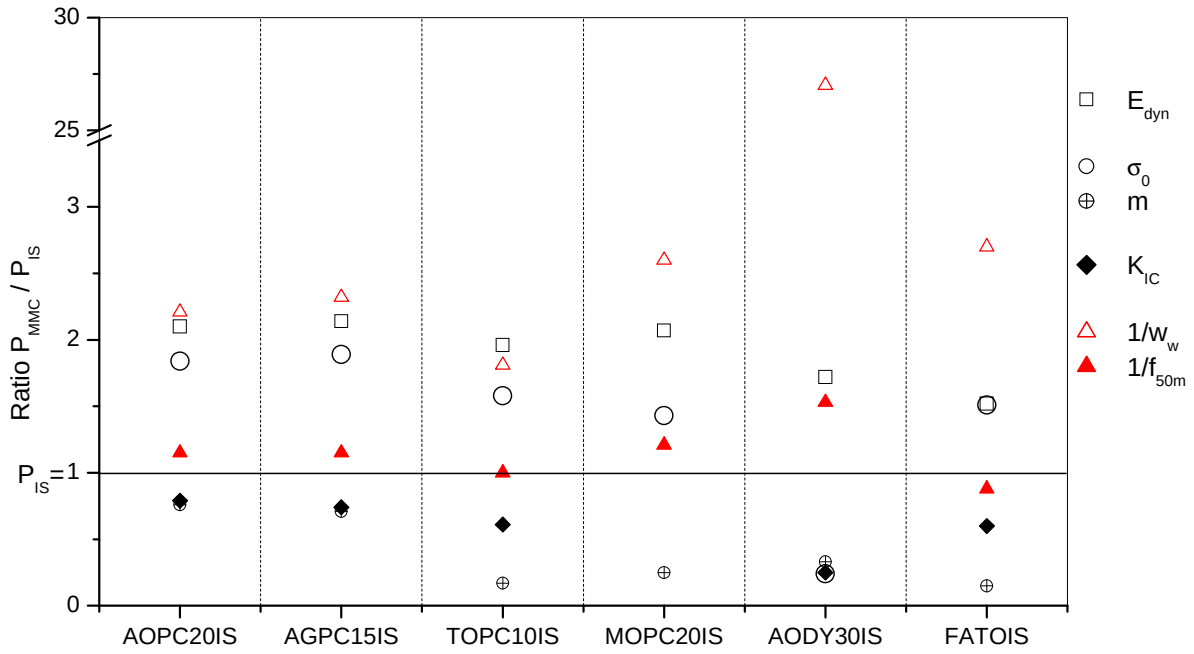

Figure 5.1 Relative characteristic performance of the MMCs in relation to the pure alloy IS. E_{dyn}: elastic modulus; σ_0: characteristic strength and its Weibull modulus m; K_{IC}: fracture toughness. Reciprocal value of the ratio for w_w: width of wear path and f_{50m}: friction coefficient.

All MMCs had higher elastic moduli than the pure alloy IS. Hashin and Shtrikman [55] proposed a model (Equation 5) to calculate the upper and lower bounds ($E_{c,upper}$, $E_{c,lower}$) of the composite´s elastic modulus E_c based on the moduli of the two constituents (E_1, E_2) and their volume fractions (V_f, $1-V_f$), neglecting the morphology of the reinforcing phase. The moduli of the reinforcing phases listed in Tables 3.3 and 3.7 were taken from the

literature [149]. The moduli of the MMCs investigated ($E_{dyn,MMC}$), those reported elsewhere [51, 54] (FA13.5IS, FA20.0IS, AODY25), the predicted range of E_c and the values calculated using the rule of mixture (E_{ROM}) are shown in Figure 5.2. FA13.5IS and FA20.0IS were Saffil™ fibre reinforced MMCs with a matrix similar to IS and V_f of 0.135 and 0.20 [51] respectively. The MMC based on a foamed preform [54] had a similar structure to AODY30IS of the present work but a different ceramic volume fraction of 0.25 and is designated as AODY25. As shown in Figure 5.2, the rule of mixtures overestimates ($E_{c,ROM}$) the moduli of all MMCs. Hashin and Shtrikman [55] initially found similar trend issues and therefore introduced their model which gave ranges of values which were lower than $E_{c,ROM}$.

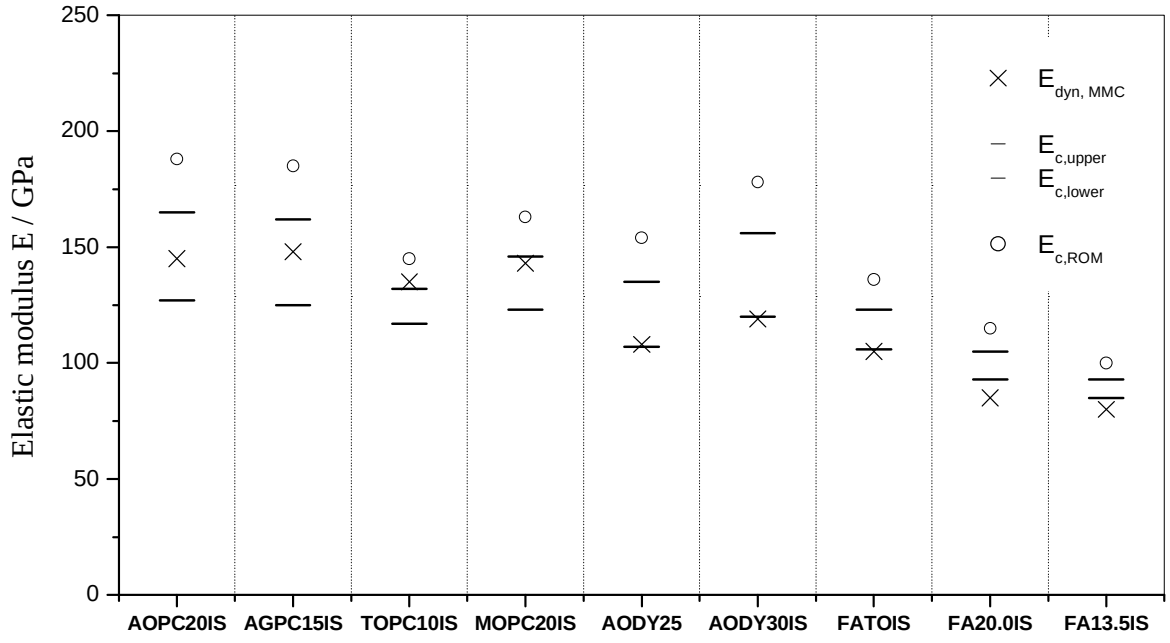

Figure 5.2 Comparison of experimental results of the MMCs moduli ($E_{dyn,MMC}$) and predictions based on the rule of mixture ($E_{c,ROM}$) and upper ($E_{c,upper}$) and lower ($E_{c,lower}$) bound of E_c in accordance to Hashin and Shtrikman [55]

The alumina reinforced MMCs, AOPC20IS and AGPC15IS, showed good agreement with the model of Hashin and Shtrikman [55], as indicated by the experimental values lying between $E_{c,lower}$ and $E_{c,upper}$. With a similar reinforcement chemistry, the model overestimates the modulus of AODY30IS which can be attributed to the morphology of the ceramic phase or

interfacial debonding: Peng *et al.* [54] found that in preforms similar to AODY30, a gap was formed along the metal-ceramic interface, attributed to feeding deficiencies during solidification. By variation of the pressure holding times and the cooling schedule, they could optimize the structural integrity of the MMC. In the present work, the optimization of the preform infiltration process enabled the melt feeding into the preform cavities during solidification to be maintained, resulting in dense MMCs as shown in Figure 4.52. Therefore interfacial debonding was not present in AODY30IS as further shown by the microstructure in Figure 4.58. As aforementioned the model matches the measured E_c for AOPC20IS and the deviation in AODY30IS has to be attributed to the reinforcement morphology and its distribution.

5.1.3 Influence of homogeneity

The porosity was reduced significantly when a chill was used in the DSQC tool to promote directional solidification from the bottom punch towards the top tool. Therefore, the porosity of castings made in the tool prior to modification can be attributed to insufficient feeding during solidification. In HPDC the infiltration tool was not optimized in terms of directional solidification and similar feeding defects were observed. Typical defects of this type are shown in the macrostructures of AODY30IS in Figure 4.71 where the porosity was concentrated in the centre. It is interesting to note that, when using similar processing conditions, the AOPC20 preform gave a lower porosity in the MMC but large pores on top of it (Figure 4.71) but compressed significantly more (22%) than AODY30 (3%). The compression in AOPC20IS was at the expense of the larger pores, as shown exemplarily in Figure 4.72 b) and c). The absence of porosity in the MMCs produced with the optimized SQC tool, as well as in the AOPC20IS infiltrated in HPDC, is evidence that the gas in the preform does not influence the infiltration results. Infiltration occurs from the top and the four outer faces, forcing the air out of the preform through the bottom face.

Even though air is forced out of the preform, oxygen was consumed during infiltration due to the high oxygen affinity of liquid Al and its alloys. When liquid Al is exposed to air, oxygen is consumed to a large extent before nitrogen [8]. Cappleman *et al.* [116] reported that due to the kinetics of aluminium oxide formation a reaction leading to an alumina monolayer can keep pace with a superficial velocity v_0 up to 10^{-2} to 10^{-1} m/s in Saffil™ fibre preform infiltration with Al melts. In the present infiltration experiments v_0 varied between $2 \cdot 10^{-2}$ m/s and 1.44 m/s (Table 3.8) for DSQC and for the maximum velocity in ISQC, respectively. Therefore oxide film formation on a newly formed melt surface seems probable during DSQC. In contrast, at higher infiltration velocities, pure metal surfaces have to be assumed, leading to oxide-free reinforcement contact. Therefore, for high infiltration velocities, a separation layer between the reinforcement and the metal matrix is prevented, shown schematically in Figure 2.17. This seems favourable in terms of interfacial bonding and the resulting mechanical properties [31]. Nevertheless, the present work concentrated on the evaluation of mechanical properties of the MMCs produced in DSQC as the ISQC-infiltrated MMCs were not free of infiltration defects.

The threshold velocities proposed by Cappleman [116] were based on Saffil™ fibre preforms. The reinforcement morphologies in the present investigations were different and therefore a simple calculation accounting for this was developed. Assuming that the die cavity was sealed from the outer atmosphere, oxygen for Al oxidation is only supplied from inside the preform. Assuming complete consumption of oxygen, coverage of at least a monolayer of aluminium oxide between the reinforcing phase and the metal is reached when the specific area per unit preform volume of newly formed aluminium oxide S_{ml} is larger than the specific inner surface per preform volume S_{pHg} (Table 4.2):

$$S_{ml} > S_{pHg} \qquad \text{Equation 47}$$

The area S_{ml} was derived using data for the standard atmosphere at a given processing temperature of 800°C ($\rho_{T,air}$, $v_{f,O2}$) the molar mass fractions of oxygen in alumina ($3M_O/M_{Al2O3}$), its density (ρ_{Al2O3}) and the nominal thickness of a monolayer of Al_2O_3 (d_{ml}) as:

$$S_{ml} = \frac{M_{Al_2O_3} \Phi_{tot} \rho_{T,air} v_{f,O_2}}{d_{ml} \rho_{Al_2O_3} 3M_O} \qquad \text{Equation 48}$$

The O_2 volume fraction of the standard atmosphere $v_{f,O2}$ is reported as 0.2095 and the density of air $\rho_{T,air}$ at 800°C as 348 g/m³ [160]. The mean pore volume fraction Φ_{tot} of the preforms was 0.65. Using the density of Al_2O_3 in Table 3.3, neglecting probable differences in Al_2O_3 allotropy which was reported [6] to consist of amorphous γ-alumina rather than of α-alumina immediately after reaction, and assuming a monolayer thickness of d_{ml} of $8 \cdot 10^{-8}$ m [116], the monolayer would cover an area of $3.2 \cdot 10^4$ m² per m³ of preform. When comparing this value with the S_{pHg} values of the preforms in the target volume content range presented in Table 4.2, which were between $1.05 \cdot 10^6$ m²/m³ (MOPC20) and $6.5 \cdot 10^6$ m²/m³ (FATOIS), it is obvious that these are more than two orders of magnitude larger. Based on these calculations, less than 3% of the newly formed liquid surface was oxidized with a monolayer of alumina and further kinetic calculations were discarded. The ratio gets even lower when the air is expelled from the preform during infiltration, as was obviously the case in the present preform infiltration experiments. Therefore the predominant melt fraction had a non-oxidized contact with the reinforcing phase. Nevertheless the residual air fraction inside the preform, consisting predominantly of nitrogen, may be consumed by the melt to form AlN. Zheng and Reddy [8] proposed that AlN formation does not start until the oxygen partial pressure is reduced to 10^{-17} Pa. This low value may not be reached in relatively fast infiltration and it is proposed that nitride reactions are absent.

In summary, the large surface area of the particulate preforms is favourable in terms of clean aluminium melt surfaces and hence pure Al-reinforcement interfaces are formed, resulting in improved interfacial bonding and improved composite properties. This statement is probably valid for inert systems such as AOPC20IS fabrication and may be the main factor leading to its significantly higher strength compared to Saffil™ fibre-reinforced MMCs: AOPC20IS showed a σ_0 value of 443 MPa (Figure 4.79 b) whereas Saffil™ fibre-reinforced MMCs, which were limited to a maximum ceramic volume fraction of 0.20 to 0.25, showed a maximum tensile strength of 295 MPa (Table 2.1). The lower value may further be attributed to the silicate binder obligatory in Saffil™ preform fabrication which is, as shown in Figure 2.13, distributed all along the fibre-matrix interface, leading to a brittle silicate interfacial phase preventing pure metal Al-Al_2O_3(f) contact during infiltration. Further, the binder is concentrated in the contact areas between the single fibres. Therefore the load transfer at the contact points is restricted to the silicate binder. This configuration led to brittle failure of the contact point and deterioration of the reinforcing network when the composite was extended.

Porosity of less than 3% by volume in a MMC significantly influences its strength. When comparing the local strength of MMC before and after optimisation of the thermal conditions of the infiltration tool presented in Figure 4.76, the strength was lowered by 100 MPa to 300 MPa due to the pores. An example of the microstructure is shown in Figure 4.77 a) where metal filled the interparticle cavities but not the larger pores of the initial preform. Under constant pressure infiltration at two different pressures, the large pores were filled prior to the smaller ones as shown in Figure 4.43 a) and b). As similar behaviour was assumed under DSQC, the porosity in the MMC has to be attributed to a post-infiltration effect i.e. shrinkage of the metal during solidification. This is supported by the fact that the porosity was found in the centre of the MMC. This position represented the hot spot of the originally fully-infiltrated preform. The solidification started on the die walls and progressed toward the centre of the

MMC. Due to the solidification shrinkage, the melt extruded toward the direction of the advancing solidification front, toward the outer areas of the MMC. The larger pore extrusion phenomenon is in conflict with Washburn´s equation which is the basis of the mercury porosimetry (Equation 21) and valid for non-wetting fluids in a porous network. According to this, extrusion of the fluid would start from the smallest pores. If wetting occurs, the fluid is retained in both the small and the large cavities. Nevertheless, non-wetting of the investigated systems was demonstrated in the sessile drop experiments (Figure 4.6) as well in a spontaneous infiltration test of a metal droplet on a preform sample, where no intrusions were achieved during 30 min holding. In all experiments, wetting angles were larger than 90°.

Premature solidification of the metal phase in the small pores may be further assumed. Even though a large surface area is offered to the melt in the intragranular region enabling easy nucleation, the temperature gradient between the melt in the large pore channels and the ceramics does not differ significantly. This inhibits the formation of nuclei on the surface of the ceramics and therefore prevents premature solidification in the intragranular region.

The effect of hysteresis reported in the mercury intrusion (-extrusion) porosimetry (MIP) literature [110] seems applicable to the aforementioned extrusion. The hysteresis term in MIP describes the difference in the intrusion and extrusion curves shown in Figure 4.25 for the AO and AOPC20 preforms. Leon [110] attributed the effect mainly to the structural hysteresis characterised by the presence of bottle-neck shaped pores. The latter is characterised by the intragranular region in Figure 4.60 a) and b). The AOPC20IS and TOPC10IS MMCs had bottle-neck porosity which hinders extrusion of the melt out of the intragranular areas. Therefore the hysteresis is most likely to result in the large pore extrusion phenomenon.

Some residual porosity was found in the ceramic struts of AODY30IS (Figure 4.58). To produce fully-infiltrated MMCs, the melt had to enter all pores during infiltration which is

fulfilled when the total porosity Φ_{tot} is equal to the open cell porosity Φ_{op}. As summarized in Table 4.1, the differences between Φ_{tot} and Φ_{op} (the closed cell porosities Φ_c) were in the range of 0.2 to 2.0% for the preforms fabricated with pore forming agent (PFA) and measured using the an method based on the Archimedes´ principle [159]. The lower value was for AOPC20 and the highest for AGPC15. The latter was sintered at relatively low temperatures (1000°C) using a glassy frit. As AOPC20 was fabricated using similar powder without a frit, the porosity of AGPC15 may be attributed to the closed cell pore formation during sintering. No reactions were found between the frit and alumina, which would lead to inaccuracies in bulk density and therefore unreliable porosity parameter calculations. However, the 2% measured closed porosity was not found in the microstructure of the MMCs. This may be a result of the fuzzy appearance of the reinforcing phase caused by the transparency of the glassy frit. Alternatively, the porosity may have become closed during the metal infiltration. Due to the fact that the MMC strength of AGPC15IS was higher than that of AOPC20IS and that residual porosity has a detrimental effect on strength (exemplified by TOPC10IS in Figure 4.77) closure of the residual porosity during infiltration has to be assumed. This is supported by the fact that the frit softens at the preform preheating temperature [154] (800°C), leading to plastic deformation of the preform. The high compression of AGPC15IS during DSQC (Table 4.8) supports this hypothesis.

The Φ_c values were not confirmed by mercury intrusion porosimetry (MIP - section 4.6.2 - Table 4.2). In identical preforms, the difference between total porosity, Φ_{tot}, and intruded porosity, Φ_{Hg}, which is assumed to represent the closed cell porosity, was significantly higher, between 4 and 9%. The maximum error in the measured intrusion volume was less than 1% [153]. According to Rootare and Prenzlow [109], the difference between the two values resulted from the compression of the preform samples during mercury intrusion

measurements which resulted in a lower apparent total porosity. The amount of compression is reported to correlate with the strength of the test sample [109]. This corresponds to the differences between Φ_{tot} and Φ_{Hg}. For example, Φ_{tot}-Φ_{Hg} was 9% in TOPC10 compared to 0% for TO which was produced without PFA (Table 4.2). TO had a ceramic volume content of 56% compared to 38% in TOPC10 (38%). The strength of TO was correspondingly higher than that of TOPC10 but was not evaluated in the present work. Beyer [53] reported the bending strength of a titania preform similar to TO to be 27.7±2.3 MPa compared to a value of 1.1 MPa found for TOPC10.

The foamed preform AODY30 exhibited a relatively high compression strength of 245 MPa which was 35 times higher than that of FATO and 220 times higher than that of TOPC10 (Figure 4.33). Therefore, in a similar way to TO, a minor difference between Φ_{tot} and Φ_{Hg} should have been found. However, 1% difference was measured, which has to be attributed to closed cell porosity and not to preform compression. It is therefore concluded that MIP is not a suitable method to determine closed cell porosity as the difference between Φ_{tot} and Φ_{Hg} is an effect of both preform compression and effective closed cell porosity and could not be attributed to individual parameters.

5.1.4 Influence of the ceramic structure

As reported by Legzdins *et al.* [41], brittle interfacial phases are detrimental to elastic and plastic properties of the composite. It has been shown (Figure 4.60 a) that a non-contaminated interface between the matrix and the reinforcing phase was achieved with the non-reactive preform AOPC20. Nevertheless, it has also been shown that silicate binder additions in similar volume fractions as those used in Saffil™ fibre preforms did not have a detrimental influence on composite properties in particulate preforms. On the contrary, the higher σ_0 values of AGPC15IS compared to AOPC20IS indicated an improved microstructure. This is

attributed to the finer reinforcement size of AGPC15IS compared to AOPC20IS, as shown by comparing Figure 4.54 a) and c). In the AOPC20 preform, the alumina particles were sintered at higher temperatures leading to coarser ceramic grains, whereas the liquid phase sintering at lower temperatures (1000°C) preserved the initial grain size in AGPC15.

In general a small interparticle spacing is regarded as the main factor for improved mechanical properties. This is supported by comparing AOPC20IS to AODY30IS which have a similar chemical composition. The metal ligaments in AODY30IS were up to 300 µm long compared to less than 40 µm in the intergranular regions and less than 3 µm in the intragranular regions of AOPC20IS. For the latter composite, the strength and fracture toughness were more than 7 and 3 times higher respectively. The relatively low mechanical properties of MOPC20IS were a result of its coarser ceramic structure (Figure 4.56 a) which may be improved in the future by lowering the preform sintering temperature. The latter preform type offers a unique possibility to influence the grain size of the ceramics, which is discussed in section 5.2.2.

The bend test and SEVNB bars measured 3 mm wide and 4 mm thick. The micrograph of AODY30 in Figure 4.58 indicates that the bubble diameters were up to 300 µm and the strut thickness between two single bubbles around 40 µm. Therefore, in the worst case of an agglomeration of larger bubbles in the stressed region, just 6 bubbles and struts were loaded on the tensile area of the beam sample, which makes the validity of the results questionable. Therefore, testing samples of larger volume would be preferable. Nevertheless, the Weibull modulus of 13 indicates a medium scatter in properties and therefore the results are sufficiently reliable for the present comparative study.

5.1.5 Influence of reactions

No reactions were found in the microstructure of MOPC20IS when infiltrated (Figure 4.60 c) and after thermal analysis (Figure 4.64 b). In contrast, the titania-reinforced MMCs showed reactions in both the as-cast and the heat treated states, but with different amounts of reaction products. After DSQC infiltration with IS, a 50- 100 nm thick reaction layer was visible (Figure 4.60 c) whereas, when using the alloy IM in the reaction, the central area of the MMC (Figure 4.65 b) reached thermodynamic equilibrium similar to that obtained after the thermal analysis (Figure 4.63 a). As the oxidation of the melt surface was far from complete in the present preform configurations, the difference in reaction behaviour between IS and IM was not a result of the differences in melt oxide layer chemistry, which was reported to be MgO in IM-type alloys [11] and Al_2O_3 in IS [6]. It was attributed to the reactivity between the Mg in the alloy and the TiO_2 of the preform. In the centre, the exothermic reaction released sufficient energy to maintain the reaction whereas, in the outer areas, the heat flow towards the die walls prevented a temperature rise, leaving unreacted areas. This shows that the preform technology, coupled with fast infiltration methods, enables the combination of phases far from equilibrium which would not be achievable by techniques where the reinforcement is in prolonged contact with the liquid alloy like gas pressure infiltration of the reinforcement, where contact times of more than 100 s are required [103,132].

The elastic modulus E_{dyn} of TOPC10IS, which was higher than the predicted upper bound shown in Figure 5.2, was a further result of the reaction between TiO_2 and Al, with a brittle interfacial phase exhibiting a higher E_{dyn} than the unreacted constituents [53]. The metal ligaments in TOPC10IS were finer than those in AOPC20IS, yet its strength was lower. This is attributed to the reaction layer which consisted of $TiAl_3$, titanium suboxides (Ti_xO_y) and reaction-formed Al_2O_3 [53,94]. This reaction layer reduced the strength and fracture toughness due to brittle failure of the interface, as shown in Figure 4.81. In the case of fully-reacted

material, similar to that resulting from the thermal analysis test, K_{IC} was as low as 3 $MPa \cdot m^{1/2}$ [163]. This was a result of the brittle character of the intermetallic $TiAl_3$ [53,163] in combination with the presence of 11% porosity (Figure 4.63 a) resulting from the volumetric change due to the reaction products which were predicted by the thermodynamic calculations (Figure 4.3).

The K_{IC} values of the MMCs based on the self-fabricated preforms with a bimodal pore structure were higher than the MMCs made using the two purchased preforms: FATO, a hybrid preform with Al_2O_3 fibres (Saffil™) and fine TiO_2 particles, and AODY30 in which the predominant porosity was formed by bubbles in the ceramic slurry. The processing of the latter resulted in relatively large spherical porosity as shown in Figure 4.23 in the as-purchased condition (AODY30) and in the MMC (AODY30IS) in Figure 4.58. AODY30IS showed the lowest K_{IC} and strength of all MMCs investigated, but gave superior tribological properties which were attributed to the differences in microstructure.

Three main influencing factors were identified for tailoring the mechanical and tribological properties of MMCs at constant reinforcement volume fractions:

a) Porosity in the MMC microstructure.
b) Interface between the metal phase and the reinforcement
c) Small interparticle spacings filled with the metal phase

The porosity in the MMC has to be subdivided into pores generated by the melt solidification, which were discussed together with the interfacial aspects in this section, and those resulting from the saturation during infiltration which is discussed in section 5.3. The interparticle spacing is built into the preform during fabrication and is discussed in the following section.

5.2. Preform pore formation

The target preform porosity range in the present work was between 60 and 70%. Neglecting compression, the size of the porosity measured in the ceramic preforms represents the size of the metal phase after infiltration. It has been shown that the reinforcing effect is superior in terms of mechanical properties for a fine distribution of metal ligaments compared to extensive ceramic and metal ligaments e.g. the MMC of the foamed preform AODY30IS.

5.2.1 Foamed preforms

A window diameter of 10 µm and a cell diameter of 120 µm were measured in the microstructure of AODY30 (Figure 4.23). The window size, representing the bottleneck pathway between the single spherical cavities, was confirmed by the mercury intrusion and extrusion results: the main intrusion peak was at 9 µm, and 97% of the mercury was not extruded after pressure release to ambient pressure, which corresponded to a pore diameter of 11 µm, shown in Figure 4.32 and Table 4.2 respectively. The cell sizes assessed on the cross sections of the MMCs shown in Figure 4.58 ranged between 10 µm and more than 500 µm. The range of values resulted from the position of the section: as the bubbles in the ceramics were randomly distributed, the probability of cutting along the diameter of a single sphere was low. Nevertheless, there were larger spheres than the aforementioned 120 µm which indicates inhomogeneities in the preform blowing process. Peng *et al.* [125] claimed a uniform cell diameter distribution of about 150 µm, but bubbles of up to 350 µm in diameter were visible in their microstructures. This confirms that deviations from the mean cell size of more than 100% are characteristic for this pore forming method.

In Equation 35 the relation between pore fraction V_{po} and the ratio of window to cell size (k) of foamed preforms is given. According to this model at a k-value of zero, which means a window diameter of zero and therefore a closed cell foam, a V_{po} of 0.74 results. Even when

the 10% uncertainty of the model [125] is taken into account this minimum is higher than the V_{po} of 0.68 found in AODY30. Consequently no windows may be expected in AODY30 which was not the case as the predominant pore fraction in this preform type was reached by the infiltration alloy and therefore most of the pores were interconnected with windows. For the AODY30 preform the model (Equation 35) is not valid and may be improved in the future.

5.2.2 Pyrolised pore formers

For the self-fabricated preforms, the target porosity range of 60 to 70% was achieved by using incomplete densification of the particles to give the intragranular fine pores, in combination with larger pores which were formed by the pyrolysis of the pore forming additive (PFA). At the relatively low sintering temperatures and times employed, the volume diffusion was kept low and sintering led to small contact points, as shown in the preform microstructure (Figure 4.22). Despite this ability to control the microstructure, the target porosity range was only reached with PFA, indicated by Φ_{tot} of 37% (AO) to 50% (MO) for preforms without PFA.

Particles with d_{50} values between 1 and 3 µm were selected as a compromise between ease of infiltration and maximum strengthening effect. Figure 2.6 shows the relationship between particle diameter and strength. The maximum gradient was reached with particles below 0.1 µm [31]. Even though the infiltration process was optimized in order to reduce residual porosity, the fine pores of MOPC20 sintered at 800°C with pore diameters below 0.2 µm (Figure 4.30) prevented full infiltration into interparticulate pores, Figure 4.56 b).

As an already established [155,163] wet powder processing route was used for the current investigations, ceramics with high hydrolysis potential like CaO were discarded. As reported by Kuang *et al.* [180], waterless agents were obligatory for CaO powder processing. Even though it is well known that MgO forms hydroxides when in contact with water, the reaction

kinetics were reported to be rather slow, depending on parameters such as the pH-value of the aqueous solution and the surface area of the powder [181]. The latter was reported to play the predominant role. However, even at very large specific surface areas, the overall room temperature hydrolysis reaction rate was shown to be comparatively slow when nanosized MgO was exposed to different aqueous solutions [182]. The reaction kinetics were characterized by a fast initial reaction followed by gradual slowing to a low rate steady-state reaction. The main reason for the different kinetics between CaO and MgO hydrolysis lies in the solubility of the respective hydroxids in water. The solubility product of $Mg(OH)_2$ is five decades lower than that of $Ca(OH)_2$ [171]. On the basis of these results, it proved possible to fabricate MgO preforms using the aqueous processing route applied to Al_2O_3 and TiO_2 preforms. Mass loss measurements of magnesia preforms, Figure 4.16, confirmed that the hydrolysis of MgO during aqueous processing led to marginal $Mg(OH)_2$ fractions compared to the feed powder, therefore demonstrating that it is possible to process MgO in an aqueous solution.

The fundamentals of PC-type pore formation in TiO_2 (TOPC) and Al_2O_3 preforms (AGPC) were investigated by Schneele [163] and Staudenecker [155] respectively. No additions were used to aid sintering in the pure oxide systems and the intergranular porosity was controlled by the sintering temperature. In order to preserve the fibre properties in the purchased fibre reinforced system (FA), glass forming binders were added and the sintering temperatures were lowered accordingly below 1000°C [117].

The pyrolysis behaviour of carbon fibres (PF) was compared to that of cellulose particles (PC). In contrast to PC, the thermogravimetric investigations for PF showed that minor mass losses occurred in an inert atmosphere up to 800°C (Figure 4.16 a). Under oxidizing conditions (air), the main decomposition started 200°C higher (at 500°C - Figure 4.16 a),

indicating stronger bonds to crack and oxidize in PF. It is interesting to note that preforms fabricated with PC with a total pore fraction, Φ_{tot}, above 0.65 could not be used for further MMC processing as they were cracked and often too weak for handling. In contrast, 81% porosity could be obtained with PF and the preforms were still suitable for further processing. The behaviour with PC was attributed to the significant expansion of up to 7.5% during sintering, as shown in Figure 4.20. This was a result of thermally-induced relaxation of the cellulose particles due to weakening of the polyvinyl alcohol (PVA) binder during heating. Mattern [114] reports that swelling of cellulose during an aqueous preform forming route led to preform cracking during drying. In the present work instead of the aqueous route a dry pressing route was applied with which preform cracking was prevented. As low cost MMC was targeted, the PF route was discarded since the cost was 10 times higher than that of PC.

Apart from the magnesia preforms (MOPC20), where two distinct peaks were found in the incremental pore size distributions, relatively homogenous pore size distributions were found for the preforms produced with PC (Figures 4.27 and 4.28). The difference in pore size distributions with similar pore former concentrations resulted from the decomposition products of the PFA. PC degraded significantly in air in the temperature interval between 250°C and 310°C where a mass loss of 85% occurred. As reported by Capart *et al.* [183], dehydro-cellulose and water vapour were formed and further decomposition in the same temperature range led to water vapour, CO and CO_2 and charcoal (char), Figure 5.3.

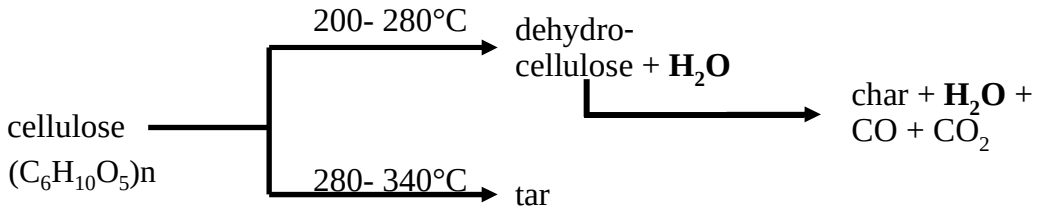

Figure 5.3 Cellulose decomposition in an inert atmosphere [183].

The newly formed water vapour led to the differences in shrinkage and pore size distribution (Figure 4.27) of MOPC20 compared to the other preforms where pores were formed with PC. The proposed progress and influence of the decomposition during heat treatment of the magnesia green parts is shown schematically in Figure 5.4. At the beginning of heat treatment (25°C), the green MOPC20 consisted of MgO, cellulose particles and PVA binder. Decomposition of cellulose started at 250°C and water vapour was formed. At this temperature, magnesia is highly reactive with water and forms $Mg(OH)_2$ according to:

$$MgO(s) + H_2O(g) \longrightarrow Mg(OH)_2(s) \qquad \text{Equation 49}$$

In the present investigations it was found, that the specific surface area of the initial MgO powder when enriched with 1.71% of moisture increased from 4.8 m²/g to 6.0 m²/g indicating the formation of $Mg(OH)_2$. This process has been reported [184] to produce high surface area catalyst support materials. A multiple hydroxide formation-calcination procedure applied to MgO powder with a surface area of less than 50 m²/g increased it to 300 m²/g.

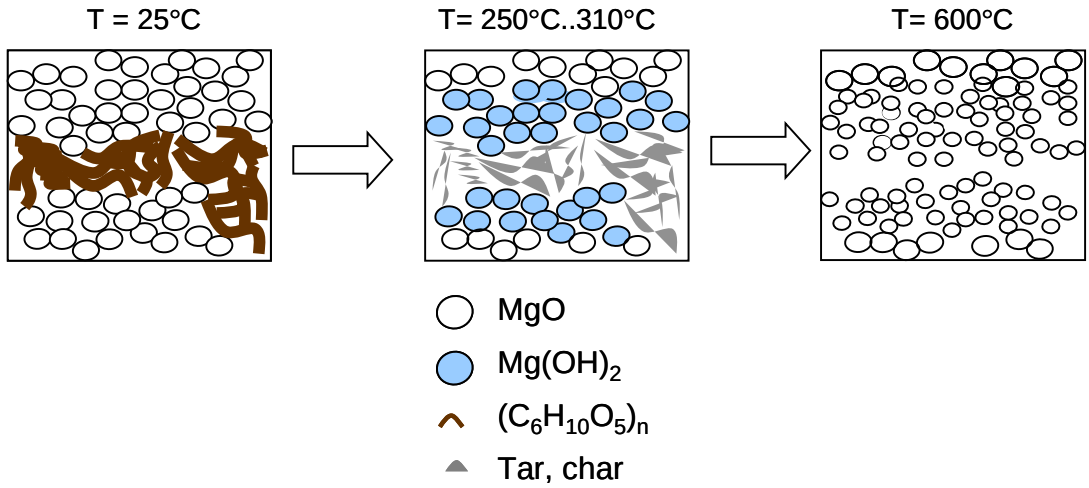

Figure 5.4 Schematic of the influence of cellulose decomposition and its solid products on the microstructure and phase composition of the MOPC20 preforms during heat treatment in an inert atmosphere.

Between 310 and 600°C the organic residues, tar and charcoal, cracked and oxidized and the $Mg(OH)_2$ calcinated. After calcination up to 600°C, further heat treatment resulted in

coarsening of the fine MgO, as indicated by a reduction in the S_{iHg} at increased sintering temperatures, Figure 4.31. The reason for the steep decrease from 3.78 m²/g to 0.70 m²/g when the sintering temperature was increased from 1200 to 1300°C is unclear and may be investigated in future.

The pore size distributions of the MOPC20 preforms sintered at 800°C and 1300°C in Figure 4.30 show a shift of the main peaks towards lower values and was attributed to the coarsening of the ceramic particles and associated neck growth at higher sintering temperatures. It is interesting to note that the large pore peak also shifts towards smaller pore sizes, as a result of a reduction in the diameter of the PFA formed channels. Thus, there had to be a migration of particles from the border toward the inside of the channel which was found in the microstructure of the MMC in Figure 4.56 b). The migration was a result of the volume increase as MgO reacted to $Mg(OH)_2$ during the degradation of PC. The density of the oxide is 3580 kg/m³ whereas that of the hydroxide is 2410 kg/m³ [160] which led to a volume increase of 32.7%. The expansion was predominantly towards the cavity originally occupied by the pore former. The particles remained in this arrangement after calcination. This was observed in the MOPC20IS where the preform was sintered at 800°C (Figure 4.56 a). Sintering at higher temperatures (e.g. 1300°C) led to coarsening of the particles due to volume diffusion. Further migration from the PFA-formed cavity toward the intergranular regions occurred and resulted in a shift of the large pore peak toward larger values.

5.3. Saturation of porous media

As shown in section 5.1, residual porosity is detrimental to the MMC properties. It is therefore important to strive for full infiltration. A prerequisite for this is an open-cell structure. In the preforms investigated in this thesis, the predominant fraction was accessible to the fluid as the preforms had between 0.2 and 2.0% closed cell porosity.

In order to achieve minimum porosity during infiltration processing, the influencing factors have to be known. During the constant pressure infiltration of SiC particle compacts, an uneven infiltration front was found where larger pores were filled prior to the smaller ones [103]. Even though Darcy´s law is based on the saturated flow assumption, characterised by a distinct infiltration front, Garcia-Cordovilla *et al.* [103] proposed it to be applicable to their infiltration problem. Consequently, their modelling accuracy was rather poor. Dopler *et al.* [113] also found unsaturated flow in Saffil™ fibre infiltration and reported that the dynamic variable saturated flow infiltration of Saffil™ fibre preforms could be modelled accurately using the saturation relation developed by van Genuchten [115] (Equation 29) which originated from soil sciences.

Evidence of unsaturated flow was found in the preforms of the present investigation. This was indicated in the saturation profiles of the constant pressure infiltrated AOPC20 preforms, where a saturation gradient was visible (Figure 4.43). This was further supported by the shape of the infiltration curves obtained in constant flux infiltration in the DSQC mode, shown for IS infiltration in Figure 4.48. The non-linearity at higher saturations indicates Darcy´s law is not fulfilled.

Table 5.1 Preform parameters of FA24 [105], AOPC20 and TOPC10 relevant for preform infiltration modelling..

		FA24[105]	**AOPC20**	**TOPC10**
Preform porosity Φ_{tot}		0.76	0.65	0.62
Specific permeability K_{SI}	$10^{-14}\cdot m^2$	96	23.7	13.1
Threshold pressure P_0	$10^{6}\cdot Pa$	0.25	0.72	2.02
Shape factor α	$10^{-6}\cdot Pa^{-1}$	21	2.25	1.25

In order to solve Equation 29 for the present preforms, Φ_{tot}, P_0 and the shape factor α have to be known. The parameters were evaluated (Table 5.1) for AOPC20 and TOPC10 using their

characteristic DSQC infiltration curves, Figure 4.47. As a reference, data for a Saffil™ fibre preform with 0.24 of ceramic volume fraction (FA24) were taken from Mortensen *et al.* [105]. With the latter values, Dopler *et al.* [113] successfully validated the unsaturated flow model.

Figure 5.5 shows the graphs of the calculated saturation function (Equation 29) between P_0 and 100 MPa. By definition, P has to be larger than P_0. Complete saturation (S=1) may never be reached in preform infiltration whereas, in the saturated flow assumed in Darcy´s model, it is by definition fully saturated behind and unsaturated in front of the infiltration front.

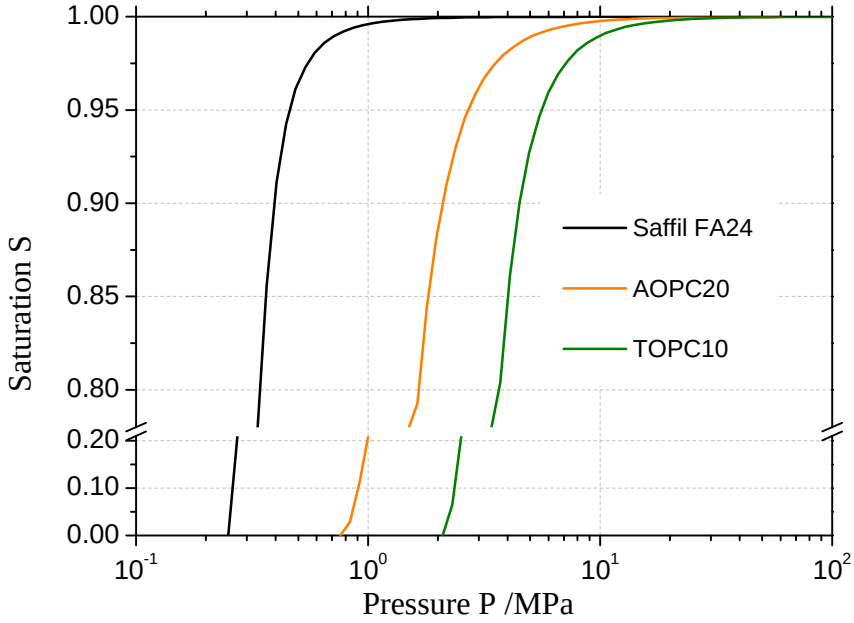

Figure 5.5 Saturation S as a function of the applied pressure P, plotted using Equation 29 with parameters of FA24 [105] , AOPC20 and TOPC10 presented in Table 5.1.

FA24 showed a saturation of 0.99 at about 1 MPa whereas the same saturation in AOPC20 was reached at 10 MPa and in TOPC10 at 20 MPa. This was the result of the lower P_0 and higher shape factor α of FA24. In terms of technical applications, the fibre preform may be infiltrated with relatively high saturation in the constant pressure gas pressure infiltration (GPI) mode, whereas residual porosity has to be expected for AOPC20 and TOPC10 since the maximum pressure of GPI is usually maintained below 15 MPa for safety reasons. Therefore, infiltration methods with higher final pressures had to be used for the particulate preforms in

the present work. These pressures were delivered by plunger driven melt pressurisation such as in squeeze (SQC) and high pressure die casting (HPDC) techniques which are constant flux methods to a first approximation. The unsaturated flow model of Dopler *et al.* [113] originated from water flow modelling in water reservoirs having a permeable soil base and were based on a constant pressure mode. An adaption of the model to the constant flux mode is discussed in the following section and validated with experimental preform infiltration results.

5.4. Modelling of fluid flow in preform infiltration

As reviewed by van Dam [185], Richards' equation (Equation 30) has been predominantly used in hydrogeology to model unsaturated dynamic water flow in soils but was recently adapted to dynamic preform infiltration in the constant pressure (CP) mode by Dopler *et al.* [113]. In collaboration work with Pokora [186] and based on these two publications, a simple numerical modelling tool has been derived and additionally an impermeable wall and the constant flux mode have been introduced. In order to solve Equation 30, the model parameters have to be evaluated experimentally, which is the main contribution of the author. The parameters were: the saturation specific parameters P_0 and α, the geometrical parameters such as preform thickness and ceramic volume fraction $(1-\Phi_{tot})$, and the relative and specific permeabilities K_r and K_s. The dynamic fluid viscosity μ of the melt was set to $1.15 \cdot 10^{-3}$ Pa·s for all calculations, in accordance to Dopler *et al.* [113]. In the following section, the factors influencing the threshold pressure of infiltration P_0, such as the wetting behaviour, and the specific permeability K_s are considered and the implication of their use in the calculations. Subsequently, the model is presented and its applicability is validated.

5.4.1. Reactivity of the metal-ceramic systems

Several research groups [71,87,88,103] have proposed that reactivity between the fluid and the porous medium enhances wetting by reducing the wetting angle θ which, in accordance to

Equation 20, reduces P_0. However, Beyer [53] and Mattern [114] proposed complete non-wetting conditions ($\cos\theta = -1$) in TiO_2 and Al_2O_3 preform infiltration with Al alloys.

The ΔG value in the systems at any given temperature and concentration is a measure of reactivity. The temperature dependencies of the standard free energies of formation ΔG_0 of metal-metal oxide systems of the Me-Me_xO_y type are usually presented in form of Ellingham-Richardson-Jeffes diagram [89], of which an extract was given in Figure 2.11. At constant temperature, oxides of Me-Me_xO_y systems with higher ΔG_0 values than that of Al-Al_2O_3 are reduced by Al and therefore represent reactive systems. This is the case for the Si-SiO_2, Ti-TiO_2 and Ti-Ti_xO_y, which are rated as reactive, in contrast to Al-MgO and Al-CaO whose curves are below that of Al-Al_2O_3 and therefore no reaction with Al is expected. Experimental results reported by Niu *et al.* [187] did not confirm the passivity of the Al-CaO system at elevated temperatures. Here a CaO coating was dissolved partially by liquid Al, due to the formation of $AlCa_2$ intermetallics. Therefore statements about the non-reactivity of a given metal - oxide ceramic system based on the position of the curve in Ellingham-Richardson-Jeffes diagram are not sufficient for a full classification of the system.

Numerical thermodynamic modelling was considered to be a more accurate tool to classify reactive systems. Using metal and ceramic data bases, the modelling of metal-ceramic reactions with the FACTSAGE software led to accurate results for the Al-TiO_2 system [94]. In the present work, this code was used to calculate the systems (section 4.1.1). For Al-CaO the phases found in the experiments [187] were confirmed to be the most stable phases, Figure 4.2. Further, the reactivity of the system was confirmed, indicated by a negative ΔG, Figure 4.1.

As shown in the thermodynamic calculations and reported by others [7,77], the Al-Al_2O_3 system is assumed to be non-reactive at temperatures below 800°C which are used for preform infiltration. Similarly, Al-ZrO_2 and Al-Y_2O_3 were identified as non-reactive,

indicated by zero values of the free energy of formation ΔG, Figure 4.1. Only the Al-Al_2O_3 was taken as a reference non-reactive system and the other non-reactive systems (Al-Y_2O_3, Al-ZrO_2) were not included in the present experiments.

It has been shown that the reduction of SiO_2 with liquid Al can be used to synthesise Al(Si)-Al_2O_3 composites [77,23,101]. The Si formed by reduction dissolved in the melt and subsequently solidified to an Al-Si alloy matrix between the reaction-formed Al_2O_3. The pure Al-SiO_2 was not investigated due to the low mechanical performance of SiO_2 [149], presumably resulting in a low reinforcing effect of the resulting MMC. However, an alumina preform (AGPC15) with silicate binder surfaces was investigated.

The thermodynamic calculations confirmed the high reactivity of the Al-TiO_2 system. This has been reported by others [53,155,163] aiming to synthesise ceramic-intermetallic composites (CIC) consisting of reaction-formed Al_2O_3 in a Ti_xAl_y matrix. In contrast to the Al-SiO_2 systems, reduction to metallic Ti was not observed experimentally. This conforms with the thermodynamic calculations where TiO_2 is partially reduced to form suboxides like TiO and Ti_2O_3 in combination with the aluminides $TiAl_3$ and TiAl, see section 4.1.1. Beyer [53] found that the squeeze casting of an Al alloy into TiO_2 preforms with a median grain size of 0.3 µm resulted in strong exothermic reactions and temperature increases of up to 1300°C inside the preform. Due to the drastic temperature increase, the viscosity and surface tension of the alloy, whose temperature dependency is described by Equation 1, decreased significantly. As a result of this heating, the die system could not be sealed by solidification and resulted in hazardous spurting of the melt out of the tool. Thus, the processing of fine grain TiO_2 preforms was considered to be uncontrollable. Beyer [53] also showed that macroscopic reactions could be observed with TiO_2 powders having a median grain size of 1 to 5 µm [155,163]. A subsequent heat treatment up to 800°C with low heating rates led to consistent

composites comprising a Ti_3Al matrix with embedded Al_2O_3 and Ti suboxides of the Ti_2O_3 and TiO type. In the present study, the resulting CIC composite was reproduced and this was confirmed by differential thermal analysis on TOPC10IS composites (section 4.8.9).

In order to alter the reactivity of the ceramics in contact with molten Al, other oxide ceramics were considered. The Al-MgO system exhibited low ΔG values, resulting from the reaction of Al and MgO to the ternary spinel phase $MgAl_2O_4$ (Figure 4.2).

5.4.2. Static wetting

The sessile drop test was employed to investigate the influence of the substrate chemistry on the static wetting behaviour of the Al-alloys (IM and IS) in contact with Al_2O_3 (AF), TiO_2 (TF) and MgO (MO). Fine grained powders and relatively high sintering temperatures were used to produce substrates of maximum density. Residual porosity ranged between 1.9 and 4.9% (Table 4.1).

A vacuum furnace was used for the sessile drop test in which a minimum pressure of 10^{-3} Pa could be achieved. The oxygen partial pressure $p_{O2,calc}$ in the sessile drop equipment was estimated using FactSage thermodynamic software and input variables as close as possible to the experimental set-up. Here residual oxygen was gettered using 100 g of Ti-sponge placed directly on the heating coils whose energy input was controlled to give a substrate temperature of 750°C. The furnace volume was 9 dm³ and was assumed to be completely filled with the Ar flushing gas containing 1 volume part per million of oxygen. Calculations were performed first taking into account Ti and the gas, second with the additional 2 g of Al representing the alloy droplet and third with an additional 0.2 g of Mg, the alloying element in IM. As the alloy had no contact with the Ti, the Ti_xAl_y and Ti_xMg_y phases were suppressed.

The calculated $p_{O2,calc}$ was $4.5 \cdot 10^{-41}$ Pa for the first combination and $8.5 \cdot 10^{-42}$ Pa for the second and third variations. The latter similarity indicates that the Mg addition had no

influence on the $p_{O2,calc}$. The lower value reported for Al indicates that Al oxidation takes place prior to that of Ti. This may be the reason for the oxidation of a liquid alloy IS in sessile drop tests prior to droplet formation. As proposed [83], oxidation may only be prevented with metals such as Zr. The calculation also indicated that alumina is more stable than magnesia, which further supports the reactivity of the Al-MgO system. Zhen *et al.* [76] reported the maximum oxygen partial pressure to prevent oxidation of Al melts at 700°C to be 10^{-44} Pa. This is lower than the calculated value of $8.5x10^{-42}$ Pa for the system with Al. However, as oxide stability decreases at higher temperatures the value is plausible.

In contrast to the alloy IS (Al-12 wt.% Si), a droplet with a bright surface was formed (Figure 4.4) with the alloy IM (Al- 9 wt.% Mg) which was attributed to the different alloying element. Anson *et al.* [19] reported a shell of Mg vapour surrounding liquid Al-Mg-Si alloys in high vacuum experiments, which protected the melt from oxidation of Al. In the present experiments it has to be assumed that oxidation of the metal droplet was prevented by evaporation of Mg which led to a shielding atmosphere around the droplet and enabled the formation of a droplet.

All systems were identified as non-wetting with no change in contact angle during the holding period of 30 min. Sobczak *et al.* [80] found no decrease in wetting angle in the pure Al-Al_2O_3 system within this period. They found wetting angles of 120° to 123° which were significantly smaller than those of 148° and 155° found for IM-Al_2O_3 in the present research. The difference in wetting angle has to be attributed to the difference in the alloy chemistry and pinning of the droplet´s triple line on the substrate by intrusions into the substrate´s microporosity in combination with gravity-driven segregation of an iron rich phase. Figure 4.8 a) shows a micrograph of both phenomena.

The macroscopic wetting angle data indicate non-wetting behaviour and therefore spontaneous infiltration into open pores is only possible by applying an external pressure. The metallostatic pressure on the substrate due to the droplet height was calculated as 10^{-4} MPa. By applying Washburn´s relation (Equation 21) in combination with the mean θ_{st} of 152° and the surface tension γ_{lv} of the alloy IM of 0.871 N/m [19,20], the pressure required to fill a 2 µm diameter pore was calculated to be 0.625 MPa. This is nearly 5 times higher than the calculated metallostatic pressure. Despite this, some pore infiltration was observed and these micro-intrusions must result from the wetting conditions on the micro-scale under the droplet. In conclusion, the intrinsic wetting angle θ_{intr} has to be lower than 90° and therefore much smaller than θ_{st} measured in the sessile drop test. Sobczak *et al.* [80] found the same behaviour but at significantly higher process temperatures (>1000°C). Here evaporation of Al_2O takes place as a result of the high temperature (described by Equation 9). As a result, local rupture of the oxide film at the microscopic asperities of the interface under the weight of the droplet could facilitate the penetration of surface pores by the metal. This local loss of the oxide could lower θ_{intr} at the pore/metal interface, thus allowing the metal to penetrate the pore under conditions where the macroscopic θ_{st} based on the drop profile has a large obtuse value. The enhanced wetting at lower temperatures (750°C) in the present experiments was a result of evaporation of Mg which prevented oxidation of the droplet surface and therefore enhanced wetting below the droplet.

In contrast to the micro-intrusions, segregation of the Fe-rich phase prevented movement of the triple line. An example of the interface after the test is shown in Figure 4.9. No published literature could be found for commercial casting alloy - ceramic wetting couples. Flores *et al.* [145] published work on the purification of iron-contaminated Al alloys, stating that the quarternary $Al_8FeMnSi_2$ intermetallic phase segregates to the melting furnace walls

during extended holding and acts as nuclei for further crystallization of Fe-rich phases, resulting in a decrease of Fe in the liquid phase. Similarly, an Al-Fe-Mn-Si phase was found on the substrate, Figure 4.9, which indicates that this phase solidified prior to the residual droplet. As further indicated by the crack plane passing through the pure substrate, bonding between the iron-rich phase and the substrate was stronger than the substrate´s tensile strength which further supports adhesion forces between the Fe-rich phase and the substrate, resulting in pinning of the droplet.

Taking into account the inaccuracy of angle measurement of ± 5°, similar wetting behaviour was found when IM-AO was compared with the reactive systems IM-TO (TiO_2) and IM-MO (MgO). This has to be attributed to the segregation effect which prevents direct contact between the substrate and the alloy.

In summary, in the sessile drop tests, Fe-rich intermetallics nucleated on Al_2O_3 and hindered spreading of the droplet. Where the intermetallic layer was interrupted, the metal could penetrate open porosity of the substrate. As a consequence, the measured θ_{st} did not represent the wetting angle of an Al alloy melt on a ceramic substrate.

5.4.3. Dynamic wetting

Mortensen and Wong [121] stated that, even in optimised experimental conditions, the static wetting angles were not able to describe wetting in dynamic preform infiltration and θ_{st} is not equal to the dynamic wetting angle θ_{dyn}. Garcia-Cordovilla *et al.* [103] proposed a relation between P_0 and θ_{dyn} (Equation 20). In the present study the P_0 values were determined from the pressure-saturation curves in DSQC according their procedure and an example is shown in Figure 4.48. In any given system, the bulk density of the ceramic phase ρ_p, the surface tension of the infiltration alloy γ_{lv}, the ceramic phase volume fraction V_p and the specific surface area S_i were assumed to be constant during infiltration. Compression, which appeared

in all preforms during infiltration, may influence the parameters V_p and S_i. In the DSQC process it was rather low, between 0.02 and 0.04 (Table 4.8), leading to negligible variations in V_p. The parameters of the preforms investigated as well as P_0 and the resulting cos θ_{dyn} are listed in Table 5.2 for both IS and IM infiltration.

As reported by Koeber and Loehberg [25], the surface tension γ_{lv} of Al-12 wt % Si, (composition similar to IS), is similar to that of pure Al at any given temperature. Therefore Equation 1, which is valid for pure Al, is also applicable for calculating γ_{lv} in IS. At the initiation of preform infiltration, the melt temperature T_m was 665°C, resulting in a surface tension of 0.883 N/m, which agrees with experimental values [19] which were in the range of 0.801- 0.889 N/m for an Al-Si alloy.

The specific surface area S_{iHg} was measured experimentally using mercury intrusion porosimetry (MIP) and was used in preference to gas absorption (BET) as it is closer to the preform infiltration procedure. This is supported by Garcia-Cordovilla *et al.* [103] who showed that BET results are not relevant in pressure infiltration.

Table 5.2 Preform specific and infiltration parameters and calculated θ_{dyn} with IS and IM infiltrations derived where required from Equation 20.

	P_0 MPa	S_{sHg} m^2/g	$1-\Phi_{tot}$	ρ_p kg/m^3	S_{iHg} $10^6 m^2/m^3$	cos θ_{dyn}	θ_{dyn} °
Infiltration with IS							
AOPC20	0.72	0.86	0.35	3980	1.84	**-0.44**	**116**
AGPC15	1.27	1.49	0.34	3956	3.04	**-0.47**	**118**
TOPC10	2.02	2.30	0.38	4260	6.01	**-0.38**	**112**
TOPC20	0.91	0.76	0.38	4260	1.98	**-0.51**	**121**
MOPC20	0.95	0.75	0.38	3580	1.65	**-0.65**	**131**
AODY30	0.65	2.41	0.32	3920	4.45	**-0.17**	**100**
FATO	0.94	5.85	0.29	3830	9.15	**-0.12**	**97**
Infiltration with IM							
TOPC10	2.31	2.30	0.38	4260	6.01	**-0.43**	**116**
MOPC20	1.05	0.75	0.38	3580	1.65	**-0.72**	**136**
FATO	1.35	5.85	0.29	3830	9.15	**-0.17**	**100**

Compared to Hg, the Al melt may contain impurities or oxide films which are retained on the preform in a similar manner to the effect of ceramic filters in the gating system of castings [6]. The pores of preforms are significantly smaller though and retention may block the entrances to the pores. This effect was reported by Papworth and Fox [138] who observed delamination of the metal phase on the top of the squeeze cast infiltrated MMC due to oxide film agglomeration. In the present work, there was no evidence of this oxide layer retention effect in the microstructural analysis of the interface (Figure 4.59) and therefore blocking effects were discounted.

Preforms with PC did not have significant bimodality in their pore size distributions (Figure 4.27). This configuration was found suitable for dynamic wetting angle evaluation [103]. With a θ_{dyn} of 116°, the pure Al_2O_3 preform AOPC20 in contact with IS showed similar behaviour to Al_2O_3 with a silicate binder (AGPC15) which had a θ_{dyn} of 118°. Therefore, no significant influence of the binder on θ_{dyn} was found.

For the study the binder content of AGPC15 was in the range of that used for Saffil™ preforms [118, 120]. The θ_{dyn} values reported for pure Al into Saffil™ fibre preforms was in the range of 102° to 111° [121] and therefore lower than that found for AGPC15 (118°). With Saffil™ fibre preforms, a maximum ceramic volume fraction V_f of 0.25 is achievable which is significantly less than the V_p of 0.35 of AGPC15. A trend of decreasing θ_{dyn} with lower V_f was found [121]. By a linear interpolation of their results in the $\theta_{dyn}(V_f)$ diagram to a V_f of 0.35, a θ_{dyn} of 119° was found. Taking into account the scatter in θ_{dyn}, which was assessed as ± 3° based on the scatter in P_0 measurements of identical preforms, AGPC15 and Saffil™ fibre preforms show similar θ_{dyn}.

The reactive preforms TOPC20 and MOPC20 infiltrated with alloy IS showed higher θ_{dyn} than that found for AOPC20. In contrast, the TiO_2 preform TOPC10 with identical chemical composition but finer porosity and grains, showed lower θ_{dyn} than TOPC20. Reaction products were only found in TOPC10IS as shown in Figure 4.60, which may explain this variance. In contrast to Garcia-Cordvilla *et al.* [103] who stated that the reaction layer would partially block the entrance and thereby increase P_0 and θ_{dyn}, a lower θ_{dyn} was found in the present investigations when a reaction layer was formed. This behaviour has to be attributed to the aforementioned exothermic reaction and a resulting increase of the melt temperature, possibly to 1300°C [53]. Applying Equation 1 at this melt temperature, γ_{lv} is 0.650 N/m and therefore 26% lower than at 665°C. The lower surface tension of the melt close to the ceramic grain presumably acts as an lubricant, facilitating infiltration and leading to a lower θ_{dyn} than observed in TOPC20, where no reactions were found.

Even though MOPC20 was rated as reactive, θ_{dyn} was significantly higher than in the AO-type preforms. In contrast to the TiO_2 preforms, no evidence of reaction products was found in the infiltrated MMC microstructure (Figure 4.60 c) or post SDTA (Figure 4.63 b). Therefore the predicted spinel phase $MgAl_2O_4$ was not formed which has to be attributed to its kinetic inhibition [106,140]. This agrees with Jonas *et al.* [106] who reported that Mg additions had no significant influence for pressure infiltration of Al into Al_2O_3 preforms. However, others [15,17,140] have proposed that $MgAl_2O_4$ formation is the key factor required to facilitate infiltration of Mg-containing alloys in Al_2O_3. The present investigations concentrated on AlMg alloy (IM) infiltrations into the reactive preforms TOPC10, FATO and MOPC20 as here reactions were most probable. Similar to Jonas *et al.* [106], the change of the main alloying element from Si (IS) to Mg (IM) showed only a marginal increase in θ_{dyn} of 3° to 5°. In contrast to infiltration with IS, the reaction products Al_2O_3 and $TiAl_3$ were formed in the TiO_2

preforms with IM, Figure 4.67. For TOPC10IS, the reaction started after the preform was infiltrated, indicated by the similar infiltration curve gradients for IS (Table 4.5) and IM (Table 4.6). The reduced gradient in FATO indicates that the reaction had already started during the recording of the infiltration curve, at about 3.8 mm infiltration depth, Figure 4.64. This behaviour was attributed to the different grain size of the reactive TiO_2 phase, which was between 1 and 10 µm in TOPC10 and below 0.2 µm in FATO. Beyer [53] found spontaneous reaction during infiltration for fine (d_{50} < 0.5 µm) TiO_2 whereas no reactions were found with coarser powders (d_{50} > 2 µm). Even though reactions in FATO occurred immediately after the melt entered the preform, there was no influence on P_0 and, as a consequence, no influence on θ_{dyn}. The retardation of the reaction was a result of the relatively high activation energy for the aluminothermic reaction, which was reported as 474 kJ/mol TiO_2 [53].

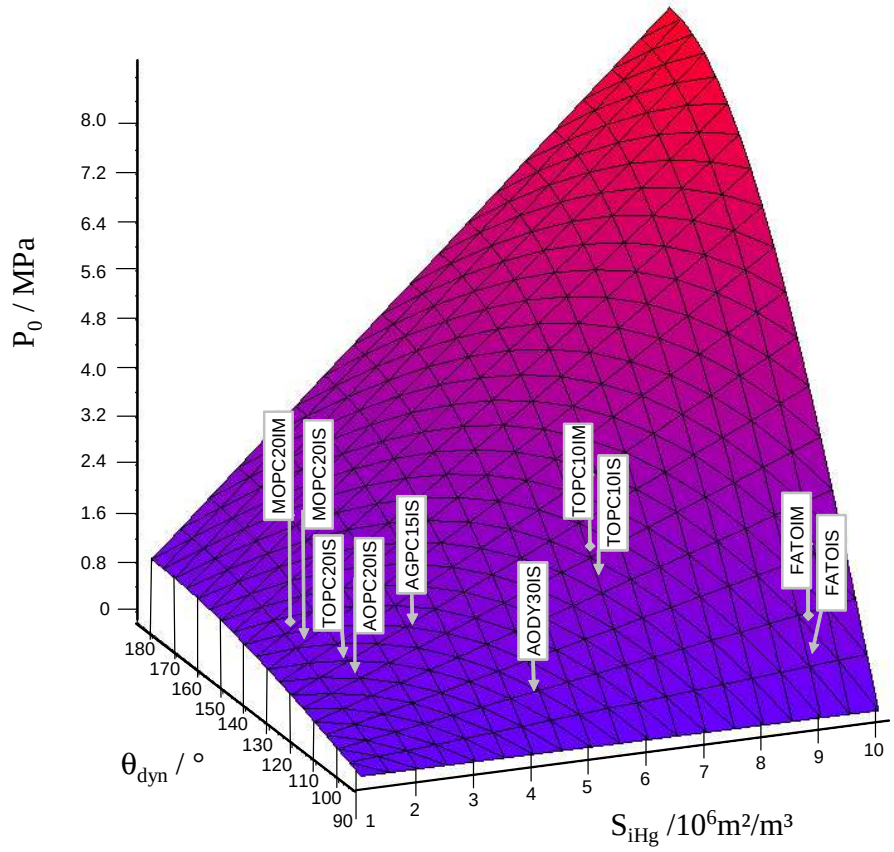

Figure 5.6 Threshold pressure P_0 as a function of wetting angle θ_{dyn} and the specific surface area per unit volume S_{iHg}.

As a summary, P_0 is shown as a function of S_{iHg} and θ_{dyn} in Figure 5.6. The surface in the 3D cartesian coordinate system was calculated using Equation 20 on the assumption of a fixed ceramic volume fraction V_p of 0.35 and fluid surface tension γ_{lv} of 0.883 N/m. Figure 5.6 also shows the positions of the experimental preforms and infiltration data presented in Table 5.2.

From a technical standpoint it seems favourable to achieve low P_0. To do so, it is necessary to target low S_{iHg} and θ_{dyn}. As shown in the present investigations, the latter could not be influenced significantly, even though reactivity was observed. However, S_{iHg} could be influenced significantly by varying the preform processing conditions as demonstrated for TOPC10 and TOPC20 by varying the PFA content and sintering temperature, Table 5.2. The conditions were even stronger for MOPC20, where S_{iHg} could be influenced by a factor of 8 by variation of sintering temperature (Figure 4.31). Variations in S_{iHg} influenced ligament sizes of the metal phase. Lowering of S_{iHg} led to coarsening of the ligaments and, as discussed in 5.1, to a lower mechanical performance. Therefore a compromise between low P_0 and high mechanical performance has to be found.

The assumption of complete non-wetting of non-reactive and reactive preforms [53,114] could not be confirmed and may falsify modelling results. For example, AOPC20 has a θ_{dyn} of 115° the cosine of which is equal to -0.44 and therefore 2.4 times lower than would be expected for non-wetting ($\cos \theta_{dyn} = -1$). The difference in absolute values is significant for the AO preforms. Assuming θ_{dyn} is identical to that of AOPC20, at S_{iHg} of 9.96 m^2/m^3 (Table 4.2), P_0 is equal to 4.0 MPa compared to 9.5 MPa for the complete non-wetting assumption.

The present investigations showed that even if reaction phases were observed in the resulting MMC, the reaction had no influence on P_0 due to the delayed initiation of the reaction. Nevertheless, an interesting phenomenon in TOPC10 infiltration in ISQC has to be attributed to reactions and its effect on reducing P_0. Figure 4.75 shows that, for all but TOPC10, the

preform compression, c_{pr}, increased with increasing v_0. At a v_0 of 0.36 m/s the preform TOPC10 showed an intermediate low c_{pr}, which was as low as that found for the slowest infiltration (DSQC). The homogeneity of the resulting MMC was comparable or even better than the MMC resulting from DSQC infiltration, as indicated by low void fractions shown by comparing the CT-images in Figures 4.73 and 4.51.

An intermediate minimum of θ_{stat} was proposed in reactive systems [87], shown schematically in Figure 2.10. This minimum is reached when the spreading velocity keeps pace with the formation of the newly-formed interfacial phase. In ISQC_10, the preform TOPC10 was infiltrated dynamically, where the pressurized melt was forced to fill the preform porosity and therefore a θ_{dyn} has to be implemented. For TOPC10, S_{iHg} was $6.01 \cdot 10^6$ m^2/m^3 (Table 5.2). Therefore, with 38% porosity and for the standard preform size of 61 mm x 42 mm x 8 mm, the overall preform inner surface area was 123 m^2 and the overall pore volume $1.27 \cdot 10^{-5}$ m^3. For ISQC_10 the latter was filled with a v_0 of $2.8 \cdot 10^{-3}$ $m^3 s^{-1}$ (Table 3.8) which therefore took 4.5 ms. Assuming coverage of the entire inner surface area, the rate of new surface formation dA/dt was 27.3 m^2/ms. Taking into account the low porosity and the compression of the preform, this is assumed ideal for easy infiltration in terms of low P_0 and the shape factor α. On the other hand, at similar v_0 of 0.36 m/s (HPDC_18), the phenomenon of intermediate low compression was not observed in HPDC infiltration of TOPC10. This has to be attributed to the significantly higher turbulence in HPDC_18, indicated by a Weber number We of 2015, compared to 252 for ISQC_10 during die filling. As reported by Campbell [6], in HPDC significant amounts of oxide films are formed on liquid Al which increase with rising We. In contrast to DSQC, in HPDC a massive amount of oxide film was formed and filtered on the surface of the preform when the melt entered it. This is supported by the fact that, for corresponding v_0, the preform compression was higher in HPDC than in ISQC. Future work should focus on the applicability of the model of Aksay *et al.* [87] on pressure infiltration of

reactive preforms in order to determine optimum v_0 to S_{iHg} combinations resulting in easy infiltration and attain maximum MMC performance.

5.4.4. Preform permeability

The specific permeabilities of the preforms were investigated and compared to reported Saffil™ fibre preform (FA) data [112]. For FA, the reinforcement was reported to be aligned perpendicular to the direction of fibre sedimentation during preform fabrication [119]. This results in a strong anisotropy in permeability and the parameter $K_{S||}$ along the fibres was measured to be 2.4 times higher than $K_{S\perp}$ (in perpendicular direction) [113]. Based on their experimental results, a model was proposed [112] to predict the preform permeability of FA for $K_{S||}$ (Equation 31) and $K_{S\perp}$ (Equation 32) directions, depending on the volume fraction (V_{sf}) and mean radius (r_{sf}) of the fibres. The permeabilities for the different directions as a function of V_{sf} are shown in Figure 5.7. These were calculated for r_{sf} of 0.5, 1.0 and 2.0 µm. This also includes the measured data of this project (Table 4.4) and data reported for FA with V_{sf} of 0.24 (FA24) [112]. The latter showed good agreement for a r_{sf} value between 1 and 2 µm, confirming the applicability of the model.

Similar to FA, an anisotropic permeability was found in the fabricated particulate preforms as indicated by K_{SP} to K_{Sl} ratios larger than unity (1.5 to 4.8 - Figure 4.38). K_{SP} and K_{Sl} represent the permeability in the perpendicular and in the plane direction within particulate preforms, respectively. This behaviour results from the alignment of the pore formers PC or PF during pressing and led to pores arranged along the X-Y plane of the preform. Consequently, the main axes of the metal ligaments were aligned along the x- and y-directions of the resulting MMCs. This is illustrated to good effect in TOPC20IS in Figure 4.54 (b).

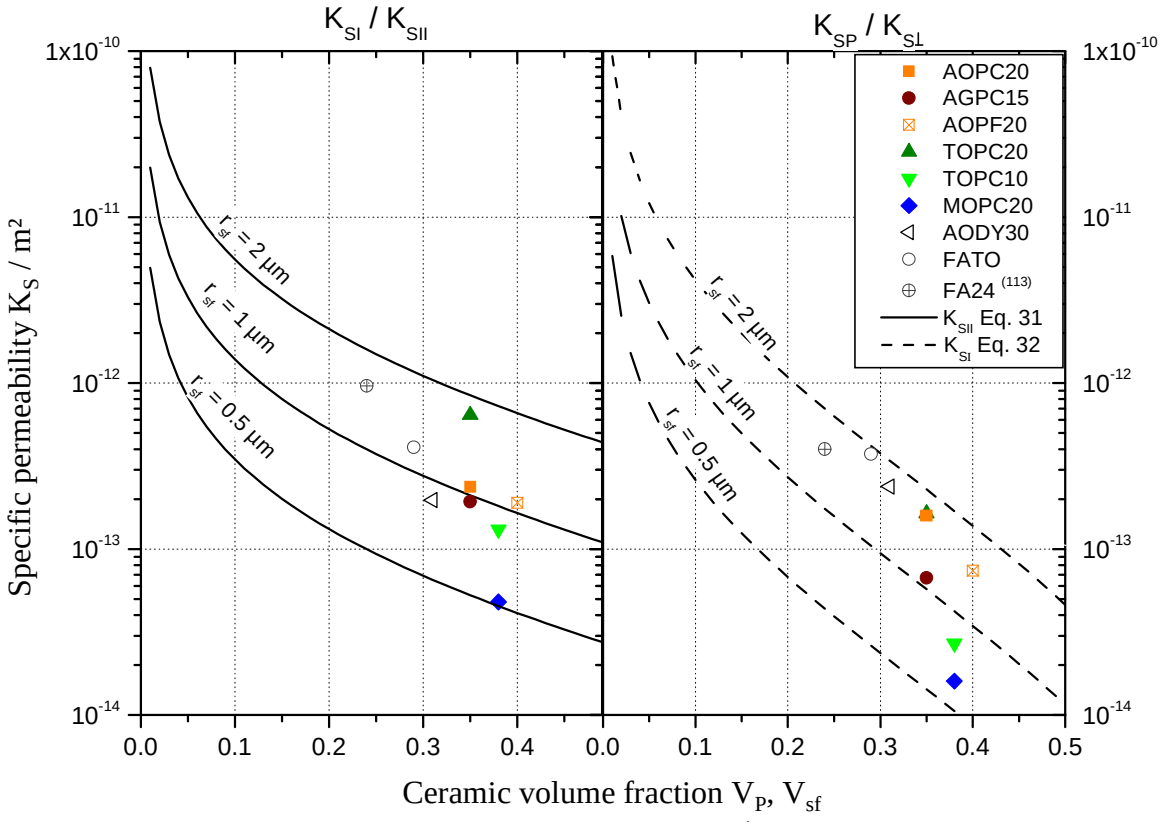

Figure 5.7 Modelling and experimental K_s as a function of V_p (particulate preforms) or V_{sf} (FA type): parallel (K_{SI}, K_{SII}) and perpendicular (K_{SP}, $K_{S\perp}$) to the direction of: sedimentation (FA) or expansion (AODY30), green pressing (with PFA).

The anisotropy of the pore structure is reflected in the preferential filling seen in Figure 4.40 when working at constant pressure. The melt flowed predominantly along the x-direction, the direction of the highest permeability (K_{SI}). Additionally, the compression of the preform during constant flux (CF) infiltration in the ISQC mode was influenced by the anisotropy, as the microstructure of TOPC10IS shows in Figure 4.72. Here the width of the uncompressed region surrounding the initial preform was 1.9 times smaller along the z-direction relative to the x-direction. This value corresponds exactly to the ratio of K_{SI} to K_{SP} for TOPC10. It is concluded that, for both CP and CF modes, the main saturation of the preform took place along the direction of higher permeability (x-axis). This is a disadvantage as the x-axis was the longest dimension of the present preforms.

In order to achieve low infiltration pressures, short filling distances with high permeability should be aimed for. Therefore high permeability along the z-axis should be targetted. This was investigated by Mattern [114] as a part of a project parallel to the present investigations. So called freeze cast preforms were synthesized using directional crystallization of an aqueous ceramic slurry. The microstructures of TOPC20IS is compared to that of the MMC resulting from the freeze cast preform (FC) and is shown in Figure 5.8 a) and b).

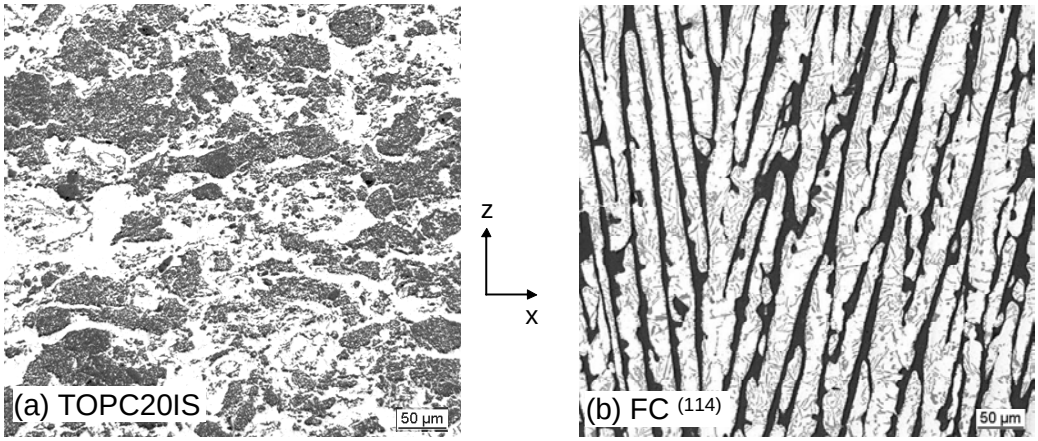

Figure 5.8 Microstructure of a) TOPC20IS and b) Freeze cast (FC) of Mattern [114]. Light and grey phases are the metal and dark the ceramic.

As discussed in 5.1 for AODY30IS, in the freeze-cast preform MMCs it was similarly found that mechanical properties were rather poor due to the large ligaments. In order to optimize both high permeability and mechanical behaviour, future work should target a compromise between short ceramic ligaments between the metal matrix and isotropic permeability.

Apart from S_{iHg}, it would be advantageous to evaluate the permeability from intrusion porosimetry. Leon [110] proposed that the permeability K_{MIP} of a porous body should be calculated using Equation 23. Using the mercury intrusion porosimetry (MIP) data, mean volumetric pore diameter d_{Hg} and the porosity Φ_{Hg} (Table 4.2), it was found that there were significant deviations of up to an order of magnitude between measured and calculated values, as shown in the comparisons of K_{MIP} with K_{SP} and K_{SI} in Figure 5.9.

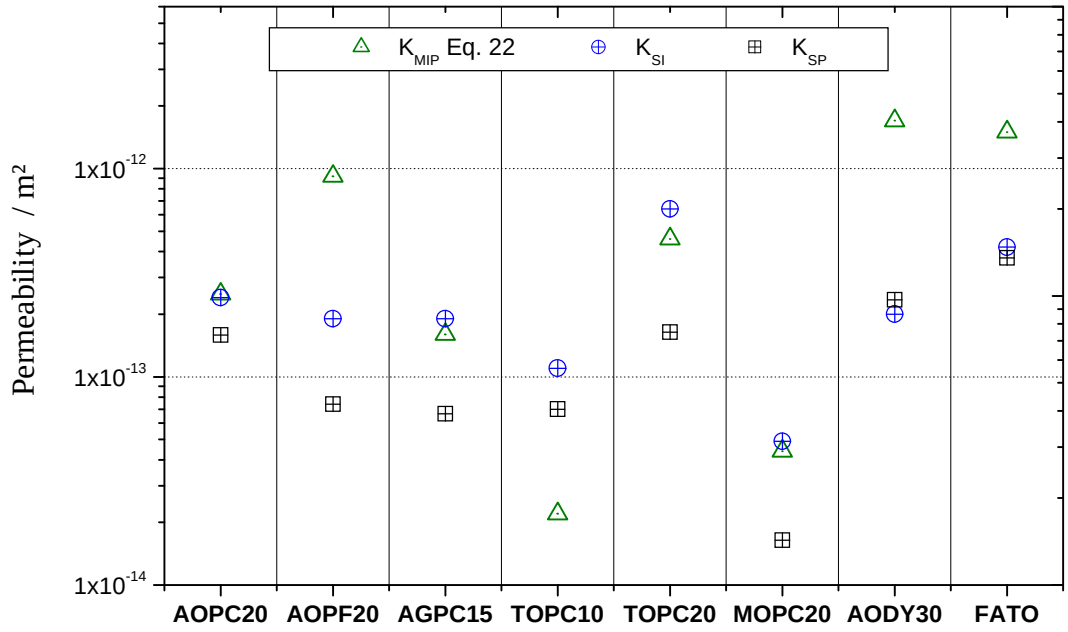

Figure 5.9 Permeability of preforms: K_{MIP} calculated using Equation 23 [110] with results of mercury intrusion porosimetry experiments. K_{SI}, K_{SP}: results of water flow experiments (4.6.4).

For AOPF, AODY30 and FATO the model overestimates the values while for TOPC10 it underestimates the value. For AOPC20, AGPC15, TOPC20 and MOPC20 the calculated values are between K_{SP} and K_{SI}. MIP data seem only applicable for calculating preform specific values if the pore size distribution is smooth such as that for AOPC20. The AOPF20 and the procured preforms had bimodal distributions and therefore large deviations were found. Further, directional properties within the preforms (e.g. the anisotropy in permeability) cannot be resolved with the present MIP equipment. In summary, the permeability calculated from MIP results is not sufficiently accurate to characterise the pore structures and therefore it is recommended that additional characterisation methods, such as water permeability measurements, are also used.

Apart from the specific permeability, the relative permeability K_r , defined in Equation 27, is required. It is a function of the saturation S and the two parameters A and B in Equation 27. As reported [113] for preform infiltration, accurate modelling results could be achieved with A and B set at unity. A similar behaviour was assumed for the present preforms and therefore

Equation 27 leads to Equation 50, which was used for modelling dynamic preform infiltration in the following section.

$$K_r = S \qquad \text{Equation 50}$$

5.4.5. Dynamic preform infiltration model

In Richards' model, phase changes during infiltration in the liquid or porous solid are generally neglected and isothermal conditions are assumed. The latter was not the case for the present experiments. In the constant flux infiltrations, a plunger was used to press the melt into the pores of the preform. In order to achieve dense MMCs, pores in the sub-micron scale had to be infiltrated. The gap between the plunger and the die was about 10 µm and, as a result, when under isothermal conditions at temperatures above the solidus, the melt would be forced out of this gap rather than filling the porosity. The gaps between the plunger and die and the die parting line were sealed by solidifying the melt in the gap achieved by using die temperatures below the metal solidus [143]. The die was held at 250°C in HPDC and ISQC and at 450°C in DSQC. The latter was still about 100°C below the solidus of the alloy IS and sufficient as no melt was lost in any of the experiments.

The temperature profile recorded in the centre (T_{centre}) near the preform during infiltration in DSQC (Figure 4.46) and the measured solidus of 566°C of the alloy IS (Figure 4.45) suggested that the melt was in the liquid state for more than 10 s inside the preform. In the constant flux mode, infiltration took less than 1 s to fill the entire porosity of the preform and therefore it was assumed that no premature solidification occurred. Therefore an isothermal process of a rigid porous preform was assumed during infiltration modelling. Consequently, momentum and energy balance equations became irrelevant and the solid metal fraction was considered to be nil throughout.

As the predominant fluid flow was along the high permeability x-axis of the preforms fabricated using pore forming agents (e.g. AOPC20), a one-dimensional flow was assumed for the present simple infiltration model.

Richards' equation for variably saturated soil water flow has a clear physical basis. Therefore, it is generally applicable and can be used for fundamental research and scenario analysis. The equation is difficult to solve because of its parabolic form in combination with strong non-linearity of the soil hydraulic functions which relate water content, soil water pressure head and hydraulic conductivity. The results depend largely on the structure of the numerical scheme and the applied time and space steps [185]. Special attention has to be paid to the procedure with respect to the boundary conditions. Both finite difference and finite element methods are used to solve Richards' equation. In one dimensional modelling, the finite difference approach is advantageous because it needs no mass lumping to prevent oscillations and is easier to implement in numerical routines.

A mass conservative finite volume scheme was used to solve Richards' equation. As shown in Figure 5.10, fixed nodes and temporal spacing were used. The spatial and temporal discretization was performed as shown graphically in Figure 5.10. The subscript i is the node number which is increasing toward higher x-values whereas the superscript j is the time level and $\Delta t^{j} = t^{j+1} - t^{j}$. All the nodes were in the centre of the control volumes with $\Delta x_u = x_{i-1}$, $\Delta x_l = x_i - x_{i+1}$ and Δx_i the cell thickness. The spatial averages of K were calculated as geometrical means on the border of the control volumes. The values of K and S were taken at the old time level j (explicit linearization), which made it possible to calculate the new pressure p and simultaneously p_l^{j+1} without iteration. Details of the finite difference code used for preform infiltration modelling have been published by Pokora [186].

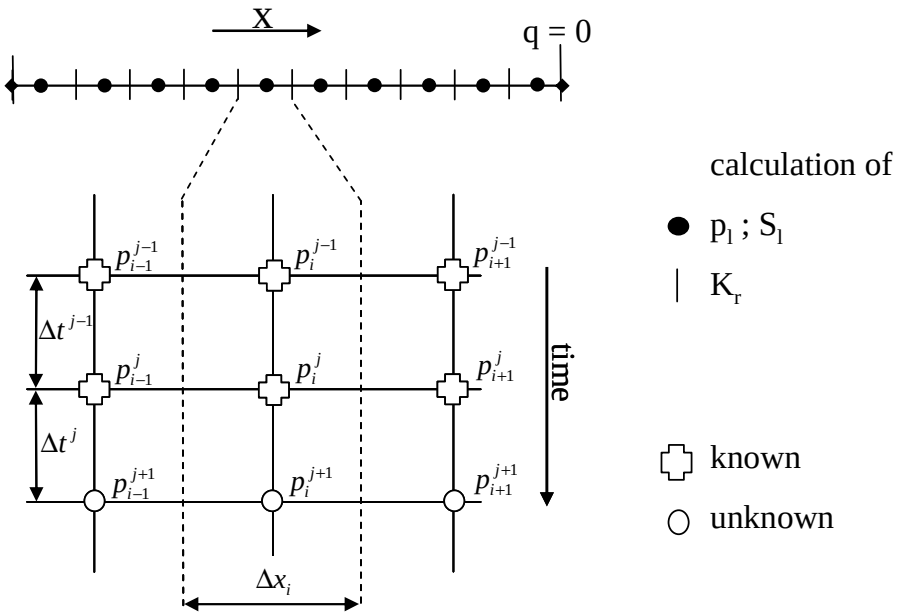

Figure 5.10 Constant distance grid for 1D modelling of preform infiltration and model used for spatial and temporal discretization to solve Richards' equation [185].

Both constant pressure (CP) and constant flux (CF) infiltration modes were implemented into the Preform 1D finite difference code. Pokora [186] adapted the code to the solution presented by van Dam [185]. The published work using Richards´ principles of unsaturated flow were for the CP infiltration mode. The CF solution was derived in accordance to Sander [188]. A maximum infiltration distance of x = 0.03 m was assumed for modelling the linear preform infiltration. In order to account for the collision of the two melt fronts in the centre at x = 0.03 m, an impermeable (q = 0) boundary was introduced into the code. The result of the Preform 1D calculations were the local pressure P_{loc} (x,t) and local saturation S_{loc} (x,t).

5.4.6. Validation of the infiltration model

Three different preforms were used to validate the infiltration model: FA24, a Saffil™ fibre preform reported by Dopler *et al.* [113], and two particulate preforms, AOPC20 and TOPC10. The latter two represented the two extremes in terms of threshold pressure P_0 and specific permeability K_s, which were a result of the different pore structures, particle sizes and reactivity. The parameters for each preform are listed in Table 5.1.

In the CP mode, the Preform 1D code was validated using the reported FA24 preform infiltration results [113] and compared to the saturated flow calculation results based on Darcy´s law (Equation 27). Similar to Dopler *et al.* [113], an inlet pressure of 0.4 MPa and an infiltration period of 21 s were used. Values of P_{loc} were calculated using the data in Table 5.1 and the results are shown in Figure 5.11 a) in combination with the isobar of the threshold pressure $P_{0,\,FA24}$ of FA24.

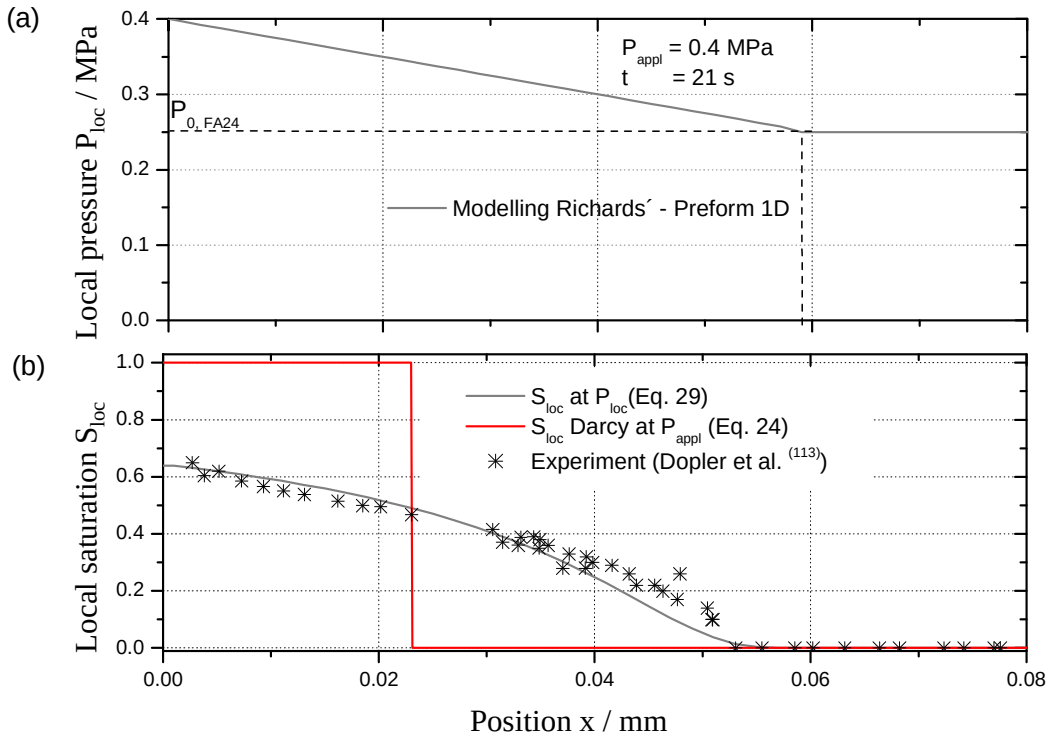

Figure 5.11 a) Modelling of local pressure P_{loc} of Saffil™ preform FA24 with Preform 1D. b) Resulting local saturation calculated using Equation 29 with experimental saturation data of Dopler *et al.* [113] (symbols) and in accordance to Darcy (Equation 24)

As the saturation function (Equation 29) was used, S_{loc} could be calculated from P_{loc} and the result is presented in Figure 5.11 b). This also shows local saturation results based on Darcy´s law and experimental results [113]. It is obvious that the modelling results of the Richards´ model are close to the experimental results. With the Preform 1D tool the experiments of Dopler *et al.* [113] could be reproduced satisfactorily. In contrast, full saturation up to a depth

of 0.023 m and nil saturation behind that point was found with Darcy´s model, demonstrating its inaccuracy.

Having validated the Preform 1D code for Saffil™ fibre preforms (FA24), focus turned to AOPC20. Based on the preform parameters listed in Table 5.1, the modelling results were compared to the experimental results of local saturation after CP infiltration at different pressures, as shown in Figure 5.12. As shown in Figure 5.11 b) the melt did not reach the end of the FA 24 preform and therefore the end drag phenomenon could be omitted which is similar to the experimental infiltration results of AOPC20 at a constant pressure of 0.8 MPa shown in Figure 4.39. In contrast, at 1.2 MPa, the melt fronts contacted each other and therefore influenced each other. In order to allow for this, the centre of the preform was set as an impermeable boundary in the Preform 1D code which led to a time dependent increase in saturation in front of it, as shown by the results at different infiltration times of 2, 4 and 16 s in Figure 5.12. At an early stage, a negative gradient toward higher x-values was found, whereas a homogenous saturation profile was reached at an extended pressurisation (16 s).

For applied pressures of 0.8 and 1.2 MPa at 16s, the calculated S_{loc} were homogenous at 0.23 and 0.61 respectively. At constant pressure, the respective saturation at the ingate (x = 0 m) was similar for different infiltration times. As, by definition, the ingate pressure is constant in the constant pressure mode, similar pressure and hence similar saturations were calculated for all infiltration times at the ingate. This behaviour is expressed by the saturation function in Equation 29 where all preform parameters were assumed to be constant during the entire infiltration process apart from the applied pressure P_{appl}.

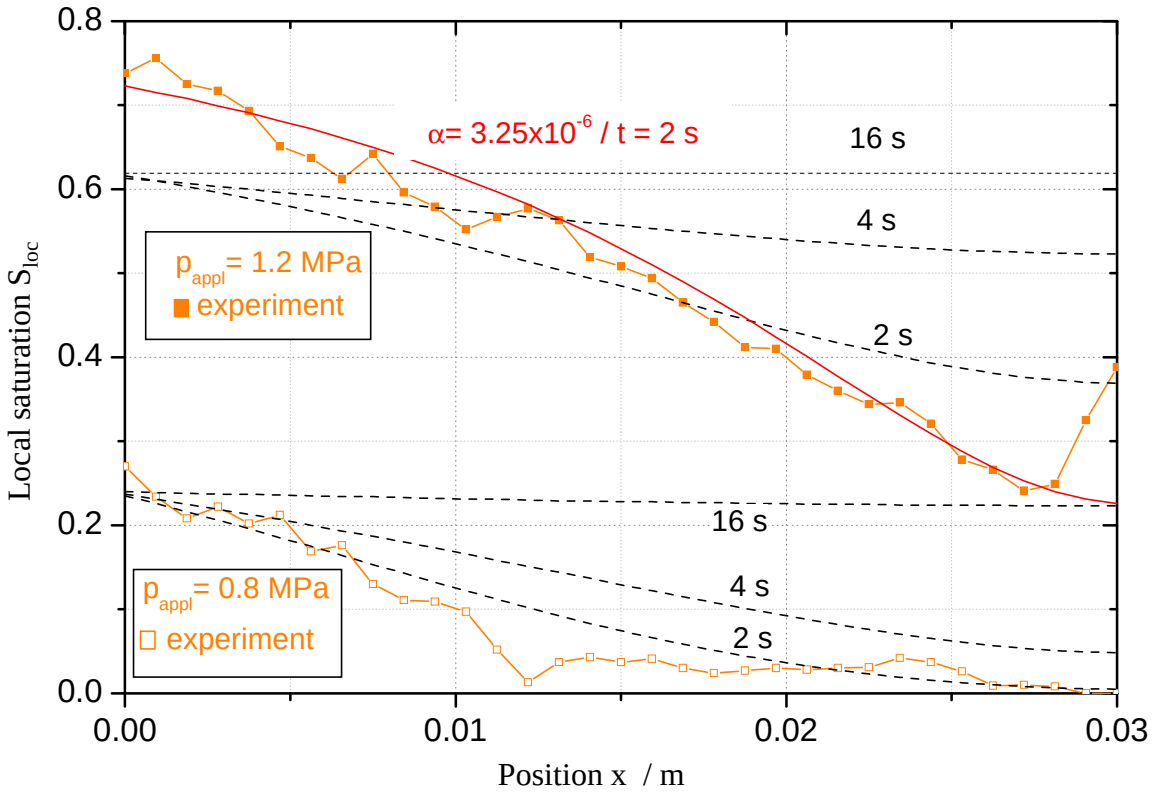

Figure 5.12 Experimental S_{loc} of MMC after infiltration of AOPC20 in CP mode at 0.8 and 1.2 MPa and modelling results after different infiltration periods (dashed lines) and variation of α for the applied pressure of 1.2 MPa (red line).

With only minor deviations between x = 0.007 and 0.015 m, at 0.8 MPa, the negative slope toward the centre observed in the experiments could be best reproduced at an infiltration time of 2 s. However, in the experiments the pressure was kept constant for more than 60 s. It is therefore assumed that metal flow stopped 2 s after pressurization and therefore prior to pressure release. This has to be attributed to solidification of the metal at the die walls as these were held below the solidus of the alloy.

The experimental results for a P_{appl} of 1.2 MPa showed a steep decrease in saturation which started from 0.73 and reached a minimum of 0.25 at x = 0.028 m. After that point, a steep increase could be observed. A symmetric saturation was assumed in CP infiltration but the centreline was shifted by 0.002 m toward the half of the investigated sample, which may be a result of marginal differences in permeability of the initial half of the preform.

The calculations at a P_{appl} of 1.2 MPa showed the best agreement with the experimental results at t = 2 s. However here there were deviations with overestimation when x > 0.017 m and underestimation at the surface (x = 0 m). As, by definition, the inlet saturation depends directly on P_{appl}, higher pressures than the nominal 1.2 MPa may be assumed. However, as a calibrated pressure system was used and the inlet saturation at 0.8 MPa could be modelled accurately, another effect may be responsible for the mismatch, such as variation of the shape parameter α during infiltration process. In order to achieve an improved fit of the experimental results for the calculations α was altered in steps of $0.25 \cdot 10^{-6}$ Pa^{-1} starting from the original value of $2.25 \cdot 10^{-6}$ Pa^{-1}. The best agreement was found at $\alpha = 3.25 \cdot 10^{-6}$ Pa^{-1} (Figure 5.12.) and therefore a change in α during infiltration at the higher pressure of 1.2 MPa seems likely. Variations in α may result from changes in the preform pore structure, such as widening of the pores due to the forces from the intruding pressurized metal. However, such widening would result in an expansion of the preform along the z-axis during the experiments. This could not be measured as chipping occurred in the lowest part of the preform (originally in contact with the bottom punch of the infiltration tool), presumably due to mechanical stresses during infiltration and cooling. Variations in α and its effect on constant pressure infiltration results should be investigated in more detail in the future work.

As the Preform 1D tool was found suitable to describe CP infiltration of FA and AOPC20, its capability for CF mode was investigated. As reported in section 4.7, the DSQC infiltration could not be stopped at an early stage in order to study partially filled preforms. However the preform infiltration curves were recorded and the model was validated against these experimental data (Figures 4.44 and 4.47). To do so the inlet pressure P_{met} at x = 0 m was calculated as a function of the integral saturation S_{int} for DSQC, in which v_0 was measured as 0.017 m/s. This value and the specific parameters of the preforms AOPC20 and TOPC10

listed in Table 5.1 and 5.3 were used for the calculations. Figure 5.13 shows the experimental infiltration curves and the calculated curves for saturated flow using Darcy equation (Equation 24) and unsaturated flow using the Preform 1D code.

For saturated flow, the capillary backpressure at the inlet is a steady linear function, starting from the P_0 and leading to maximum pressures of 3.7 and 5.9 MPa for AOPC20 and TOPC10 respectively. Even though good agreement was found up to S_{int} of 0.8, the subsequent steep increase in pressure was not reproduced. The deviations resulted from the saturated flow assumption, which implies that a fully saturated melt front advances until the impermeable wall is reached and at this point the preform is fully infiltrated.

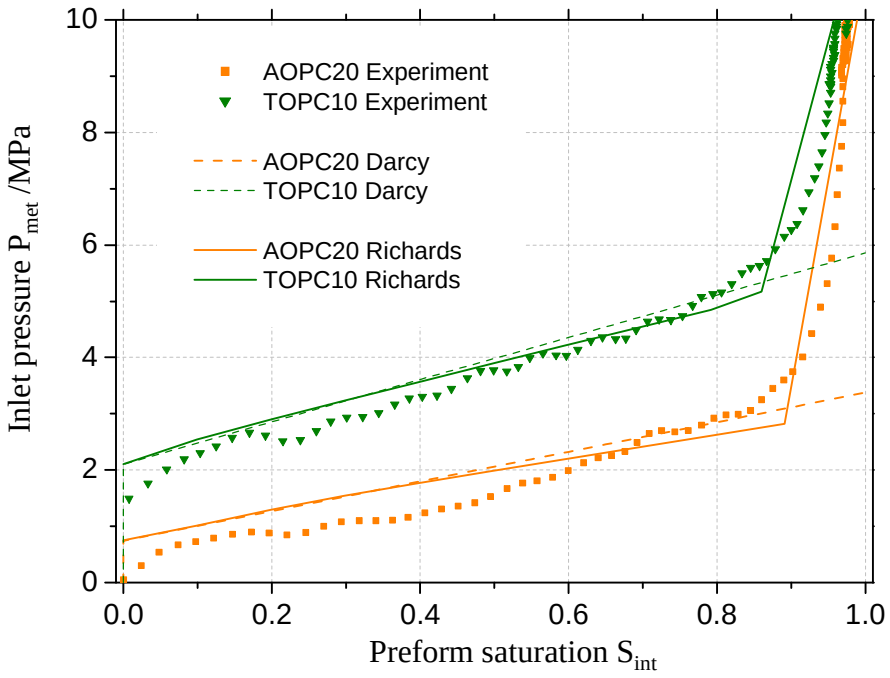

Figure 5.13 Experimental infiltration curves of AOPC20 and TOPC10 infiltrated with IS and modelling of infiltration curves using Darcy´s and Richards´ equations.

The Richards´ model showed the steep increase in pressure, similar to the experiments. This asymptotic behaviour is a result of the phenomenon of unsaturated flow which, by definition, leads to a decrease in permeability with increasing saturation. As long as the metal front moved unhindered, both models led to equal S_{int}. When the metal fronts influenced each other and the partial saturation had to be further increased, a steep increase in the applied pressure

resulted. This was the case for the S_{int} higher than 0.85 and 0.90 for TOPC10 and AOPC20, respectively. In contrast to the CP mode, accurate modelling could be achieved in the CF mode without variations in shape factor α, indicating a constant value for the entire infiltration period.

It was demonstrated that Richards´ model was valid even in the dynamic CF infiltration mode. Here, and for the constant pressure infiltrations, good agreement was observed with the Preform 1D code, providing that all the relevant parameters were well characterised. It is possible to use this tool to optimize the process parameters in order to minimize residual porosity in the MMC and maintain the preform integrity.

6. CONCLUSIONS

1. An aqueous processing route and subsequent partial sintering can be used to produce preforms from commercial Al_2O_3, TiO_2 and MgO powders with a minimum ceramic volume fraction (V_p) of 0.50 and open porosity between the grains (intragranular porosity).

2. To achieve a lower V_p of 0.30- 0.40, a pore forming additive (PFA) was incorporated into the slurry leading to a bimodal pore structure consisting of intragranular pores combined with larger cavities obtained by pyrolysis of the PFA during sintering. As a result, the target V_p could be reached by systematic variation of the processing parameters.

3. The lower limit of V_p for the cellulose pore former (PC) was 0.35, as below this value the preform was too weak to use to produce a MMC. In contrast, substitution of PC with carbon fibres (PF) allowed V_p to be lowered to 0.19.

4. A novel route for MgO preform and the subsequent MMC fabrication was investigated. The combination of MgO with the pore former PC gave an intermediate magnesium hydroxide during sintering. This offers the possibility for tailoring the preform specific surface area. The surface area achieved was from 0.7 to 5.7 m^2/g. The latter value is higher than that of the starting powder.

5. By combining a conventional AlSi alloy matrix with the ceramic preform through melt infiltration, a new material resulted with significantly enhanced mechanical and tribological properties in comparison to monolithic alloys and Saffil™ fibre-reinforced MMCs. Preform MMCs made from conventional fine powders with $V_p < 0.40$ have not to the authors knowledge been previously reported in the literature.

6. MMCs with tensile strength and elastic modulus 1.9 times higher (456 MPa / 148 GPa) than that of the pure infiltration alloy (241 MPa / 69 GPa) have been achieved. Additionally, the wear resistance was more than twice that of the alloy, whereas fracture toughness K_{IC} was only marginally lowered by the reinforcement.

7. The interpenetration fineness, which is defined by the pore structure of the initial preform and not V_p, plays a significant role on the MMC´s mechanical properties. Ceramic foam MMCs with similar ceramic loading, exhibiting large alloy ligaments between ceramic struts, gave mechanical properties lower than those of the pure alloy, but with superior tribological properties.

8. The literature contains a significant body of information on chopped alumina fibre preforms (Saffil™ - FA) where the upper limit of V_p was 0.25 and was therefore lower than the present particulate preforms. As would be expected, the current particulate preforms exhibited different infiltration behaviour. The specific permeability K_s was lower whereas the threshold pressure P_0 and infiltration curve shape factor α were higher, which in combination impeded low pressure infiltration compared to FA.

9. Because of the factors outlined in the above paragraph, the pressure for full infiltration was between 10 and 100 MPa which precluded constant pressure infiltration which is usually limited to a pressure of 15 MPa. The solution was to use squeeze casting (SQC) and high pressure die casting (HPDC) processes to achieve constant flux infiltration.

10. Similar to reported data on FA, the fabricated particulate preforms showed a process related anisotropy in specific permeability K_s. In the direction of higher permeability, the predominant one for fluid flow during melt infiltration, K_s ranged between 4.8 and $64.2 \cdot 10^{-14}$ m^2.

11. Reactivity between the infiltration alloy and the ceramics has a marginal influence on the threshold pressure P_0 , as demonstrated with the TiO_2 preforms. The reaction started after the majority of the porosity was infiltrated.

12. A novel method of characterizing the dynamic wetting of preforms by molten metal during infiltration has been developed based on parameters obtained from mercury intrusion porosimetry in combination with P_0 evaluated from constant flux infiltration.

13. A representative dynamic wetting angle θ_{dyn} could be measured only in preforms which had a homogenous pore size distribution, found in those fabricated with PFA. Here θ_{dyn}

ranged between 112 and 131° for the Al-Si alloy and 116 to 136° for the Al-Mg alloy having similar molar fractions of the alloying element. The addition of Mg showed no influence on wetting behaviour in the infiltration experiments even though the reactions found in the microstructure were more pronounced than those found with the Al-Si alloy.

14. The static wetting angles θ_{st} found in the sessile drop tests of similar systems ranged between 143 and 155° and therefore were significantly higher than θ_{dyn} and higher than those reported for pure Al on the ceramics used. This was a result of the Fe content in the alloy, leading to pinning of the droplet during holding on the substrate in combination with micro-intrusions into the substrate. Therefore the values of θ_{st} were not representative of the investigated systems.

15. High infiltration velocities and cooling rates in SQC and HPDC minimised the contact time between the melt and the reinforcement and therefore reactive metal-ceramic systems could be synthesised with minor reaction products, as shown for the AlSi-TiO_2 system.

16. An increase in the infiltration velocity resulted in greater preform compression. At the highest infiltration velocity, where the preform was infiltrated within 1 ms, the compression of the fabricated preforms was 35%. In contrast, high strength, foamed preforms were robust with low compression, but infiltration stresses resulted in severe cracking of the ceramic struts.

17. In contrast to previous work on preform infiltration models, the saturated flow model could not be confirmed in the present investigation, as unsaturated flow was found during constant pressure infiltration.

18. Based on the hydrogeological unsaturated flow model of Richards and the preform specific parameters, a one-dimensional flow code was applied successfully to simulate preform filling behaviour during constant flux and constant pressure infiltration with an impermeable centre boundary.

7. FUTURE WORK

The preform processing route with a cellulose pore former (PC) offers the unique possibility of tailoring the pore structure of MgO preforms by taking advantage of the hydrolysis of MgO. It offers the possibility of systematic variation of the grain size, pore size distribution and specific surface area, which influence the infiltration relevant parameters such as permeability and shape factor α. Furthermore the mechanical and tribological properties will be influenced.

The highest porosity (81%) of all self-fabricated preforms could be achieved with carbon fibres instead of cellulose incorporated in to the ceramic slurry. Their addition may be interesting for future investigations aiming to reduce the ceramic fraction of preform-MMCs below the lower limit of the present research (0.30).

As a result of the uniaxial green part pressing in combination with the pore former geometry, the self-fabricated preforms had the highest permeability in the xy- plane and therefore in the longer dimensions of the preforms . In order to get isotropic permeability, isostatic pressing of the preform may be appropriate to facilitate infiltration.

Only for the reactive TOPC10 was an optimum between reaction rate and infiltration behaviour was found in the dynamic ISQC mode. In order to get a better understanding, the infiltration mode and parameters should be investigated further, which offers the unique opportunity of high velocity infiltration in combination with consistent MMCs.

The bending test set-up will have to be improved to allow fracture of the non-reinforced alloy. In order to get an deeper understanding of the mechanical properties of the MMCs the microstructures should be investigated more thoroughly e.g. with TEM methods.

8. REFERENCES

1. Altenpohl, D.: *Aluminium- und Aluminiumlegierungen*, Springer-Verlag, (1965).
2. Clarke, D.R.: "Interpenetrating Phase Composites", Journal of the American Ceramic Society, **75** (4), (1992), 739-759.
3. Newnham, R.E., Skinner, D.P. and Cross, L.E. : "Connectivity and Piezoelectric-pyroelectric Composites", Material Research Bulletin, **13**, (1978), 525-536.
4. Gruzelski, J.E. and Closset, B.M.: "The Treatment of Liquid Al-Si Alloys", Proceedings of the American Foundrymen Society Conference, Des Plaines, IL, (1990), 13-15.
5. Saigal, A. and Berry, J.T. : "A Finite Element Method Analysis of the Effect of Chilling and Modification on Localized Yielding and Crack Initiation in AlSi-Alloys", Transactions of the American Foundry Society, **92**, (1984), 703-708.
6. Campbell, J. : *Castings*, Butterworth-Heinemann, Oxford, 2003.
7. Champion, J.A., Keen, B.J. and Sillwood, J.M. : "Wetting of Aluminium Oxide by Molten Aluminium and Other Metals", Journal of Materials Science, **4**, (1969), 39-49.
8. Zheng, Q. and Reddy, R.G.: "Mechanism of In Situ Formation of AlN in Al Melt Using Nitrogen Gas", Journal of Material Sciences, **39**, (2004), 141-149.
9. John, H. and Hausner, H. : "Influence of Oxygen Partial Pressure on the Wetting Behaviour in the System Al/Al_2O_3", J. of Materials Science Letters, **5**, (1986), 549-551.
10. Gourmi, L. and Joud, J.C. : "Auger Electron Spectroscopy Study of Aluminium-Tin Liquid Systems", Acta Metallurgica, **30**, (1982), 1397-1405.
11. Ransley, C.E. and Neufeld, H. : "The Solubility of Hydrogen in Liquid and Solid Aluminium", J. of the Institute of Metals, **74**, (1948), 599-620.
12. McLeod, A.D. and Gabryel, C.M.: "Kinetics of the Growth of Spinel $MgAl_2O_4$, on Alumina Particulate in Aluminium-Alloys containing Magnesium", Metallurgical Transactions A, **23A,** (1992), 1279-1283.
13. Iida, T. and Gruthrie, R.I.L. : *The Physical Properties of Liquid Metals*, Clarendon press, Oxford (1988).
14. Silva, M.P. and Talbot, D.E.J. : "Oxidation of Liquid Aluminum-Magnesium Alloys", Tech. Sessions, TMS Light Metals Committee, 118th Ann. Meeting, Las Vegas, Nevada, March 1989, 1035-1040.
15. Pai, B.C., Ramani, G. and Pillai, R.M. : "Role of Magnesium in Cast Aluminium Alloys Matrix Composites", Journal of Materials Science, **30** (8), (1995), 1903-1911.
16. Urquhart, A.W.: "Novel Reinforced Ceramics and Metals: A Review of Lanxides´s Composite Technologies", Materials Science and Engineering, **A144,** (1991), 75-82.
17. Rao, B.S. and Jayaram,V. : "New Technique for Pressureless Infiltration of Al Alloys into Al_2O_3 Preforms", Journal of Materials Research, **16**, (2001), 2906-2913.
18. Allen, B.C. : *Liquid Metals, Chemistry and Physics*, Marcel Dekker Inc., (1972).
19. Anson, J.P., Drew, R.A.L. and Gruzleski, J.E. : "The Surface Tension of Molten Al-Si-Mg Alloys under Vacuum and Hydrogen Atmospheres", Metallurgical and Materials Transactions B, **30B**, (1999), 1027-1032.
20. Keene, B.J. : "Review of Data for the Surface Tension of Pure Metals", International Materials Reviews, **38** (4), (1993), 157-192.
21. Rocher, J.P., Quenisset, J.M. and Naslain, R. : "Wetting Improvement of Carbon or Silicon-Carbide by Aluminium Alloys based on a K_2ZrF_6 Surface-Treatment-Application to Composite-Material Casting", Journal of Materials Science, **24** (8), (1989), 2697-2703.

22. Li, J.G., Coudurier, L. and Eustathopoulos, N. : “Wetting and Interfacial Energy in Liquid Metal-Ceramic Systems”, Journal of Materials Science, **24**, (1989), 1109-1116.

23. Shen, P., Fujii, H., Matsumoto, T. and Nogi, K. : “The Influence of Surface Structure on Wetting of Alpha-Al_2O_3 by Aluminium in a Reduced Atmosphere”, Metallurgical and Materials Transactions A, **35A** (2), (2004), 583-588.

24. Smith, J.W. : “Some Developments of Guggenheim's Simplified Procedure for Computing Electric Dipole Moments”, Transactions of the Faraday Society, **46**, (1950), 394-400.

25. Koerber, K. and Loehberg, K. : “Oberflächen- und Grenzflächenenergien von Aluminium-Silicium-Schmelzen”, Gießereiforschung, **23** (4), (1971), 173-177.

26. Pech-Canul, M., Katz, R. and Makhlouf, M. : “The Role of Silicon in Wetting and Pressureless Infiltration of SiC(p) Preforms by Aluminium Alloys”, Journal of Materials Science, **35,** (2000), 2167-2173.

27. Hansen, M. : *Binary Alloy Phase Diagrams*, Mc Graw Hill, 1958.

28. Emadi, D., Gruzleski, J.E. and Toguri, J.M. : “The Effect of Na and Sr Modification on Surface Tension and Volumetric Shrinkage of A356 Alloy and their Influence on Porosity Formation”, Metallurgical Transactions B, **24B**, (1993), 1055-1063.

29. Ibe, G. : “Grundlagen der Verstärkung in Metallmatrix-Verbundwerkstoffen”, Proceedings of the DGM Seminar: Metallische Verbundwerkstoffe - TU Clausthal- Germany, Ed. K.U. Kainer, (1994), 3-41.

30. Kaufmann, H., Auer-Knöbel, R. and Degischer, H.P. : “Elevated Temperature Properties of Short-fiber Reinforced AlSi9Cu3 Produced by Pressure Die-casting”, Zeitschrift für Metallkunde, **85**, (1994), 241–248.

31. Clyne, W.E. and Withers, P.J. : *An Introduction to Metal Matrix Composites*, Cambridge University Press, 1993.

32. Das, S.K., Ballard, C.P., and Marikar, F. : “Metal Matrix Composites in the 1990s and Beyond- A Market Overview”, *High performance composites for the 1990´s and beyond*, TMS, (1991), 487-497.

33. Jolly, M.R. : “Opportunities for Aluminium Based Fibre Reinforced Metal Matrix Composites in Automotive Castings“, The Foundryman, **83** (11), (1990), 509-513.

34. Kainer, K.U. : “Partikel, Fasern und Kurzfasern zur Verstärkung von metallischen Werkstoffen ”, Proceedings of the DGM Seminar: Metallische Verbundwerkstoffe - TU Clausthal - Germany, Ed. K.U. Kainer, (1994), 43- 64.

35. Dwivedi, R.: “Development of Advanced Reinforced Aluminum Brake Rotors”, Society of Automotive Engineers - SAE, Paper 950264, (1995).

36. Beffort, O. : “Metal Matrix Composites (MMCs): Properties, Applications & Machining”, Presentation 6. International IWF-Colloquium, 18/19.04.2002, Egerkingen- Switzerland, (2002).

37. Biermann, D. and Meister, D. : “Spanende Bearbeitung von faser- und partikelverstärkten Leichtmetall-Verbundwerkstoffen”, Proceedings of the DGM Seminar: Metallische Verbundwerkstoffe - TU Clausthal - Germany, Ed. K.U. Kainer, (1994), 261- 283.

38. Zhaowei, Z. and Nguyen, P.H.: “Grinding of Al/Al_2O_3 composites”, Journal of Materials Processing, **123**, (2002), 13-17.

39. Brown, A and Klier, E.M. : “Machinable MMC and Liquid Metal Infiltration Process for Making Same”; US-Patent 5511603, Chesapeake Composites Corporation, 1996.

40. Ejiofor, J.U. and Reddy, R.G. : “Developments in the Processing and Properties of Particulate Al-Si Composites”, JOM, **49** (11), (1997), 31-27.

41. Legzdins, C.F., Samarasekera, J.V. and Meech, J.A.: ” MMCX- An Expert System for Metal Matrix Composite Selection and Design”, Canadian Metallurgical Quarterly, **36** (3), (1997), 177-202.

42. Chawla, N. and Shen, Y.L. : “Mechanical Behaviour of Particle Reinforced Metal Matrix Composites”, Advanced Engineering Materials , **3** (6), (2001), 357-370.

43. Davis, L.C. and Allison, J.E. : “Residual Stresses and their Effects on Deformation Behaviour in Particle Reinforced MMC”, Metallurgical Transactions A, **24A,** (1993), 2487-2496.

44. Shi, S.; Taya, M.; Mori, T. and Mura, T.: "Dislocation punching from spherical inclusions in a metal matrix composite", Acta Metallurgica et Materialia **40** (11) (1992), 3141-3148.

45. Corbin, S.F. and Wilkinson, D.S. : “Low Strain Plasticity in a Particulate MMC”, Acta Metallurgica and Materialia, **42**, (1994), 1319- 1327.

46. Humphreys, F.J., Basu, A. and Djazeb, M.R. : “The Microstructure and Strength of Particulate Metal-Matrix Composites”, Conference Proceedings: MMC- Processing, Microstructure and Properties; 1991; Roskilde, Denmark, 51-66.

47. Taya, M. : “Strengthening Mechanism of Metal Matrix Composites”, Materials Transactions JIM, **32** (1), (1991), 1-19.

48. Wu, Y. and Lavernia, E.J. : “Strengthening Behaviour of Particulate Reinforced MMCs”, Scripta Metallurgica et Materialia, **27** (2), 173-178.

49. Long, S., Beffort, O., Cayron, C. and Kübler, J.: “Structure and Properties of SiCp/AlCuMg squeeze cast composites for structural applications ”, http://www.empa.ch/deutsch/fachber/abt126/1.3.hybrid/1.3.8.literatur_mmc/literatur/aluminium/particle_re/cimlss.pdf, 1-8, (1999).

50. Long, S., Beffort, O., Moret, G. and Thevoz, P. : “Processing of Al-based MMCs by Indirect Squeeze Infiltration of Ceramic Preforms on a Shot-Control High Pressure Die Casting Machine”, Aluminium, **76** (1-2), (2000), 82-89.

51. Kniewallner, L. : “Einsetzbarkeit des Druckgießverfahrens zur Herstellung von kurzfaserverstärkten Aluminium-Gußstücken”, Disseration Montanuniversität Leoben - Austria, 1992.

52. Prielipp, H., Knechtel, M., Claussen, N., Streiffer, S.K., Müllejans, H., Rühle, M. and Rödel, J. : “Strength an Fracture Toughness of Aluminum/Alumina Composites with Interpenetrating Networks”, Materials Science and Engineering, **A197**, (1995), 19-30.

53. Beyer, P. : *Verstärkung von Al-Bauteilen durch lokale In-Situ Synthese von Al_2O_3/Ti_xAl_y-Verbunden im Squeeze Casting*, Fortschritt-Berichte VDI, Reihe 5: Grund- und Werkstoffe/Kunststoffe, Band 643, 2002.

54. Peng, H.X., Fan, Z., Evans, J.R.G. and Busfield, J. : “Microstructure of Ceramic Foams”, Journal of European Ceramic Society, **20** (7), (2000), 807-813.

55. Hashin, Z. and Shtrikman, S. : “A Variational Approach to the Theory of the Elastic Behaviour of Multiphase Materials”, Journal of Mechanical Physics of Solids, **11** (2), (1963), 127-140.

56. Feest, E.A. : “Interfacial Phenomena in Metal Matrix Composites”, Composites, **25** (2), (1994), 75-82.

57. Rack, H.J. and Ratnaparkhi, P. : “Damage Tolerance in Discontiniously Reinforced MMCs”, JOM, **40** (11), (1988), 55-62.

58. Gesing, A.J. and Burger, G. : “Crack Stability and Crack Velocity Considerations in Fracture of Metal-Ceramic Composites”, *Processing of Ceramic and Metal Matrix Composites*, Edited by H. Mostaghaci, Pergamon Press, New York (1989), 71-79.

59. Aradhya, K.S. and Surappa, M.K. : “Estimation of Mechanical Properties of 6061 Al-SiCp Composites using FEM methods”, Scripta Metallurgica et Materialia, **25**, (1991), 817-823.

60. Couper, M.J. and Xia, K. : “Development of Microsphere Reinforced MMC”, Conference Proceedings: MMC-Processing, Microstructure and Properties, (1991), Roskilde- Denmark, 291-298.

61. Arsenault, R.J. and Shi, N.: “Dislocation Generation due to Difference between the Coeffients of Thermal Expansion”; Material Science and Engineering, **81** (1-2), (1986), 175-182.

62. Agrawal, P., Conlon, K., Bowman, K.J., Sun, C.T., Cichocki, F.R. and Trumble, K.P. : “Thermal Residual Stresses in Co-continuous Composites”, Acta Materialia, **51**, (2003), 1143–1156.

63. Nogowizin, B. : “Druckgußlegierungen und ihre Eigenschaften”, Druckguss-Praxis, April 2003, 161-168.

64. Hoffmann, M., Skirl, S., Pompe, W. and Roedel, J.: "Thermal Residual Strains and Stresses in Al_2O_3/Al Composites With Interpenetrating Networks", Acta Materialia, **47** (2), (1999), 565- 577.

65. Hoffmann, M., Fiedler, B., Emmel, T., Prielipp, H.; Claussen, N., Gross, D. and Roedel, J.: "Fracture Behaviour in Metal Fibre Reinforced Ceramics", Acta Materialia, **45** (9), (1997), 3609-3618.

66. Evans, A.G.: "Design and Life Prediction Issues for High-Temperature Engineering Ceramics and their Composites", Acta Materialia, **45** (23), (1997), 23-28.

67. Kolhe, R., Hui, C.Y., Ustundag, E. and Sass, S.L.: "Residual Thermal Stresses and Calculation of the Critical Metal Particle Size for Interfacial Crack Extension in Metal-Ceramic-Matrix Composites", Acta Materialia, **44** (1), (1996), 279-287.

68. Knechtel, M., Prielipp, H., Müllejans, H., Claussen, N. and Rödel, J.: "Mechanical Properties of Al/Al_2O_3 and Cu/Al_2O_3 Composites with Interpenetrating Networks", Scripta Metallurgica et Materialia, **31** (8), (1994), 1085- 1090.

69. Mizumoto, M., Murano, T. and Kagawa, A.: "Microstructure Control of Particle Reinforced MMC Fabricated by Low-Pressure Infiltration Process", Journal of the Japan Institute of Metals, **66** (4), (2002), 371-376.

70. Young, T. : "An essay on the cohesion of fluids", Phil. Transactions of the Royal Society London, **65** ,(1805), 98-102.

71. Naidich, J.V. : "Wettability of Solids by Liquid Metals", Progress in Surface and Membrane Science, **14**, (1981), 353-485.

72. Gallois, B.M. : "Wetting in Non-reactive Liquid Metal-Oxide Systems", JOM, **49** (6), (1997), 48-51.

73. Diemer, M., Neubrand, A., Trumble, K.P. and Rödel, J. : "Influence of Oxygen Partial Pressure and Oxygen Content on the Wettability in the Copper-Oxygen-Alumina System", Journal of the American Ceramic Society, **82** (10), (1999), 2825- 2832.

74. Kubaschewski, O. and Hopkins, B.E. : *Oxidation of Metals and Alloys*, Butterworth, London, 1968.

75. Rocha-Rangel, E., Becher, P.F. and Lara-Curzio, E. : "Reactive Wetting of Alumina by Molten Aluminium Alloys", Materials Science Forum, **442,** (2003), 97-102.

76. Shen, P., Fujii, H., Matsumoto, T. and Nogi ,K. : "Critical Factors Affecting the Wettability of Alpha-Alumina by Molten Aluminium", Journal of the American Ceramic Society, **87** (7), (2004), 1265-1273.

77. Saiz, E. and Tomasia, A.P. : "Kinetics of Metal-Ceramic Composite Formation by Reactive Penetration of Silicates with Molten Aluminium", Journal of the American Ceramic Society, **81** (9), 1998, 2381-2193.

78. Brewer, L. and Searcy, A.W. : "The Gaseous Species of the Al-Al_2O_3 System", Journal of the American Ceramic Society, **73** (11), (1951), 5308-5314.

79. Nakae, H., Inui, R., Hirata, Y., and Saito, H. : "Effect of Surface Roughness on Wettability", Acta Materialia, **46** (7), (1998), 2313-2318.

80. Sobczak, N., Asthana, R., Ksiazek, M., Radziwill, W. and Mikulowski, M. : "The Effect of Temperature, Matrix Alloying and Substrate Coatings on Wettability and Shear Strength of Al/Al_2O_3 Couples",: Metallurgical and Materials Transactions A , **35A** (3), (2004), 911-923.

81. Ksiazek, M., Sobczak, N., Mikulowski, M., Radziwill, W. and Surowiak, I. : "Wetting and Bonding Strength in Al/Al_2O_3 System", Materials Science and Engineering A, **324** (1-2), (2002), 162-167.

82. Li, J.G. : "Wetting and Interfacial Bonding of Metals with Ionocovalent Oxides", Rare Metals, **10** , (1992), 255-261.

83. John, H. and Hausner, H. : "Influence of Oxygen Partial Pressure on Wetting Behaviour in the System Al/Al_2O_3", Journal of Materials Science Letters, **5**, (1986), 549-551.

84. Asthana, R. : "An Analysis for Spreading Kinetics of Liquid Metal on Solids", Metallurgical and Materials Transactions A, **26** (5)**,** (1995), 1307-1311.

85. Gennes, P.G. : “Wetting: Statics and Dynamics”, Reviews of Modern Physics, **57** (3-1), (1985), 827-863.

86. Asthana, R. : “Dynamic Wetting Effects during Infiltration of Metals”, Scripta Materialia, **38** (8), (1998), 1203-1210.

87. Aksay, I.A., Hoge, C.E. and Pask, J.A. : “Wetting under Chemical Equilibrium and Non-Equilibrium Conditions”, Journal of Physical Chemistry, **78**1(12), (1974), 1178-1183.

88. Laurent, V., Chatain, D. and Eustathopoulos, N. : “Wettability of SiO_2 and Oxidized SiC by Aluminium”, Materials Science and Engineering A, **135**, (1991), 89-94.

89. Schmalzried, H. and Navrotsky, A. : *Festkörperthermodynamik*, Verlag Chemie, Weinheim, 1975.

90. Landry, K., Rado, C., Voitovich, R. and Eustathopoulos, N. : “Mechanism of Reactive Wetting: The Question of Triple Line Configuration”, Acta Materialia, **45** (7), (1997), 3079-3085.

91. Kritsalis, P., Coudurier, L. and Eustathopoulos, N. : “Contribution to the Study of Reactive Wetting in the $CuTi/Al_2O_3$ System”, Journal of Material Science, **26**, (1991), 3400-3408.

92. Kritsalis, P., Drevet, B., Valigna, N. and Eustathopoulos, N. : “Wetting Transitions in Reactive Metal/Oxide Systems “, Scripta Metallurgica et Materialia, **30** (9), (1994), 1127-1132.

93. Espié, L., Drevet, B. and Eustathopoulos, N. : “Experimental Study of the Influence of Interfacial Energies and Reactivity of Wetting in Metal/Oxide Systems”, Metallurgical and materials transactions A, **25A** (4), (1994), 599-605.

94. Friedrich, B., Hammerschmidt, J. and Steophasius, J.-C.: “Aluminothermische Reduktion von Titandioxid”, Erzmetall **56** (2), (2003), 82-93.

95. Sobczak, N., Stobierski, L., Radziwill, W., Ksiazek, M. and Warmuzek, M. : “Wettability and Interfacial Reactions in Al/TiO_2”, Surface and Interface Analysis, **36**, (2004), 1067-1070.

96. Arpon, R., Narciso, J., Louis, E. and Garcia-Cordovilla, C. : “Interfacial Reactions in Al/TiC Particulate Composites Produced by Pressure Infiltration”, Materials Science and Technology, **19** (9), (2003), 1225-1230.

97. Odegard, C. and Bronson, A. : “The Reactive Liquid Processing of Ceramic-Metal Composites”, JOM, **49** (6), (1997), 52-54.

98. Weirauch, D.A. : “Interfacial Phenomena Involving Liquid Metals and Solid Oxides in the Mg-Al-O System”, Journal of Materials Research, **3** , (1988), 729-739.

99. Nakae, H., Fujii, H. and Sato, K. : “Reactive Wetting of Ceramics by Liquid Metals”, Materials Transactions JIM, **33** (4), (1992), 400-406.

100. Shen, P., Fujii, H., Matsumoto, T. and Nogi-K.: “Critical factors affecting the wettability of alpha-alumina by molten aluminium”, Journal of the American Ceramic Society **87** (7), (2004), 1265-1273.

101. Zhou, X.B., and Hosson, M. : “Reactive Wetting of Liquid Metals on Ceramic Substrates”, Acta Materialia, **44** (2), (1996), 421-426.

102. Mortensen, A. : “Interfacial Phenomena in the Solidification Processing of MMC”, Materials Science and Engineering, **A135**, (1991), 1-11.

103. Garcia-Cordovilla, C., Louis, E. and Narciso, J. : “Pressure Infiltration of Packed Ceramic Particulates by Liquid Metals”, Acta Materialia, **47** (18), (1999), 4461-4479.

104. Asthana, R. and Rohatgi, P.Z. : “Melt Infiltration of Silicon Carbide Compacts” Zeitschrift der Metallkunde, **83** (12), (1992), 887-892.

105. Mortensen, A. and Michaud, V. : “Infiltration of Preforms by a Binary Alloy: Part I. Theory”, Metallurgical Transactions A, **21A** (7), (1990), 2534-2547.

106 Jonas, T.R., Cornie, J.A. and Russell, K.C. : “Infiltration and Wetting of Alumina Particulate Preforms by Aluminium and Aluminium-Magnesium Alloys”, Metallurgical and Materials Transactions A, **26A**, (1995), 1491-1497.

107. Travitzky, N.A. and Shlayen, A. : "Microstructure and Mechanical Properties of Al_2O_3/Cu–O Composites Fabricated by Pressureless Infiltration Technique", Materials Science and Engineering, **A244**, (1998), 154-160.

108. Cardinal, S., R'Mili, M. and Merle, P. : "Improvement of High Pressure Infiltration Behaviour of Alumina Platelet Preforms: Manufacture and Characterization of Hybrid Preforms", Composites Part A, **29A**, (1998), 1433–1441.

109. Rootare, H.M. and Prenzlow, C.F.: "Surface Areas from Mercury Porosimeter Measurements", Journal of Physical Chemistry, **71** (8),(1967), 2733-2743.

110. Leon, C.A.: "New perspectives in mercury porosimetry", Advances in Colloid and Interface Science **76-77**, (1998), 341-372.

111. Bear, J. : *Dynamics of fluids in porous media*, Dover Publications, 1988.

112. Mortensen, A., Masur, L.J., Cornie, J.A. and Flemings, M.C. : "Infiltration of Fibrous Preforms by a Pure Metal: Part I – Theory", Metallurgical Transactions A, **20A** (11), (1989), 2535-2547.

113. Dopler, T., Modaressi, A. and Michaud, V. : "Simulation of Metal Matrix Composite Isothermal Infiltration Processing", Metallurgical and Materials Transactions B, **31B** (4), (2000), 225-234.

114. Mattern, A. : *Interpenetrierende Metall-Keramik-Verbundwerkstoffe mit isotropen und anisotropen Al_2O_3-Verstärkungen*, Dissertation of the University of Karlsruhe, 2004.

115. Genuchten-Van, M.T.: "A closed form equation for predicting the hydraulic conductivity of unsaturated soils", Journal of the Soil Science Society of America, **44**, (1980), 892-898.

116. Cappleman, G.R., Watts, J.F. and Clyne, T.W. : "The Interface Region in Squeeze-Infiltrated Composites containing Delta-Alumina Fibre in an Aluminium Matrix", Journal of Materials Science, **20,** (1985), 2159-2168.

117. Kang, C.G. and Yun, K.S. : "Fabrication of MMC by the Die Casting Technique and the Evaluation of their Mechanical Properties", Journal of Materials Processing Technology, **62**, (1996), 116-123.

118. Jolly, M.R. and Haour, G.: "Fibre Reinforcement of Aluminium by Squeeze Casting", Proceedings of the Solidification Processing Conference, 21-24 Sept 1987, Sheffield, Ed. H. Jones and Beech, Institute of Metals, (1987), 505-509.

119. Hegeler, H., Buschmann, R. and Elstner, I. : "Herstellung von faserverstärkten Leichtmetallen unter Benutzung von faserkeramischen Formkörpern (Preforms)", Proceedings of the DGM Seminar: Metallische Verbundwerkstoffe - TU Clausthal - Germany, Ed. K.U. Kainer, (1994), 101-116.

120. Requena, G., Lasagni, F. and Degischer, H.P. : "Lokale Verformung in diskontinuierlich verstärktem Aluminium", Proceedings of the 14. Symposium Verbundwerkstoffe und Werkstoffverbunde, 02.-04. Juli 2003, Vienna – Austria , (2003), 171-176.

121. Mortensen, A. and Wong, T. : "Infiltration of Fibrous Preforms by a Pure Metal: Part III - Capillary Phenomena", Metallurgical Transactions A, **21A,** (1990), 2257-2263.

122. Michaud, M.J., Sommer, J.L. and Mortensen, A. : "Infiltration of a Fibrous Preform by a Pure Metal: Part V: Influence of Preform Compressibility", Metallurgical and Materials Transactions A, **30** (2), (1999), 471-482.

123. Lange, F.F., Velamakanni, B. and Evans, A. : "Method for Processing Metal-Reinforced Ceramic Composites", Journal of the American Ceramic Society, **73** (2), (1990), 388-393.

124. Cichocki, F.C., Trumble, K. and Rödel, J. : "Tailored Porosity Gradients via Colloidal Infiltration of Compression-Molded Sponges", Journal of the American Ceramic Society, **81** (6), (1998), 1661-1664.

125. Peng, H.X., Fan, Z., Evans, J.R.G. and Busfield, J. : "Microstructure of Ceramic Foams", Journal of European Ceramic Society, **20** (7), (2000), 807-813.

126. Xu, Y. and Chung, D.D.L. : "Low-Volume-Fraction Particulate Preforms for making Metal-Matrix Composites by Liquid Metal Infiltration", Journal of Materials Science, **33** (19), (1998), 4707–4709.

127. Corbin, S.F., Lee, J. and Qiao, X. : "Influence of Green Formulation and Pyrolyzable Particulates on the Porous Microstructure and Sintering Characteristics of Tape Cast Ceramics", Journal of the American Ceramics Society, **84** (1), (2001), 41-47.

128. Mattern, A., Oberacker, R. and Hoffmann, M. : "Multiphase Ceramics by Computer-Controlled Pressure Filtration", Journal of the European Ceramic Society, **24** (10-11), (2004), 3219-3225.

129. Konopka, K., Wodzynski, M. and Szafran, M. : "Fabrication of Al_2O_3-Al Composites by Infiltration Method", Proceedings of the 12th International Scientific Conference, Achievements in Mechanical and Material Engineering, Gliwice-Poland, (2003), 491-494.

130. Cayron, C. : *TEM Study of Interfacial Reactions and Precipitation Mechanisms in Al_2O_3 Short Fiber or High Volume Fraction SiC Particle Reinforced Al-4Cu-1Mg-0.5Ag Squeeze-Cast Composites*, Dissertation EPFL- Ecole Polytechnique Fédérale de Lausanne- Switzerland., 2000.

131. Nagata, S. and Matsuda, K. : "Effects of some Factors on the Critical Preheating Temperature of Particles in Producing Metal-Particle Composites by Pressure Casting", Journal of the Japan Foundrymen Society, **53** (12), (1981), 35-43.

132. Otte, B. and Reichstein, S. : German Patent DE10202184C1, *Lasernitrieren von Aluminiumbasis-Verbundwerkstoffen*, 2003.

133. Molina, J.M., Saravanan, R.A., Arpon, R., Garcia-Cordovilla, C., Louis, E. and Narciso, J. : "Pressure Infiltration of Liquid Aluminium into Packed SiC Particulate with a Bimodal Size Distribution", Acta Materialia, **50** (2), (2002), 247-257.

134. Weber, L., Grüningen, C. and Frigeni, N. : "Entwicklung neuer teilchenverstärkter MMCs mit Cu- und Ag-Matrix für hohe thermische Leitfähigkeit und geringe thermische Dehnung", Proceedings of the 14. Symposium Verbundwerkstoffe und Werkstoffverbunde, July 2003, Vienna- Austria , (2003), 802-807.

135. Ghomashchi, M.R. and Vikhrov, A. : "Squeeze Casting: An Overview", Journal of Materials Processing Technology, **101** (1-3), (2000), 1-9.

136. Catterjee, S. and Daas, A.A. : "Effects of Pressure on Solidification of some Commercial Aluminium-Base Casting Alloys", The British Foundryman, **11**, (1990), 420-427.

137. Epanchistov, O.G. : "Structure and Properties of Metals Solidified under High Pressure", Russian Casting Production, **6**, (1972), 34-37.

138. Papworth, A. and Fox, P.: "Oxide film casting defects in squeeze cast metal matrix composites", Materials Letters **29**, (1996), 209-213.

139. Eskin, D., Du; Q., Ruvalcaba, D. and Katgerman, L. : "Experimental Study of Structure Formation in Binary Al-Cu Alloys at Different Cooling Rates", Materials Science and Engineering A; **405 (1-2),** (2005), 1-10.

140. Levi, C.G., Abbaschian, G.J. and Mehrabian, R. : "Interface Interactions During Fabrication of Aluminium Alloy- Alumina Fiber Composites", Metallurgical Transactions A, **9** (5), (1978), 697-702.

141. Campbell, J. : "The Concept of Net Shape for Castings", Materials and Design, **21** (4), (2000), 373-380.

142. Fagschlunger, C., Eichlseder, W., Sonsino, C.M., Poetter, K., Brune, M. and Gaenser, H.P. : "Abschätzung der tolerierbaren Oxidhautgröße in schwingend belasteten Druckgussbauteilen", Giesserei Rundschau, **52** (3-4), (2005), 60-66.

143. Brunhuber, E.: *Praxis der Druckgussfertigung*, Schiele und Schön, Berlin, 1991.

144. Khalifa, W., Samuel, F-H. and Gruzleski, J.E.: "Iron intermetallic phases in the Al corner of the Al-Si-Fe system", Metallurgical and Materials Transactions A; **34A** (2), (2003), 807- 825.

145. Flores, V., Sukiennik, M., Castillejos, E., Acosta, G and Escobedo, B.: "A kinetic study on the nucleation and growth of the Al8FeMnSi2 intermetallic compound for aluminum scrap purification", Intermetallics, **6** (3), (1998), 217- 227.

146. Rasmussen, N.W., Hansen, P.N. and Hansen, S.F. : "High Pressure Die Casting of Fibre Reinforced Aluminium by Preform Infiltration", Materials Science and Engineering A **135**, (1991), 41-43.

147. Eriksson, G. and Hack, K. : “Chemsage: A Computer-Program for the Calculation of Complex Chemical-Equilibria”, Metallurgical Transactions B, **21** (6), (1990), 1013-1023.

148. European Standard EN 1706, *Aluminium and aluminium alloys. Castings. Chemical composition and mechanical properties*, 1998.

149. Munz, D. and Fett, T. : *Ceramics*, Springer-Verlag, 1999.

150: FACTSAGE: Thermodynamic Software package, Version 5.2, GTT Technologies, Aachen -Germany.

151. Kingery, W.D., Bowen, H.K. and Uhlmann, D.R. : *Introduction to Ceramics*, Wiley Interscience Publication, 1976.

152. Gmelin, L. : *Handbuch der anorganischen Chemie*, Deutsche Chemische Gesellschaft, 1976.

153. Micrometrics Corporation Georgia-USA: Operators Manual ASAP 2010, 1997.

154. DMC^2, *Data sheet 90263*, Cerdec AG, Germany, 2001.

155. Staudenecker, D. : *Entwicklung von porösen Keramik-Preforms und Herstellung von Metall-Keramik-Verbundwerkstoffen*, Diploma Thesis FH Aalen- Germany, 2001.

156. SGL Carbon group, online data sheet: *SIGRAFIL C – milled or pelletized carbon fiber*, www.sgl-carbon.com, 12.04.2006.

157. J.Rettenmaier & Söhne GmbH+Co.KG, online data sheet: *Arbocell P290*, www.jrs.de. 13.04.2006.

158. Nagel, A., Staudenecker, D., Huchler, B., Mattern, A., Neubrand, A. and Ulrich, O.: *Final report of the research project “Interpenetrierte Metall-Keramik-Verbundwerkstoffe (Preform-MMC) für thermisch und tribologisch hochbeanspruchte Leichtbauteile”*, Hochschule Aalen - Germany, 2006.

159. German Standard DIN 51918: *Bestimmung der Rohdichte nach der Auftriebsmethode und der offenen Porosität durch Imprägnieren mit Wasser*, November 1986.

160. Lide, D.R. : *CRC Handbook of Chemistry and Physics*, 76th Edition, CRC Press, 1995.

161. German Standard DIN-ENV 658: *Mechanische Eigenschaften von keramischen Verbundwerkstoffen bei Raumtemperatur*, May 1993.

162. Sambrook, R. : US Patent: 20040094284, Dytech Corporation LTD; *Bicontinious composites*, 2004.

163. Schneele, T. : *Gefügedesign zur Zähigkeitssteigerung von Metall-Matrix-Verbundwerkstoffen*, Diploma thesis FH Aalen- Germany, 2001.

164. Nagel, A., Staudenecker, D., Huchler, B., Schneider, G., Pfeifer-Schäller, I., and Klein, F. : “Preform-Verstärkung von Druckgussteilen”, Proceedings of VDG Giessereisymposium-FH Aalen-Germany, 2003, 71-77.

165. Bernthaler, T., Nagel, A., Huchler, B., Barth, T., Schneider, G. and Smolej, V. : “Quantitative Gefügeanalyse und Eigenschaftskorrelation an Metall-Keramik-Verbundwerkstoffen”, Proceedings of DGM Metallographie-Tagung 2004, Düsseldorf –Germany , 44-60.

166. American Standard ASTM-E 1876-99, *Standard Test Method for Dynamic Young´s Modulus by Impulse Excitation of Vibration*, 1999.

167. European Standard EN 843-1, *Monolithic Ceramics: Mechanical Properties at Room Temperature. Part 1: Bending test*, 1997.

168. European Standard EN 843-5, *Monolithic Ceramics: Mechanical Properties at Room Temperature. Part 5: Statistics*, 1997.

169. Kübler, J.J. : *Fracture Resistance Testing of Monolithic and Composite Brittle Materials*, ASTM STP 1409, (Editors.: J.A. Salem, G.D. Quinn, M.G. Jenkins), American Society for Testing and Materials, West Conshohocken, PA, USA, 2002, 93-106

170. Optimol Triboligical Testing, *Manual SRV II testint system*, 2000.

171. Gmelin, L. : *Handbook of Inorganic and Organometallic Chemistry*, Online Version of MDL Information Systems GmbH, 2005. Gmelin Institut fuer Anorganische Chemie und Grenzgebiete der Max-Planck-Gesellschaft zur Foerderung der Wissenschaften, Version 4 - June 2005.

172. Quested, P.N., Dinsdale, A.T., Robinson, J, Mills, K.C. and Hunt, J.D.: "The Prediction of the Thermophysical Properties and the Solidification Path of Commercial Alloys", preliminary version handed over to Richard Harding – University of Birmingham - to be published, 1-38.

173. Irmscher, S.: *Dispersability of carbon fibres in a ceramic slurry*, Student research project report, University of Applied Sciences Aalen, Germany, 2005.

174. Schumann, H. : *Metallographie*, Deutscher Verlag für Grundstoffindustrie, Leipzig, 1991.

175. Neubrand, A.: "Metall-Keramik-Verbundwerkstoffe für die Automobilindustrie", Konstruktion, **9**, (2006), 10-11.

176. Chan, K.S., Jones, P. and Wang, Q.: "Fatigue Crack Growth and Fracture Paths in Sand Cast B319 and A356 Aluminium Alloys", Materials Science and Engineering A, **341** (1-2), (2003), 18-34.

177. Ogrisa, E., Wahlen, A., Lüchinger, H. and Uggowitzer, P.J.: "On the Silicon Spheroidization in Al–Si Alloys", Journal of Light Metals, **2** (4), (2002), 263-269.

178. Ogrisa, E., Wahlen, A., Lüchinger, H. and Uggowitzer, P.J.: "On the Silicon Spheroidization in Al–Si Alloys", Journal of Light Metals, **2** (4), (2002), 263-269.

179. Kounga Njiwaa, A.B., Fett, T., Lupascua, D.C. and Rödel, J.: "Effect of Geometry and Electrical Boundary Conditions on R-curves for LZT ceramics", Engineering Fracture Mechanics, **73** (3) (2006), 309-317.

180. Kuang, J.P., Harding, R.A. and Campbell, J. : "Investigations into Refractories as Crucible and Mould Materials for Melting and Casting of Gamma-Ti-Al alloys", Materials Science and Technology, **16** (11-12), (2000), 1007-1016.

181. Choudhary, V.R.; Pandit, M.Y.: "Surface Properties of Magnesium Oxide obtained from Magnesium Hydroxide: Influence on Preparation and Calcination Conditions of Magnesium Hydroxide", Applied Catalyst **71** (2), (1991), 266-274.

182. Wagner, G.W., Bartram, P.W., Koper, O. and Klabunde, K.J.: "Reactions of VX, GD, and HD with nanosize MgO", Journal of Physical Chemistry B **103** (16), (1999), 3225-3228.

183. Capart, R., Khezamia, L. and Burnhamb, A.K.: "Assessment of Various Kinetic Models for the Pyrolysis of a Microgranular Cellulose" , Thermochimica Acta, **417** (1), (2004), 79–89.

184. Gulkova, D., Solcova, O. and Sradzil, M.: "Preparation of MgO Catalytic Support in Shaped Mesoporous High Surface Area Form", Microporous and Mesoporous Materials, **76** (1-3);. 2004, 137-149.

185. Dam, J.C.: *Field-scale water flow and solute transport*, Doctoral Thesis Wageningen University - The Netherlands, http://library.wur.nl/wda/dissertations/dis2836.pdf, 2000.

186. Pokora, E.: "Preform 1D: Modelling of variably saturated flow in particulate preforms"; Introdution to the finite difference code - Preform 1D", ARGE Metallguss, Aalen-Germany, 2005.

187. Niu, J.P., Sun, F.X., Jin, T., Yong, K.N., Guan, H.R. and Hu, Z.Q.: "Investigation into Deoxidation during Vacuum Induction Melting of Nickel Base Alloys using CaO crucibles", Materials Science and Technology, **19**, (2003), 435-439.

188. Sander, G.C., Parlange, J.Y., Kühnel, V., Hogarth, W.L., Lockington, D. and O'Kane, J.P.J.: "Exact Nonlinear Solution for Constant Flux Infiltration", Journal of Hydrology, **97** (3-4), (1988), 341-346.